

Electronic Theses and Dissertations, 2004-2019

2010

Near-field Optical Interactions And Applications

David Haefner
University of Central Florida

 Part of the [Electromagnetics and Photonics Commons](#), and the [Optics Commons](#)
Find similar works at: <https://stars.library.ucf.edu/etd>
University of Central Florida Libraries <http://library.ucf.edu>

This Doctoral Dissertation (Open Access) is brought to you for free and open access by STARS. It has been accepted for inclusion in Electronic Theses and Dissertations, 2004-2019 by an authorized administrator of STARS. For more information, please contact STARS@ucf.edu.

STARS Citation

Haefner, David, "Near-field Optical Interactions And Applications" (2010). *Electronic Theses and Dissertations, 2004-2019*. 4312.
<https://stars.library.ucf.edu/etd/4312>

NEAR-FIELD OPTICAL INTERACTIONS AND APPLICATIONS

by

DAVID P. HAEFNER

B.S. East Tennessee State University, 2004

M.S. University of Central Florida, 2007

A dissertation submitted in partial fulfillment of the requirements
for the degree of Doctor of Philosophy
in the College of Optics and Photonics
at the University of Central Florida
Orlando, Florida

Spring Term
2010

Major Professor: Aristide Dogariu

© 2010 David P. Haefner

ABSTRACT

The propagation symmetry of electromagnetic fields is affected by encounters with material systems. The effects of such interactions, for example, modifications of intensity, phase, polarization, angular spectrum, frequency, etc. can be used to obtain information about the material system. However, the propagation of electromagnetic waves imposes a fundamental limit to the length scales over which the material properties can be observed. In the realm of near-field optics, this limitation is overcome only through a secondary interaction that couples the high-spatial-frequency (but non-propagating) field components to propagating waves that can be detected. The available information depends intrinsically on this secondary interaction, which constitutes the topic of this study. Quantitative measurements of material properties can be performed only by controlling the subtle characteristics of these processes.

This dissertation discusses situations where the effects of near-field interactions can be (i) neglected in certain passive testing techniques, (ii) exploited for active probing of static or dynamic systems, or (iii) statistically isolated when considering optically inhomogeneous materials. This dissertation presents novel theoretical developments, experimental measurements, and numerical results that elucidate the vectorial aspects of the interaction between light and nano-structured material for use in sensing applications.

To my family, friends, coaches, and teachers who continue to inspire me to work hard.

ACKNOWLEDGMENTS

No words I write can express the gratitude and appreciation I have for all that my advisor has taught me throughout my graduate studies. After my first semester, when I had all but given up on pursuing a career in optics, Professor Dogariu took time out of his busy schedule to take me out for coffee and discuss the possibilities of working in his lab. No matter what topic was troubling me, be it research or life, Dr. Dogariu was always available to discuss it. I couldn't ask for a better mentor, it really has been a privilege working for him.

I would like to thank my committee for their constructive remarks on my thesis work and for sharing their expertise and knowledge in optics.

Of course, nobody completes a PhD on their own, and the best work is produced by the minds of many people working together. The Photonics Diagnostics of Random Media Group here at CREOL has provided me with a wonderful environment to work and learn in. The members of the Random Group have always gone above and beyond the role of colleagues and are always willing to lend a hand in figuring out troubling problems. I specifically would like to thank Dr. Adela Apostol for taking the time out of writing her thesis to teach me NSOM and experimental near-field optics. I would like to thank Dr. Erwan Baleine for teaching me MatLab and for always being a great friend, who I could count on. I would also like to especially acknowledge Dr. Sergey Sukhov, a great man and researcher; he has taught me so much about optics, and I have really enjoyed working with him for the last three years. The rest of the Random Group, both past and present: Janghwan Bae, Dr. Gabriel Biener, John Broky, Lorrene

Denney, Kyle Douglass, Dr. Jeremy Ellis, Dana Kohlgraf-Owens, Thomas Kohlgraf-Owens, Dr. Chaim Schwartz, and Dr. Mohamed Salem, and honorary member Dr. Clara Rivero-Baleine, I can't thank you enough for everything.

One of the greatest things about working at CREOL is the quality of the people, and their willingness to share their expertise. The faculty and staff have made my graduate experience one that I will never forget. Also, my fellow students, my friends here at CREOL, have greatly added to this experience by making coming to work everyday enjoyable.

Clann roimh uile--Gaelic for family comes first. My family has always supported me in everything I have ever done and I wouldn't have accomplished much of anything with out their support. Mom, Dad, Bob, Jess, KC, Grandma, and everyone else, thank you so much for always being there for me, and I love you all very much (and I expect all of you to read the rest of this document).

Throughout my graduate work I was fortunate enough to become an honorary family member of the Souto-Xavier family. Mae, Pai, Debora, Daniel, Fabiana, Brandon, Patricia, Luciana, and Shadow, thank you so much for always being there for me and supporting me. I would like to thank the Ireys family for supporting me when I first started CREOL; I don't think I would have made it through the start without their support. Mi hermano Dr. Oscar Martinez; thanks for everything. I would also like to thank my newest family, the Arriaran - De La Fuente family; it is so wonderful to have such loving and inspirational people as family.

And finally, I would like to thank my beautiful wife, mi esposita bonita. Tati, you are my life, and I can't thank you enough for always being there and supporting me. I can't wait to start the next chapter of our life together. Te amo mas que a nadie.

TABLE OF CONTENTS

LIST OF NOMENCLATURE	ix
LIST OF FIGURES	x
LIST OF TABLES	xvii
CHAPTER 1: OUTLINE – SCOPE OF THESIS.....	2
CHAPTER 2: OPTICAL NEAR-FIELDS - GENERAL CONCEPTS	6
2.1. Field-Material Interaction - Scattering.....	8
2.2. The Resolution Limit	14
2.3. Experimental Methods	21
2.4. Numerical Techniques	26
2.5. Statistical Optics	32
CHAPTER 3: PASSIVE PROBING OF COMPLEX NEAR-FIELDS	38
3.1. Redistribution of Energy in Single Scattering	39
3.2. Angular Momentum Conservation	44
3.3. Observing Direction of Intermediate-Field Energy Flow	50
3.4. The Virtual Shift and Spin Hall Effect for Light	53
3.5. Summary	55
CHAPTER 4: NEAR-FIELD INTERACTIONS IN SIMPLE MATERIAL SYSTEMS	57
4.1. Coupled Scattering from Small Spheres.....	58
4.2. Numerical Modeling Interaction in Larger Systems.....	63

4.3.	Dynamical / Mechanical Effects on Interaction in Large Systems.....	67
4.4.	Observing Coupling Effects in the Near-Field	82
4.5.	Summary	86
CHAPTER 5: NEAR-FIELD SCATTERING IN COMPLEX MEDIA		88
5.1.	Scale Dependent Optical Response	90
5.2.	Intensity Statistics of Near-Field Experiments	96
5.3.	Local Anisotropic Polarizability of Inhomogeneous Media.....	104
5.4.	Summary	114
CHAPTER 6: STOCHASTIC POLARIMETRY FOR NEAR-FIELD SCATTERING.....		116
6.1.	Stochastic Scattering Polarimetry	118
6.2.	Task Optimized Stochastic Scattering Polarimetry	134
6.3.	Stochastic Polarimetry Applied to Near-Field Measurements.....	145
6.4.	Summary	153
CHAPTER 7: CONCLUSIONS AND SUMMARY OF ORIGINAL CONTRIBUTIONS		155
7.1.	Publications and Presentations.....	161
APPENDIX: SUPPORTING MATERIALS		165
A.	Derivation of Abbe-Rayleigh Resolution Limit.....	166
B.	Convolution Method Details for CDA	175
C.	Derivation of Optical Forces.....	176
D.	Sub-sampling and Non-Gaussian Statistics	187
E.	Additional Details for SSP	191
LIST OF REFERENCES.....		197

LIST OF NOMENCLATURE

u	Scalar notation
\mathbf{u}	Vector notation
$\hat{\mathbf{u}}$	Unit vector notation
$\bar{\mathbf{u}}$	Tensor notation
CDA	Coupled Dipole Approximation
CDA SLAB	Coupled Dipole Approximation with 2D periodic boundary conditions
LAP	Local Anisotropic Polarizability
MMC	Metropolis Monte Carlo
NSOM	Near-field Scanning Optical Microscope
OAM	Orbital Angular Momentum
OB	Optical Binding or Optically Bound
PDF	Probability Density Function
SAM	Spin Angular Momentum
SHESS	Spin Hall Effect in Scattering from Spheres
SOI	Spin-Orbit Interaction

LIST OF FIGURES

Figure 2-1 An incident wave impinging on a scatterer of some volume V_p and permittivity $\epsilon_p(\mathbf{r})$	9
Figure 2-2 Sphere of size a excited by radiation of wavelength λ . The different radiation zones are (i) near-field region $d \ll r \ll \lambda$, (ii) the intermediate-field $d \ll r \sim \lambda$, and (iii) the far-field $d \ll \lambda \ll r$	12
Figure 2-3 Plots of the normalized electric field magnitude of a small scatterer (electric dipole) polarized in the x direction at distances of 0.1λ (A), 0.37λ and 10λ (C)	13
Figure 2-4 Coupling evanescent fields to propagating one in a second medium	18
Figure 2-5 Schematic of detection of evanescent waves by diffraction or scattering	19
Figure 2-6 Schematic of tapered optical fiber probe. (A) shows a cartoon representation of the path the light travels. (B) shows a tapered cantilevered fiber probe used for a beam bounce method of monitoring the amplitude of vibration for feedback (Image from www.nanonics.co.il/) (C) shows a probe mounted to a tuning fork, (Image from www.azonano.com) another method for monitoring feedback	22
Figure 2-7 Schematic of Nanonics NSOM -100, where all three measurement modalities of emission (transmission or reflection far-field detection), collection (transmission or reflection far-field illumination), and dual (emission and collection) are available	24
Figure 2-8 Coupled dipole approximation of a sphere by an array of dipoles (small scatterers)	29
Figure 2-9 Intensity PDF for large number of random waves interfering having a uniform phase distribution	36
Figure 3-1 Intensity distributions in the plane (blue) and perpendicular to the plane (red) of a linear polarized excitation for three different observation distances $r = 0.25\lambda$ (A), $r = 1.5\lambda$ (B) and $r = 10\lambda$ (C)	40
Figure 3-2 Angular intensity distributions in the plane (blue) and perpendicular to the plane (red) of a linear polarized excitation for three different observation distances $r = 0.25\lambda$ (A), $r = 1.5\lambda$ (B) and $r = 10\lambda$ (C)	41

Figure 3-3 Polarization state of the scattered field measured at a distance r from a scatterer excited with a field linearly polarized along x . The observation distances are $r = 0.25\lambda$ (A), $r = 1.5\lambda$ (B) and $r = 10\lambda$ (C)..... 43

Figure 3-4 Polarization state of the scattered field measured at a distance r from a scatterer excited with a circularly polarized field. The observation distances are $r = 0.25\lambda$ (A), $r = 1.5\lambda$ (B) and $r = 10\lambda$ (C)..... 44

Figure 3-5 Distribution of Poynting vector in the x - z plane (A), y - z plane (B) and x - y plane (transverse to the direction of excitation) for a 100nm radius sphere for the case of linear polarization along the x direction with a wavelength $\lambda=532\text{nm}$ 46

Figure 3-6 Distribution of Poynting vector in the x - z plane (A), y - z plane (B) and x - y plane (transverse to the direction of excitation) for a 100nm radius sphere for the case of circular polarization with a wavelength $\lambda=532\text{nm}$ 47

Figure 3-7 (A) In the far field, the perceived location of the volume of the interaction is shifted by an about Δ . The shift is in opposite directions for the different circularly polarized excitations states (blue and red curves) and is equal to 0 for any linearly polarized excitation state (green curve). This transversal shift Δ occurs in any plane Σ and its absolute value depends on the angle θ with respect to the forward scattering direction. 48

Figure 3-8 Poynting vector field lines projected on the plane perpendicular to the direction of excitation and containing the center of the scattering sphere. Different size spheres, (a) smaller than the wavelength λ and (b) larger than λ , exhibit a spiraling of the flow of energy in the intermediate region. Most interesting is the winding of Poynting vector field lines in (b) due to the complex process of scattering from large spheres (Results are presented using an adaptation of the Matlab vector field visualization toolbox []). 50

Figure 3-9 Schematic of the experimental setup using a single mode optical fiber as a means for sensing local power flow direction. 51

Figure 3-10 Comparison between the analytical prediction (a) and the experimental results (b) for the coupled power through a single mode fiber scanned across a polystyrene sphere of $4.6\mu\text{m}$ diameter. The graphs depict the difference between the scattered intensities corresponding to pure states of excitation plotted as a function of fiber's position with respect to the center of the sphere. 52

Figure 3-11. (A) A beam of light incident on a planar refractive index gradient, (B) beam shifts observed in far-field corresponding to incidence in pure states of polarization (right circular, left circular), and (C) the observable result corresponding to an incident beam in a mixed state. (D) A plane wave incident on a planar refractive index gradient, (E) the far-field shifts corresponding to incidence in pure states of polarization, and (F) the result of an incident plane wave in a mixed state of polarization. (G) A plane wave scattering from a sphere, (H) the transversal shifts in the perceived sphere center as observed in far-field for pure incident states, and (I) the result of scattering for incident wave in a mixed state. 54

Figure 4-1 Schematic of two coupled sphere geometry..... 58

Figure 4-2 Plot of extinction cross section for two 10nm polystyrene interacting spheres normalized to the extinction cross section for independent spheres when the exciting polarization is along the direction of separation (blue) and perpendicular to the separation (red) with a wavelength of 532nm..... 61

Figure 4-3 Extinction cross section for two interacting spheres normalized by extinction cross section for independent spheres varying the angle of the applied linear polarization state to the separation vector (A) keeping one sphere fixed and varying the location of the other (B) a comparative plot with collinear to the separation (blue) and perpendicular to the separation (red). 62

Figure 4-4 Computational space of two sphere system as modeled with the conventional coupled dipole formalism. 64

Figure 4-5 Comparison of analytical results (solid lines) and numerical results (dots) for extinction cross section of two 10nm polystyrene interacting spheres normalized by extinction cross section for independent spheres when the exciting polarization is along the direction of separation (blue) and perpendicular to the separation (red) with a wavelength of 532nm. 66

Figure 4-6 (A) Plot of extinction cross section for two 475nm radius polystyrene spheres interacting spheres normalized by extinction cross section for independent spheres when the exciting polarization is along the direction of separation (blue) and perpendicular to the separation (red) with a wavelength of 532nm. (B) Keeping one sphere fixed at the origin, a map of the normalized extinction cross section as the function of the position of a second sphere for an applied linear exciting field..... 67

Figure 4-7 Optical binding in elliptically polarized light EI. Apart from the binding force FR, interacting particles experience tangential forces FT. Note the existence of differential forces ΔF leading to individual spinning in addition to common orbiting of particles around the system's center of mass. 71

Figure 4-8 (A) Plot of the potential energy for a 100nm polystyrene sphere of refractive index 1.59 in water excited with linear states along the separation direction x (blue curve), at 45 degrees (green curve) and orthogonal (red curve) with an incident power of 0.1W per square micron. The wavelength was 632nm. (B) shows the corresponding forces for the same system for the three different polarization states normalized to the unitless quantity $Const = (4\pi\epsilon_0|E_0|^2(10^{-23}m^2))^{-1}$. The dots in B correspond to a numerical simulation of the same scattering situation using CDA to calculate the forces. 73

Figure 4-9 Contours of constant intensity for an x-polarized excitation of a 2 dipole system, keeping one dipole at the origin and varying the location of the other (contours are linear with $\log(\log(I))$). The black line correspond to the positions of optical binding (if a second sphere was near by, it would travel along the black line until it was along the y axis (vertical))..... 74

Figure 4-10 Contours of constant phase an x-polarized excitation of a 2 dipole system, keeping one dipole at the origin and varying the location of the other. The black line correspond to the

positions of optical binding (if a second sphere was near by, it would travel along the black line until it was along the y axis (vertical))..... 75

Figure 4-11. Torques in an optically bound system of silica spheres of radius $a = 0.1\lambda_m$ solid lines, $a = 0.2\lambda_m$ dashed lines, $a = 0.4\lambda_m$ dot-dashed lines: (A) orbital torque about the system's center of mass and (B) spin torque of a sphere about its own axis. The spheres are in water and are excited with a field polarized linearly at an angle θ with respect to the optical binding vector. The torques are normalized to $\Gamma_0 = 10^4 |\mathbf{E}_l|^2 a^4 / \lambda$ 77

Figure 4-12. Magnitude of orbital torque as a function of the radius of interacting spheres for the first (curve 1, blue) and second (curve 2, red) stationary orbits. The plus symbols indicate regions where the torque has opposite sign. The dashed lines indicate the analytical predictions based on Eq.(4.19) for Rayleigh particles. The calculations are for silica spheres in water excited with a plane wave of intensity $50mW/\mu m^2$ and wavelength in vacuum $\lambda = 532$ nm. The black line shows the magnitude of torque due to Brownian force at 290K in the first stationary orbit. The inset depicts the symmetric potential energy landscape and the trajectory of a bound particle due to nonconservative orbital torques. 80

Figure 4-13 Magnitude of spin torque Γ_s as a function of the radius of interacting spheres for the first (curve 1, blue) and second (curve 2, red) stationary orbits. The plus symbols indicate regions where the torque has opposite sign. The calculations are for silica spheres in water excited with a plane wave of intensity $50mW/\mu m^2$ and wavelength in vacuum $\lambda = 532$ nm. The black line shows the magnitude of absorption-induced spin torque of one silica sphere with refractive index $n_i = 1.59 + 10^{-7}i$ 81

Figure 4-14 Schematic of modeling 2 sphere system excited locally with a single dipole acting as the local excitation (NSOM probe), using the separation of local and distant fields for the compression of the computational system. 83

Figure 4-15 (A) Plot of integrated intensity scattered from two 475nm radius polystyrene spheres interacting spheres normalized by extinction cross section for independent spheres locally excited with a small sphere with the polarization along the direction of separation (blue) and perpendicular to the separation (red) with a wavelength of 532nm. (B) Map of extinction cross section as the function of the orientation for an applied linear exciting field of the single sphere exciting the coupled system..... 83

Figure 4-16 (A) AFM topographical image of monolayer of silicon spheres compared to near-field intensity (B) distribution, and the selection of inner and outer spheres to analyze. 84

Figure 4-17 Individual images of topography and intensity distribution for inner and outer spheres analyzed over an area with near equal slope. (A), inner topography , (B) inner intensity, (C) outer topography, (D) outer intensity, 85

Figure 5-1 (A) Example of a Gaussian distributed surface profiled with varying observation scales corresponding to the microscopic, mesoscopic, or macroscopic averaging. (B) An

optically inhomogeneous medium with refractive index variations due to inclusions and the corresponding scale lengths determined by the material properties (see text).	90
Figure 5-2 (A) Distributions observed considering n sampling points. (B) Convergence of the contrast to the global distribution contrast as a function of the number of sampling points n	92
Figure 5-3 Plot of von Mises probability density function for varying ν	94
Figure 5-4 Plot of phase distribution (A) and corresponding contrast (B) as a function of N , for different values of ν	96
Figure 5-5 NSOM scan of optical coating consisting of 100 parts latex and 25 parts TiO ₂ particulates. (A) is AFM topography, (B) Intensity distribution	98
Figure 5-6 Typical histogram of an NSOM scan. The solid curve corresponds to the Fresnel reflection predicted for the corresponding effective index of the inhomogeneous sample.	99
Figure 5-7 Variation of detected interaction volume as a function of incident intensity $I_2(\text{red}) > I_1(\text{green})$	101
Figure 5-8 (Left) PDF of phase distribution used to fit experimental data. (Right) Plot of experimental and random walk model	102
Figure 5-9. (A) An inhomogeneous material system probed at mesoscopic scales through a local excitation provided by a near-field optical probe. (B) The observed far field response of the material system may be interpreted as being determined by a discrete array of anisotropic Rayleigh scatterers with different local magnitudes and orientations. (C) An inhomogeneous material system where the physical dimensions of the object limit the extents of the field material interaction and the effective anisotropic Rayleigh scatterer (D) producing an equivalent scattered field.	105
Figure 5-10. Probability density functions of ordered (see text) diagonal elements of the reconstructed polarizability tensor. The volume of interaction corresponds to a sphere of 50 nm in diameter having a host refractive index of 1.33 and a) inclusions with a refractive index of 2 and a volume fraction of 0.27 and b) inclusions with a refractive index of 2.4 and a volume fraction of 0.18. The dots are the results of the numerical simulations while the solid lines are guessed 'best fit' of numerical data.	109
Figure 5-11. Effective anisotropy factor Δ as a function of excitation volume R normalized by inclusion diameter d for spherical inclusions with a refractive index of 1.5 randomly distributed in vacuum. The continuous lines correspond to inclusions with diameter $\lambda/32$ while the dashed lines correspond to inclusions of diameter $\lambda/64$. Curves 1 to 4 correspond to a volume fractions of inclusions of 0.3, 0.2, 0.1, and 0.025, respectively.....	112
Figure 5-12. Maximum anisotropy length (Λ) normalized by the diameter of inclusions d versus the volume fraction of inclusions f . Open circles and crosses represent MAL values	

corresponding to inhomogeneous media with inclusions of diameters of $\lambda/64$, $\lambda/32$ respectively. The solid line corresponds to the volume containing on average 3 inclusions. 113

Figure 5-13. Maximum of anisotropy factor Δ_{\max} as a function of volume fraction f of inclusions with 50nm in diameter and having different refractive index contrasts. 113

Figure 6-1. A generic scattering process where a scatterer with unknown polarizability $\bar{\alpha}$ is illuminated by a constant, arbitrarily polarized field \mathbf{E}_{inc} . An intensity measurement is performed in the far-field through a polarizer \mathbf{P} oriented in the plane xy 118

Figure 6-2 The geometry of near-field scattering polarimetry. The probe of near-field microscope \mathbf{P} scans the heterogeneous sample having regions V_d with uniformly oriented polarizability. 131

Figure 6-3 Reconstructed polarizability (the c-component of diagonalized polarizability tensor) as a function of normalized domain volume V_d/V_m where V_d is the volume of uniform orientation of anisotropic polarizability and V_m is the volume of interaction (solid line). Dashed line shows the exact value of polarizability. The parameters of CDA simulations are: tip-sample separation 10nm, modeling cube of 0.8 wavelength in size with $4 \cdot 10^3$ dipoles..... 133

Figure 6-4 Error in reconstructing the polarizability tensor components, α_a (dashed green line), α_b (solid red line), and α_c (dotted blue line), as a function of concentration of inclusions within the sphere of interaction. The number of inclusions is constant in (A) and it varies in (B) (see text). The calculations are performed for a host sphere with radius $r_s = 0.16\lambda$ and refractive index $n_s = 1.33$ which contains inclusions of radii $r_i = 0.05\lambda$ and refractive index $n_i = 2.9$.. 141

Figure 6-5 Error in reconstructing the polarizability tensor components, α_a (dashed green line), α_b (solid red line), and α_c (dotted blue line), using the two polarimetric measurements method. The number of inclusions is constant in (A) and varies in (B); the parameters for the calculations are the same as in Figure 6-4. 145

Figure 6-6 AFM measured topography (top) and NSOM measured intensity (bottom) for two optical coatings A (left) and B (right)..... 147

Figure 6-7 Normalized intensity distributions for samples A (blue) and B (red)..... 148

Figure 6-8 Polarimetric intensity distributions normalized by the average of the total intensity for samples A (A) and B (B). 148

Figure 6-9 Plot of measured polarization states for samples A (A) and B (B) on the Poincare sphere 149

Figure 6-10 Polarimetric intensity distributions normalized by the average of the total intensity measured (solid lines) for samples A (A) and B (B) compared to the fixed anisotropic polarizability reconstructed distributions (dashed lines).	151
Figure A-1 Schematic of simple two lens imaging system.....	166
Figure A-2 Plot of incoherent and coherent illumination of 2 point objects separated by $\lambda/2$...	170
Figure A-3 Plot of coherent illumination of 2 point objects separated by 0.711λ	171
Figure A-4 Plot of incoherent and coherent illumination of 2 point objects separated by $\lambda/2$...	173
Figure A-5 Plot of coherent illumination of 2 point objects separated by 0.82λ	174
Figure C-1 Schematic of an electric dipole as two equal and opposite point charges. These two point charges, q^+ and q^- give rise to a dipole moment p	180
Figure E-1 Plot of magnitude of field for different models of field generated by diffraction from a small aperture. Bouwkamp, magnetic dipole, magnetic + crossed electric dipole, and the solutions found from evaluating numerically Eq.(E.17) – Eq.(E.19)	196

LIST OF TABLES

Table 2-1 Comparison of analytical Mie theory calculation of extinction cross section vs. the numerical calculation using the coupled dipole approximation for varying numbers of dipoles in the modeling volume.....	32
Table 6-1 Percentage error of reconstructed polarizability for different shapes of particles, different field orientations, and different number of realizations for the case of an elliptically polarized excitation field, $\psi = 0, \Phi = 0$	127
Table 6-2 Percentage error of reconstructed polarizability for different shapes of particles, different field orientations, and different number of realizations for the case of a linearly polarized excitation field ($\varepsilon = 0, \Phi = 0$).....	129

CHAPTER 1: OUTLINE – SCOPE OF THESIS

Electromagnetic fields provide noninvasive means for probing material systems. The interaction with particles, surfaces, or any other material modifications, breaks the symmetry of propagation for electromagnetic fields, and the resulting field properties will manifest some memory of the interaction, i.e. modifications of intensity, phase, polarization, angular spectrum, frequency, etc. However, the propagation of electromagnetic fields away from the material system imposes a fundamental limit regarding the length scales over which the material properties can be recovered. Information about higher spatial frequencies is made available only through a secondary interaction that couples the non-propagating fields confined to the surface to the wave components that can be detected away from the object. In reality, this so-called high resolution information intrinsically depends on a secondary interaction. It is only through an understanding of the subtleties of this optical interaction, inherently vectorial in nature, that the primary information may be correctly identified. Through theoretical developments, measurements, and numerical modeling, this dissertation will focus on specific vectorial aspects of light interaction with material nano-structures.

In the context of information retrieval, one can identify two type of sensing processes: passive and active. In the case of passive sensing, the presence of the second medium (the probe) does not influence the field distribution to be measured. Passive probing provides the simplest relationship between the detected propagating signal and the local field distribution, as the material and probe may be treated as separate components of a linear system. In this interaction regime, one is only required to characterize the transfer function of the probe in order

to determine how the material modifies the field structure and how this modification depends on the polarization state of the excitation field. This information is of relevant not only for material characterization purposes but also for understanding and controlling the properties of intricate photonic structures. Even in the most symmetric case of a single sphere excited by a plane wave, the light interaction with the material manifests in a complex polarization structure in the vicinity of surface. This complicated redistribution of energy from a scattering process can lead to rather intriguing results, such as a polarization dependent shift in the observed interaction volume as will be discussed in Chapter 3.

In active sensing on the other hand, the probe not only couples the non-propagating fields to the far-field, but it also changes the field to be probed. Naturally, this is a more complex situation and the sensing procedure cannot be treated anymore as a separable linear system; rather, a self consistent effective field distribution must be accounted for. To deal with this complication, specialized analytical and numerical methods are necessary to decouple the complicated resultant information. This is also true when dealing with complex, inhomogeneous materials; numerical models are necessary to further understand the near-field measurements performed by scanning a small probe in the system's proximity. Another important example of near-field interactions is the situation of two pieces of material that are close to one another. This coupled scattering occurs also in the case of local excitation with a small probe; it leads to morphology dependent response in the near-field scan of a complex system such as a monolayer of spheres as will be seen in Chapter 4.

In all cases mentioned so far, the material systems were assumed to be mechanically rigid with respect to the local field. However, the interaction of light with matter may also change the structural properties of a material system (laser damage, optical trapping, etc.). The so-called

“optical trapping” is one example where the location of a particle may be manipulated by means of an interaction with an external electromagnetic field. When actively probing the local field distribution surrounding a dynamic material system, the interaction with the field will change the materials response. Probing a local field distribution actively may also be accomplished through the observation of the dynamics of a coupled system. For instance, in the situation where a two sphere system is excited with a plane wave, due to their mutual optical interaction, the spheres will move to some stationary location in space as dictated by the forces induced by the scattered field. The interaction between an electromagnetic field and a material system is polarization sensitive and, therefore, the interaction between material objects mediated by an electromagnetic field will also depend on the exciting polarization as will be discussed in detail in Chapter 4.

In many practical situations one is faced with the task of characterizing complex media that are optically inhomogeneous. In this case, one single wave-matter interaction does not yield much valuable information and a statistical treatment of the entire process is necessary. One must obtain ensembles of measurements, and then relate the statistical descriptors such as the moments of measured distributions to the material properties of interest. Although local field is altered due to the active interaction with the probe, some statistical properties of the tested medium may still be related to the stochastic properties of scattered fields. In certain conditions, a statistical treatment of the scattered fields may even permit decoupling between contributions to the far-field signal, such as variations in topography and dielectric properties as will be demonstrated in Chapter 5. Moreover, the use of a localized excitation for the probing of optically inhomogeneous properties can sometimes result in an insufficient averaging of the microscopic properties, leading to a volume-dependent response. As discussed in Chapter 5, when examining the material at different levels of spatial averaging, a characteristic length scale

can be identified which relates to material's responsivity to the specific polarization of the exciting electromagnetic field.

The purpose of many optical measurements is to determine some unknown system properties; this means solving some kind of inverse problem. For inhomogeneous material systems, this procedure involves performing an ensemble of measurements and then solving stochastic equations for the statistical descriptors of the material properties. A refined technique requires performing polarimetric measurements and using statistical tools based on fluctuations of polarimetrically measured intensities to determine the local anisotropic polarizability associated with the scattering medium. As will be discussed in Chapter 6, stochastic equations may be developed and inverted such that even in the situation when the incident field is unknown, structural information may still be retrieved. The more knowledge one has about the experimental and physical scattering situation, the more efficient the unknown information can be found. For instance, if an inhomogeneous material is probed with a field having a known polarization state, the stochastic equation can be inverted using data from one single measurement, drastically simplifying the experimental requirements.

Throughout this dissertation, different physical situations leading to specific manifestations of near-field interactions will be discussed. In addition to understanding their subtle influences on the measurement outcomes, we will demonstrate efficient means for observing experimentally the effects of these interactions. In doing so, we will develop efficient numerical tools for modeling complex aspects of near-field interactions and we will derive the statistical procedures necessary to differentiate between different interaction effects.

CHAPTER 2: OPTICAL NEAR-FIELDS - GENERAL CONCEPTS

The ever growing need in information processing for faster computational speeds and higher storage density carries high demands on the reduction of the physical bit size. The feature sizes in ultra large scale integrated electronics circuitry are continually getting smaller reaching down to nanometers scale. The ability to use light to provide real time images of the fabricated material structures would be of critical importance to quality control and in line corrections. There is also great interest in the functionality of biological molecules and systems. The size of sub-cellular biological building blocks is often also in the nm range [1], and light offers a noninvasive means of probing this information from a distance. However, for all this to occur, the behavior of light in confined spaces such as very close to a surface must be understood, and material responses at dimensions much smaller than the wavelength must be able to be manipulated.

Conventional optical apparatus have been used for centuries to transform the information from a distant (object) plane to a more convenient, perhaps magnified, image plane. The optical tool of imaging is by far the most widely used and historically the most researched. However, conventional imaging requires propagation of the electromagnetic fields, which inherently imposes a cutoff in terms of the spatial information available in an image. Thus, the spatial resolution in a conventional microscope in the visible is limited to around 200nm [2]. To lower the resolution optically down to the nanometer scale requires detecting non-propagating (evanescent) fields that carry the information about the high spatial frequency content. Evanescent fields however, are confined to the material surface, and their magnitude decays

exponentially as one moves away from the material; therefore any detection scheme must either be placed in the vicinity of the structure, or provide a means to couple the fields to propagating wave in a predetermined manner.

The quest to obtain information on the nanometer scale has been taken up in many different fields, each building from the experience the others. Many of the mechanical, electronic, magnetic, optical, and other techniques that were first successful at micron scales evolved toward better resolution in the nano region. It was generally found that scanning probe microscopy (SPM) techniques provide a local response from the material through the use of specialized probes. Scanning probe techniques have been implemented in almost all above fields [3]: atomic force microscopy (AFM) for mechanical [4], scanning tunneling microscope (STM) for electronic [5], magnetic force microscopy (MFM) for magnetic [6], and near-field scanning optical microscopy (NSOM) for optical. Currently, STM and AFM claim a resolution at the atomic level [7], in MFM the resolution is a couple nanometers [8], and NSOM in the visible is typically about 50nm [9] (although some claim as low as 12nm [10]).

To complement the experimental methods, certain analytical models for the different experimental geometries have been derived. However, in many situations, the field-material interaction results in very complicated field distributions in the vicinity of the volume of interaction. For these situations, and when the experiment lays outside the analytical approximations, numerical models exist that may be tuned to the materials in question. Complications also arise when intense optical fields are used to probe a dynamic material system. In such situations, the electromagnetic force applied by the probing field may contribute or change the behavior of the dynamic material. Also, care must be taken when assessing situations when the material system is complicated, i.e. spatially non-uniform or random. To

properly characterize such classes of materials, statistical processing tools must be used in addition to any numerical tool, as a single wave matter interaction may not suffice to describe how the material ensemble behaves.

As described in the introduction chapter, depending on the physical situation (material/experimental controls) one may select from any number of tools to aid in interpreting the results of an experiment. In this chapter, we review some general near-field concepts and tools that we will draw upon throughout this dissertation. We discuss how a material redistributes energy upon interacting with a field, and comment on how such redistribution may be analyzed for characterization or manipulated for some other purpose. We discuss the spatial limitations of the information available when observing far away from where the field-material interaction occurred, the so called diffraction limit and its implications in experiments. The basic experimental geometries for sub-diffraction limited imaging and detection are reviewed. Also, as not all field matter interactions may be easily interpreted, for example when dealing with complex material systems where a single wave matter interaction does not suffice, we discuss some numerical and statistical tools that may be used to provide insight into the complicated near-field images one measures.

2.1. Field-Material Interaction - Scattering

In the 1850s James Clerk Maxwell summarized the existing knowledge of electromagnetism into a set of mathematical equations. In this set of equations, he unified the interaction of electric fields, magnetic fields, electric polarization, magnetization with material systems; for both static and dynamic charges. In general, Maxwell's equations establish relationships between the electromagnetic field at any interface where a change in the material properties exist (permittivity or permeability), establishing "boundary conditions". These

boundary conditions link the electron currents inside matter to the external electromagnetic field. When excited, (by some internal or external field) oscillating charges induce electromagnetic field variations along the surface. Continuity of electromagnetic field requires that the fields near the objects surface be related to the surface currents and field distribution within the object.

To see how and electromagnetic field is modified through the interaction with a material, let us consider the situation of elastic scattering, where after the interaction with the material, the field is merely redistributed, the so-called Rayleigh scattering. Consider some incident field \mathbf{E}_{inc} impinging on some scatterer with a volume V_p and permittivity $\epsilon_p(\mathbf{r})$, as shown below in Figure 2-1.

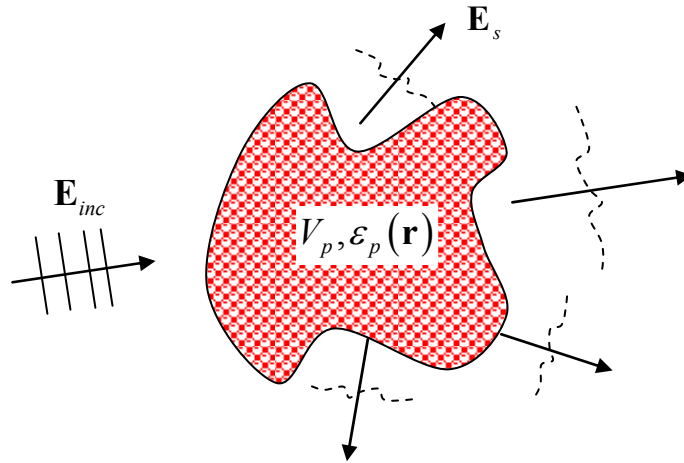


Figure 2-1 An incident wave impinging on a scatterer of some volume V_p and permittivity $\epsilon_p(\mathbf{r})$

From Maxwell's equations, one may construct an integral equation for the field at some arbitrary point as:

$$\mathbf{E}(\mathbf{r}) = \mathbf{E}_{inc}(\mathbf{r}) + k^2 \int_{V_p} d\mathbf{r}' \bar{\mathbf{G}}(\mathbf{r} - \mathbf{r}') (\epsilon_r(\mathbf{r}') - 1) \mathbf{E}(\mathbf{r}') \quad (2.1)$$

Where here ϵ_r is the relative permittivity with respect to the surrounding space ($\epsilon_r = \epsilon_p / \epsilon$), $k = \omega / c$ is the wave number, and a sinusoidal time dependence of $\exp(-i\omega t)$ is

assumed; we can also recognize the presence of the susceptibility $\chi(\mathbf{r}) = (\varepsilon_r(\mathbf{r}) - 1)$. Also, in Eq.(2.1) is the dyadic Green's function $\bar{\mathbf{G}}(\mathbf{r} - \mathbf{r}')$ defined in terms of the scalar Green's function as:

$$\bar{\mathbf{G}}(\mathbf{r} - \mathbf{r}') = \left(\bar{\mathbf{I}} - \frac{\nabla\nabla}{k^2} \right) g(\mathbf{r} - \mathbf{r}'). \quad (2.2)$$

where the scalar Green's function is

$$g(\mathbf{r} - \mathbf{r}') = \frac{\exp(ik|\mathbf{r} - \mathbf{r}'|)}{4\pi|\mathbf{r} - \mathbf{r}'|}. \quad (2.3)$$

As can be seen in Eq.(2.3), before any volume integration may be performed, one must account for the singularity. To take into account the singularity of the dyadic Green's function, one may make use of the three-dimensional Dirac delta function and the principal value of the integral:

$$\bar{\mathbf{G}}(\mathbf{r} - \mathbf{r}') = \bar{\mathbf{G}}_{PV}(\mathbf{r} - \mathbf{r}') - \frac{\bar{\mathbf{L}}\delta(\mathbf{r} - \mathbf{r}')}{k^2}. \quad (2.4)$$

Here, $\bar{\mathbf{G}}_{PV}(\mathbf{r} - \mathbf{r}')$ represents the principal value of the integral neglecting some infinitesimal volume V_δ , and the tensor $\bar{\mathbf{L}}$ is related to the shape of the exclusion volume. Substituting Eq.(2.4) back into the total field expression, yields:

$$\mathbf{E}(\mathbf{r}) = \mathbf{E}_{inc}(\mathbf{r}) + k^2 \int_{V_p - V_\delta} d\mathbf{r}' \bar{\mathbf{G}}(\mathbf{r} - \mathbf{r}') \chi(\mathbf{r}') \mathbf{E}(\mathbf{r}') - \bar{\mathbf{L}}\chi(\mathbf{r}) \mathbf{E}(\mathbf{r}) \quad (2.5)$$

If the object V is small, we can assume that the field inside is uniform, therefore the field inside V is the same as the local field at V_δ ; solving (2.5) for the field inside, we find:

$$\mathbf{E}(\mathbf{r}_0) = \frac{\mathbf{E}_{inc}(\mathbf{r}_0)}{1 + \chi(\mathbf{r}_0)} \quad (2.6)$$

When the particles composition is homogeneous:

$$\chi(\mathbf{r}) = \begin{cases} \chi_0 & \mathbf{r} \in V_p \\ 0 & \text{else} \end{cases}, \quad (2.7)$$

and the object is very small compared to the location where the field is calculated, the field outside the particle is:

$$\mathbf{E}(\mathbf{r}) = \mathbf{E}_{inc}(\mathbf{r}) + k^2 \bar{\mathbf{G}}(\mathbf{r} - \mathbf{r}_0) V_p \chi_0 \mathbf{E}(\mathbf{r}_0) \quad (2.8)$$

Upon substituting in the expression for the local field $\mathbf{E}(\mathbf{r}_0)$ in terms of the incident field, one can readily identify the presence of the polarizability:

$$\bar{\mathbf{a}} = V_p \frac{\chi_0}{1 + \bar{L} \chi_0}, \quad (2.9)$$

giving the scattered field:

$$\mathbf{E}(\mathbf{r}) = \mathbf{E}_{inc}(\mathbf{r}) + k^2 \bar{\mathbf{G}}(\mathbf{r} - \mathbf{r}_0) \bar{\mathbf{a}} \mathbf{E}_{inc}(\mathbf{r}_0) \quad (2.10)$$

With the polarizability and the local field, we can express the scattered field for this small scattering object in terms of its dipole moment,

$$\mathbf{E}_s(\mathbf{r}) = k^2 \bar{\mathbf{G}}(\mathbf{r}) \mathbf{p} \quad (2.11)$$

Eq.(2.11) is simply the field of an electric dipole oriented along \mathbf{p} . The scattered electric and magnetic fields scattered from a small object in terms of the dipole moment \mathbf{p} are found to be:

$$\mathbf{E}_s = \frac{\exp(ikr)}{4\pi\epsilon_0} \left(\frac{3\hat{\mathbf{r}}(\hat{\mathbf{r}} \cdot \mathbf{p}) - \mathbf{p}}{r^3} - ik \frac{3\hat{\mathbf{r}}(\hat{\mathbf{r}} \cdot \mathbf{p}) - \mathbf{p}}{r^2} + k^2 \frac{\hat{\mathbf{r}}(\hat{\mathbf{r}} \cdot \mathbf{p}) - \mathbf{p}}{r} \right) \quad (2.12)$$

$$\mathbf{H}_s = \frac{c}{4\pi} \exp(ikr) \left(\frac{k^2(\hat{\mathbf{r}} \times \mathbf{p})}{r} + ik \frac{(\hat{\mathbf{r}} \times \mathbf{p})}{r^2} \right).$$

The above expressions represent the electric and magnetic field generated by a single oscillating electric dipole [11].

One can readily identify three different regions where the field is decaying at different rates. If the spatial size of a scatterer is denoted as d and the wavelength is $\lambda = 2\pi c/\omega$, the three different regions are qualitatively shown below in Figure 2-2.

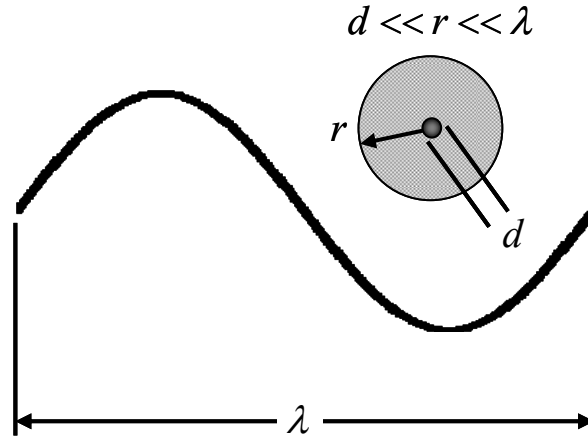


Figure 2-2 Sphere of size a excited by radiation of wavelength λ . The different radiation zones are (i) near-field region $d \ll r \ll \lambda$, (ii) the intermediate-field $d \ll r \sim \lambda$, and (iii) the far-field $d \ll \lambda \ll r$.

The three regions shown in Figure 2-2 are commonly described as:

The near-field (static zone)	$d \ll r \ll \lambda$
The intermediate-field (induction zone)	$d \ll r \sim \lambda$
The far-field (radiation or wave zone)	$d \ll \lambda \ll r$

The behavior of the field in these three regions have significantly different properties. In the near-field, ($kr \ll \lambda$), the scattered field decays rapidly, where as in the far-field zone where $r \gg \lambda$, it is adequate to approximate $|\mathbf{r} - \mathbf{r}'| \approx r - \hat{\mathbf{n}} \cdot \mathbf{r}'$. The field appears as that of an outgoing spherical wave, and the electric and magnetic fields in the far-field are transverse to the radius vector and have an amplitude falling as $1/r$.

From Eq.(2.12), it can be seen that the magnetic field is transverse to the radius vector at all distances. The electric field on the other hand has components both parallel and perpendicular

to \mathbf{r} and, moreover, these components depend on the distance away from the interaction site. What is most important is that the field distributions look very different, depending on the observation point.

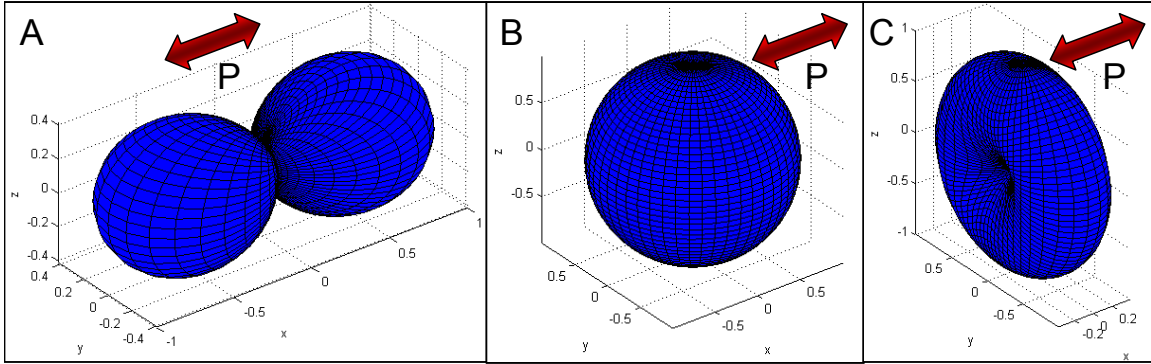


Figure 2-3 Plots of the normalized electric field magnitude of a small scatterer (electric dipole) polarized in the x direction at distances of 0.1λ (A), 0.37λ and 10λ (C).

Figure 2-3 shows the magnitude of the electric field at different distances from a small sphere excited with light polarized along the x axis. At ten wavelengths away from the source (Figure 2-3 C), the field magnitude has the familiar “donut” shape that is commonly attributed to dipolar radiation (field is zero along the polarization axis). However, in the vicinity of the sphere, the near-field, the magnitude along the polarization axis dominates the intensity distribution and the field tends to zero perpendicular to the polarization direction (Figure 2-3 A). In other words, the field magnitude is dominant along the dipole moment in the near-field, where as the field along the excitation dipole moment becomes zero in the far-field.

In the transition from near to far-field, there should be a distance where the field magnitudes along and perpendicular to the polarization direction are equal as illustrated in (Figure 2-3 B). This situation occurs at a distance of $r = \sqrt{2(5 + \sqrt{37})} / 2k \approx 0.3747\lambda$. At this distance, the distribution of field’s magnitude is spherical regardless of the excitation

polarization. In the near- and intermediate- regions, one can expect rather unusual properties of the scattered field that depend on both location and polarization.

In the case where the scattering object is a sphere, the polarizability tensor is diagonal; moreover it is constant on the diagonal and can be represented as a scalar. Of course, not all small objects are spherical in shape, which is where the depolarization factor \bar{L} of Eq.(2.9) becomes important, leading to an anisotropic polarizability. The polarizability, isotropic or anisotropic relates the material information to the scattered field. Specifically when the polarizability is anisotropic, there may be significant differences in the field strength for different orientations of the exciting field.

As we will describe later in Chapters 5 and 6, the general expression for Rayleigh scattering in terms of an anisotropic polarizability can be very useful in understanding how variations in intensity from subwavelength volumes are determined by the material. Also, the scattering from a subwavelength volume may be treated as some effective polarizability when considering an ensemble of Rayleigh scatterers. In this case, as we will discuss in Chapter 6, the material properties are scale dependent, meaning they vary depending on what volume they are observed.

2.2. The Resolution Limit

As apparent from Eq.(2.12), the scattering from a single dipole results in fields oscillating both parallel and perpendicular to the radial vector. However, as is evident from the wave equation, only those fields oscillating perpendicular to the direction of propagation propagate; therefore the information in the longitudinal waves does not reach the far-field. Losing this information means that there is a limit in the resolution in the far-field. One simple classical example of the limits of resolution in far-field optics is describing the imaging of a grating.

Essentially, any material system may be thought of as a summation of gratings with appropriate periods, phase relation, and orientation. One can say that the entire information concerning the structure of a grating is contained in the different diffracted orders it produces and, therefore, detecting all or some of the diffracted orders can be interpreted as having the object more or less resolved. The expression for the angles of different propagating diffracted orders is given in the simple grating equation [2]

$$\sin \theta - \sin_i = \frac{m\lambda}{d}, \quad (2.13)$$

where θ and θ_i describe the diffracted and incident angle respectively, λ is the wavelength in the region, d is the period of the structure, and m is the integer diffracted order. It can be immediately seen that for a period of $d < \lambda/2$, there are no angles θ and θ_i that will result in a propagating diffracted order. Therefore, in this case, the information about the structure must be embedded in waves that are bound to the surface, the so called evanescent waves. This limit $\lambda/2$ of resolution for conventional far-field systems is the well known Abbe-Rayleigh limit. A derivation of this limit for a two slits object for both coherent and incoherent illumination for two common apertures can be found in Appendix and the results of which are shown below in Eq.(2.14). Eq.(2.14) provides the incoherent (a) and coherent (b) limits in resolution for an ideal system with a rectangular aperture. Also shown are the limits in resolution for an ideal system with a circular aperture for both incoherent (c) and coherent (d) illumination [12].

$$\begin{aligned} \text{a.) } \Delta_o &\geq 0.5000 \frac{\lambda}{\eta \sin \theta_o}, & \text{b.) } \Delta_o &\geq 0.7110 \frac{\lambda}{\eta \sin \theta}, \\ \text{c.) } \Delta_o &\geq 0.6098 \frac{\lambda}{\eta \sin \theta}, & \text{d.) } \Delta_o &\geq 0.8190 \frac{\lambda}{\eta \sin \theta}. \end{aligned} \quad (2.14)$$

According to the Rayleigh criterion, two images are regarded as being resolved when the principal maximum of one coincides with the first minimum of the other. This definition is independent on the threshold in intensity that one may place (for the situation of an incoherent illumination and a rectangular aperture, the intensity between the two maxima is 81% of the maximum); as detectors improve, this concept of resolution may need to be revised. However, for now we can consider that the best possible resolution of a conventional far-field imaging microscope, assuming a perfect imaging system with no aberrations and the highest possible numerical aperture of one, is still only half the wavelength of the exciting light. This is the same resolution found when we considered the imaging of a grating. What is interesting is that the resolution limit (as found from the grating example with no aperture and coherent light) of half the wavelength of a two slit object is valid only for a rectangular aperture and incoherent illumination. From Eq.(2.14) one could infer that it is possible to decrease the resolution limit by immersing an object in some higher index material, thus obtaining information about the smaller features. This is the basic concept of the immersion microscope [13]. This technique leads to an improvement of resolution inversely proportional to the refractive index of the second material and is thus limited by the concepts of more exotic materials.

One such instrument that achieves the diffraction limited resolution is laser scanning confocal microscopy. In the simplest form, a confocal microscope involves using high NA objective lenses (usually oil or water immersion lenses) to probe the material with the diffraction limited focal spot. The focal spot is typically raster scanned on the surface by two scanning mirrors, one for each lateral axis. After scattering, the back scattered radiation from the surface is used to generate an image of the surface by plotting intensity bit by bit on each scan point. An aperture of appropriate diameter is overlapped exactly with the image position of the focal

volume. The aperture in the collected beam path serves in addition as a spatial-filter for the vertical direction, discrimination signals coming from different heights in the optical axis around the focal volume. Higher axial resolution is made available utilizing point spread function engineering via 4π confocal microscopy and stimulated emission depletion [14,15].

2.2.1. Beyond the Resolution Limit

It is evident that in order to obtain information about a sample with a resolution beyond those described in Eq.(2.14), it is necessary to detect the information stored in the high spatial frequency evanescent waves. The first demonstration was achieved by Newton using two prisms where the evanescent fields were generated by total internal reflection in one prism. A second prism with a slightly curved surface was then brought into contact with the first. It was observed that the spot size of the light exiting the second prism was larger than the area of contact. Thus some of the evanescent waves that were confined to the surface were converted to propagating in the second prism, see Figure 2-4. Total internal reflection creates waves at the surface that do not satisfy the conditions for propagation, however when refracted into the second prism, the conditions for propagation are met. Due to the exponential decay in intensity of these surface waves, the prisms must be within a fraction of the wavelength of one another. This technique is known as frustrated total internal reflection, and leads to an increase in resolution similar to that of the immersion microscope.

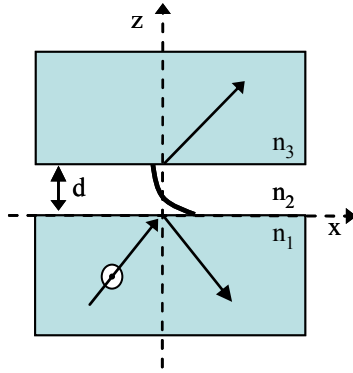


Figure 2-4 Coupling evanescent fields to propagating one in a second medium.

This method relies on refraction to couple non-propagating waves to propagating, but a similar treatment can be applied in terms of diffraction. On the other hand, diffraction or scattering from an object results in the creation of both propagating and non-propagating waves. As demonstrated in the case of a grating, when the structural details are very small, information about the object is carried in the non-propagating components of the scattered or diffracted fields. Since light propagation is symmetric with respect to changes in both time and space (the reciprocity relation) if a small object is placed in an evanescent field, scattering or diffraction from this object will result in some of the evanescent fields being converted to propagating. A schematic of such a situation is pictured below in Figure 2-5. This concept of a sub-wavelength probe or aperture scattering light very near to the surface was first proposed by Synge in 1928 [16]. Synge proposed that an image can be accumulated by scanning a sub wavelength aperture very near to the surface and collecting the light in the far-field.

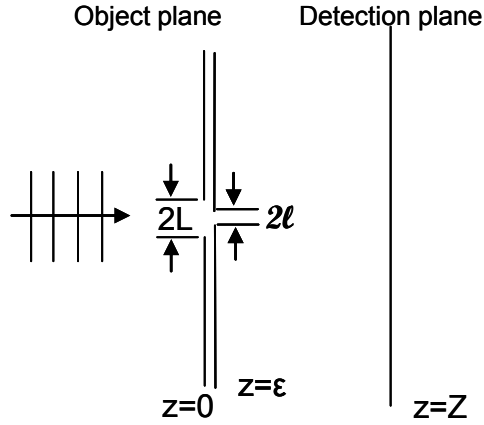


Figure 2-5 Schematic of detection of evanescent waves by diffraction or scattering

Figure 2-5 is a fundamental picture that can be used to describe most of the different modalities of near-field microscopy. To give a simple demonstration of this concept, let us consider the diffraction of a plane wave through a slit of $2L$. In the far-field, the problem is described via the well-known Rayleigh-Sommerfield equation [17]

$$E_d(x, z = Z) = \int_{-\frac{\omega}{c}}^{\frac{\omega}{c}} \exp(ik_x x) E_o \frac{\sin(k'_x L)}{k'_x} \exp(-i\sqrt{k^2 - k'^2_x} \epsilon) dk_x. \quad (2.15)$$

which is not exact for objects that are smaller than the wavelength; however as a simple demonstration of the principles it should suffice. If the second aperture is placed a very small distance away from the first aperture, then it may be assumed that all of the high spatial frequencies are being seen by this second aperture. However, in reality, the higher the spatial frequency, the faster the field will decay away from the surface, therefore there should be dependence in the limits of integration on the value of ϵ . The diffracted fields in the plane $z=Z$, using the limits of integration to account only for propagating waves giving:

$$E_d(x, z = Z) = \int_{-\frac{\omega}{c}}^{\frac{\omega}{c}} \int_{-\infty}^{\infty} \exp(-ik_x x) \exp\left(-i\sqrt{k^2 - k_x^2} (Z - \varepsilon)\right) E_o \frac{\sin(k'_x L)}{k'_x} \times \exp\left(-i\sqrt{k^2 - k_x'^2} \varepsilon\right) \frac{\sin((k_x - k'_x)l)}{(k_x - k'_x)} dk'_x dk_x \quad (2.16)$$

If one envisions detecting only one spatial frequency at a time, the expressions for far-field can be greatly simplified using $E(k_x, z = 0) = \delta(k_x - K)$. It follows that for the situation without the small aperture in front of the first slit the field is

$$E_d(x, z = Z) = \begin{cases} \exp(iKx) \exp\left(-i\sqrt{k^2 - K^2} Z\right) & \text{for } K < \frac{\omega}{c} \\ 0 & \text{for } K > \frac{\omega}{c} \end{cases} \quad (2.17)$$

while in the case where the aperture is brought closer to it, one obtains

$$E_d(x, z = Z) = \exp\left(-i\sqrt{k^2 - K^2} \varepsilon\right) \times \int_{-\frac{\omega}{c}}^{\frac{\omega}{c}} \exp(-ik_x x) \frac{\sin((k_x - K)l)}{(k_x - K)} \exp\left(-i\sqrt{k^2 - K^2} (Z - \varepsilon)\right) dk_x \quad (2.18)$$

From Eq.(2.17) dealing with the situation of diffraction from a small slit, when $K > \omega/c$, there is no information about these spatial frequencies in the far-field. If this delta function in k space was generated by a high frequency grating, the image in the far-field would look like a polished piece of glass. However, in the second situation, where a small aperture was placed very near to the first, due to the diffraction from the second aperture, fields still contribute to the far-field for these high spatial frequencies. The expression for the second case Eq.(2.18), can be interpreted as sort of convolution with a sinc function that depends on the size of the second slit. The smaller the aperture dimensions, the larger the width produced for the function $\text{sinc}((k_x - K)l)$. Basically, the aperture can detect anything that is larger than itself! The smaller the aperture-object distances the higher the spatial frequency components that can be

detected. As can be seen when examining Eq.(2.18), when the width of the second aperture increases significantly, the two expressions become the same.

The above treatment of diffraction as a means to detect evanescent fields is merely a simple scalar treatment of the complicated behavior. In reality, any diffractive element or aperture will depend on the complete vectorial properties of the field. As such, simple analytical expressions for coupling efficiency or observed field distributions are usually used only as a guide to aid in understanding the underlying structures rather than quantitative analysis.

However, this coupling of the high spatial frequency evanescent fields to propagating waves through scattering is the fundamental high resolution mechanism in near-field microscopy. In Figure 2-5, due to the time reversibility of electromagnetic fields, one can envision a situation where light is traveling from right to left, and the observation is in the far-field on the left. In this situation, the high spatial frequency components of the field near the object are generated by the scattering object (probe). If this scattering probe is placed near the edge of the object's aperture, the interaction of the evanescent fields with the subwavelength structure will couple some of the evanescent fields to propagating waves for far-field detection. This is exactly the situation proposed by Synge in 1928 [16], using a small aperture to image a surface with sub-wavelength resolution in the visible regime.

2.3. Experimental Methods

In his original letter to Einstein, (April 22, 1928) Synge suggested that scattering from a small particle could be used to couple the evanescent waves from a subwavelength object to the far-field for detection. A few letters went back and forth discussing the many difficulties with practical implementation of such an idea, and although he doubted any experimental realization, Einstein convinced him to publish anyways [18]. In his paper, Synge suggested using either a

subwavelength pinhole in a metal plate or a quartz cone tapered to a point (on the order of 10nm) that is coated with a metal except for the very end. It wouldn't be for a couple of decades before such an idea was experimentally realized. The first experimental demonstrations of the concepts above were performed in the visible independently by Lewis [19] and Pohl [20] in 1984. In their experiments, the small aperture was replaced with a tapered optical fiber probe. This optical fiber was tapered to have an aperture much smaller than the wavelength of light. This probe is the key feature in NSOM and determines the coupling efficiency of evanescent fields to propagating. The creation of such a probe, seen in Figure 2-6, can be accomplished in a variety of different methods: chemical etching, heating and pulling, focused ion beam shaping, etc. [21]. Once the desired size of the fiber is obtained, typically around 100nm, the probe is then coated in a metal such as aluminum or gold to confine the fields that are no longer propagating in the fibers core.

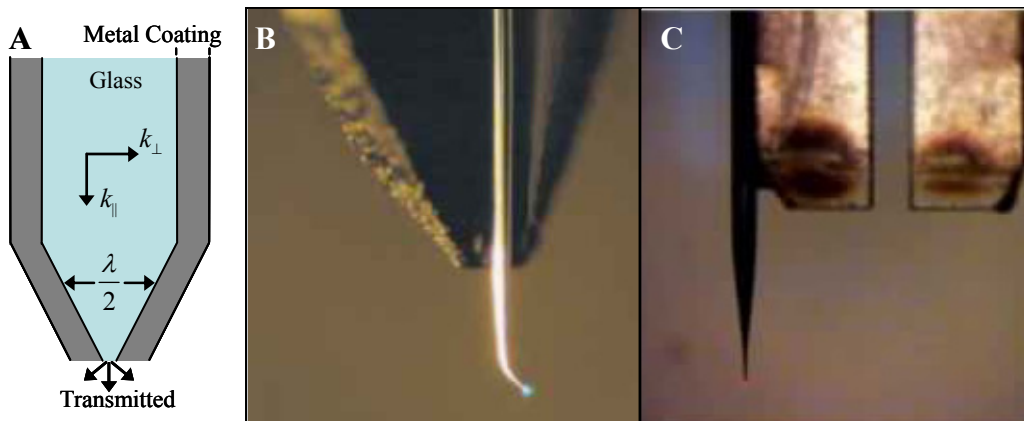


Figure 2-6 Schematic of tapered optical fiber probe. (A) shows a cartoon representation of the path the light travels. (B) shows a tapered cantilevered fiber probe used for a beam bounce method of monitoring the amplitude of vibration for feedback (Image from www.nanonics.co.il/) (C) shows a probe mounted to a tuning fork, (Image from www.azonano.com) another method for monitoring feedback.

As nanofabrication techniques improve, one would imagine that reproducibility and smaller apertured probes will follow. However, another feature that limits the resolution

available by the scanning aperture technique is the optical throughput. Essentially, light propagating in a fiber has a wave vector defined as $k^2 = k_{\perp}^2 + k_{\parallel}^2$, where here k_{\perp} and k_{\parallel} are the wave vector components perpendicular and parallel to the optical fiber axis. The magnitude of the wave vector in the material is:

$$k = \varepsilon\mu k_0 = \frac{\varepsilon\mu 2\pi}{\lambda} \quad (2.19)$$

where μ and ε are the permeability and permittivity of the fiber, and λ is the wavelength of the radiation. The perpendicular component of the wave vector is determined by the diameter of the fiber and the refractive index contrast of the core and cladding [22]. When the diameter is small enough that $k_{\perp} > \varepsilon\mu 2\pi/\lambda$, the fields no longer propagate, and the components parallel to the optical fiber become purely imaginary. Therefore, when the fiber diameter reaches such sizes, the optical field along the fiber exhibits an exponentially decreasing evanescent behavior toward the tip. If the taper is too long, most of the power will be reflected back in addition to the metal coating around the fiber attenuating the field due to absorption. Because of this absorption, the input field amplitude cannot be increased to arbitrarily high values, as at the aperture absorption may damage the metal coating with excessive heat generation. The optical transmission coefficients in standard SNOM probes are reported to be around 10^{-5} [23]. Of course the transmission and collection efficiency will vary from probe to probe (due to different coating thicknesses), as well as depend on the tip sample separation.

Creating a subwavelength aperture is but the first step, the most important step is to bring this probe near the surface in a controlled manner. There are many variations on how to achieve and maintain such a small distance from the sample without destroying the probe or sample. Many of these methods were first achieved with the advent of atomic force microscopy, AFM

[4]. In most AFM instruments, a sharpened tip is dithered vertically at some resonant frequency. The amplitude of this vibration changes when the tip is brought to within nanometers from the surface due to the interaction between matter at such small scales. The AFM probe is sensitive to forces arising from mechanical contact force, Van der Waals forces, capillary forces, chemical bonding, electrostatic forces, magnetic forces, Casimir forces, solvation forces, etc. [7]. Through the use of a force feedback mechanism, the probe may be kept at a constant amplitude of oscillation; thus at a constant separation from the sample. The two most common methods of monitoring this amplitude are a beam bounce setup with a cantilevered probe Figure 2-6 (b), or by a tuning fork attached to the tip Figure 2-6 (c) [24]. The probe may be kept at a constant amplitude of vibration, which maintains a constant tip sample separation, or at a constant height, where the tip is brought to some distance, and the force feedback is disabled. The latter requires accurate knowledge about the sample a priori. A schematic of a typical NSOM system can be seen below in Figure 2-7.

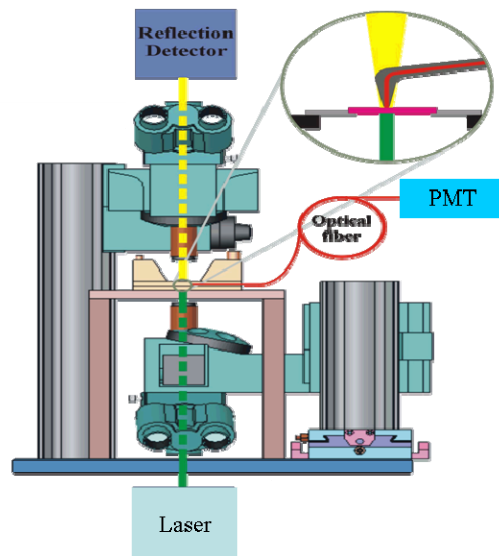


Figure 2-7 Schematic of Nanonics NSOM -100, where all three measurement modalities of emission (transmission or reflection far-field detection), collection (transmission or reflection far-field illumination), and dual (emission and collection) are available.

There are three main geometries of NSOM, which can each be interpreted from the schematic seen in Figure 2-5. In the basic collection geometry, light is focused on to a sample that may contain sub-wavelength variations in the topography and the dielectric function and collected by the near-field probe. As seen in Figure 2-5, the probe must be brought in close proximity to the sample surface as the evanescent fields decay exponentially in the propagation direction. The probe used in the collection geometry allows for the detection of evanescent field through some secondary scattering from the probe of the evanescent fields to propagating modes in the fiber. In this geometry, a large illumination area is created by focusing light onto the sample. The interaction of this light with the sample produces both propagating and evanescent fields. When placed very near to the surface, the small aperture of the probe will couple both these contributions such that they may be detected in the far-field.

NSOM can also operate in emission mode when light is coupled into the fiber and emitted from the tapered fiber probe. This geometry is also pictured in the basic evanescent field detection schematic in Figure 2-5, however in this case the light is traveling from right to left. The tip generates evanescent fields that probe the sample when the distance between the sample and tip is very small. In principle, the emission and collection modes of operation are reciprocals of one another, however depending on the sample and the desired measurements, one method may be preferable over the other. The third mode of operation is that of both emission and collection. This mode is somewhat difficult to envision from Figure 2-5, however if one considers that the tip can be used both to generate and collect evanescent fields, it is possible to consider the light reflecting from the sub-wavelength features. This technique in particular carries the possibility of a near-field phase detection, as the collected signal will always beat with the signal reflected from the end of the fiber. Through out this dissertation, the NSOM in Figure

2-7 was used to both experimentally measure optical near-fields (as in Chapter 5) and as a basis for derivations of near-field modeling (Chapter 6).

Another type of near-field microscopy is the so-called scattering (apertureless) scanning near-field microscopy. It is similar to the ones described above however; in this case the fields are generated by focusing light onto the tip in the vicinity of the sample. Notably, the field near the end of the tip may be locally enhanced due to the evanescent fields generated from diffraction from the tip. In this geometry, there is no need to fabricate an aperture at the end of the probe and evanescent fields will also be created due to the focused lights interaction with the sample. This type near-field microscope allows for two different mechanisms of coupling evanescent fields to propagating: scattering of the evanescent fields created by the sample from the tip, and scattering of the fields generated by the tip from the sample. As such this method requires some sort of modulation of the detected signal, usually with a frequency near that of the tip to cancel out the large background [25].

There is also a type of near-field system known as the photon scanning tunneling microscope. Again, this type is very similar to the NSOM mentioned above, however, in this case the evanescent fields are generated by total internal reflection. The near-field tip is scanned very near to the surface and convert or detect some of these evanescent components. This type of microscope is commonly used in conjuncture to very thin samples which, sometimes, can support surface plasmons [26].

2.4. Numerical Techniques

Due to the complexity of the near-field probes and scattering geometries, analytical solutions are usually not applicable. Rather, complex scattering problems are often approached using numerical modeling. There are a variety of numerical methods that are currently being

used in the modeling of electromagnetic responses and scattering from a material in the near-field. Depending upon the specifics of the problem at hand, one may use: finite difference time domain (FDTD), Mie scattering, T-matrix, finite element method (FEM), coupled (discrete) dipoles approximation (CDA), etc. These techniques often offer varying degrees of accuracy as a trade off for computational time and required memory storage.

Different numerical techniques rely on different assumptions and methods of approximating solutions to these equations. The finite difference time domain formulation first discussed by Yee [27], involves discretising both space and time in order to approximate the curl equations by finite difference quotients. In using this technique, the scatterer and the surrounding space are approximated by a grid. Artificial boundaries are created by use of a perfectly absorbing material or perfectly matched layer to minimize artificial reflections. This method is most useful in describing a well characterized piece of material or semi-infinite structure. If time is also discretised, then the fields that are generated with a pulse excitation can also be modeled. This technique is very powerful, however due to the requirement of expanding the grid to locations outside the scattering region; some accuracy in describing the material is sacrificed.

The finite element technique is similar to FDTD, however FEM is an approximation to the solution to the differential equations where as FDTD an approximation to the differential equation themselves. Typically FEM is preformed in the frequency domain. FEM also requires that the entire space be discretised, however with FEM, the lattice does not necessarily need to be cubic. This allows for a lattice to be specified that will better approximate the shape of the scattering particle or material. FEM solves the boundary conditions of only neighboring cells, thus creating a banded diagonal system of equations, which many numerical techniques may be

used to solve. Like FDTD the main drawback to FEM is the requirement of taking into account the space outside the scattering volume. The boundary conditions at the edge of the particle and those of the computational domain must be specified. The edge of the domain must account for the behavior of the fields at infinity and ensure no reflections back into the scattered region.

Mie scattering is a very specific analytical solution for the scattering from spheres. However, currently, analytical solutions for irregular shapes have not been developed [28]. We use Mie theory extensively in Chapter 3 where we analyze the vectoral scattering from a single sphere.

Another technique, the coupled dipole approximation CDA (also known as the discrete dipole approximation) approximates a continuum volume as a finite array of polarizable points [29]. The basic idea for the coupled dipole approximation was first conceived in 1964 by DeVoe, who was studying optical properties of molecular aggregates [30]. In 1973 Purcell and Pennypacker improved upon DeVoe's treatment and applied this technique to the study of interstellar dust grains. In the original derivation by DeVoe, retardation effects were not included and the original method was only suitable for particles of size less than a wavelength. Purcell and Pennypacker created a flexible general technique for calculating the scattering and absorptive properties of particles of arbitrary shapes. CDA gives an approximation of the correct solution, the accuracy of which will depend greatly on the number of lattice point used to approximate the shape.

2.4.1. The Coupled Dipole Approximation

CDA and similar integral methods do not suffer from the important disadvantage of FDTD and FEM, namely the need to discretise space outside the particle, and the need to implement suitable boundary conditions to prevent non-physical reflections from the boundary

of the computational domain. Throughout this dissertation, some of the tasks require exploiting the available computational resources to best model the scattering from an arbitrary shaped scatterer or collection of scatterers. CDA is the method of choice as it is relatively simple to implement and is well suited for inhomogeneous materials of arbitrary composition.

As described in Section 2.1, the interaction of an electromagnetic wave and an inhomogeneous material can be described in terms of the integral equation Eq.(2.1), in which the field at some observation point is the sum of the incident field and that of the surrounding medium. The coupled dipole approximates this integral (Eq.(2.5)) by a discrete summation (Figure 2-8). The fields resulting from the integration become those of dipoles on a lattice that can best approximate the shape of the scatterer.

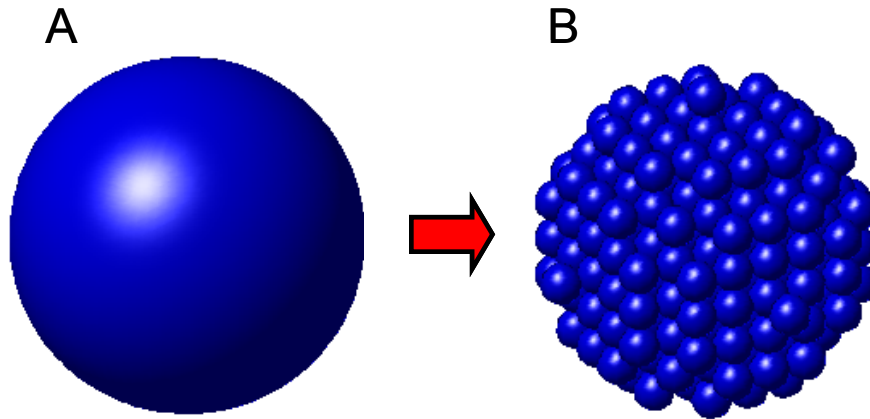


Figure 2-8 Coupled dipole approximation of a sphere by an array of dipoles (small scatterers)

The field at each of the dipoles can be written as the summation of both the incident field and the contributions occurring from the interaction with all the other dipoles on the lattice

$$\mathbf{E}(\mathbf{r}_j) = \mathbf{E}_{inc}(\mathbf{r}_j) + \sum_{k=1}^N \mathbf{E}_k(\mathbf{r}_j) \quad (2.20)$$

where $\mathbf{E}_k(\mathbf{r}_j)$ is the electric field radiated to the point \mathbf{r}_j by the k^{th} point dipole \mathbf{P}_k . Considering a point dipole at an arbitrary orientation and at an arbitrary location \vec{r}_k , the radiated field can be written as:

$$\mathbf{E}_k(\mathbf{r}_j) = -[\bar{\mathbf{A}}(\mathbf{r}_j, \mathbf{r}_k)] \cdot \mathbf{P}_k, \quad (2.21)$$

where $\bar{\mathbf{A}}(\mathbf{r}_j, \mathbf{r}_k)$ is the interaction matrix accounting for both near- and far-field coupling components as a result of the dyadic Green's function. This matrix is a dense, symmetric positive definite matrix of size $3N \times 3N$ where N is the number of dipoles used. The elements of $\bar{\mathbf{A}}(\mathbf{r}_j, \mathbf{r}_k)$ can be found by[31]:

$$\bar{\mathbf{A}}_{j,k} = \frac{\exp(ikr_{jk})}{4\pi\epsilon_0\epsilon_r r_{jk}} \left[k^2 (\hat{\mathbf{r}}_{jk} \hat{\mathbf{r}}_{jk} - I_3) + \frac{ikr_{jk} - 1}{r_{jk}^2} (3\hat{\mathbf{r}}_{jk} \hat{\mathbf{r}}_{jk} - I_3) \right], \quad (2.22)$$

where the magnitude is defined as $r_{jk} \equiv |\mathbf{r}_j - \mathbf{r}_k|$ and the normal vector as $\hat{\mathbf{r}}_{jk} \equiv (\mathbf{r}_j - \mathbf{r}_k)/r_{jk}$. By considering the self interaction term, when $j=k$, where the induced dipole moment is related to the incident electric field by

$$\alpha_j \mathbf{P}_j = \bar{\boldsymbol{\alpha}} \mathbf{E}_{inc}(\mathbf{r}_j). \quad (2.23)$$

The unknown individual dipole moments can be found by solving the system of equations in terms of their interaction and the incident field.

$$\mathbf{P}_j \cdot [\bar{\boldsymbol{\alpha}}_j]^{-1} + \sum_{k=1, k \neq j}^N [\bar{\mathbf{A}}(\mathbf{r}_j, \mathbf{r}_k)] \cdot \mathbf{P}_k = \mathbf{E}_{inc}(\mathbf{r}_j). \quad (2.24)$$

The self-interaction term ($j=k$) is equal to the inverse of the atomic polarizability of the dipole representing the volume at that location. The atomic polarizability is directly related to the dielectric properties of the material and is found from the Clausius-Mossotti relation Eq.(2.9).

At the heart of a CDA calculation lays the self consistent solution to the system of linear equations seen in Eq.(2.24). There are many techniques for solving large systems of equations. However this system under consideration is both large and dense, so no sparse techniques may be used. One common technique is the conjugate gradient algorithm for symmetric positive definite matrixes [32]. At every iteration of the conjugate gradient algorithm, the method of steepest decent is used to search for a minimum of the function describing the solution. As this system of equations is dense, and the accuracy depends on the number of lattice points, storing such a large system is one of the primary constraints when looking to approximate larger pieces of material. To greatly reduce the amount of memory space required, it is possible to consider storing only the unique interaction vectors and make use of the symmetries of the problem [33]. To allow for such a large reduction in storage, an algorithm must exist for manipulating the stored values.

The derivation of a method of reducing the matrix vector multiplication of the dense system to a convolution of only the unique values is presented in Appendix 0 Upon implementing this tool, it is only necessary to calculate the interaction for lattice points of unique vector separations. After the system of equations has been solved to within a certain tolerance specified. The resulting field at some location \mathbf{r} can be found by using Eq(2.20). If in the far-field, Eq.(2.20) can be simplified to[31]:

$$\bar{\mathbf{E}}_{sca}(\mathbf{r}) = \frac{k^2 \exp(ikr)}{r} \sum_{k=1}^N \exp(-ik\hat{\mathbf{r}} \cdot \mathbf{r}_j)(\hat{\mathbf{r}}\hat{\mathbf{r}} - \bar{\mathbf{I}}_3)\mathbf{P}_k. \quad (2.25)$$

As a demonstration of the ability to calculate the scattering from a sphere, a table of a comparison between the calculation of the extinction cross section predicted through Mie theory and the numerical computation using the coupled dipole approximation is shown below in Table 2-1. As can be seen in Table 2-1, the accuracy of CDA increases with the number of modeling

locations (as would be expected), however, when the size of the object is small, good agreement can be found with less dipoles.

Table 2-1 Comparison of analytical Mie theory calculation of extinction cross section vs. the numerical calculation using the coupled dipole approximation for varying numbers of dipoles in the modeling volume.

		Extinction Cross Section for Radius:		
Cube of Dipoles	Sphere	0.5	1	1.5
16 x 16 x 16	1856	1.191	11.0985	20.8278
32 x 32 x 32	15624	1.1613	10.8588	18.188
64 x 64 x 64	131040	1.1719	10.8657	17.603
Mie Theory		1.1745	10.852	17.4276

The CDA method outlined above is used through out this dissertation to provide quantitative measurements of different scattering characteristics. Moreover, we will describe how one may expand upon the current CDA formulism to describe interaction between larger objects (Chapter 4). Also, we use CDA for the calculation of the electromagnetic force experienced by a particle interacting with a field and analyze how interaction in multiple scattering systems modifies the dynamics.

2.5. Statistical Optics

Most material systems in nature are not perfectly homogeneous with constituents distributed in a nice periodic fashion; rather they exhibit different degrees of disorder both spatially and temporally. When considering the optical responses of such materials, one single realization of the wave matter interaction does not reveal the entire wealth of information about the global properties. Actually, as we will discuss in Chapter 6, the optical response really depends on the scales over which the material is probed. To describe the properties of such systems, one has to utilize statistical tools and consider ensembles of different interactions in

order to quantify specific properties of the material system. Statistical tools such as the moments of an ensemble, correlations, allow one to develop relationships based on the entire distribution of possible events without the need to know what exactly happens at one specific moment in space or time. This is the concept of a stochastic experiment.

A stochastic experiment is a test where the outcome is not known a priori even if all is known about the process; for example, the flipping of two coins. The exact outcome of one experiment only exists as a probability of occurrence. The probability of occurrence can be measured as a frequency of number of times an event occurs in regard to the number of experiments performed. The exact value of the probability of an event occurring is then found in the limit of an infinite number of experiments; mathematically, for some event A, occurring n times in N experiments:

$$P(A) = \lim_{N \rightarrow \infty} \frac{n}{N}. \quad (2-26)$$

To perform a random experiment, one defines a random variable. A random variable takes on the value of one possible event from the ensemble of all possible events and does so with the probability of that event occurring. The random variable concept allows for observing how different systems change the both the exact value of event and the associated probabilities. From the properties of a random variable taking on the events and probabilities of an experiment, one may define a cumulative probability function (CDF) for describing a random variable U:

$$F_U(u) = \text{Prob}(U \leq u) \quad (2-27)$$

Analyzing the CDF, one can see that it is monotonically increasing over the range from negative infinity to infinity. The value of the CDF at negative infinity is 0, and at infinity is 1. This definition of the CDF is equally valid for discrete or continuous random variables. The

probability of the occurrence of an event occurring may be defined from the CDF of Eq.(2-27) as:

$$f_U(u) = \lim_{\Delta u \rightarrow 0} \frac{F_U(u) - F_U(u - \Delta u)}{\Delta u} = \frac{dF_U(u)}{du}. \quad (2-28)$$

which is known as the probability density function (PDF). The PDF shows how the events of an experiment are distributed across all the possible values they may take. The probability that the random variable U takes a value between the limits of a and b is simply:

$$\text{Pr ob}(a < U \leq b) = \int_a^b f_U(u) du. \quad (2-29)$$

The PDF is what is easily measured in an experiment by taking many of the outcomes of an experiment and separating them into bins (creating a histogram). To compare different measured PDF's, we may assess the shape through calculating the moments. The general definition of the moments of an ensemble may be found from the PDF as:

$$M_U^{(n)} = \int_{-\infty}^{\infty} u^n f_U(u) du. \quad (2-30)$$

The first moment (mean, average) defines the event most likely to occur. Higher order moments define how different the events are from the first moment, the spread. If the first moment is not enough to discern different experiments, then higher order moments may be used. Through out this dissertation we will discuss many different PDF's and how they may be found and interpreted through real and simulated experiments.

2.5.1. Gaussian Statistics in Optics

As a simple demonstration of how statistical models may be applied to describe a physical situation, let us consider the situation of scattering of light from a random medium and the familiar appearance of a speckle pattern [34]. A speckle pattern can be perceived as the

random interference of harmonic waves with random phases. In general the complex amplitude of a polarized speckle field can be written as [35]:

$$U(x) = U_r(x) + iU_i(x) \quad (2-31)$$

where U_r and U_i are the coherent summation of N harmonic waves with random phases:

$$\begin{aligned} U_r(x) &= \sum_{j=1}^N a_j \cos \theta_j \\ U_i(x) &= \sum_{j=1}^N a_j \sin \theta_j \end{aligned} \quad (2-32)$$

It can be thought that the different phases acquired can be due to the reflection or transmission from a surface with a certain roughness. If the surface in question is significantly rough with respect to the wavelength, the resulting phase distribution would be uniform over the interval $[-\pi, \pi]$, giving the probability density function (PDF):

$$f_\theta(\theta) = \begin{cases} \frac{1}{2\pi} & -\pi < \theta < \pi \\ 0 & elsewhere \end{cases} \quad (2-33)$$

If also the amplitudes are assumed to be uniform, i.e. $a_1=a_2=a_N$, then the probability density function of the intensity is well known and can be expressed in terms of a Fourier-Bessel series [36]:

$$f_h(h) = \frac{1}{2} \int_0^\infty J_0^N(au) J_0(u\sqrt{h}) u du \quad (2-34)$$

where h is the intensity: $h = (U_r^2 + U_i^2) = |U|^2$. At large N , the PDF can be approximated as:

$$f(h) \sim \frac{1}{Na^2} \exp\left(\frac{-h}{Na^2}\right), \quad (2-35)$$

and is plotted in Figure 2-9.

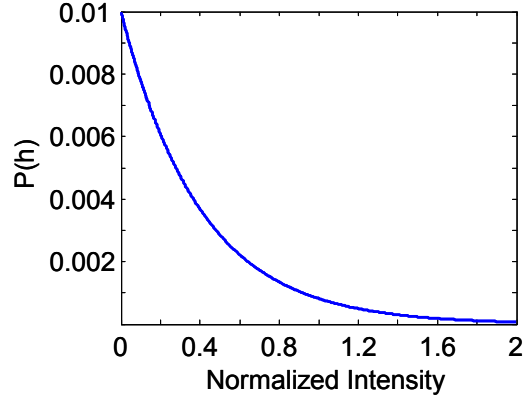


Figure 2-9 Intensity PDF for large number of random waves interfering having a uniform phase distribution.

In the Gaussian regime, where the number of scatters is large, the PDF of the total phase $\psi = \arctan(U_i/U_r)$ becomes independent of N:

$$f_{\psi}(\psi) = \begin{cases} \frac{1}{2\pi} & -\pi < \psi < \pi \\ 0 & \text{elsewhere} \end{cases} \quad (2-36)$$

To characterize the shape of the PDF, we can look at the first and second moments of the distribution using Eq.(2-30), we find $M_h^{(1)} = Na^2$, and $M_h^{(2)} = 2N^2a^4$. In order to have some sort of normalized method of characterizing the shape, we can look at the central spread, the standard deviation:

$$\sigma = \sqrt{\text{var}} = \sqrt{(M_h^{(2)}) - (M_h^{(1)})^2}, \quad (2-37)$$

normalized by the mean, known as the optical contrast:

$$C = \frac{M_h^{(1)}}{\sigma}. \quad (2-38)$$

From the expressions for the PDF (Eq.(2-35)) for a large number of random harmonic waves with a uniform phase distribution and constant amplitudes, the mean and standard deviation are exactly proportional; yielding a contrast of 1. This is the definition of a fully

developed Gaussian speckle pattern [37]. When in the Gaussian statistics regime, increasing the number of contributing random waves does not change the statistics when each wave is of constant amplitude and arises from a uniform phase distribution.

A typical example of situations where such a speckle pattern can be described in terms of Gaussian statistics is that of a near-field scan in the collection geometry [38]. In such a situation, a large area is illuminated and probed locally with a tapered fiber probe. In this case, a large number of independent scattering centers are excited upon propagation through the material. A test of these concepts could be performed by considering the number of scattering centers to be proportional to the interaction volume of the detection system. In this case, the interaction volume, for a significant excitation is governed by the aperture size of the probe. If the probe size is large enough a number of scattering centers such that the PDF is described by Eq.(2-35) then increasing the size of the tip should not have an effect on the optical contrast.

A rather different statistical situation is observed when the probe is used to excite a random media, and only a small number of scatterers are observed in the far-field. This is the subject discussed in Chapter 5 and how varying the intensity of the probing field affects the statistics.

CHAPTER 3: PASSIVE PROBING OF COMPLEX NEAR-FIELDS

As discussed in Chapter 2, in reality there is no means of passively measuring optical near-fields. The required secondary interaction to couple the non-propagating fields to the far-field for detection changes the local EM field until some self-consistent field results. The material system (probe) influences the field to be tested and therefore the measurement is “active”. Attempting to solve the complicated interaction for each experimental situation proves to be a daunting task, and is in many cases impossible. If one instead probes the intermediate field, where the coupling of evanescent or decaying fields no longer influences significantly the result of the primary scattering event, a “passive” interpretation may be valid. Because the material and probe may be treated as separate components of a linear system, passive probing provides the simplest relationship between the detected propagating signal and the local field distribution. In this interaction regime, one only needs to know the transfer function of the probe in order to characterize how the material modifies the field structure.

As apparent from Figure 2-3, the intermediate zone of field propagation, the behavior of scattered electromagnetic fields can have some very interesting and unexpected structures. Because the field material interaction is vectorial in nature, the redistribution the incident energy usually depends on the polarization state of the excitation field, which can typically be controlled experimentally. This information is of fundamental relevance not only for material characterization purposes but also for understanding and controlling the properties of the EM field itself in intricate photonic structures.

The separation of the detected signal into components of a linear system simplifies significantly the interpretation of a measurement. However, away from the primary volume of interaction, the influence of the complex field components diminishes rapidly becomes difficult to assess and one must devise clever experiments to reveal them. In this chapter, we will first discuss how a material system modifies the local field distribution and how these modifications in the near field affect in the measurable characteristics of the intermediate and far fields. We will discuss how one observe experimentally the influence of the decaying fields in the intermediate zone and how a change in the polarization state can lead to a perceived shift in the volume of interaction with a sphere [P7]. Finally, we will discuss how this shift can be interpreted as a manifestation of a general “spin”-dependent effect, known as the Spin Hall effect for light.

3.1. Redistribution of Energy in Single Scattering

As was discussed in Chapter 2, even in the case of scattering from a sphere, the most symmetric three dimensional objects, the field distribution in the near zone exhibits a complicated behavior. In the case of linearly polarized excitation, we have seen that the spatial distribution of scattered intensity changes dramatically depending on the observation distance. Actually, the intensity patterns are also altered when the polarization state of the excitation field is changed. For electromagnetic most detectors sense the time averaged energy flow (or magnitude of the time averaged Poynting vector) [22]. As such, a detector can not sense the evanescent components in the scattering from a small sphere, where the evanescent fields manifest in static field conditions (no net energy flow). However, if instead of a conventional detector, we consider a sensing mechanism by some point like fluorophore, it will be sensitive to the instantaneous magnitude of the field squared, sensing both propagating and static fields. In

the intermediate and far fields, where there are only propagating fields remain, the magnitude of the electric field squared is equivalent to the magnitude of the Poynting vector. This is due to the fact that in the far-field, the electric and magnetic fields have a deterministic relationship.

In a passive measurement, the intensity (the magnitude squared of the E field) scattered from a dielectric sphere varies with angle of observation and with the radial distance of observation as shown below in Figure 3-1.

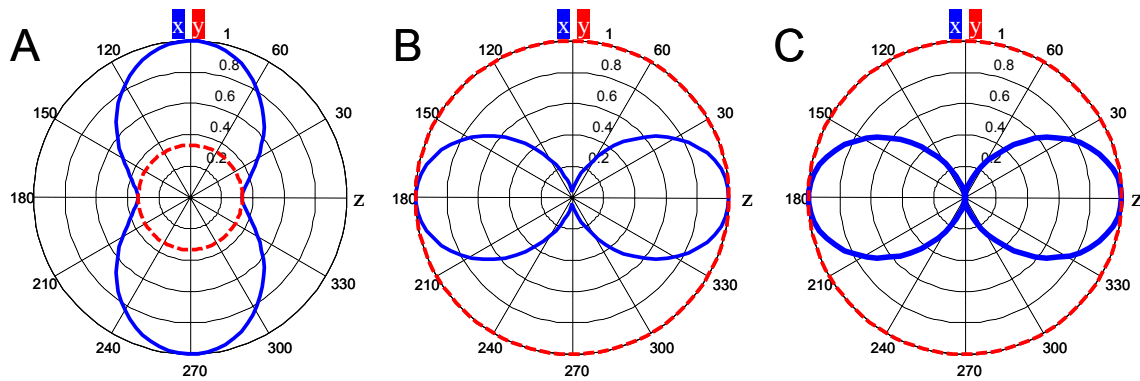


Figure 3-1 Intensity distributions in the plane (blue) and perpendicular to the plane (red) of a linear polarized excitation for three different observation distances $r = 0.25\lambda$ (A), $r = 1.5\lambda$ (B) and $r = 10\lambda$ (C).

As can be seen in Figure 3-1, the intensity is constant in the y-z plane regardless of the observation distance. However, in the xz plane and close to the scatterer, the measured intensity along the polarization direction can be quite large; this is near-field effect diminishes when the increasing the radial distance from the scatterer. Nevertheless, one can imagine situations where distance-selective excitations are required such as the practice of scattering-based NSOM, for instance [39]) In this case, the far field intensity peak can be moved along the polarization axis by simply rotating a half waveplate that controls the excitation field.

Depending on the specific application, there may be situations where asymmetric intensity distributions are not desired. If the excitation field is in a some elliptical or circularly polarized state as shown in Figure 3-2, the magnitude of the scattered field is the same in both

the xz and yz planes. As can be seen, the magnitude is not independent of the azimuthal angle of observation in these planes; however a similar local field enhancement may be generated along the plane for which the dipole is rotating.

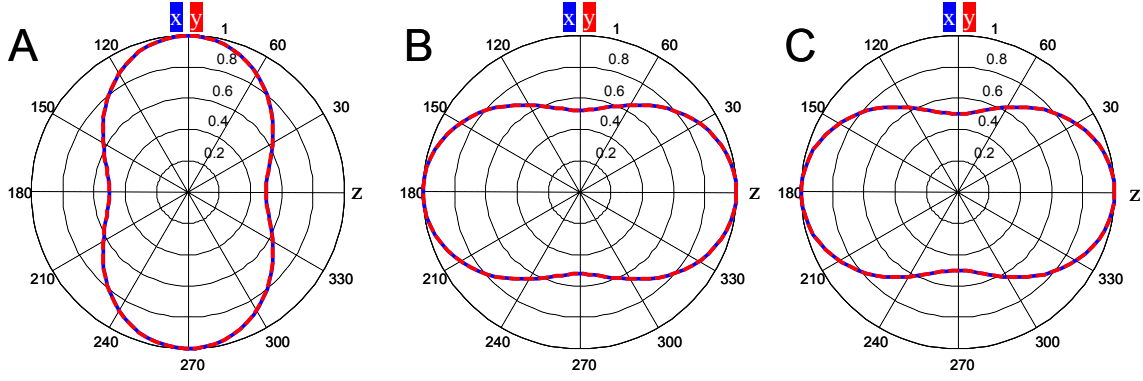


Figure 3-2 Angular intensity distributions in the plane (blue) and perpendicular to the plane (red) of a linear polarized excitation for three different observation distances $r = 0.25\lambda$ (A), $r = 1.5\lambda$ (B) and $r = 10\lambda$ (C).

Of course, one can consider that the detection is not only sensitive to the magnitude of the field squared but also the local polarization state. Understanding the vectorial problem provides ample information about how the scatterer modifies the field. This would be desirable again in the practice of scattering NSOM for determining polarization dependent features. To describe the polarization state of the scattered field at any arbitrary point, one needs to first identify the most suitable basis in which to represent a three-dimensional (3D) polarized field. Any fully polarized 3D field will have the electric field vector confined to some plane and a phase relationship tracing out an ellipse [40]. An arbitrary 3D field may be considered as:

$$\mathbf{E}(\mathbf{r}, t) = \Re\left((\mathbf{p} + i\mathbf{q})e^{-i\omega t}\right), \quad (3.1)$$

where \mathbf{p} and \mathbf{q} represent the real and imaginary vectoral components of the 3D field. If we want to define the relationship between \mathbf{p} and \mathbf{q} to be on some ellipse, we can define the major and minor axis as:

$$\mathbf{p} + i\mathbf{q} = (\mathbf{a} + i\mathbf{b})e^{i\varepsilon}, \quad (3.2)$$

where ε is a scalar parameter, writing the parameters of the ellipse in another form, we have:

$$\begin{aligned} \mathbf{a} &= \mathbf{p} \cos(\varepsilon) + \mathbf{q} \sin(\varepsilon) \\ \mathbf{b} &= -\mathbf{p} \sin(\varepsilon) + \mathbf{q} \cos(\varepsilon) \end{aligned} \quad (3.3)$$

The scalar parameter ε should be chosen such that \mathbf{a} and \mathbf{b} are mutually orthogonal. Also, to have a uniquely defined ε we can choose the magnitudes to be such that $|\mathbf{a}| \geq |\mathbf{b}|$ allowing us to construct the following relationship:

$$\tan(2\varepsilon) = \frac{2\mathbf{p} \cdot \mathbf{q}}{\mathbf{p}^2 - \mathbf{q}^2}. \quad (3.4)$$

From \mathbf{a} and \mathbf{b} , we can also calculate the ellipticity of the 3D field:

$$ellipticity = \frac{|\mathbf{b}|}{|\mathbf{a}|}. \quad (3.5)$$

The ellipticity goes to 0 for linearly polarized light and to 1 for circularly polarized

Far away from a scatterer, the polarization ellipse will lay in a plane perpendicular to the direction of propagation (the radial vector), as the field is two dimensional. In the near and intermediate fields, where there is a superposition of many plane waves, the polarization may not be perpendicular to the radial vector. If now examine again the case of a linearly polarized excitation, in Figure 3-3, we can see how the polarization state is modified upon scattering from the small sphere. As can be seen, when looking very close to the scatterer, $r = 0.25\lambda$ (Figure 3-3 A), the plane of the polarization ellipse is not perpendicular to the radial vector (the plane of polarization does not lay on the surface of the sphere), more over, we can see that there are some locations where the field has become elliptically polarized. Since this is the instantaneous polarization state, the non-propagating evanescent fields also play a role in the final state further

away from the object, $r = 1.5\lambda$ (Figure 3-3 B), the contributions from the evanescent components of the scattered field are less visible, and the polarization is along the surface of the sphere (tracing the electric field lines). This is even more pronounced when we look in the far field (Figure 3-3 C).

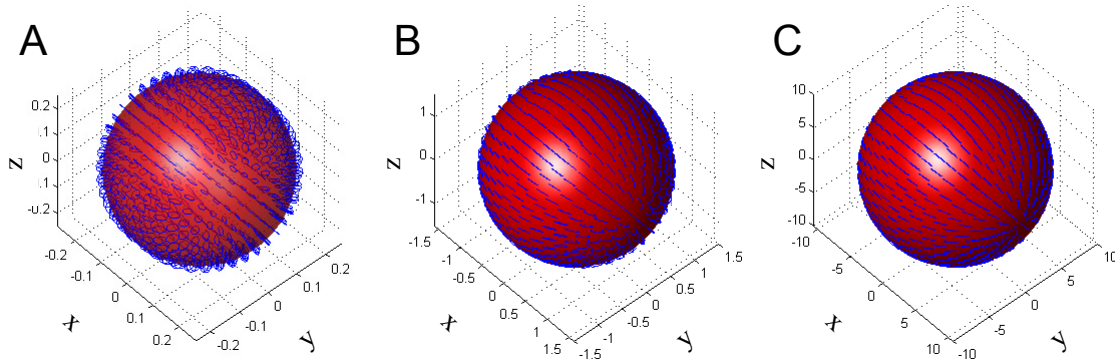


Figure 3-3 Polarization state of the scattered field measured at a distance r from a scatterer excited with a field linearly polarized along x . The observation distances are $r = 0.25\lambda$ (A), $r = 1.5\lambda$ (B) and $r = 10\lambda$ (C).

It is also interesting to see how the scatterer modifies the polarization when the incident field is circularly polarized Figure 3-4. Close to the scatterer (Figure 3-4 A) one can see again that the polarization ellipse is not confined to the plane perpendicular to the surface normal (the radial vector). The transformation of the polarization state is this time from circular in the forward direction to linear in the plane perpendicular to the propagation direction of the incident field ($z=0$ plane). To assess how the polarization state evolves as the observation point is moved away, we can look a little further (Figure 3-4 B). In this case, unlike the linear polarized case, the change in the polarization state remains. Looking further (Figure 3-4 C) we can see that this transformation from circular to linear still remains. This fact is obvious when we consider that a small sphere (equivalently and electric dipole) in the plane of oscillation, there is no means to scatter any other state aside from linear. This particular feature in the scattering from a single

sphere has some rather intriguing implications when considering the conservation laws for electromagnetics.

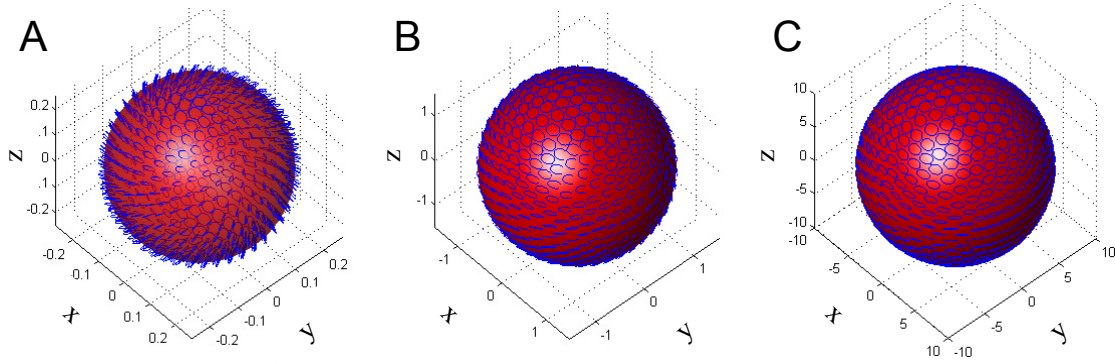


Figure 3-4 Polarization state of the scattered field measured at a distance r from a scatterer excited with a circularly polarized field. The observation distances are $r = 0.25\lambda$ (A), $r = 1.5\lambda$ (B) and $r = 10\lambda$ (C).

3.2. Angular Momentum Conservation

Conservation laws are ubiquitous in all physical disciplines. In optics, the conservation of energy, and conservation of linear and angular momentum are of particular interest. To compliment our analysis on how the scatterer modified the polarization state, we can also consider how the momentum was exchanged. Specifically here, we are interested in the angular momentum in elastic scattering of circularly polarized light on a sphere. The angular momentum of a propagating electromagnetic field is [41]:

$$j_z(x, y, z) = \frac{c\mathcal{E}_0}{i2\omega} \mathbf{E}^* (\hat{\mathbf{r}} \times \nabla) \mathbf{E}|_z + \frac{c\mathcal{E}_0}{i2\omega} \mathbf{E}^* \times \mathbf{E}|_z \quad (3-6)$$

where the first term represents the orbital angular momentum (OAM) and the second term accounts for the spin angular momentum (SAM). The orbital angular momentum term is determined by the macroscopic energy flow with respect to an arbitrary reference point and does not depend on the wave's polarization. The spin angular momentum on the other hand, relates to the phase between orthogonal field components and is completely determined by the state of

polarization. Because the total angular momentum is conserved along propagation, when a wave encounters a refractive index inhomogeneity (including interfaces between otherwise homogeneous media), a momentum transfer appears between the orbital and spin terms. This angular momentum exchange, or, in other words, the spin-orbit interaction (SOI), explains a number of polarization effects [42,43].

Of course, a linearly polarized plane wave exhibits no angular momentum while a circularly polarized one carries all of its angular momentum in the spin term. Therefore, in the case described above in Figure 3-4, the spin angular momentum from the incident field must have been completely transformed into orbital in the plane perpendicular to the direction of propagation. The orbital angular momentum of a field is observed as a curvature of the Poynting vector, which is defined as

$$\langle \mathbf{S} \rangle = \frac{1}{2} \Re(\mathbf{E} \times \mathbf{H}^*). \quad (3-7)$$

Using the expressions described in Chapter 2 for a single dipole, the Poynting vector for some arbitrary dipole moment (excitation polarization) may be found as [44]:

$$\langle \mathbf{S} \rangle = \frac{ck^4}{32\pi^2 \epsilon_0 r^2} \left((\mathbf{p} \cdot \mathbf{p}^* - (\mathbf{p} \cdot \hat{\mathbf{r}})(\mathbf{p}^* \cdot \hat{\mathbf{r}})) \hat{\mathbf{r}} - \frac{2}{kr} \left(1 + \frac{1}{kr^2} \right) \Im((\mathbf{p} \cdot \hat{\mathbf{r}}) \mathbf{p}^*) \right). \quad (3-8)$$

As can be seen in Eq.(3-8), the time averaged Poynting vector consist of two terms, one that points along the radial vector, and another that depends on the polarization state. To show the difference between the two polarization states we have discussed so far, from Eq.(3-8) we can deduce the expression specifically for the case of a linearly polarized excitation as:

$$\langle \mathbf{S} \rangle = \frac{ck^4 |\mathbf{p}|^2}{32\pi^2 \epsilon_0 r^2} \sin^2(\alpha) \hat{\mathbf{r}}, \quad (3-9)$$

where α is the angle between the linear polarization state and the observation location. We can see from Eq.(3-9), the energy is flowing radially outward for any linear state. This means that no matter where one observes the energy flow, the magnitude will change but the shape remains the same. A plot of the normalized Poynting vector of the field scattered from by a small sphere excited with linearly polarized light is shown below in Figure 3-5.

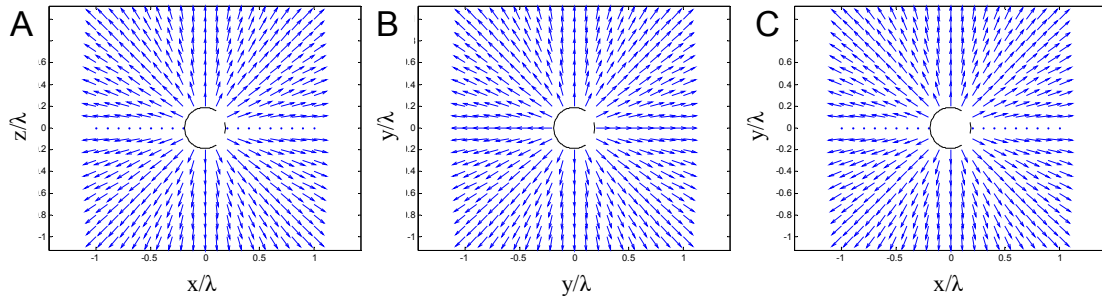


Figure 3-5 Distribution of Poynting vector in the x-z plane (A), y-z plane (B) and x-y plane (transverse to the direction of excitation) for a 100nm radius sphere for the case of linear polarization along the x direction with a wavelength $\lambda=532\text{nm}$.

As expected, all three planes are identical aside from the 0 intensity along the direction of the induced dipole. The Poynting vector in the case of excitation with circularly polarized light exhibits a rather different functional form. Following from Eq.(3-8), one finds that

$$\langle \mathbf{S} \rangle = \frac{ck^4 |\mathbf{p}|^2}{32\pi^2 \epsilon_0 r^2} \left((2 - \sin^2 \theta) \hat{\mathbf{r}} \pm \frac{2}{kr} \left(1 + \frac{1}{kr^2} \right) \sin(\theta) \hat{\boldsymbol{\phi}} \right), \quad (3-10)$$

where here $\hat{\boldsymbol{\phi}}$ is the azimuthal angle in the xy plane. As we can see from Eq.(3-10), the behavior for circularly polarized excitation is quite different than the one observed for linearly polarized case. In addition to the same radially symmetric component, there is an additional element that depends on the polar angle θ (angle with the z axis). Interestingly, the distribution of the Poynting vector changes with the angle of observation and it also changes depending on where one observes it. This is a consequence of contributions from the radially decaying components of

the scattered fields. A vectorial plot demonstrating this behavior of the Poynting vector is presented in Figure 3-6.

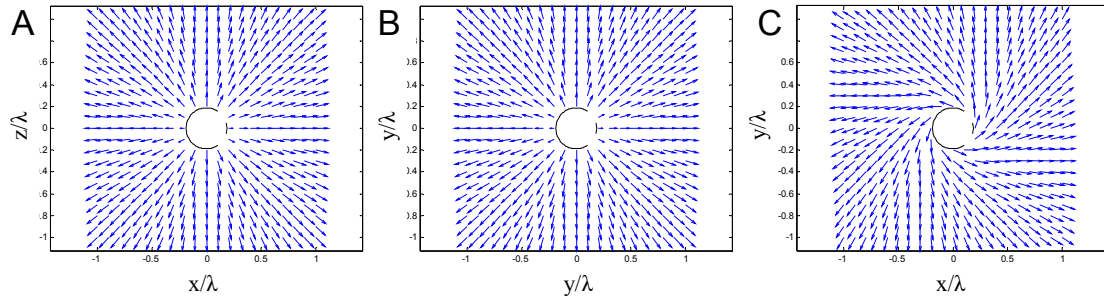


Figure 3-6 Distribution of Poynting vector in the x-z plane (A), y-z plane (B) and x-y plane (transverse to the direction of excitation) for a 100nm radius sphere for the case of circular polarization with a wavelength $\lambda=532\text{nm}$.

As can be seen, the flow of energy is the same in the x-z plane (Figure 3-6 A) and y-z plane (Figure 3-6 B) as one would expect for a circularly symmetric excitation. What is not seen however is that the energy actually flows out of plane, as illustrated in Figure 3-6 C for the x-y plane. The amount of energy flowing out of plane in Figure 3-6 A and B is 0 in the forward and backward directions, and reaches its maximum in the x-y plane.

3.2.1. A Consequence of Angular Momentum Conservation

In Ref [45] it was discussed that upon projecting the lines from the Poynting vector back to the plane of the original volume of interaction, there will be a perceived shift in the scattering location. What is most interesting in this situation is that the amount of this shift, and its direction will depend on the ellipticity of the excitation polarization. As can be seen in Figure 3-7 A., the curved Poynting vector of Figure 3-6 C in the xy plane leads to a spiral trajectory which converges to a perceived shift in the volume of interaction in the far field. While rotating a quarter wave plate, the perceived shift goes from its maximum for circular polarization, to 0 for

linear, and to a maximum in the opposite direction of circular polarization of opposite handedness.

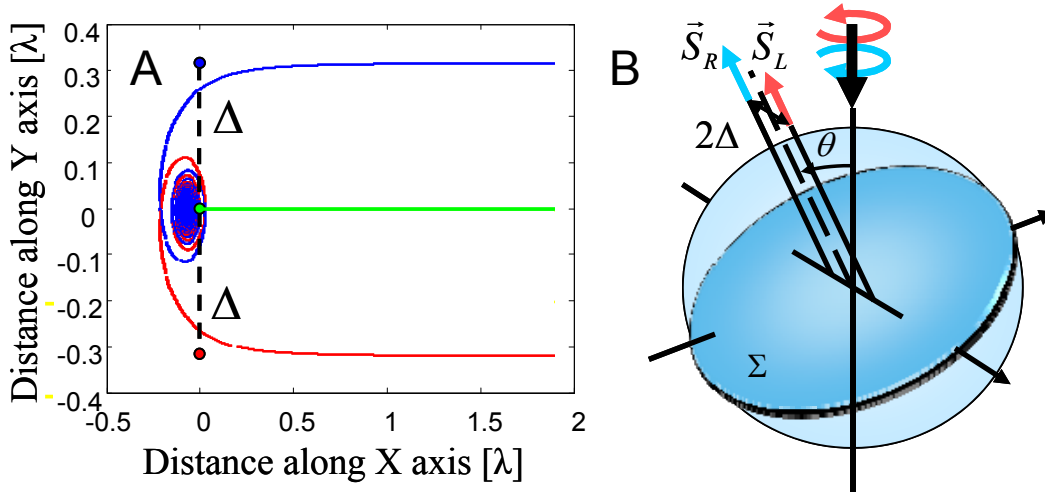


Figure 3-7 (A) In the far field, the perceived location of the volume of the interaction is shifted by an about Δ . The shift is in opposite directions for the different circularly polarized excitations states (blue and red curves) and is equal to 0 for any linearly polarized excitation state (green curve). This transversal shift Δ occurs in any plane Σ and its absolute value depends on the angle θ with respect to the forward scattering direction.

This shift will occur at any observation angle aside from the exact forward and backward directions. The magnitude of this shift in the far field can be calculated from the angle $\langle \mathbf{S} \rangle$ makes with the line of direct sight (radial vector \mathbf{r}) [45, 46]. The shift is perpendicular to the plane of scattering, and has opposite signs for excitations with different handed excitations as seen in Figure 3-7. Its value [46]

$$\Delta_{dipole} = (\lambda / 2\pi) \left[\sin \theta / (1 - 1/2 \sin^2 \theta) \right] \quad (3.11)$$

depends on the polar angles of scattering θ and reaches a maximum in the plane where a full transformation from SAM to OAM occurs: the plane perpendicular to the direction of propagation of the incident wave ($\theta = \pi/2$). Note that this shift does not depend on the optical

properties of the scatterer [45,46]. For a sphere of finite size, in the far field, the shift in perceived location is

$$\Delta = \lim_{r \rightarrow \infty} \left[\mathbf{r} \left(\frac{|S_{\perp}|}{|S_r|} \right) \right], \quad (3.12)$$

where S_{\perp} and S_{ρ} are the components of \mathbf{S} perpendicular and parallel to ρ . In general the transformation of SAM to OAM is not complete. However, for certain sets of parameters (sphere radius, refractive index) there are one or several angles θ where transformation is total and the scattered light is linearly polarized. The value of Δ corresponding to these angles attains local maxima and can reach tens of wavelengths in magnitude.

An analytical solution to Maxwell's equations for the scattering from larger spheres is the well known Mie theory. The expressions are well known and a complete derivation may be found in Ref [47]. A comparison between the energy flow near and around a larger sphere, is shown in Figure 3-7. Due to the SAM to OAM transformation in the case of a Rayleigh scatterer, the Poynting vector propagates along conical and spiral trajectories [44] (Figure 3-8 A). For larger spheres, the more complicated process of scattering results in a complex, sometimes winding trajectory of \mathbf{S} . For instance, Figure 3-8b illustrates the projection of \mathbf{S} on the plane perpendicular to the direction of excitation and containing the center of the sphere. Notably, the bending of the Poynting vector field lines as seen in Figure 3-8 determines large angles between the $\langle \mathbf{S} \rangle$ and \mathbf{r} , resulting in experimentally measurable SOI effects. This intermediate zone spans up to several λ , and, therefore, an observation can be performed without significantly disturbing the field near the sphere's interface. The large intermediate zone for a sphere is due to the evanescent fields, which in this case exhibit an inverse power law decay, as opposed to the exponential decay for a planar interface[48].

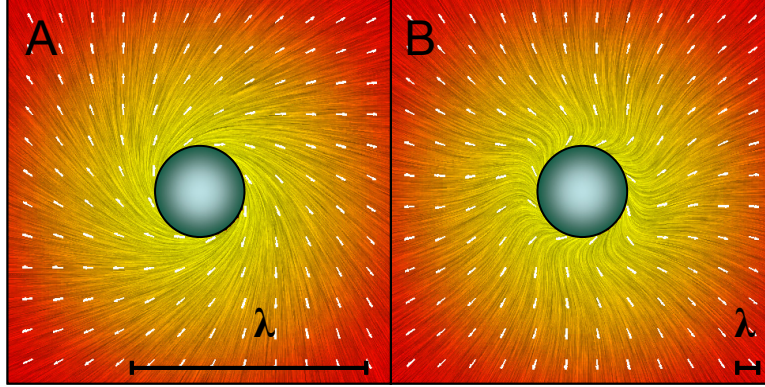


Figure 3-8 Poynting vector field lines projected on the plane perpendicular to the direction of excitation and containing the center of the scattering sphere. Different size spheres, (a) smaller than the wavelength λ and (b) larger than λ , exhibit a spiraling of the flow of energy in the intermediate region. Most interesting is the winding of Poynting vector field lines in (b) due to the complex process of scattering from large spheres (Results are presented using an adaptation of the Matlab vector field visualization toolbox [49]).

3.3. Observing Direction of Intermediate-Field Energy Flow

Observing the circulation of the Poynting vector in scattering from a sphere requires a detection scheme that is sensitive to the local energy flow. One such experiment could involve optical forces, where the trajectories of probe scatterers are analyzed in the proximity of the sphere. A much simpler procedure however can be based on a common tool having angular selectivity, i.e. a single-mode optical fiber. In the context of various experimental methods for coupling evanescent fields in Chapter 2, we discussed how a tapered optical fiber can be used to interact with the non-propagating fields and couple them to propagating in the fiber. In the coupling to a fiber, the field distribution is modified to match the propagating mode structures of the fiber. Thus, an optical fiber provides insight to the local field distribution through its coupling efficiency. The coupling efficiency of a single mode fiber is found as [50]:

$$C = \tau/2 \int_{\sigma} (\mathbf{E}_s \times \mathbf{F}^*) \cdot \hat{\mathbf{y}} d\sigma, \quad (3.13)$$

where \mathbf{E}_s and \mathbf{F} are the scattered field and fiber mode, \hat{y} is the unit vector along the fiber and τ is the electric field transmission coefficient. The integration is performed in the plane σ perpendicular to the fiber.

To measure the described shift, an experiment based on the directional sensitivity in the coupling to a single-mode optical fiber was performed (Figure 3-9). Polystyrene spheres with a diameter of $4.62 \mu\text{m}$ were sparsely distributed upon a microscope slide. To minimize the interference effects of the substrate, index matching fluid was used to create conditions equivalent to those of spheres in suspension. Circularly polarized coherent laser light ($\lambda=532 \text{ nm}$) was used as an excitation and a prism was employed to adjust the plane of illumination as shown in Figure 3-9. An ensemble of a half-wave and quarter-wave plates allowed the generation of any polarization state. A second quarterwave plate and polarizer in conjuncture with a silicon detector were used to ensure that the desired circular state of polarization is incident on the spheres.

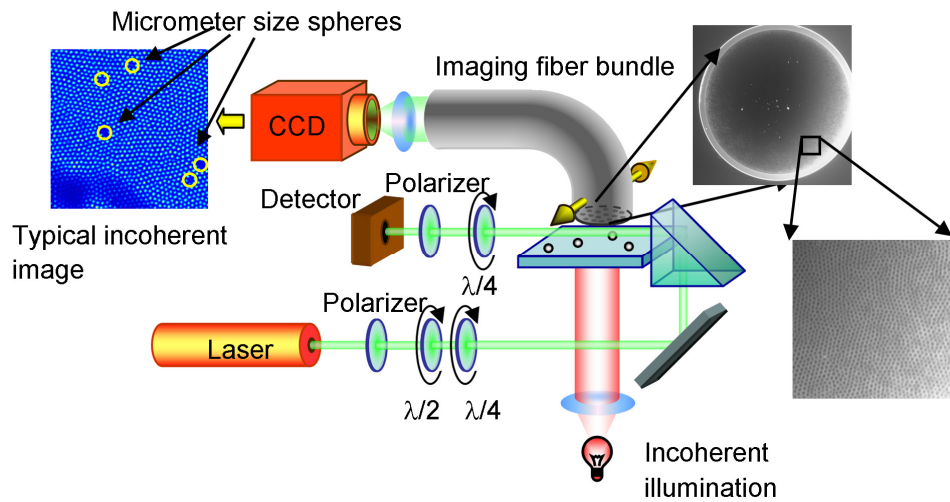


Figure 3-9 Schematic of the experimental setup using a single mode optical fiber as a means for sensing local power flow direction.

The scattered light was collected through a coherent imaging fiber bundle (Sumitomo IGN-08/30), containing 30 000 single-mode fibers. Individual fibers have a core diameter of 1.6

μm and the fiber to fiber separation is $4 \mu\text{m}$. The positions of individual particles were detected and monitored using an additional, incoherent illumination from underneath the sample. A cooled CCD array (Andor IXON) was used to both image the spheres at the opposite end of the bundle and to detect the scattered intensity at desired locations.

The position of the imaging fiber in the close proximity of the spheres was controlled via a microscopic stage (not shown in the figure). Using a piezomotion controller (Newport model ESP 300), the imaging fiber was scanned in the intermediate region of dielectric spheres ($1 \mu\text{m}$ away) with a step size of 150 nm , parallel to the slab and perpendicular to the direction of the excitation propagation. For each location of the fibers, sequential images were recorded with left- and right-circularly polarized coherent excitation, as well as with incoherent illumination. To expose the asymmetry in the field distribution, the detected intensities were then subtracted to reveal the shift in the direction of S (Figure 3-10b). The measurements were repeated to provide a statistical data analysis. For instance, in Figure 3-10b, error bars represent the 95% confidence interval in the measured results.

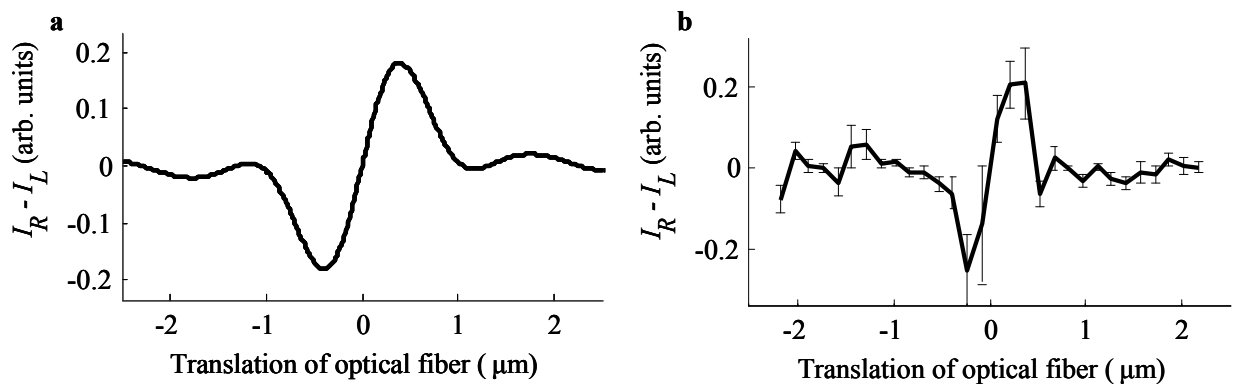


Figure 3-10 Comparison between the analytical prediction (a) and the experimental results (b) for the coupled power through a single mode fiber scanned across a polystyrene sphere of $4.6 \mu\text{m}$ diameter. The graphs depict the difference between the scattered intensities corresponding to pure states of excitation plotted as a function of fiber's position with respect to the center of the sphere.

As a comparison, the analytical prediction of the intensity coupled through single-mode optical fibers after scattering from a sphere is calculated through the use of Mie theory and compared to the experimental results. The remarkable agreement is illustrated in Figure 3-10 and demonstrates not only the asymmetry of the scattered fields, but also our capability to infer a shift in the perceived location of the interaction volume (sphere's location).

3.4. The Virtual Shift and Spin Hall Effect for Light

This modification in the perceived location of the sphere as shown in Figure 3-7 may also be interpreted as a manifestation of the spin Hall effect in scattering from a finite object. The analogy with electron transport in describing electromagnetic wave propagation provides is increasingly becoming more popular [51- 62], allowing one to draw similarities to transport phenomena such as the spin Hall effect in semiconductors [63].

Recently, it was suggested and demonstrated that an equivalent spin Hall effect of light (SHEL) exists and can be measured for a beam impinging on a dielectric interface [43,64,65] (Figure 3-11 A). In SHEL, the electron spin is replaced by the wave's polarization, and the role of an applied electric field generating the electronic current is taken by the refractive index gradient. The effect is observed as a displacement of the beams carrying spin, i.e. a transversal shift in the perceived location of the interaction volume. For different incident spins, the shift is in opposite directions, which is analogous to the induced electron spin flux perpendicular to the initial electronic current. When the incident beam is in a pure state (circularly polarized), a shift in the beam's center of mass may be observed as illustrated in Figure 3-11 B. Exciting with a mixed state, results in a separation of spin, where the region of overlap is still in a mixed state of polarization as suggested in Figure 3-11 C.

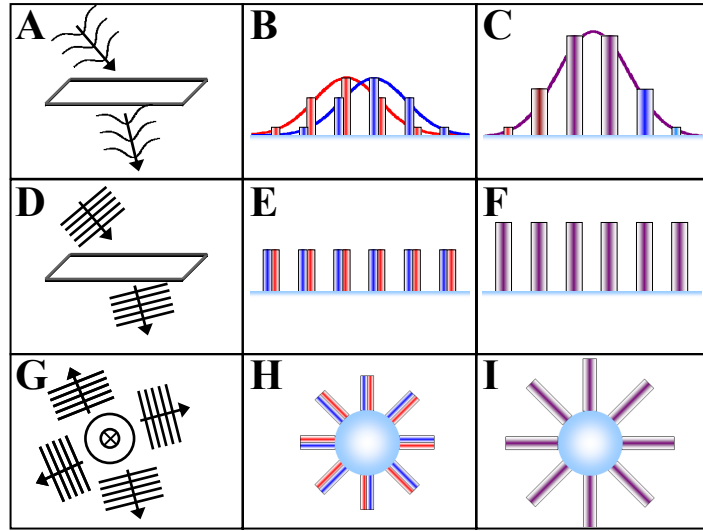


Figure 3-11. (A) A beam of light incident on a planar refractive index gradient, (B) beam shifts observed in far-field corresponding to incidence in pure states of polarization (right circular, left circular), and (C) the observable result corresponding to an incident beam in a mixed state. (D) A plane wave incident on a planar refractive index gradient, (E) the far-field shifts corresponding to incidence in pure states of polarization, and (F) the result of an incident plane wave in a mixed state of polarization. (G) A plane wave scattering from a sphere, (H) the transversal shifts in the perceived sphere center as observed in far-field for pure incident states, and (I) the result of scattering for incident wave in a mixed state.

As depicted in Figure 3-11 D, due to the infinite extent of the interaction, the transverse shift cannot be observed (Figure 3-11 E), as the refracted field is still an infinite plane wave and no reference point can be identified. When the incident field is not in a pure state, for example, linearly polarized, in spite of the transversal spin fluxes, there is no net photon current and therefore there will be no observable effect (Figure 3-11 F).

If the refractive index gradient is spherical and the excitation is a plane wave as illustrated Figure 3-11g, the conservation of angular momentum results in transversal spin flows tangent to the spherical surface[45,46]. In this case, performing sequential excitations with pure states and using a detection scheme sensitive to the local direction of energy flow, the transversal shifts can be observed as will be shown later. The presence of this shift breaks the symmetry of

the field distribution relative to any plane that contains the propagation vector and the center of the sphere. In other words, the result of the interaction between circularly polarized light and a sphere depends on the incident spin: the sphere distinguishes between left and right. For excitation with a mixed state, the transversal shift that occurs cannot be directly observed because, again, there is no net transverse photon flux as in the case of plane wave impinging on a plane interface. It should be noted that the similar considerations may be applied in a cylindrical geometry. These circumstances are similar to the Corbino disk geometry in electronic systems, where counter-propagating spin currents are generated but no net electron fluxes can be detected[66].

3.5. Summary

Even in the most symmetric of 3D structures, a sphere, interaction of an electromagnetic field with a material yields a very complicated energy distribution near to the object. Moreover, the relative orientation of the observation point with respect to the exciting polarization state adds additional complexity. Polarization related phenomena in both single and multiple scattering can be attributed to processes in which angular momentum is exchanged between the electromagnetic wave and the scattering medium [45, 67]. Solving the corresponding Mie problem, we demonstrated that there are directions where the angular momentum can completely transform into orbital momentum.

The transformation of spin momentum into orbital momentum results in a spiral flow of energy in the near-field and intermediate zones around a scattering particle for a circularly polarized incident field. When the incident light is linearly polarized (no angular momentum), such behavior is not observed in the same scattering plane as required by the momentum conservation law. We presented both analytical and experimental confirmation that spin to orbit

interaction leads to a perceived shift in the location of the volume of interaction. The measurement of this shift constitutes the first observation of transversal spin transport (a manifestation of the spin Hall effect) in scattering from finite size objects, using an object rather than the exciting field to localize the interaction. The significance of this demonstration of the complicated behavior resulting from field-material interaction is manifold. Optical experiments are suitable tools to model spin phenomena that in electronic conduction may be difficult or even impossible to approach. This could lead to the discovery of novel manifestations of spin transport in confined geometries where effects such as loss of coherence and dissipation are expected to be minimized.

Understanding subtle aspects of conservation laws in optical scattering should provide insights into phenomena such as spin transfer and power flow which, in turn, are essential for developing new sensing approaches at nanoscales. Manipulating the polarization properties of electromagnetic fields may also have consequences for controlling the subwavelength behavior of optical forces. Lastly, circular polarization is rather exotic in nature. The ability to distinguish between left and right may provide unique communication channels similar to the circular polarization vision recently discovered in some crustaceans [68]. In addition, controlling and manipulating the polarization properties of an excitation field has consequences that manifest themselves in the conservation laws determining the subwavelength behavior of optical forces which will be discussed in the following chapter.

CHAPTER 4: NEAR-FIELD INTERACTIONS IN SIMPLE MATERIAL SYSTEMS

As discussed in Chapter 3, even when a simple object such as a sphere interacts with an electromagnetic field, the redistribution of energy through scattering can become very complicated near the object. As the material system itself becomes more complicated, i.e. multiple scattering objects, the energy distribution near the objects have an extra degree of complexity, and interpretation of near-field measurements becomes even more difficult. Just as a single mode optical fiber provided means of probing the local field distribution as shown in the preceding chapter, a second scattering object can act a means to probe the local field. However, when in the near-field of one another, the presence of the probe will affect the local field. As a result, “active sensing” cannot be treated as a separable linear system; rather, the self-consistent effective field distribution must be accounted for.

In this chapter, we will discuss the scattering from simple material systems that are electromagnetically coupled and interact with an incident field to change both the local and the distant energy flow. First, the situation of coupled scattering from two small objects will be addressed and treated analytically. Specifically, we will show how different measurable quantities are being modified through coupling and its relation to the incident field. We will then discuss numerical approaches necessary to deal with larger scale material systems, where analytical solutions cannot be obtained. Using these numerical tools developed, we will study the dynamics of a non-rigid system of two sphere system and show it can be manipulated mechanically using the polarization of the incident field. Finally, we describe means to observe

experimentally the presence of near-field coupling effects and will discuss the implications for near-field experiment.

4.1. Coupled Scattering from Small Spheres

Let start by considering the canonical case of two lossless identical spheres excited with a plane wave (Figure 4-1). The total field at the location of one scatterer that lies within a system of scatterers is the summation of the incident field and the fields' scatterer by all other objects in the system. As was discussed in Chapter 2, in general, this may be found from the vector integral equations. One approximation to the vector integral equations involves replacing the integral with a discrete sum of interacting dipoles. This approximation is especially accurate when the system of scatterers pertains to a system of small spheres.

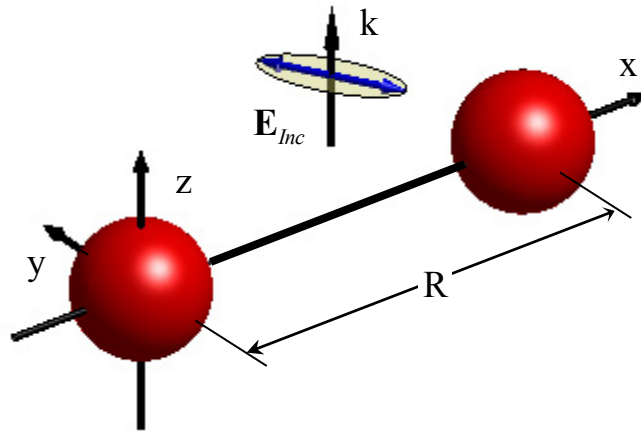


Figure 4-1 Schematic of two coupled sphere geometry

For the case when two spheres are mutually excited with the same fields, the total field \mathbf{E} is found by solving self-consistently the system of equations that takes into account the mutual interaction between the particles [69]

$$\begin{aligned}\mathbf{E}(\mathbf{r}_1) &= \mathbf{E}_{inc}(\mathbf{r}_1) + \bar{\mathbf{G}}\bar{\boldsymbol{\alpha}}_2\mathbf{E}(\mathbf{r}_2), \\ \mathbf{E}(\mathbf{r}_2) &= \mathbf{E}_{inc}(\mathbf{r}_2) + \bar{\mathbf{G}}\bar{\boldsymbol{\alpha}}_1\mathbf{E}(\mathbf{r}_1).\end{aligned}\tag{4-1}$$

In Eq.(4-1), \mathbf{r}_1 and \mathbf{r}_2 represent the dipole locations, $\mathbf{E}_{inc}(\mathbf{r})$ is the incident field, $\bar{\boldsymbol{\alpha}}$ corresponds to the individual polarizabilities of the two different scatterers, and the tensor $\bar{\mathbf{G}}$ is the inter-dipole propagator (dyadic Green function). The inter-dipole propagator is a symmetric tensor that depends only on the vectorial separation. The general solution to such a coupled system for the field at the second scatterer is found as:

$$\mathbf{E}(\mathbf{r}_2) = (\bar{\mathbf{I}} - \bar{\mathbf{G}}^2\bar{\boldsymbol{\alpha}}_2^2)^{-1} (\mathbf{E}_{inc}(\mathbf{r}_2) + \bar{\mathbf{G}}\bar{\boldsymbol{\alpha}}_1\mathbf{E}_{inc}(\mathbf{r}_1)).\tag{4-2}$$

If we consider a plane wave exciting two identical spheres, the coupled system becomes highly symmetric. For a sphere, the polarizability tensor becomes a scalar. Also, a great simplification to the tensorial mathematics is achieved if one writes the dyadic Green function in its diagonal frame:

$$\bar{\mathbf{G}} = \begin{bmatrix} \eta & 0 & 0 \\ 0 & \mu & 0 \\ 0 & 0 & \mu \end{bmatrix};\tag{4-3}$$

where $\eta = 2 \exp(ikR)(-ikR + 1) / R^3$ and $\mu = \exp(ikR)(k^2R^2 + ikR - 1) / R^3$ are eigenvalues of $\bar{\mathbf{G}}$, and R is the scalar distance between particles as depicted in Figure 4-1 .

For the separation geometry chosen to be along the x axis Figure 4-1, the components to the field at second scatterer are found to be:

$$\begin{aligned}
E_x(\mathbf{r}_2) &= \frac{E_{x,Inc}(\mathbf{r}_2) + \eta\alpha E_{x,Inc}(\mathbf{r}_1)}{1 - \eta^2\alpha^2}, \\
E_y(\mathbf{r}_2) &= \frac{E_{y,Inc}(\mathbf{r}_2) + \mu\alpha E_{y,Inc}(\mathbf{r}_1)}{1 - \mu^2\alpha^2}, \\
E_z(\mathbf{r}_2) &= \frac{E_{z,Inc}(\mathbf{r}_2) + \mu\alpha E_{z,Inc}(\mathbf{r}_1)}{1 - \mu^2\alpha^2}.
\end{aligned} \tag{4-4}$$

In terms of observables, the two sphere system will collectively scatter the incident field, and as we saw in both Chapters 2 and 3, the magnitude, polarization, and Poynting vector will all depend on the location of the observation point. Rather than discuss an observation dependent quantity, we can focus on some global descriptor such as, for instance, the extinction cross section which describes the degree to which a material can scatter and absorb electromagnetic radiation [47]. The cross section represents an apparent area used to describe by what amount the radiation interacts with the target, and it is usually not the same as the geometrical cross section. The extinction cross section, which accounts for both scattering and absorption may be found from [47]:

$$C_{ext} = 4\pi k \int_V d^3r' \Im(\chi(\mathbf{r}') \mathbf{E}(\mathbf{r}') \cdot \mathbf{E}_{Inc}^*(\mathbf{r}')). \tag{4-5}$$

In the case of a single dipole or a system of dipoles, the extinction cross section relates to the induced dipole moment as [31]:

$$C_{ext} = 4\pi k \sum_j \Im(\mathbf{P}_j \cdot \mathbf{E}_{Inc,j}^*), \tag{4-6}$$

where the subscript j represents the j th dipole in the system.

Examining behavior of the extinction cross section for the case of a linearly polarized excitation field, we can first consider the two situations, when the separation vector is collinear to the polarization direction, and when the separation vector is perpendicular to the polarization

vector. As a basis for comparison, we can look at the extinction cross section of the interacting spheres as normalized to the extinction cross section from independent scattering (Figure 4-2).

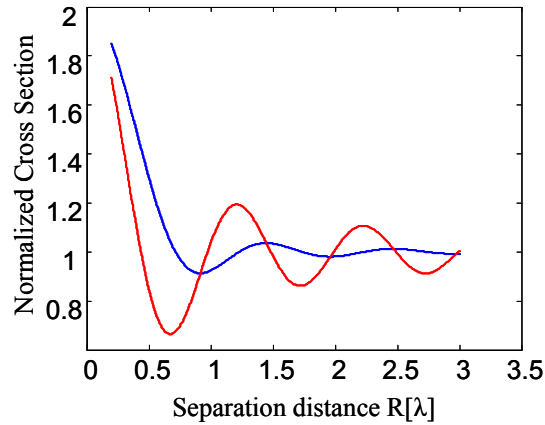


Figure 4-2 Plot of extinction cross section for two 10nm polystyrene interacting spheres normalized to the extinction cross section for independent spheres when the exciting polarization is along the direction of separation (blue) and perpendicular to the separation (red) with a wavelength of 532nm.

As can be seen in Figure 4-2, the presence of interaction changes the perceived size of the scattering object. Also evident from Figure 4-2 is that the magnitude and locations of maxima depend on the polarization state. Note that the periodicities observed for both polarization states are equal to the wavelength of the exciting field, which implies that there are interference effects. Due to the symmetry, one would expect that these two situations are the extrema in terms of the dependence on the polarization state. If we now plot the cross section for any arbitrary linear polarization state between parallel and perpendicular to the separation vector, we have Figure 4-3.

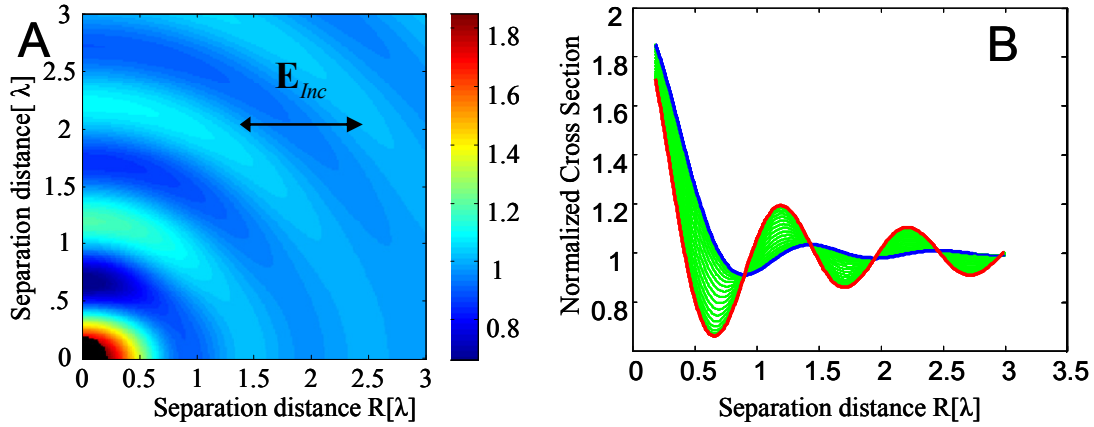


Figure 4-3 Extinction cross section for two interacting spheres normalized by extinction cross section for independent spheres varying the angle of the applied linear polarization state to the separation vector (A) keeping one sphere fixed and varying the location of the other (B) a comparative plot with collinear to the separation (blue) and perpendicular to the separation (red).

As can be seen in Figure 4-3, the situations when the polarization is collinear and perpendicular specify the bounds of the extinction cross section for all other polarization states. Also, there is a smooth transition between these two situations shifting the locations and magnitudes of the corresponding maxima and minima. Of course, as we witnessed in Chapter 3, the ellipticity may also play a role in the determining certain scattering quantities. However, in this situation, the extinction cross section depends only on the relative magnitudes of the orthogonal field components and has no dependence on their phase relationship. As the magnitudes of the orthogonal components for field circularly polarized and when linearly polarized at 45 degrees, the extinction cross section behavior is also equivalent when the field is circularly polarized and polarized at 45 degrees with respect to the separation vector.

The case of small scatterers is interesting, because one can derive well behaved analytical solutions for scattering cross sections for both independent and coupled systems. However, there are many practical situations when the idealization of objects much smaller than the wavelength

may not be relevant; therefore other approaches must be used. In the following we will extend this analysis to the realistic case of finite size interacting objects.

4.2. Numerical Modeling Interaction in Larger Systems

In order to model scattering from larger systems of particles, two competing numerical techniques are most appealing: T-matrix method and the coupled dipole approximation. As described in Chapter 2, the T-matrix involves solving Maxwell's equations via decomposing the fields into spherical harmonics. In the case of a single sphere, the T-matrix is equivalent to the exact analytical solution proposed by Mie [47]. In multiple spheres, the interaction between neighboring spheres as well as the incident field is also decomposed into spherical harmonics. If the object is not spherical or made of some arbitrary composition, the T-matrix method suffers in accuracy. For dealing with both homogeneous and arbitrarily shaped objects, CDA is more appealing. For generality of the approach of modeling near-field interactions as we will throughout this dissertation, CDA was chosen such.

As described in Chapter 2, CDA is essentially a numerical method for solving a discrete form of the vector integral equations. The response of some object of arbitrary shape and composition is modeled as a cloud of interacting dipoles. The field at one of these dipoles is the summation of the incident field, and the field resulting from its interaction with all the other dipoles:

$$\mathbf{E}(\mathbf{r}_j) = \mathbf{E}_{inc}(\mathbf{r}_j) + \sum_{k=1}^N \mathbf{E}_k(\mathbf{r}_j) \quad (4.7)$$

In many numerical approaches, modeling of interacting systems requires modeling the entire volume consisting of both the scatterers and the space between them (depicted below in Figure 4-4).

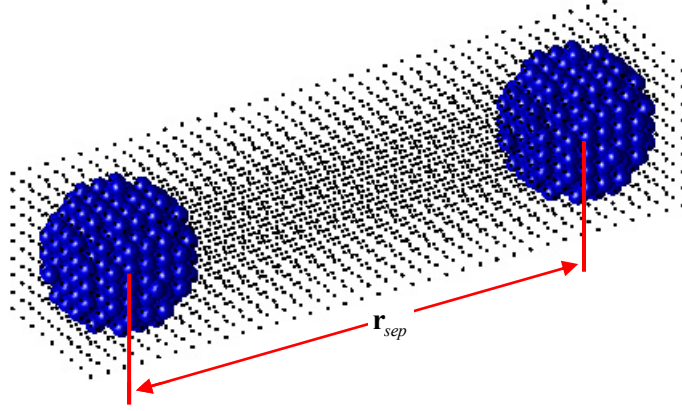


Figure 4-4 Computational space of two sphere system as modeled with the conventional coupled dipole formalism.

As the majority of the modeling locations don't contribute to the final field distribution, this method is terribly inefficient. To save on the valuable and limited computational resources, obviously, one would like to use the available modeling points to only model where the material physically exist. In order to model multiple interacting objects in CDA, it is necessary to consider the total field at one location as a summation of local and distant scattered field terms[70]:

$$\mathbf{E}(\mathbf{r}_j) = \mathbf{E}_{inc}(\mathbf{r}_j) + \sum_{k=1}^N \mathbf{E}_k(\mathbf{r}_{j,local}) + \sum_{k=1}^{N_{distant}} \mathbf{E}_k(\mathbf{r}_{j,distant}) \quad (4.8)$$

The system of equations of a multiple particle system will still be symmetric, and consist of many of the same symmetries of the original CDA interaction matrix; just the large matrix must be constructed a little differently. For a two particle system, the interaction tensor is of the following form:

$$\bar{\mathbf{A}}_{jk} = \begin{bmatrix} \bar{\mathbf{A}}_{jk}(\mathbf{r}_{local,1}) & \bar{\mathbf{A}}_{jk}(\mathbf{r}_{distant,1-2}) \\ \bar{\mathbf{A}}_{jk}(\mathbf{r}_{distant,2-1}) & \bar{\mathbf{A}}_{jk}(\mathbf{r}_{local,2}) \end{bmatrix} \quad (4.9)$$

where \mathbf{r} denotes the separation between modeling points of system 1, system 2, or between the two systems. The size of interaction tensors will be

$$\bar{\mathbf{A}}_{jk} = \begin{bmatrix} 3N \times 3N & 3N \times 3M \\ 3M \times 3N & 3M \times 3M \end{bmatrix}, \quad (4.10)$$

for systems 1 and 2 consisting of N and M dipoles respectively. Although straight forward, it is also necessary that the separation vectors of both the local and distant components lay on a cubic lattice such that one may still make use of convolution technique for accounting for the matrix vector multiplication as outlined in Chapter 2. While on a cubic lattice, the matrix vector product necessary for iterative methods to solve the system of equations may still be expressed as a convolution. In this case of two objects, the convolution must be separated into components, i.e. for a two particle system will consist of four 3-d convolutions. In terms of computations, this is indeed more than the single 3-d convolution required if the intermediate space was also included; however, with this separation of field trick, the available locations for the separation vector are no longer confined to the same lattice.

To verify that such a computational trick may be implemented and that no additional errors are introduced in the additional convolutions required, we can calculate the extinction cross section and compare to the analytical solutions for two small spheres (Figure 4-5).

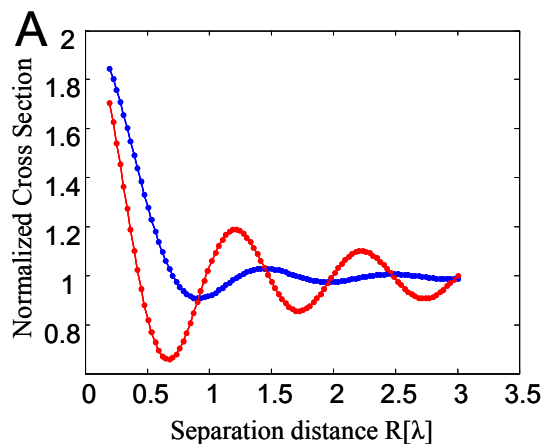


Figure 4-5 Comparison of analytical results (solid lines) and numerical results (dots) for extinction cross section of two 10nm polystyrene interacting spheres normalized by extinction cross section for independent spheres when the exciting polarization is along the direction of separation (blue) and perpendicular to the separation (red) with a wavelength of 532nm.

As can be seen in Figure 4-5, the numerical calculations using 4096 dipoles per sphere give the same normalized cross section. Accepting that this technique of separating the local and distant field contributions is accurate, we can now assess the influence of interaction in larger scatterers. For example, if we perform the same calculation for a sphere of diameter 1.8 and excite with a linearly polarized plane wave we see a similar modulation in the extinction cross section.

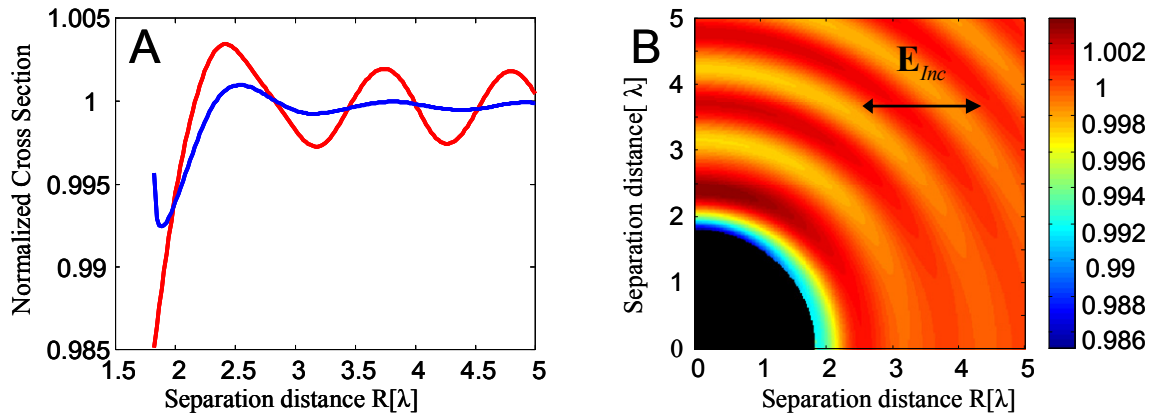


Figure 4-6 (A) Plot of extinction cross section for two 475nm radius polystyrene spheres interacting spheres normalized by extinction cross section for independent spheres when the exciting polarization is along the direction of separation (blue) and perpendicular to the separation (red) with a wavelength of 532nm. (B) Keeping one sphere fixed at the origin, a map of the normalized extinction cross section as the function of the position of a second sphere for an applied linear exciting field.

As we can see in Figure 4-6, even in the case of large sphere, the presence of a second object in its vicinity changes the perceived size. The magnitude of this change is smaller for the larger spheres because they scatterer predominantly in the forward direction. Thus it may be expected that interaction effects are larger when the two spheres are stacked on top of one another. As Figure 4-6 (B) demonstrates, the effect of electromagnetic interaction depends on the orientation of the applied field. Of course, the extinction cross section is only one possible observable quantity; other properties, such as relative position for instance, may be even more susceptible to consequences of such interaction. To analyze these effects, one needs to consider the influence the probing field has on the spheres position through optical forces.

4.3. Dynamical / Mechanical Effects on Interaction in Large Systems

The interaction of light with matter can change the mechanical properties of a material system. The so-called “optical trapping” is one example where the location of a particle may be manipulated by means of an interaction with an external electromagnetic field. The idea of

mechanical action of light has been pursued for hundreds of years. The ability to trap and maneuver small objects such as micro-particles, polymer chains, cells, etc. is undoubtedly one of the most exciting use of what is now commonly referred to as optical tweezers [71]. A host of applications are being pursued where optical forces are employed for manipulation, measurements, or for creating and controlling new states of matter. Moreover, the mutual interaction of a collection of objects in close proximity to one another offer yet another means of particle-particle manipulation.

The Lorentz force equation gives the force acting on a point charge q in the presence of an electromagnetic field [72]:

$$\mathbf{F} = q(\mathbf{E} + \mathbf{v} \times \mathbf{B}), \quad (4.11)$$

where here \mathbf{v} is the velocity, and \mathbf{E} and \mathbf{B} are the electric and magnetic fields. For larger objects, the electromagnetic force is usually found from a surface integral of the Maxwell stress tensor, which accounts for the shear force plus the time dependent change in momentum from the incident field.

$$\mathbf{F} = \oint \bar{\mathbf{T}} d\mathbf{a} - \mu_0 \epsilon_0 \frac{d}{dt} \int_V \mathbf{S} dV, \quad (4.12)$$

where here \mathbf{S} is the Poynting vector, and the elements of \mathbf{T} can be found as:

$$T_{jk} = \epsilon_0 \left(E_j E_k - \frac{1}{2} \delta_{jk} E^2 \right) + \frac{1}{\mu_0} \left(B_j B_k - \frac{1}{2} \delta_{jk} B^2 \right), \quad (4.13)$$

In the case of a small sphere, or dipole, as we discussed in part one of this chapter, there exist an analytical solution to the total force provided by Eq.(4.12). After a lengthy derivation (See Appendix C) one may find that the time averaged total force (as the frequency of optical fields far exceeds the response for which a particle can respond) on a dipole depends on the induced dipole moment and the local field as:

$$\langle \mathbf{F} \rangle = \frac{1}{2} \Re \left[(\mathbf{p} \cdot \nabla) \mathbf{E}^* + (\mathbf{p} \times (\nabla \times \mathbf{E}^*)) \right], \quad (4.14)$$

In the specific case of a sphere, there is a simple relationship between the induced dipole moment and the local field in terms of the polarizability ($\mathbf{p} = \alpha \mathbf{E}$). This allows for many equivalent methods of expressing the total force. Physically, the most obvious decomposition of the total force is into the conservative and non-conservative portions. A conservative force is one in which the total work performed on an object over the course of a closed path is 0. The conservative portion of the force is also the term found from the gradient of the potential energy, another common means of describing dynamics. The non-conservative portion of the force is typically attributed to some sort of loss, as work is done even when traveling a closed loop. Non-conservative forces lead to continuous motion where as conservative forces can lead to transient phenomena. A complete derivation starting from the Lorentz force of Eq. (4.11) through the Maxwell Stress tensor of Eq.(4.12), also deriving the force for a dipole of Eq.(4.14), and finally showing how the force may be decomposed into components may be found in Appendix C. Broken into components, the total force on a small sphere in terms of its polarizability and the local field is given by:

$$\langle \mathbf{F} \rangle = \frac{1}{2} \Re(\alpha) \nabla |\mathbf{E}|^2 + \omega \mu_0 \Im(\alpha) \langle \mathbf{S} \rangle + \frac{\omega}{\varepsilon_0} \Im(\alpha) (\nabla \times \langle \mathbf{L}_s \rangle), \quad (4.15)$$

where $\langle \mathbf{L}_s \rangle = \varepsilon_0 / i4\omega (\mathbf{E} \times \mathbf{E}^*)$ is the time averaged spin flux density, $\langle \mathbf{S} \rangle$ is the time averaged Poynting vector (Eq.(3-7)).

The first term in Eq.(4.15) that is known as the gradient force depends on the gradient of the intensity of the field; and is the only conservative portion of the force. The gradient term is the only component depending on the real part of the polarizability, and does not have any dependence on the phase of the field. The second term is depends on the time averaged energy

flux of the applied field. This term, usually referred to as the radiation pressure, depends on the imaginary part of the polarizability; and is non-conservative in nature. The third term is usually unnamed in the literature, is related to the spin momentum of the applied field and is also non-conservative in nature [73,74]. In situations where the Poynting vector has a complex behavior, one would expect that intriguing non-conservative and continuous motions may arise.

As has been described throughout the current chapter, the fields arising from mutual interaction disrupt change the local fields and modify the apparent properties of the scatterer. What was not discussed was the dynamics of coupled particle systems. One important consequence of electromagnetic particle-particle interaction is optical binding (OB), first noted by Burns et al [75]. Two particles excited by a common field can form a bound “optical dimer” when they arrange themselves to a stable position where the radial forces acting on them are zero. Since the first OB demonstration, a number of aspects have been studied including the excitation generated by counter-propagating beams [76,77], effects of beam’s structure [78], or the consequences of scattering [79]. In all situations, the resultant binding intrinsically depends on the potential energy landscape created by the conservative part of the electromagnetic forces. However, little if any attention has gone toward the non-conservative forces, and how they may have an impact in a coupled system.

Let us examine the system of two identical spherical particles illuminated by a plane wave propagating perpendicularly to the radius-vector connecting the centers of the particles, as shown in Figure 4-7. Forces are generated on the spheres due to the three-dimensional, polarized field established as a result of scattering [80]. Due to symmetry in the x - y plane, the force acting on each particle can be decomposed into radial (binding) and tangential (rotational) components.

There is also a scattering force along \mathbf{k} , but its effect is identical for the two particles and does not hamper their transversal movement. This is the classical OB geometry [75,69, 81 , 82].

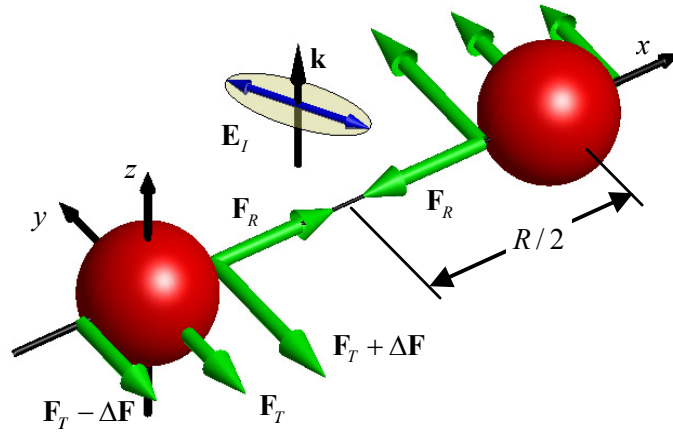


Figure 4-7 Optical binding in elliptically polarized light E_I . Apart from the binding force F_R , interacting particles experience tangential forces F_T . Note the existence of differential forces ΔF leading to individual spinning in addition to common orbiting of particles around the system's center of mass.

Just as in Section 4.1, the total field \mathbf{E} is found by solving self-consistently the system of equations (Eq.(4-1)) that takes into account the mutual interaction between the particles[69]. The field derivative is then calculated to obtain the final expression for the force in Eq.(4.14).

The calculation of optical forces acting on matter is believed to be a well established routine. The same is true for the optical forces arising in basic OB situations, even though care must be taken in describing the particle-particle interaction. A popular way for evaluating the derivative $\partial\mathbf{E}/\partial u$ is to differentiate the final solution of the system of equations Eq. (4-1) (see Eq. 4 in Ref.69). By doing so, however, the results contradict the calculation of time-averaged forces based on the well-established formalism of momentum flux tensor (Maxwell stress tensor) [83]. The correct way of evaluating the derivative $\partial\mathbf{E}/\partial u$ is to differentiate with respect to either \mathbf{r}_1 or \mathbf{r}_2 directly in Eq. Eq. (4-1). Nevertheless, it is interesting to note that the way $\partial\mathbf{E}/\partial u$ is calculated has a minor effect for the radial, binding force; this is perhaps the reason this

inconsistency has not been noticed before. When evaluating the tangential forces, however, there are situations where the way the calculation of field derivatives is conducted becomes important as it will be demonstrated here.

Using Eqs. (4.14) and Eq. (4-1) one can now evaluate the radial and tangential forces to be

$$\langle F_R \rangle = \frac{|\alpha|^2}{2} \left(\frac{|E_{\parallel}^I|^2}{|1-\eta\alpha|^2} \operatorname{Re} \left(\frac{\partial \eta}{\partial r} \right) + \frac{|E_{\perp}^I|^2}{|1-\mu\alpha|^2} \operatorname{Re} \left(\frac{\partial \mu}{\partial r} \right) \right), \quad (4.16)$$

$$\langle F_T \rangle = |\alpha|^2 \operatorname{Re} \left(\frac{\eta - \mu}{R} \right) \operatorname{Re} \left(\frac{E_{\parallel}^{I*} E_{\perp}^I}{(1-\eta^* \alpha^*)(1-\mu\alpha)} \right), \quad (4.17)$$

where E_{\perp}^I , E_{\parallel}^I are the components of incident field perpendicular and parallel to the separation vector. We can now proceed to examine the effect of the incident polarization.

4.3.1. Optical binding with Linearly Polarized Light.

Because the depth of the potential wells in the stationary points depends on the incident polarization [81], the system of optically bound particles tends to orient itself such that it occupies the most energetically favorable position. The potential energy of a single dipole is found as:

$$U = -\mathbf{p} \cdot \mathbf{E}. \quad (4.18)$$

where \mathbf{p} is the induced dipole moment. A plot of the potential energy for three different linear polarization states is shown below in

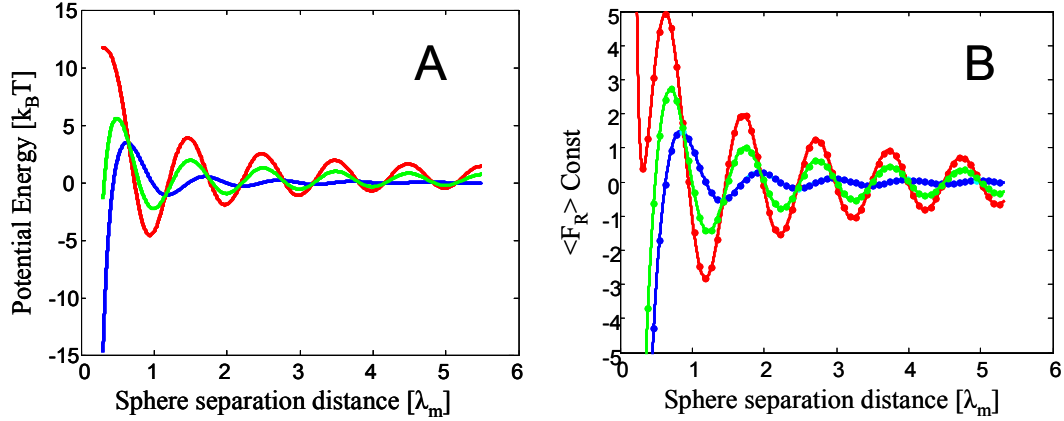


Figure 4-8 (A) Plot of the potential energy for a 100nm polystyrene sphere of refractive index 1.59 in water excited with linear states along the separation direction x (blue curve), at 45 degrees (green curve) and orthogonal (red curve) with an incident power of 0.1W per square micron. The wavelength was 632nm. (B) shows the corresponding forces for the same system for the three different polarization states normalized to the unitless quantity $\text{Const} = (4\pi\epsilon_0|E_0|^2(10^{-23}\text{m}^2))^{-1}$. The dots in B correspond to a numerical simulation of the same scattering situation using CDA to calculate the forces.

As can be seen in Figure 4-8(A), regardless of the polarization state, there exist potential wells at depths that a particle may become trapped radially. Also observed in Figure 4-8 is that the deepest potential energy well (maximum forces Figure 4-8(B)) occur when the polarization state is orthogonal to the separation vector. This means that when two small spheres are excited with a linearly polarized state, and they form an optically bound pair, they will align orthogonal to the polarization direction. One interpretation of this behavior is as a consequence of optical interaction, there is an effective anisotropy in a system of bound spheres. However, this is the opposite behavior as an anisotropic dipole or a rod would demonstrate, where preferential alignment is always along the polarization direction. To understand this phenomenon, we can step back and consider how the total field is established from the fundamental field distribution of a dipole.

As our dipole moment is induced by the field, it will be aligned along the direction of the field, the potential energy is simply $U = -|p||E|$. The most energetically favorable position is

the minimum in the potential energy, which corresponds to a maximum in the dipole moment. In the weak interaction approximation, we can think of the field at one dipole just being the result of the interference between two dipole fields. Analyzing the total field at one of the spheres location, the field may be considered as a constant field (from the incident field) interfering with the scattered field from the other dipole. The location of the second scatterer that maximizes the local field (or equivalently the dipole moment) should correspond to both a maximum of the scattered amplitude from the other dipole, and should interfere constructively (meaning the phase should play a role).

Figure 4-9 shows the behavior of the amplitude of the scattered field as compared to the optically bound locations for the different linear polarization states.

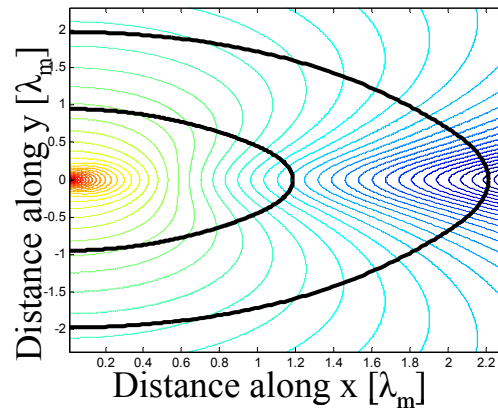


Figure 4-9 Contours of constant intensity for an x-polarized excitation of a 2 dipole system, keeping one dipole at the origin and varying the location of the other (contours are linear with $\log(\log(I))$). The black line correspond to the positions of optical binding (if a second sphere was near by, it would travel along the black line until it was along the y axis (vertical))

As we can see in Figure 4-9, the magnitude of the scattered field along the direction of the polarization is much smaller than that along the orthogonal direction once we are further than a third of the wavelength away (again we see the donut shape in far field). If we are satisfied with the concept of maximizing the field at distances comparable to the wavelength, this simple picture demonstrates why optically bound spheres align orthogonally to the incident polarization.

The scattered intensity is at a maximum orthogonal to the field polarization, and this in turn produced a minimum in the potential energy.

However, this picture does not explain why of the location of the optical binding changes with polarization. The intensity is always monotonically decreasing as a function of the separation in all directions. To understand this we can look to the phase of the scattered field, as seen in Figure 4-10, where contours of constant phase of the scattered field are plotted.

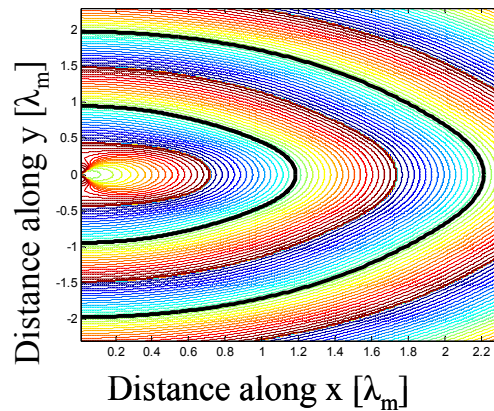


Figure 4-10 Contours of constant phase an x-polarized excitation of a 2 dipole system, keeping one dipole at the origin and varying the location of the other. The black line correspond to the positions of optical binding (if a second sphere was near by, it would travel along the black line until it was along the y axis (vertical))

As can be seen in Figure 4-10, the black lines that signify the position of the optically bound locations lay directly upon contours of constant phase. This phase corresponds to positions where the scattered fields interfere constructively with the incident field. As the phase of the scattered field from a dipole is not spherical, the separation distance changes with polarization in accordance to maintain this constructive interference.

4.3.2. Optical Torques with Linearly Polarized Light.

A fundamental consequence of an applied force is the ability to induce torque with respect to some reference point. Torques can also be induced by optical fields. Several concepts

for optical spin motors or “nano-rotators” have been discussed based on optical traps created with circularly polarized light or vortex beams and relying on object’s asymmetry, absorption, or birefringence [84-86]. Also, recently it was shown that for a single sphere in an optical trap, the subtle interplay between conservative and nonconservative forces create a “nano-fountain” with constant circulation of trapped particles [87].

One may readily find the corresponding torques $\Gamma_T = \sum_j \mathbf{R}_j^\perp \times \mathbf{F}_T(r_j) + \mathbf{p}_j^\perp \times \mathbf{E}_\perp(\mathbf{r}_j)$ by summing over all dipoles \mathbf{p}_j in the system [88]. Here \mathbf{R}_j represents the position of the dipole relative to the axis of rotation and the symbol \perp denotes the components of vectors perpendicular to the chosen axis. In the case of OB spheres, one may identify torques resulting in two special rotational motions: (i) sphere orbiting together around their common center of mass and (ii) spheres spin about their own axis.

When the interaction is weak ($\eta\alpha \ll 1$, $\mu\alpha \ll 1$), Eq.(4.17) simplifies to $\langle F_T \rangle = |\alpha|^2 |\mathbf{E}_I|^2 \cos(2\theta) \text{Re}((\eta - \mu)/R)$, where θ is the angle between polarization and separation vectors. We note that the tangential force varies in space proportionally to $\cos(kR)$ or $\sin(kR)$ having the same periodicity as the radial (binding) force (Eq.(4.16)). The tangential force acting on a dipole-like particle is zero when the field polarization is along or orthogonal to the separation vector.

For systems of larger particles, where there are no simple analytical results; one has to go beyond the simple dipole approximation and use numerical procedures. As the CDA extension described in Section 4.2 yields the local field distribution, it is straight forward to calculate the forces acting on each individual dipole as described in Ref.[89]. Typical results of CDA calculations for three different sized particles excited with different linear states are illustrated in Figure 4-11.

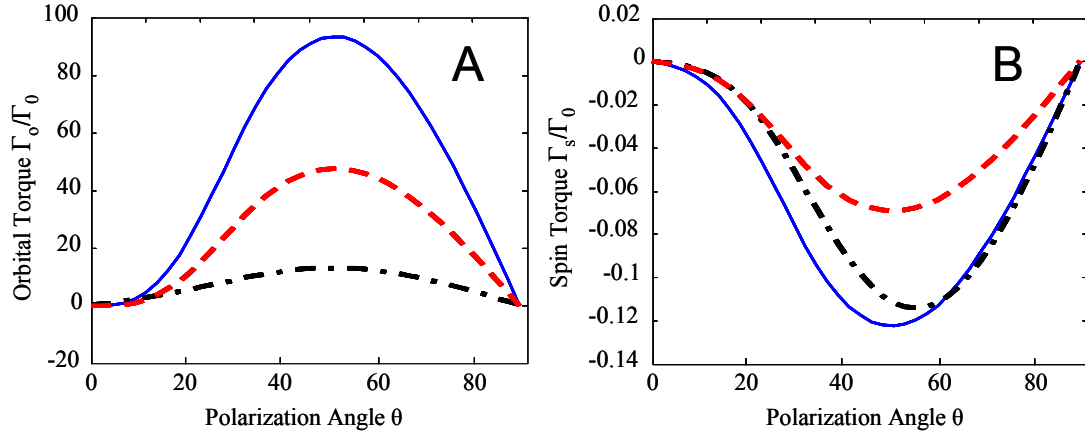


Figure 4-11. Torques in an optically bound system of silica spheres of radius $a = 0.1\lambda_m$ solid lines, $a = 0.2\lambda_m$ dashed lines, $a = 0.4\lambda_m$ dot-dashed lines: (A) orbital torque about the system's center of mass and (B) spin torque of a sphere about its own axis. The spheres are in water and are excited with a field polarized linearly at an angle θ with respect to the optical binding vector.

The torques are normalized to $\Gamma_o = 10^4 |\mathbf{E}_l|^2 a^4 / \lambda$.

As can be seen, there are no torques when the incident polarization is orthogonal or along the separation vector. However, torques arise at any other angle resulting in orbital and spin motions. Note that the torque does not reach its maximum at exactly $\theta = \pi/4$ as may have been expected. For small particles, this may be understood as a result of the asymmetry in the scattered field; for larger particles a similar asymmetry can be expected but may not be the only reason.

The unexpected appearance of spin torque is due to a gradient in the tangential force across the spheres as shown in Figure 4-7. Due to this gradient of the tangential force, the spin torque has an opposite sign compared to the orbital one. In fact, the mere existence of these spin torques is a significant result, demonstrating that OB interaction can lead to rotations of lossless dielectric objects.

The torques in Figure 4-11 are mostly determined by gradient forces and, hence, determined by the conservative part of the total force. In any system with damping, the

mechanical motion created by a conservative force will eventually cease. It follows that the OB particles will eventually align perpendicularly to the direction of polarization and that the time scales of their motion will depend heavily on the specific constraints of the damping mechanism. In the following we will reveal other situations where the non-conservative forces are the main cause for such torques, which can be controlled by the polarization of the external electromagnetic field.

4.3.3. Optical Torques with Circularly Polarized Light.

In Chapter 3, it was demonstrated that scattering of circularly polarized light from a sphere generates a spiraling energy flow around it [P7]. This effect arises from the conversion of spin angular momentum of incident light into orbital angular momentum of scattered light. One can envision that a test object placed in the vicinity of such a sphere will experience the radiation pressure from the curved power flow, causing the object to move along curled trajectory. In reality, the situation is complicated by the interaction between the two bodies as was discussed before. Moreover, together with radiation pressure, the field gradient force and the force due to gradient of phase may play a significant role. Thus, the real outcome can only be found by analyzing self-consistently the problem of electromagnetic interaction.

Starting from Eq. (4.17) in the simple case of small non-absorbing dielectric particles, the tangential force can be approximated to be:

$$\begin{aligned} \langle F_T \rangle = & \pm |\alpha|^2 \operatorname{Re}(\alpha) |\mathbf{E}_I|^2 [6kR(3 - k^2R^2) \cos(2kR) \\ & - (9 - 15k^2R^2 + k^4R^4) \sin(2kR)] / 4R^7. \end{aligned} \quad (4.19)$$

The sign is determined by the polarization's handedness. It is worth noting that the force magnitude changes as a function of R with twice the frequency compared to the optical binding force evaluated from Eq.(4.16). Furthermore, contrary to the case of linear excitation, the

potential landscape is now circularly symmetric as shown in the inset of Figure 4-12. This means that the tangential forces are completely nonconservative and create a steady-state orbital torque about the system's center of mass. Affected by this torque, particles move along stationary orbits with radii determined by the condition $\langle F_R \rangle = 0$. In addition to this continuous rotation around the common axis, the particles will also exhibit a continuous rotation around their own axes due to the gradient of the nonconservative tangential force along the radial direction.

To estimate the torques acting on larger particles we used again the CDA numerical approach. A typical summary plot of the orbital torque for the first two stable bound positions is shown in Figure 4-12 as function of particle radius. Also shown, are the analytical predictions of Eq.(4.19) for Rayleigh particles, which seem to make a good description up to a radius of about $a \approx \lambda_m / 10$, where λ_m is the wavelength in medium. As apparent in Figure 4-12, an interesting effect occurs for larger spheres: the orbital rotation can change its sense depending on the particle size. This change in the direction of rotation, not present in the case of small particles, can happen even when moving between the different stationary orbits. Our calculations also indicate that for particles with $a \approx \lambda_m$, the radial and tangential forces have now similar periodicities as a function of R and, moreover, the zeros of radial force and the zeros of the tangential force occur approximately in the same place. Thus, a slight modification in the radial position of spheres can change the direction of rotation.

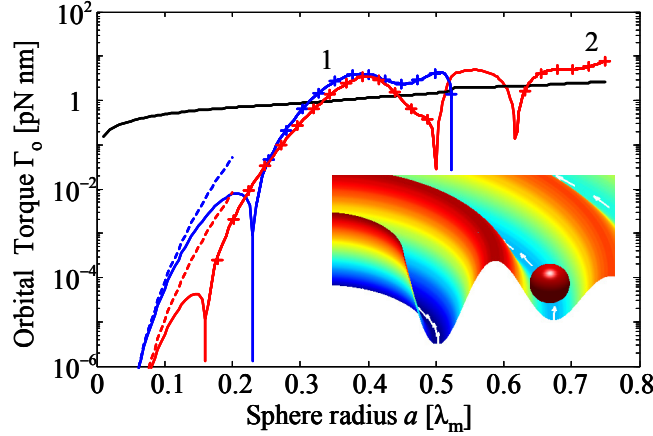


Figure 4-12. Magnitude of orbital torque as a function of the radius of interacting spheres for the first (curve 1, blue) and second (curve 2, red) stationary orbits. The plus symbols indicate regions where the torque has opposite sign. The dashed lines indicate the analytical predictions based on Eq.(4.19) for Rayleigh particles. The calculations are for silica spheres in water excited with a plane wave of intensity $50mW/\mu m^2$ and wavelength in vacuum $\lambda = 532\text{ nm}$. The black line shows the magnitude of torque due to Brownian force at 290K in the first stationary orbit. The inset depicts the symmetric potential energy landscape and the trajectory of a bound particle due to nonconservative orbital torques.

In addition to electromagnetic interaction, OB systems can also be subject to Brownian motion. Directional motion due to optical forces will be affected by the additional chaotic movement associated with some random force $\langle F_B^2 \rangle = 12\pi\eta ak_B T$ [90]. The torque resulting from the Brownian force provides a useful reference for the magnitude of orbital torques. In Figure 4-12, one can clearly see that for $a \geq 0.3\lambda_m$ and an optical intensity of $50mW/\mu m^2$, the optically induced torques dominate.

Due to the complex interaction, the OB particles are also subject to spin torque with respect to the individual axes as shown in Figure 4-13. As can be seen, for the chosen parameters, the spin torque increases with the particle size but, similar to the orbital torque, the sense of rotation is not always the same. Examining the two types of torques in Figure 4-12 and Figure 4-13, one can see that the spin and orbital torques have opposite directions for small particles but their behavior becomes more complicated when the sizes increase.

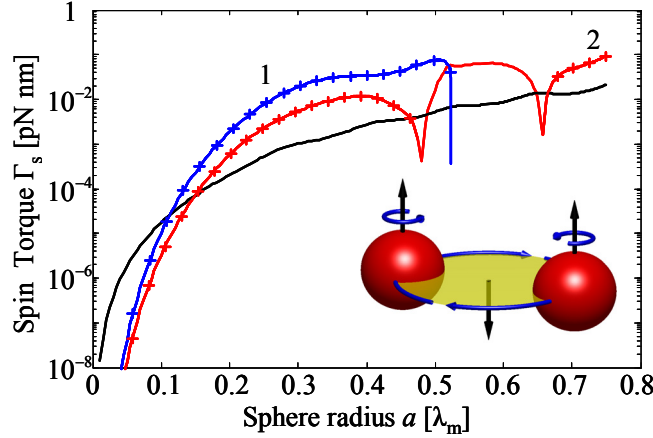


Figure 4-13 Magnitude of spin torque Γ_s as a function of the radius of interacting spheres for the first (curve 1, blue) and second (curve 2, red) stationary orbits. The plus symbols indicate regions where the torque has opposite sign. The calculations are for silica spheres in water excited with a plane wave of intensity $50mW/\mu m^2$ and wavelength in vacuum $\lambda = 532\text{ nm}$. The black line shows the magnitude of absorption-induced spin torque of one silica sphere with refractive index $n_i = 1.59 + 10^{-7}i$.

Circular polarization can induce torques on a small object due to asymmetry, absorption or birefringence. Therefore, it is instructive to compare the magnitude of OB spin torque with the optical torque exerted on a particle due to its intrinsic absorption. The later can be estimated as $\Gamma_{abs} = |E_I|^2 a^2 Q_{abs} / 4k$ [91], where Q_{abs} is the absorption coefficient. Estimations based on typical values for absorption in silica are shown in Figure 4-13, and, as can be seen, spin torque dominates for $a \geq 0.1\lambda_m$. Notably, because the OB spin torque does not necessarily have the same direction as the excitation handedness while the torque due to absorption is always in the same direction, the two torques can combine to increase or cancel the net rotation.

The magnitudes of the orbital and spin rotations of OB particles may be affected by the surrounding medium. In fluids for example, in addition to the influence of viscosity on forces and torques, hydrodynamic coupling may occur between closely placed particles. For a sphere of radius $a = 0.4\lambda_m$ and an intensity of $50mW/\mu m^2$ in the Rotne-Prager approximation [92] one

finds that, in the first stationary orbit, the orbital and spin angular velocity in water are $\Omega_o = 17 \text{ rad/s}$, $\Omega_s = -2.6 \text{ rad/s}$, respectively. It is worth mentioning that for these specific parameters, the liquid flow created by the orbiting spheres greatly affects their spin rotation forcing them to rotate in opposite direction with respect to acting torque Γ_s (as indicated by minus sign). In fact, the ratio between spin and orbital angular velocities can be optically modified. This external control together with the hydrodynamic coupling may be used to detect the presence of otherwise hardly noticeable spinning motion of OB spheres.

4.4. Observing Coupling Effects in the Near-Field

Of course, particle-particle interaction also plays a role when the system is not dynamic as we observed in Section 4.1 in the coupled cross section. What is not obvious is whether particle-particle interactions play a role when the objects are not all excited by the same field, such as the highly localized excitation generated in an NSOM. Experimentally, it is difficult to gauge the effect on one sphere due to the presence of another.

The extension of CDA discussed in Section 4.2 may be further extended to numerically model such a situation. A common model for the field generated by an NSOM probe (Section 2.1) is the field emitted from a single dipole. In the same method that the distant field was included as a separate interaction matrix in Section 4.2, an additional dipole may be added in the same manner. A schematic of the computational system can be seen in Figure 4-14.

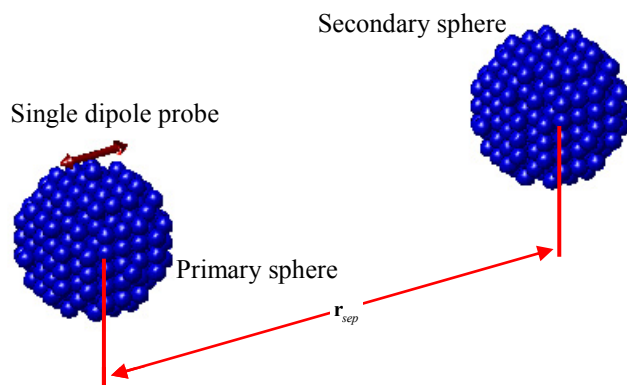


Figure 4-14 Schematic of modeling 2 sphere system excited locally with a single dipole acting as the local excitation (NSOM probe), using the separation of local and distant fields for the compression of the computational system.

Because only a single dipole is added to the system of equations, there is no need for any additional convolutions to invert the system, merely an additional matrix vector product of size $3N \times 3$, N being the total number of dipoles in the system. To test the effects of coupled scattering, we modeled two spheres with a radius of 0.3λ excited locally with a probe polarized along the direction of separation; the results are shown in Figure 4-15.

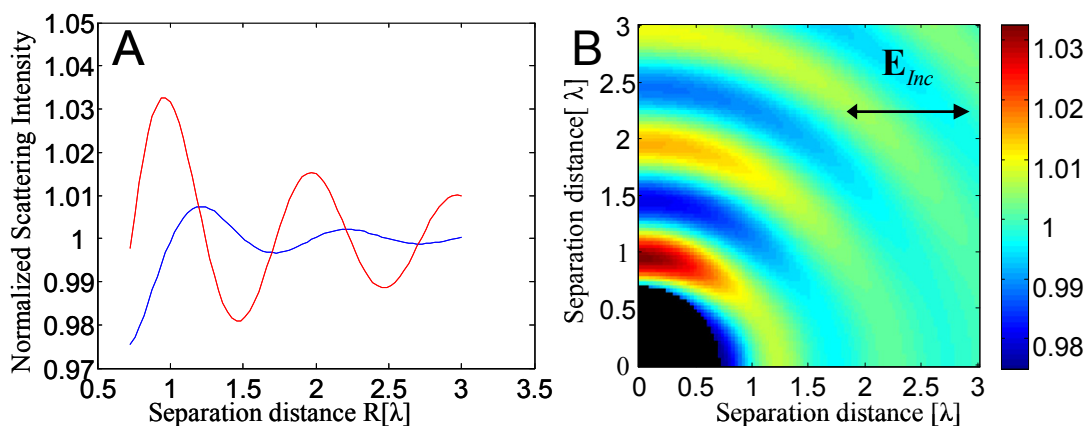


Figure 4-15 (A) Plot of intensity scattered from two 160nm radius polystyrene spheres interacting spheres normalized by extinction cross section for independent spheres locally excited with a small sphere with the polarization along the direction of separation (blue) and perpendicular to the separation (red) with a wavelength of 532nm. (B) Map of the normalized scattered intensity as the function of the orientation for an applied linear exciting field of the single sphere exciting the coupled system.

As can be seen in Figure 4-15, the presence of a second sphere changes the intensity of the scattered field from a single sphere even when the exciting field is highly localized. These collective modes of the dielectric structure can explain the intensity variations and the presence of regular fringes surrounding microspheres.

A situation where such an approach would be useful is that of a monolayer of dielectric spheres with a diameter greater than the wavelength. Due to the large size of the spheres, the topography is slowly varying, and in the case of independent scattering, the response on the top of one sphere would depend only on the local interaction between the probe and the local slope. For a monolayer of spheres, one would thus expect that the intensity distribution around one sphere would be repeated for every other equivalent sphere. However, if the sphere did not scatter independently, as is the case in the far-field illumination, the response would depend on the local morphology. In other words, the number of spheres in the proximity of a single sphere would determine the scattered intensity near and around it due to optical interaction. To test the validity of the above treatment to a monolayer of dielectric particles, we performed a near-field scan on a monolayer of $1.5\mu\text{m}$ silica spheres, shown below in Figure 4-16.

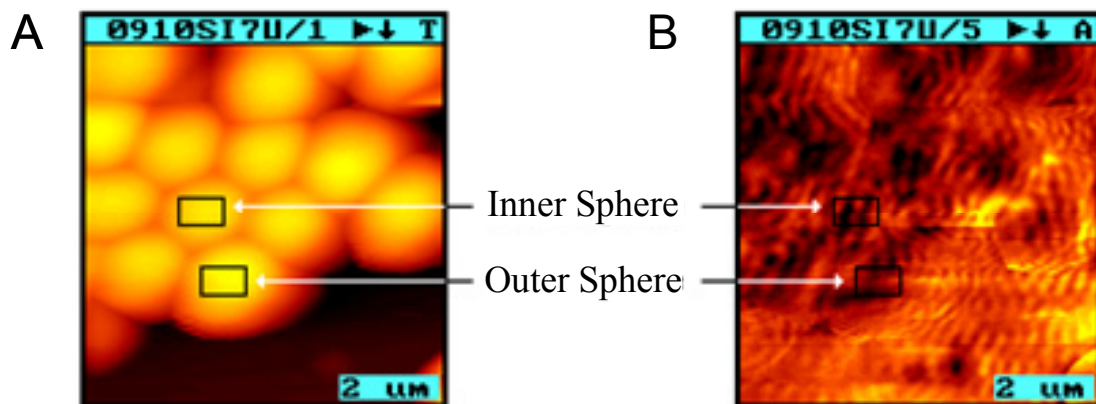


Figure 4-16 (A) AFM topographical image of monolayer of silicon spheres compared to near-field intensity (B) distribution, and the selection of inner and outer spheres to analyze.

As can be seen, the NSOM image of this deterministic situation is very complicated, the intensity distribution having regular interference fringes surrounding the microspheres. Certainly, the slowly varying slope above the sphere is not determining all the observed features of the intensity distribution. Here the presence of possible cross-talking between the silica spheres can be seen as a collective response of the dielectric micro-particles

To quantify the presence of cross-talking, we chose to analyze the intensity distributions for a sphere surrounded by a group of spheres experiencing significant cross-talking (inner sphere) and a sphere on the edge of the cluster experiencing less cross-talk (outer sphere). We chose to analyze the top of the two spheres as seen in the black rectangle (area of .94 by .53 μm^2) seen in Figure 4-16; the rectangle was chosen such that the local slopes within the area were as close as possible. A close up of the topography and intensity distributions at this location is presented below in Figure 4-17.

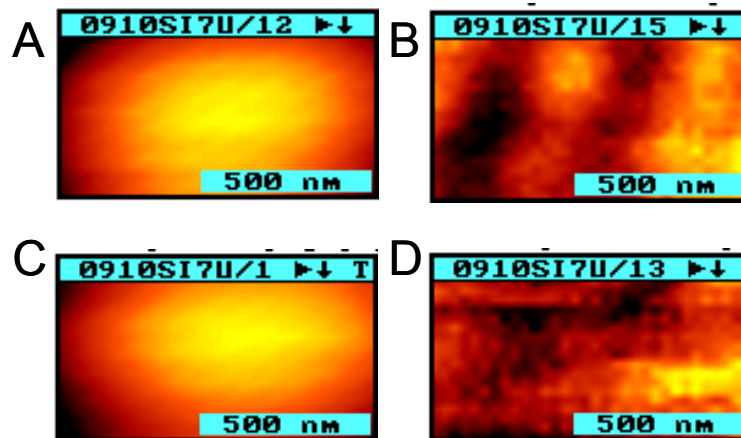


Figure 4-17 Individual images of topography and intensity distribution for inner and outer spheres analyzed over an area with near equal slope. (A), inner topography, (B) inner intensity, (C) outer topography, (D) outer intensity,

It is possible to see the interference fringes that occur in the inner sphere by looking at the intensity distribution. In order to quantify this it is necessary to compute the standard deviation and look at the amount of fluctuations that the Inner sphere has compared to the Outer.

In this example, the average intensity for the Inner and Outer sphere are 752 kHz and 760 kHz respectively. The standard deviation for the Outer sphere was calculated at 26 kHz which is 3.47% of its average intensity. The standard deviation for the Inner sphere was calculated at 41 kHz which is 5.49% of the average intensity for that sphere. This shows a significantly higher spread in the intensity for spheres surrounded by a group of spheres due to the cross-talking between spheres. Just as observed in Figure 4-15, the response of a larger sphere, even when locally excited, depends on the local morphology.

4.5. Summary

In many situations, independent objects interact collectively with an electromagnetic field. The consequences are diverse and depend on the polarization of the incident field as well as the specific positioning of the interacting objects. We showed here that this interaction leads not only to changes in the optical signatures of such coupled system but also on the mechanical properties of its constituents. Specifically, it was demonstrated in this Chapter that such near-field electromagnetic interaction provides a new mechanism for generating optical torques. Electromagnetic fields induce conservative forces resulting from field gradients as well as nonconservative forces appearing due to radiation pressure and gradients of phase. When two objects are optically bound, these forces determine conservative and nonconservative torques.

Remarkably, the interplay between the conservative and nonconservative torques can be controlled by the polarization of the incident field. For instance, when the incident field is linearly polarized, the torques are mostly conservative and affect only the transient behaviors. For circular polarization on the other hand, the nonconservative torques are significant and lead to nontrivial phenomena. In particular, bound systems can rotate not only around the common center of but also around their own axes. In the intermediate case of elliptically polarized light,

the conservative torque will determine a transient orbital motion, whereas the nonconservative one will lead to a continuous spin rotation. The whole system can be seen as a ‘nano-mixer’ with complex mutual rotations of constituents. The direction and speed of these rotations can be dynamically controlled through the intensity, state of polarization, and spatial profile of the incident radiation. Our estimations indicate that effects are easily observable under reasonable environmental conditions.

We have also shown that this electromagnetic interaction is significant even when only an individual scattering object is excited with a highly localized field. These results are significant, because they demonstrate that even when probing locally a composite medium, the scattered radiation depends on the surrounding morphology of a sample. Understanding the specific manifestation of radiation coupling should be of interest in applications of photonic crystals which are developed in the optical near-field, as well as for a range of phenomena involving multiple light scattering in the bulk of inhomogeneous materials.

CHAPTER 5: NEAR-FIELD SCATTERING IN COMPLEX MEDIA

As we saw in Chapter 3, in the near- and intermediate-fields of a scattering object, the electromagnetic energy exhibits a complex behavior that depends on the vectorial properties of the exciting field. As described in Chapter 4, additional complexity is introduced when multiple objects are immersed in the same field and optically interact with another in addition to the exciting field, acting as some effective object. We also discussed how, for dynamic material systems, one may use the complicated vectorial dependence and the mutual interaction of neighboring objects to change the dynamics of material systems. Both Chapters 3 and 4 dealt with simple material systems characterized by uniform dielectric properties. In this case, only a few parameters were required to describe the deterministic scattering object.

However, there exists a large and rather different class of material systems that are more complex because their optical properties vary randomly in space or time. These media are considered to be optically inhomogeneous and coherent scattering usually yields field variations that are also randomly distributed, commonly referred to as a speckle pattern. Usually, one single wave-matter interaction does not yield much valuable information to characterize such complex media; rather a statistical ensemble is required such that statistical characteristics like moments of distributions for instance can be related to meaningful material properties. Probing of the local field through some secondary interaction may affect the individual member of the ensemble, but not affect the statistical characteristics of the scattered fields. That is, because material descriptors are statistical in nature, the contributions from the secondary interaction may be either separated or neglected.

In general, the response of complex media will depend on the amount of averaging performed. Also, when the characterization is based on far-field measurements, there is a significant amount of averaging over the structure, which usually washes away much of the structural information. In the near- and intermediate-regions however this is not necessarily the case and specific information may be retrieved.

In this chapter, we discuss intensity and polarimetric fluctuations in near field scattering. Specifically we address the situation of scale dependent responses, and how a tapered optical fiber allows one to observe statistical variations depending on the volume of interaction. At certain scales, the material response depends strongly on the local structure; varying the volume results in unique optical signatures. As a first step, we will consider the scalar scattering treatment, and assess the intensity variations that will be interpreted in the frame of a simple scalar model based on a 2D random walk description [P1].

Nevertheless, as emphasized several times already, the real scattering problem is vectorial and only a vectorial description can elucidate the physical origins of the observed intensity fluctuations in the near-field. To accomplish this, we again turn to numerical modeling where we have direct access to the different properties of known physical systems. We will show how, by exploiting the sensitivity of optical interaction to the local material structure, one can find a characteristic length scale, maximum anisotropy length that depends on the local composition and organization of composite random media. This new length scale represents a unique and intrinsic property of optically inhomogeneous media and describes their polarimetric responses [P9].

5.1. Scale Dependent Optical Response

In general, material properties are scale dependent, and one can discuss corresponding length scales of microscopic, mesoscopic, and macroscopic regimes. Their absolute dimensions will depend on the specific material characteristics. When ever a real measurement takes place, there is some effective averaging of the material properties, and the amount of averaging will dictate whether the observation occurred in the micro-, meso-, or macroscopic regime. For instance, measuring a surface profile with an AFM will depend on the physical size of the probe. Depending on the amount of averaging (Figure 5-1(A)), the observed fluctuations in the measured signal will vary. The same is true for the optical response of optically inhomogeneous media (Figure 5-1(B)), where the corresponding length scales are determined by the material properties, for instance size of inclusions, volume fraction, packing structure, etc.

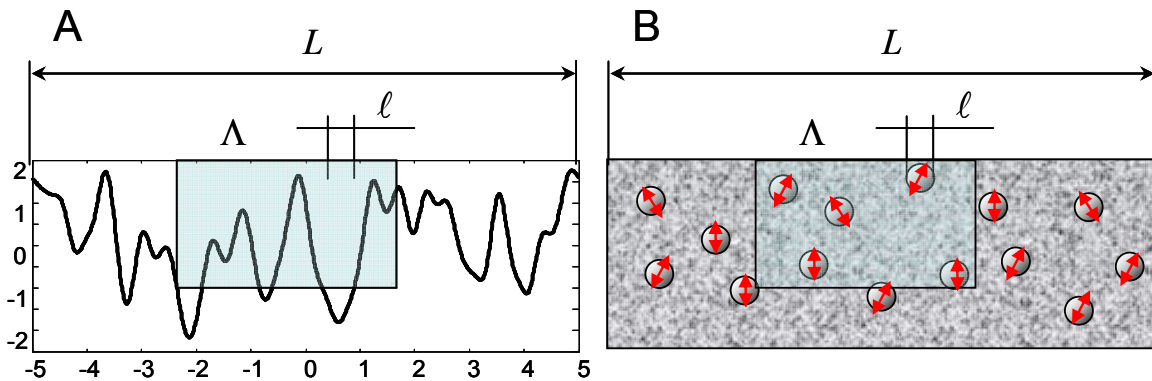


Figure 5-1 (A) Example of a Gaussian distributed surface profiled with varying observation scales corresponding to the microscopic, mesoscopic, or macroscopic averaging. (B) An optically inhomogeneous medium with refractive index variations due to inclusions and the corresponding scale lengths determined by the material properties (see text).

In terms of an inhomogeneous material, the microscopic scale (ℓ) refers to the smallest volume over which the material is homogeneous; probing this scale reveals what is usually referred to as the “intrinsic properties” of the medium. For the situation of a random surface, the

microscopic scale would correspond to probing the material with a delta function; with no averaging during the measurement.

The optical characteristics at the largest, macroscopic scale (L), involve significant averaging over volumes usually much larger than the characteristic scales of inhomogeneities. All known effective medium theories are based on this averaging principle [93]. For the case of a surface, at this scale, one usually observes the global distribution, so called Gaussian statistics with a large number of members contributing to each measurement.

The intermediate mesoscopic scale (Δ), on the other hand, involves an insufficient amount of averaging of the microscopic properties such that information is persevered. In the mesoscopic regime, fluctuations around the average become important, and may contain additional information about structural morphology. This is the scale that is available when measuring the response of a material with near-field microscope.

To demonstrate how sampling affects observed statistical properties of random phenomenon, let us consider the following simple example. The task is to sample some distribution f_x that, for the sake of the argument, can be considered to be Gaussian. Of course, in the limit of a large number n of measurement samples, the statistical characteristics of the ensemble of f_x elements will approach those of the distribution f_x . However, when n is small a non-Gaussian statistical regime develops. It can be shown (Appendix 0) that as a function of the sampling number n for a Gaussian distributed random variable the mean and standard deviation have the following dependence:

$$\begin{aligned} u_n(n) &= u \\ \sigma_n(n) &= \sqrt{\frac{n-1}{n}} \sigma \end{aligned} \tag{5.1}$$

for $n > 1$. What this means is that the mean of the observed distribution is the same independent of the type of sampling but the width of the sampled distribution is function of the number of available samples. The distribution corresponding to the surface profile of Figure 5-1(A), as a function of the number of sample elements n is shown Figure 5-2.

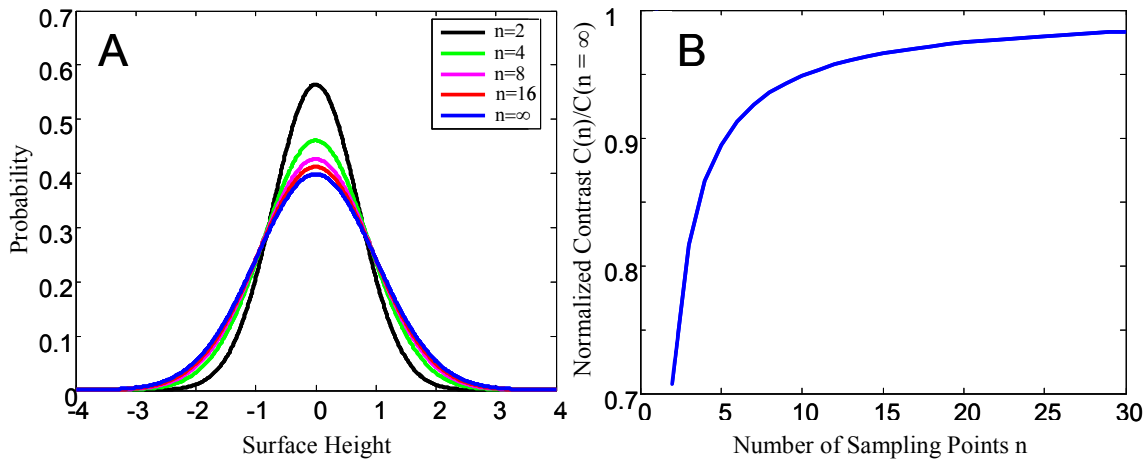


Figure 5-2 (A) Distributions observed considering n sampling points. (B) Convergence of the contrast to the global distribution contrast as a function of the number of sampling points n .

As can be seen, the observed distribution can be quite different when sampled with a small number of elements. If the observed distribution is further related to the optical properties of an inhomogeneous material, then this dependence allows examining, for instance, the number of sampling points within the measurement volume. Finally, we note that in the case of randomly inhomogeneous media, a multiscale description of the light propagation can be envisioned where the Maxwell's equations, the transport equation, and the diffusion equation can be applied to describe the microscopic, mesoscopic, and macroscopic scales, respectively. It should be anticipated that the observed optical response from a light-matter interaction depends on the volume probed experimentally. This concept has been used, for instance, to describe different statistical regimes in near-field scattering from random media [P1,38]. As we will demonstrate in

the following, in the case of near-field microscopy, the volume of effective interaction can be changed by varying the intensity of excitation or by manipulating the tip-sample separation.

5.1.1. Random Walk Model and Non-Gaussian Statistics

When a near-field intensity distribution is the result of some random process, a statistical treatment offers another means of understanding the physical origins of the intensity fluctuations [34]. As was described in Section 2.5, one standard method of analytically modeling an intensity speckle pattern is as the coherent summation of harmonic waves with an amplitude and phase distribution. In general the complex amplitude of a polarized speckle field can be written as [35]:

$$U(x) = U_r(x) + iU_i(x), \quad (5-2)$$

where U_r and U_i are the coherent summation of N harmonic waves with random phases:

$$\begin{aligned} U_r(x) &= \sum_{j=1}^N a_j \cos \theta_j \\ U_i(x) &= \sum_{j=1}^N a_j \sin \theta_j \end{aligned} \quad (5-3)$$

If the number of scattering contributions is large (N in Eq.(5-3)), as in the case of Gaussian statistics described in Section 2.5, rather simple assumptions can be made about the relative phase and amplitude distributions for the different interfering waves. However, a different situation exists where the number of harmonic waves is small. In this situation the uniform phase distribution is no longer a good assumption. Not having a uniform phase distribution means that the intensity distribution is no longer a negative exponential (as seen in Figure 2-9). A small number of contributions arise from weakly scattering systems, or when the variation in the surface topography is smaller than the wavelength of light. These situations

result in speckles that are partially developed and the contrast may be much less than unity [94]. From the random walk model described in Section 2.5, a similar treatment may be applied to understand the effects of a non-uniform phase PDF.

The phase distribution will obey some circular distribution, as its values are wrapped over 0 to 2π . One standard distribution in circular statistics that may be useful for describing the phase distribution is the von Mises distribution

$$f(\theta, \nu) = \begin{cases} \frac{1}{2\pi I_0(\nu)} \exp(\nu \cos(\theta)) & -\pi < \theta < \pi \\ 0 & \text{elsewhere} \end{cases}, \quad (5-4)$$

where I_0 is the modified Bessel function of the zero-order. The von Mises distribution has the nice characteristic that by tuning the parameter ν , one may have a uniform distribution when $\nu = 0$, and a sharp Gaussian as $\nu \rightarrow \infty$. The von Mises PDF is plotted in Figure 5-3 to demonstrate the behavior for varying ν .

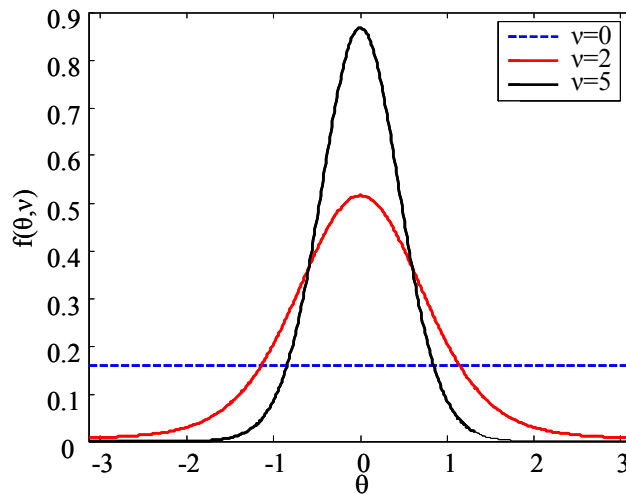


Figure 5-3 Plot of von Mises probability density function for varying ν

Following the same procedure as developed in Section 2.5 for the case of a uniform distribution, we would like to find the distribution of the scattered intensity. A full derivation of

the joint PDF of the intensity h and the phase ψ is provided in reference [36]. The probability density function of the intensity with the von Mises phase distribution is the following:

$$f(h, \nu) = I_0^{-N}(\nu) I_0 \left[\nu N \left(\frac{h}{N \langle h|0 \rangle} \right)^{\left(\frac{1}{2}\right)} \right] \cdot \sum_{j=1}^{\infty} \frac{J_0(\gamma_j / N)^N}{N \langle h|0 \rangle [J_1(\gamma_j)]^2} J_0 \left[\left(\frac{h}{N \langle h|0 \rangle} \right)^{\left(\frac{1}{2}\right)} \right] \quad (5-5)$$

where $\langle h|0 \rangle$ is the average intensity if all of the random harmonic waves were in phase, and γ_j are the positive roots of the zero-order Bessel functions. The first term of Eq.(5-5), a function of ν , characterizes the deviation from random phases with a uniform distribution, i.e. the deviation from the Gaussian regime. To examine the shape characteristic of the intensity distribution, we can again evaluate the contrast Eq.(2-38). It can be shown that the first moment, the mean of Eq.(5-5) is equal to [36]:

$$\langle h | \nu \rangle = Na^2 \left[1 + (N-1) \left(\frac{I_1(\nu)}{I_0(\nu)} \right)^2 \right], \quad (5-6)$$

and the variance is found as:

$$\begin{aligned} \text{var}(h | \nu) = N(N-1)a^4 & \left(1 + \left(\frac{I_2(\nu)}{I_0(\nu)} \right)^2 - 2 \left(\frac{I_1(\nu)}{I_0(\nu)} \right)^4 \right) + \\ & N(N-1)a^4 \left(2(N-2) \left[\left(1 + \left(\frac{I_2(\nu)}{I_0(\nu)} \right) \right) \left(\frac{I_1(\nu)}{I_0(\nu)} \right) - 2 \left(\frac{I_1(\nu)}{I_0(\nu)} \right)^4 \right] \right) \end{aligned} \quad (5-7)$$

The expressions in Eq.(5-6) and Eq.(5-7) provide a means to calculate the contrast as a function of a non-uniform phase distribution characterized by ν and for a small number of contributions N . The contrast of a speckle intensity ensemble is defined as:

$$C(N, \nu) = \left(\frac{\text{var}(h | \nu)}{\langle h | \nu \rangle^2} \right)^{\left(\frac{1}{2}\right)} \quad (5-8)$$

A plot of the speckle contrast as a function of the number of random sinusoidal waves can be seen in Figure 5-4.

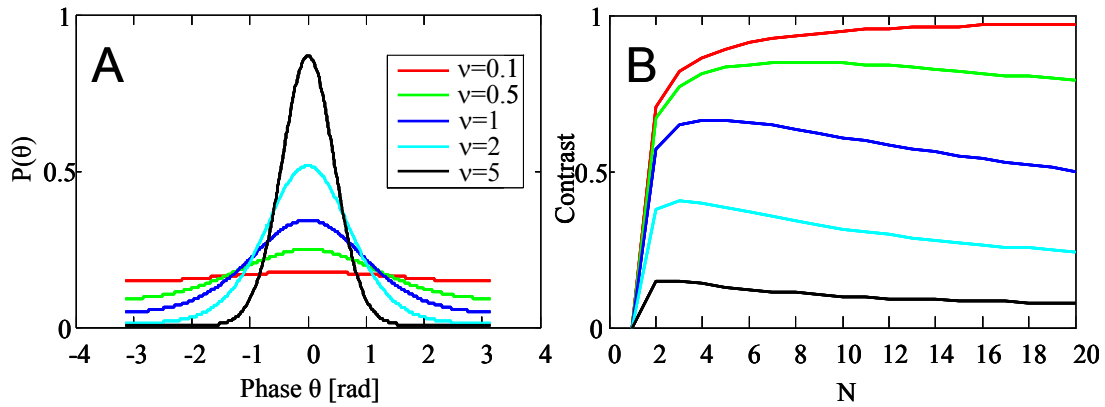


Figure 5-4 Plot of phase distribution (A) and corresponding contrast (B) as a function of N , for different values of ν

As can be seen, the narrower the phase distribution, the smaller the contrast. Also it can be observed from Eq.(5-7) that for any value of ν other than 0, the contrast will converge to 0 as N goes to infinity. In the case of a uniform phase distribution, both the mean and the standard deviation (the average and the fluctuations) grow at the same rate; whereas for a non-uniform phase distribution, the mean grows faster than the fluctuations.

In drawing the relationship between such a random walk model and the physical scattering system, one can consider that the number of scatterers is related to the volume of interaction observed in the measurement, and the phase distribution related to the material properties. As the volume increases, the contrast decreases, or as the amount of averaging over the material properties increases, the relative fluctuations decrease.

5.2. Intensity Statistics of Near-Field Experiments

This model can be used very well in the situation that arises from a near-field scan in emission mode. In emission mode, the interaction volume is governed by the diameter of the tip

aperture and the distance away from the surface. This aperture is typically much smaller than the wavelength; as such the interaction volume seen from the far-field is very small as well. This results in scattering from a small number of scatters. Unlike a global excitation, the resulting intensity probability distribution from a near-field scan in emission mode does not give that of the Gaussian regime where the PDF is negative exponential [95]. Also for such an experimental geometry, the contrast is significantly less than unity[38].

Before applying such a model directly to near-field intensity fluctuations, we should examine the different physical mechanisms that may result in such fluctuations; or what are the parameters of the material system related to the phase distribution in the random walk model. In general, in the far-field of scattering of coherent radiation from a random or inhomogeneous media it is impossible to discern whether the intensity fluctuations are the result of scattering from an optically inhomogeneous material, or from a homogeneous material with a surface roughness. Scattering from a homogenous material with a rough surface also results in a speckle pattern from the non-specular reflection at the surface. Thus, in order to know the origin of the fluctuations, one must have some information either about the samples composition or the surface.

Performing a near-field scan requires to place a probe in the close proximity of the material interface. As was described in Chapter 2, this is commonly achieved through the use of atomic force microscopy techniques. As a result, for every near-field scan, one obtains both the far-field intensity distribution resulting from the local excitation as well as the AFM topographical data. An example of a typical NSOM scan of a random media and the corresponding AFM topography can be seen below in Figure 5-5(A).

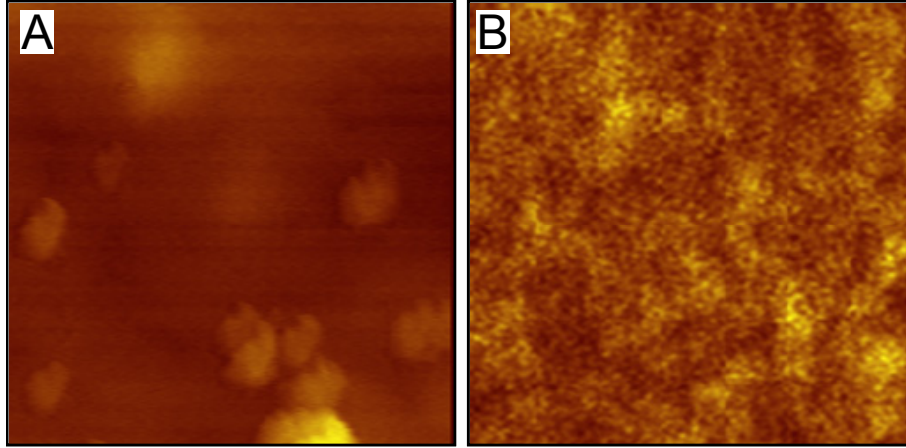


Figure 5-5 NSOM scan of optical coating consisting of 100 parts latex and 25 parts TiO₂ particulates. (A) is AFM topography, (B) Intensity distribution

As can be observed in Figure 5-5, the intensity image (B) from a random media as excited in the near-field leads to a speckle pattern in the far-field. As a means of characterizing the topography in a meaningful manner, we can look at the local slope that the near-field probe would experience. We define the local slope in the direction \hat{u} as the gradient of the topography sampled over the aperture of the probe:

$$Slope_{j\hat{u}} = \frac{T_{j+\Delta} - T_{j-\Delta}}{\Delta} \hat{u} \quad (5.9)$$

here Δ is the probe diameter and T_j corresponds to the AFM recorded height at location j . The local slopes provide a useful method of comparing the intensities recorded at different locations. We can combine the information presented in the two different images (Figure 5-5) in the form of a plot of the normalized intensity vs. the local slope as calculated by Eq.(5.9).

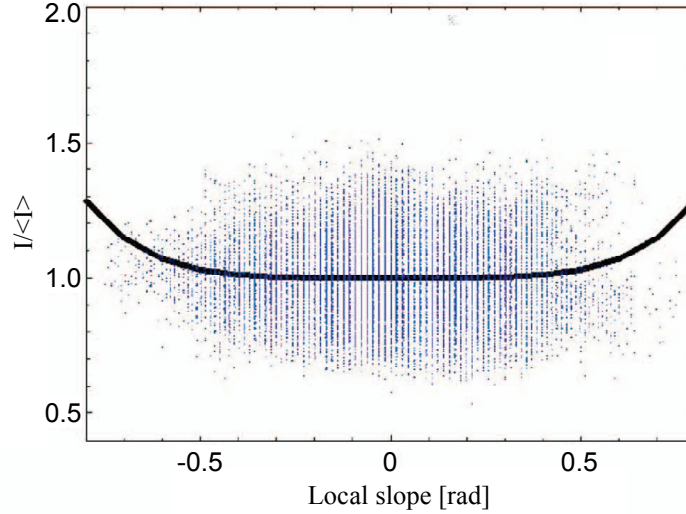


Figure 5-6 Typical histogram of an NSOM scan. The solid curve corresponds to the Fresnel reflection predicted for the corresponding effective index of the inhomogeneous sample.

As we can see in Figure 5-6 there is a significant spread of the intensity values and the correlation of intensities from similar slopes is very low. However, a great deal of qualitative statistical information may still be gathered by such a plot. The distribution of local slopes, the longitudinal spread of the histogram, describes the topographical character of the interface, accounting for both the root-mean-squared (RMS) roughness and lateral correlation length of the surface profile. The intensity fluctuations determined by the local optical permittivity can be regarded as the vertical spread of the histogram. Therefore, this representation relates the local variation of the dielectric constant to the morphology of the physical interface, offering a comprehensive (but still qualitative) description of the near-field situation.

Going back to the random walk model, the governing phase distribution, which is related to the physical scattering situation, must account both for mechanical and dielectric contributions. As the information about the mechanical fluctuations is inherently recorded with an NSOM scan, we can associate with it some geometrical phase distribution, defined as [P1]

$$\Delta\theta_p = n_0\sigma_h 2\pi/\lambda . \quad \text{Displa}$$

If the dielectric function and the topography are considered to be statistically independent, then there two contributions to the total phase distribution can be added in quadrature $\Delta\theta = \sqrt{\Delta\theta_{dielec}^2 + \Delta\theta_p^2}$. Therefore applying this model can also aid in the decoupling between the surface and sub-surface effects.

5.2.1. Scale Dependent Response and Random Walk Model

As the optical response observed from a random medium will depend on the volume for which it is probed, it would be nice to look at how the behavior changes with the volume of interaction. The most obvious method to change this volume of interaction would be to change the physical dimensions of the probe; this however highly impractical experimentally, therefore another method should be applied. Another means available is to exploit the nonlinear thresholding that the inherent noise level in detection systems impose upon the measurement[P1]. Because of this thresholding, when the intensity coupled into the medium increases, the detection system effectively collects radiation from a larger area on the surface of the medium Figure 5-7. This allows a relatively simple means of experimentally varying the volume of interaction as measured from the far field.

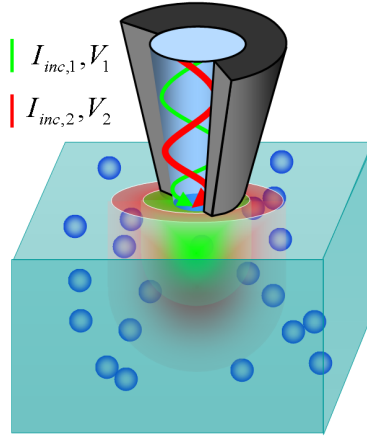


Figure 5-7 Variation of detected interaction volume as a function of incident intensity $I_2 (red) > I_1 (green)$.

In relation to the random walk model, it is considered that the area the detector sees is proportional to the incident intensity. Within this area, N independent scattering centers are being excited. Thus in this first approximation it can be considered that increasing the incident intensity and consequently the average intensity corresponds to an increase in the number of excited effective scatters. As the average intensity is increasing, the global governing phase distribution does not change; however, as was described in Section 5.1, the effective phase distribution depends on the probing size, and will be different. However, the outlined random walk model and the resulting contrast dependence described in Eq.(5-8) takes this into account.

To demonstrate the value of such a model and to experimentally probe the volume dependent response of an inhomogeneous material in the mesoscopic regime, two different materials were analyzed. For each material, multiple scans were performed over the same region as the average intensity was adjusted. The first type of samples are slabs made of calcium carbonate and kaolin micro-particles, which were compacted such that they generate pores with a size distribution centered at 20 nm as determined by the mercury porosimetry [96]. These media are optically opaque, their thickness is 1 mm, and the refractive index has small variations

centered around $n=1.5$. The r.m.s fluctuations of the surface height range between $\lambda/40$ and $\lambda/10$ while the lateral correlation length of the interface heights is comparable with the wavelength of light.

The second type of inhomogeneous media examined were optical coatings containing 100 parts latex and 25 parts TiO₂ particulates. In these samples the uniform distribution of the pigment was proven by scanning electron microscopy (SEM) and energy dispersive x-ray spectroscopy (EDS) analysis. In comparison with the first type of samples, the index of refraction now has a much broader distribution ranging between $n=1.5$ and $n=3.2$. The r.m.s fluctuations of the surface heights vary between $\lambda/10$ and $\lambda/6$. However, in this case, the lateral correlation length of surface profile is much larger than the wavelength of light Figure 5-8 shows the comparison of this model with experimental results. The points represent experimental results corresponding to multiple scans over the same area varying the intensity coupled to the tip. The continuous curves represent the results of calculations using the random walk model that describe best the experimental data. Two different locations were chosen on to investigate the effects of topography for both samples.

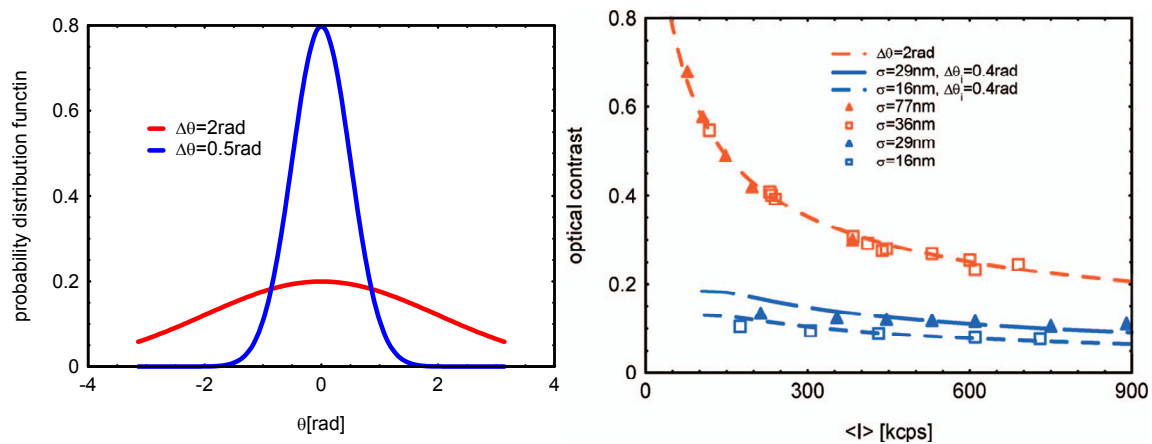


Figure 5-8 (Left) PDF of phase distribution used to fit experimental data. (Right) Plot of experimental and random walk model

As can be seen in Figure 5-8, the uniform distribution of the TiO₂ pigment in the latex matrix leads to a broad initial phase distribution of the elementary scattering centers (depicted by the red curve) and, therefore, to larger values of the optical contrast. On the other hand, due to smaller variations in the local refractive indices, the compact slabs made of calcium carbonate and kaolin micro-particles are characterized by a rather narrow phase distribution (depicted by the blue curve). Consequently, in this case the intensity fluctuations are much smaller, i.e. lower values of optical contrast as illustrated by the blue symbols. In the case of the locally inhomogeneous media, the optical contrast is a measure of the intensity fluctuations and relates to the fluctuations of the dielectric constant.

The phase from the r.m.s surface fluctuations plays a significant role when the lateral correlation length is on the order of the interaction volume. In other words, when sampling a random variable, if the duration of sampling is comparable to the order of the fluctuations, the variations will be seen; however if the duration is much longer, the fluctuations will average out.

For the first type media, the calcium carbonate and kaolin micro-particles, with a lateral correlation length approximately equal to the wavelength, the different values of the RMS roughness measured correspond to $\sigma=16\text{nm}$ and $\sigma=29\text{nm}$ as indicated in Figure 5-8. As expected, the rougher the scanned surface, the larger the values of the speckle contrast because an increase in the additional phases θ leads eventually to a broader distribution of phase and consequently to a higher contrast value

A rather different physical situation is encountered in the case of the second type of optical coatings. Here the lateral correlation length is much larger than the wavelength, and the phase distribution should be independent of the surface variations. Accordingly, the variations of the total phase θ are practically determined only by the initial phase distribution of the

exciting effective scattering centers. The red symbols in Figure 5-8 represent the dependence of the optical contrast on the average intensity for two different values of surface roughness: $\sigma=36\text{nm}$ and $\sigma=77\text{nm}$. As can be seen, the influence of the RMS roughness is negligible in this case because of the large values of the lateral correlation length.

An important consequence of the non-Gaussian nature of this scattering regime is when only a few number of events sample the global materials statistical distribution, the material may be considered vastly different. What's more is that the evolution of the observed response may be indicative of the intrinsic material structure. In this simple scalar random walk model, we considered only a simple phase fixed phase distribution as the underlying material discriminator. This treatment is very useful for decoupling the statistical influences of the mechanical and optical properties of an inhomogeneous, but lacks in provide any insight into the physical origin of the phase distribution as it relates to the materials structure properties.

5.3. Local Anisotropic Polarizability of Inhomogeneous Media

To gain more insight about the material morphology and structure, we should look into the full vectorial scattering problem as described in Section 2.1. As we saw in Eq.(2.5), the field scattered from a small object can be determined from its polarizability, which is dependent on the material properties. In general, the polarizability is anisotropic, and will exhibit a polarization signature upon scattering in addition to the intensity variations.

The interaction between constituents of composite materials can generate anisotropic responses, even in situations when both the micro- and macroscopic properties are isotropic. Such structurally induced anisotropy exists, for instance, in aggregates of metal nanoparticle [97] or in small spheres with eccentric inclusions [9899100]. As a result, unique optical signatures develop at these mesoscopic scales.

When the materials' description at mesoscopic scales involves an anisotropic response, one has to go beyond conventional effective medium approaches, which are based on assigning some effective dielectric permittivity to the local properties. In the case of an isotropic distribution of optically isotropic constituents, the effective dielectric permittivity is scalar. However, if the volume of averaging is limited, the local properties can no longer be described with a scalar permittivity. For an averaging volume much smaller than the wavelength, the polarimetric scattering properties can be described as anisotropic Rayleigh scatterers as suggested in Figure 5-9. Thus, in this case we can locally assign an effective dielectric polarizability tensor (or, equivalently, permittivity or refractive index tensors) where the magnitude of the diagonal components, degree of anisotropy, and the orientation of main axes depend on the particular location as suggested in Figure 5-9(B) or change from one mesoscopic object to another as illustrated in Figure 5-9(D).

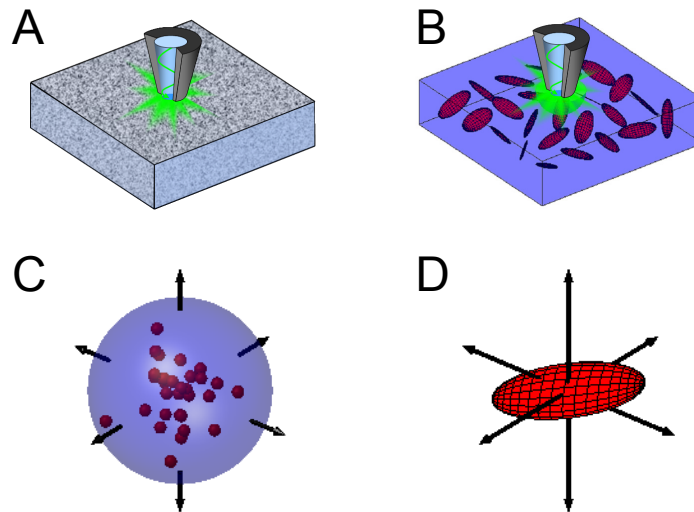


Figure 5-9. (A) An inhomogeneous material system probed at mesoscopic scales through a local excitation provided by a near-field optical probe. (B) The observed far field response of the material system may be interpreted as being determined by a discrete array of anisotropic Rayleigh scatterers with different local magnitudes and orientations. (C) An inhomogeneous material system where the physical dimensions of the object limit the extents of the field material interaction and the effective anisotropic Rayleigh scatterer (D) producing an equivalent scattered field.

In general, the characteristics of these “anisotropic scatterers” will also depend on the mesoscopic volume (level of averaging) considered. Therefore, one can define a local anisotropic polarizability (LAP) that is determined, for example, by the particles dimension if we deal with small inhomogeneous objects Figure 5-9(C,D) or by the excitation volume, as in the case of near-field optical microscopy [P1] Figure 5-9(A,B).

As an example of a mesoscopic optical response, let us consider a spherical interaction volume created either through local excitation or physical extents of the object, with dimensions smaller than the wavelength. Optical inhomogeneities within this volume effectively determine an overall anisotropic polarizability depending on the specific packing structure.

There are situations however where the degree of anisotropy may change through the measurement. One can imagine that even for isotropic hard sphere packing, situations may exist where there is some dynamic re-arrangement of inclusions resulting in changes of the effective scattering polarizability. In such conditions one can still recover information about the anisotropic polarizability but now it will be in terms of distributions of the tensor elements as we will show in the following.

In a scattering experiment, the relationship between a real polarizability $\bar{\alpha}$ and the fully polarized incident and scattered fields is commonly described in terms of the corresponding cross-spectral density matrices $W_{ij} = \langle E_i^* E_j \rangle$ as [101]:

$$\bar{\mathbf{W}}_{obs} = \bar{\mathbf{P}}^T \bar{\alpha} \bar{\mathbf{W}}_{inc} \bar{\alpha} \bar{\mathbf{P}} \quad (5.11)$$

where $\bar{\mathbf{W}}_{obs}$, $\bar{\mathbf{W}}_{inc}$ are the cross-spectral density matrices of the scattered and excitation fields, $\bar{\mathbf{P}}$ accounts for the field propagation to the detector, superscript T stands for transpose. To allow for variations in the magnitude of the polarizability not accounted for in the SSP approach, one must measure the entire polarizability tensor and determine both its magnitude and orientation.

To establish simple relationships between the polarizability tensor elements and the measured intensities, a direct procedure can be developed based on sequential excitations. For a fixed orientation of the effective polarizability $\bar{\alpha}$ there are six unknown elements in the symmetric polarizability tensor. Using Eq.(5.11), one can find a deterministic relationship for each of the polarizability elements using a scheme based on three independent excitation fields along with a polarimetric detection of scattered intensities. If the three independent excitation fields are chosen to be orthogonal, and if the scattered intensities are measured along the same direction of polarization, one can write a simple expression for the measured intensity $I_{i,j} = |\hat{\mu}_j \hat{\mu}_j^T \alpha E_i|^2$, where i and j correspond to the direction of polarization of excitation field E and the direction of polarization of detection, μ_j is the unit vector along j-direction of intensity detection. For example, when the excitation field is polarized along x and the measured intensity is co-polarized, the measurement provides directly the α_{xx} component of the polarizability tensor. Following similar steps, a system of six equations can be established and the six independent components of symmetric polarizability tensor can be retrieved. The diagonal form of the polarizability and the corresponding angles of rotation can then be found after performing eigenvalue decomposition:

$$\bar{\alpha} = \bar{\mathbf{R}}^T \bar{\alpha}_{diag} \bar{\mathbf{R}} = \bar{\mathbf{R}}^T \begin{bmatrix} \alpha_a & 0 & 0 \\ 0 & \alpha_b & 0 \\ 0 & 0 & \alpha_c \end{bmatrix} \bar{\mathbf{R}} \quad (5.12)$$

In Eq.(5.12), the matrix R is composed of the columns of the eigen-vectors and accounts for the three-dimensional rotation of the diagonalized polarizability into the detection coordinate frame. The eigenvalues are ordered such that $\alpha_a \geq \alpha_b \geq \alpha_c$.

This procedure of measuring scattered intensities and calculating the diagonal form of the polarizability will now be applied to the case of scattering from inhomogeneous spheres containing inclusions much smaller than the wavelength. We will examine the case of two different structural compositions which, at macroscopic scales, correspond to the same dielectric permittivities according to conventional effective medium theories (for instance, the Bruggeman theory) [102]. Inhomogeneous materials were modeled by randomly placing isotropic homogeneous spherical inclusions within the volume of some host characterized by a certain refractive index, and then the optical response was calculated using the coupled dipole approximation (CDA) [31]. The polarizability of these inclusions is related to their assigned refractive indices through Lorentz-Lorenz formula.

For modeling of a random distribution, a Metropolis Monte Carlo (MMC) method of packing inclusions was implemented [32]. To verify the successful packing of hard spheres, the pair correlation function was calculated and compared to the analytical 3D Percus-Yevick solution [32]. For each distribution of inclusions, the diagonal elements of the polarizability tensor ($\alpha_a, \alpha_b, \alpha_c$) and the angles specifying the orientation of its main axes were determined using the procedure based on Eq.(5.12) and Eq.(5.12) which require successive excitation with three fields in different states of polarization and the calculation of corresponding scattered intensities in two orthogonal states of polarization. In order to acquire statistically relevant information, a large number of realizations (random packing) were analyzed and the inverse problem of polarizability tensor determination was solved for each realization of the random medium. As a result, we obtain probability density functions (PDF) for the distributions of diagonal elements of the polarizability tensor. The forms of these PDF's reflect the properties of

the statistical ensemble of eigenvalues and eigenvectors that characterizes the material properties at this mesoscopic scale.

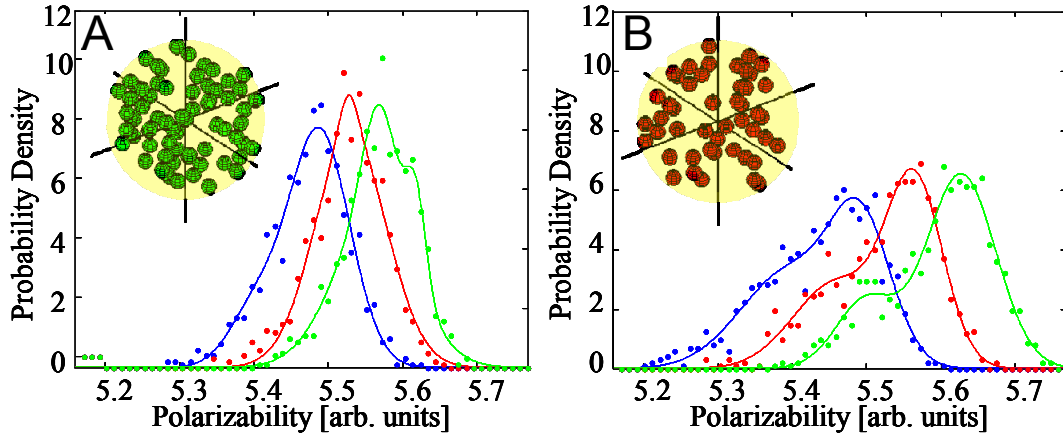


Figure 5-10. Probability density functions of ordered (see text) diagonal elements of the reconstructed polarizability tensor. The volume of interaction corresponds to a sphere of 50 nm in diameter having a host refractive index of 1.33 and a) inclusions with a refractive index of 2 and a volume fraction of 0.27 and b) inclusions with a refractive index of 2.4 and a volume fraction of 0.18. The dots are the results of the numerical simulations while the solid lines are guessed ‘best fit’ of numerical data.

In Figure 5-10 we summarize the results corresponding to the two different structural compositions examined. We note that for the uniformly random material simulated based on a hard sphere model of the inclusion packing, there is no preferential orientation of the effective polarizability. Therefore, our procedure resulted in uniform distributions of the orientations $\bar{\mathbf{R}}$ for both inhomogeneous materials. The values found for the tensor elements on the other hand indicate that, at this mesoscopic scale, the polarizabilities are not only anisotropic, they are also different for the two inhomogeneous materials as can be clearly seen in Figure 2.

For sample A, the smaller dielectric contrast between the host and the inclusions leads to a narrower distribution of the diagonal elements of the polarizability tensor and, consequently, to smaller fluctuations in the scattered fields. In the case of sample B, however, the larger

dielectric contrast results in a larger separation between α_a , α_b , α_c also contributing to larger intensity variations.

To quantitatively characterize the local anisotropic polarizability (LAP), we introduce an anisotropy factor defined as the contrast calculated for diagonal components of polarizability tensor α

$$\Delta = \frac{\sqrt{3 \text{Tr}(\bar{\alpha}_{diag}^2) - \text{Tr}(\bar{\alpha}_{diag})^2}}{\text{Tr}(\bar{\alpha}_{diag})} = \sqrt{2} \frac{\sqrt{\alpha_a(\alpha_a - \alpha_b) + \alpha_b(\alpha_b - \alpha_c) + \alpha_c(\alpha_c - \alpha_a)}}{\alpha_a + \alpha_b + \alpha_c} \quad (5.13)$$

where Tr denotes the trace of tensor α . Note that, in the past, other definitions have been used for such anisotropy factor. In Ref. [97] for instance, an anisotropy factor S was defined as the variance of depolarization factors $\bar{\mathbf{v}}(\mathbf{r}) = \frac{1}{3} \bar{\mathbf{I}} - \int_V \bar{\mathbf{G}}_0(\mathbf{r}, \mathbf{r}') d^3 r'$. Here $\bar{\mathbf{G}}_0(\mathbf{r}, \mathbf{r}')$ is the regular part of the quasistatic free-space dyadic Green's function for electric field, $\bar{\mathbf{I}}$ is the unity tensor. In this designation, the local anisotropy factor cannot depend on the excitation volume and, moreover, its locality can be violated in 3D random composites without structural self-similarity, i.e. in nonfractal composites that are of interest here. Another definition of the anisotropy factor was introduced in Ref [103]; it is similar to Eq.(5.13) except that it is based on the variance rather than the contrast of the polarizability components. The definition of Δ in Eq.(5.13) is most appropriate for our discussion, which focuses on describing the form anisotropy and not necessarily on the absolute magnitude of a specific dipole moment.

Using the definition in Eq.(5.13), the anisotropy factor Δ was calculated for every realization of the localized inhomogeneous volume. In this sense, Δ is a statistical parameter similar, for example, to the contrast measured in near-field microscopy [P1]. Of course, an averaged Δ can then be calculated from the recovered ensemble of values of this parameter. The

average anisotropy factors calculated for the two materials illustrated in Figure 5-10 are $9.2 \cdot 10^{-3}$ and $13.2 \cdot 10^{-3}$, respectively. The 30% difference clearly demonstrates that LAP is a parameter that can be used to quantify differences between macroscopically similar media.

5.3.1. Scale Dependent Local Anisotropic Polarizability

In the preceding discussion, LAP was examined over one single length scale. This situation corresponds to fixed volume of light-matter interaction imposed by the measurement procedure. In case of the two different media presented in Figure 5-10, the differences will, of course, diminish as this volume of interaction increases; the two different optical responses will converge toward the same macroscopic value corresponding to an isotropic polarizability tensor. The rate of this convergence however may be different depending on the specific structural morphology.

We will turn now our attention to LAP's dependence on the volume of interaction. We have repeated the previous analysis for spheres of different radii R and the results are presented in Figure 5-11 where we compare the anisotropy factor Δ for the case of two different sizes of spherical inclusions randomly distributed within probing volume of different sizes. The main observation is that Δ always attains a maximum that defines a new length scale characterizing the electromagnetic interaction. This maximum anisotropy length (MAL) represents the length scale over which the response of inhomogeneous medium is most sensitive to the polarization (vector) properties of the excitation field. In other words, it is at this scale that, in average, the depolarization of light during scattering occurs more effectively. Along with scattering mean free path and transport mean free path that describe the way the energy is transferred, MAL represents another interaction-specific length scale that characterizes the propagation of polarized fields through random media.

At length scales smaller than MAL, the local polarizability becomes isotropic with Δ tending to zero as the probing volume decreases. At larger scales, the macroscopic behavior is gradually approached leading again to an effectively isotropic scattering volume with $\Delta = 0$.

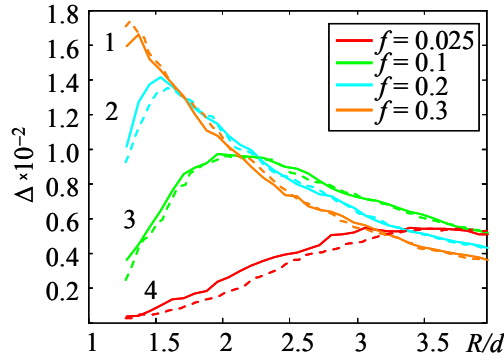


Figure 5-11. Effective anisotropy factor Δ as a function of excitation volume R normalized by inclusion diameter d for spherical inclusions with a refractive index of 1.5 randomly distributed in vacuum. The continuous lines correspond to inclusions with diameter $\lambda/32$ while the dashed lines correspond to inclusions of diameter $\lambda/64$. Curves 1 to 4 correspond to a volume fractions of inclusions of 0.3, 0.2, 0.1, and 0.025, respectively.

As can be seen in Figure 5-11, the values of the anisotropy factor appear to be independent of the size of inhomogeneities. This happens, because, in our example, the interaction inside the inhomogeneous volume considered is mostly within the electrostatic regime. Therefore, the behavior of Δ does not depend on the wavelength and is fully scalable with inclusions' dimensions. Also noticeable in Figure 5-11 is the faster decay of Δ for higher volume fractions of inclusions inside the sphere of interaction. This can also be easily explained by realizing that, for a given excitation volume, the larger number of inclusions corresponding to a higher volume fraction represents in fact a more isotropic medium.

In the particular case when the spherical inclusions can be considered as packed hard spheres, we found that MAL has a simple interpretation. As illustrated in Figure 5-12, in this case MAL defines the volume containing, in average, three inclusions. Note that three inclusions

represent the minimum number of particles necessary to form a fully anisotropic scatterer. Thus, the statistical averaging for scatterers containing more than three inclusions results in a gradual decrease of the anisotropy factor.

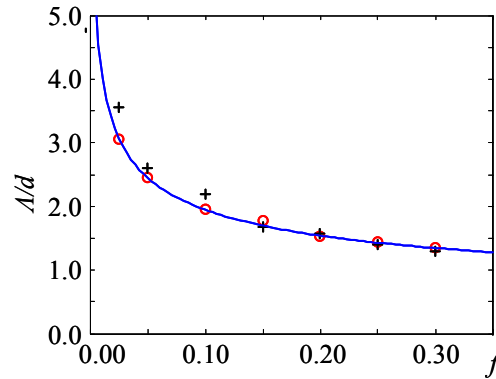


Figure 5-12. Maximum anisotropy length (Λ) normalized by the diameter of inclusions d versus the volume fraction of inclusions f . Open circles and crosses represent MAL values corresponding to inhomogeneous media with inclusions of diameters of $\lambda/64$, $\lambda/32$ respectively. The solid line corresponds to the volume containing on average 3 inclusions.

Of course, the other factors determining the optical response of a composite medium are the intrinsic properties of the components. It is expected that, in general, higher anisotropy factors will characterize materials with increasing dielectric contrasts. This is evident in Figure 5-13 where we plot the value of the maximum anisotropy Δ_{\max} as a function of dielectric contrast of inclusions

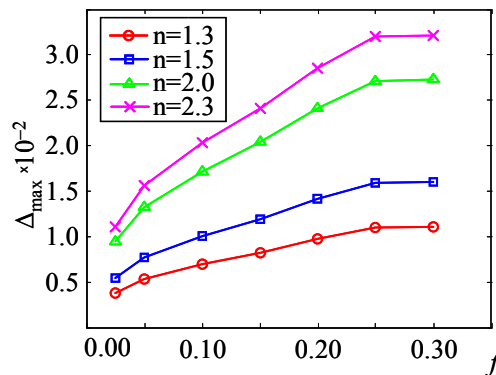


Figure 5-13. Maximum of anisotropy factor Δ_{\max} as a function of volume fraction f of inclusions with 50nm in diameter and having different refractive index contrasts.

The calculations presented Figure 5-13 demonstrate that the values of Δ_{\max} simply scale with the magnitudes of dielectric functions of components indicating that the Δ_{\max} behavior is determined only by the material's structure and not by its composition.

We have demonstrated that at mesoscopic scales, the optical response of random media consisting of optically isotropic components may be interpreted in terms of local anisotropic polarizabilities (LAP). We illustrated this concept using the example of an inhomogeneous medium containing spherical inclusions, but the model is valid for arbitrary, macroscopically isotropic inhomogeneous media. At mesoscopic scales, different materials can be characterized by their specific anisotropic polarizabilities even though they may have similar effective dielectric permittivities when described in terms of an effective medium approach.

There are, of course, different means for characterizing the local optical properties of inhomogeneous media. For instance, the scalar contrast of scattered intensities measures the relative variations of the scattering cross-section within the interaction volume discussed above in Section 5.2. When this volume increases, the scattered intensity variations decay monotonically to zero with a rate depending on the medium's properties. In this case however, only asymptotic scales can be determined which may affect the specificity. MAL on the other hand is not only derived from a tensorial feature of the material but it is also a local property. Its value is a basic characteristic of material's morphology.

5.4. Summary

As we have seen throughout this chapter, probing at varying mesoscopic scales, the optical response of random media offer means of discriminating between different materials; and if polarimetrically analyzed, demonstrate some characteristic length scale that is determined by the materials structure.

We showed how the typical information collected during a near-field optical scan allows for the surface statistics to be properly accounted for. Subsequent analysis permits differentiating between the topographical and optical contributions to the effective optical interface. This decoupling between the mechanical and the optical characteristics of the effective surface together with the stochastic properties of the scattered intensity can be used to obtain information about the local variations of the dielectric constant which, in turn, relate to the morphological properties of the inhomogeneous material.

We also demonstrate how the vectorial situation may be modeled and the existence of a characteristic length scale, maximum anisotropy length (MAL), at which the degree of local anisotropy Δ reaches its maximum. At this scale the inhomogeneous materials are most sensitive to the polarization of incident light. Thus, electromagnetic wave interaction on this scale length results in the maximal depolarization. Along with other characteristics length scales such as the scattering mean free path, the value of MAL reflects essential intrinsic properties of random media. In the case where the composite material consists of spherical inclusions in a hard sphere packing, MAL may have a purely geometrical representation, not depending on the dielectric properties of the medium's components. In the case of random packing of spheres, finding the maximum anisotropy length allows determining the size of the volume containing in average three inclusions.

These findings may also be relevant to the design of novel materials because this new electromagnetic interaction scale represents the material scale at which the polarimetric response of a medium is most sensitive to the excitation field.

CHAPTER 6: STOCHASTIC POLARIMETRY FOR NEAR-FIELD SCATTERING

In complex materials where the properties of importance are statistical quantities, the effects of secondary interaction may be neglected, so long as no additional fluctuations are introduced. Thus, statistical tools may be used to extract the material information about complex materials in a complex scattering situation such as near-field microscopy. In Section 5.2, a simple scalar model based on a random walk was used to describe the complicated scale dependent response that a near-field probe reveals when scanning inhomogeneous materials. Later, in Section 5.3, the vectorial scattering situation was studied and it was shown how an additional electromagnetic length scale related to the intrinsic structure may be revealed through analyzing the polarimetric scattering fluctuations. In this chapter, we address the topic of inverse problems for vectorial scattering problems. Specifically, we will examine how fluctuations in polarimetrically observed scattering can be related to the full vectorial properties of the scattering medium.

We can begin our polarimetric analysis by considering each individual measurement of near-field intensity to be equivalent to scattering from a material region with subwavelength size, i.e. a small scattering center. A number of different approaches have been developed to characterize the properties of small scatterers, including different microscopies, dynamic light scattering, fluorescence correlation spectroscopy, etc. [104,105]. These techniques are especially useful in providing material parameters such as diffusion coefficients, hydrodynamic radii, and average concentrations. The optical response of a single particle that is much smaller than the

wavelength is commonly described by the so-called polarizability tensor. This characteristic is of interest, for instance, for controlling the fabrication of nano-particles or for describing the conformations of polymers or biological molecules such as DNA [106].

Before getting to the details of a near-field excitation, it may be useful to quickly review some basic concepts related to polarimetric measurements. In a typical polarimetric scattering experiment, the object (polarizability) is probed with a controlled incident field for which the Stokes vector is known. From combinations of different polarizations of the incident field and polarimetric measurements, the unknown polarizability may be calculated. Equivalently, the polarizability can be found by keeping the initial polarization constant and varying the angular configuration of the source and detector. This is the only method that can provide the exact polarizability of a scattering center. However, if the material under scrutiny is some random system, and the individual member of an ensemble of an ensemble does not need to be known, statistical methods for polarimetric characterization may also be applied.

An ensemble of polarimetric data can be accumulated in a situation where measurements are taken for different orientations of the scattering polarizability while maintaining the same configuration for excitation and detection. In essence, rather than establishing the deterministic relationship between in the input and output for every member of the ensemble, one considers the statistical characteristics of distributions of measurement data and relates them to the underlying material parameters. This approach is preferable when the full experimental conditions cannot be controlled: particles suspended in solution rotate in time or, such as the case of near-field microscopy, the local polarizability acquires different orientations during the scan. The approach of relating statistical characteristics of polarimetric measurements to intrinsic material properties has come to be known as stochastic scattering polarimetry (SSP).

6.1. Stochastic Scattering Polarimetry

When measuring optical fields, one cannot measure the scattered field directly; rather one measures the intensity, or cross-spectral density. As we have described throughout this dissertation, when the scattering object is small, the scattered field distribution is related to the material properties through the objects polarizability. A generic scattering experiment, dealing with a real polarizability and a fully polarized excitation, is commonly described in terms of the cross-spectral density matrix Eq.(5.11) [101]:

$$\bar{\mathbf{W}}_{obs} = \begin{bmatrix} E_x E_x^* & E_x E_y^* \\ E_y E_x^* & E_y E_y^* \end{bmatrix} = \bar{\mathbf{P}}' \bar{\mathbf{R}}_1 \bar{\mathbf{a}}_{diag} \bar{\mathbf{R}}_1' \bar{\mathbf{R}}_2 \bar{\mathbf{W}}_{inc} \bar{\mathbf{R}}_2' \bar{\mathbf{R}}_1 \bar{\mathbf{a}}_{diag} \bar{\mathbf{R}}_1' \bar{\mathbf{P}} \quad (6.1)$$

where again $\bar{\mathbf{W}}_{obs}$, $\bar{\mathbf{W}}_{inc}$ are the cross-spectral density matrices of the scattered and excitation fields. In Eq.(6.1), the x-y plane is chosen to be perpendicular to the direction of propagation (Figure 6-1), and $\bar{\mathbf{P}}$ is a 3×2 tensor that represents the propagation to the observation point in the wave zone. In Eq.(6.1), $\bar{\mathbf{R}}_1$ and $\bar{\mathbf{R}}_2$ account for the three-dimensional rotation of the diagonalized polarizability and of the excitation polarization into the detection coordinate frame, while $\bar{\mathbf{a}}_{diag}$ denotes a diagonalized form of the polarizability Eq.(5.12):

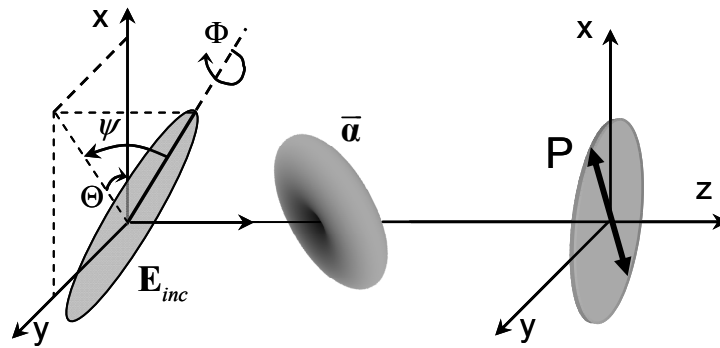


Figure 6-1. A generic scattering process where a scatterer with unknown polarizability $\bar{\mathbf{a}}$ is illuminated by a constant, arbitrarily polarized field \mathbf{E}_{inc} . An intensity measurement is performed in the far-field through a polarizer \mathbf{P} oriented in the plane xy .

The expression of the cross spectral density in Eq.(6.1) contains both the correlation between orthogonal field components and the intensities along two orthogonal directions x and y . In a polarimetric scattering experiment, one measures only intensities $I_i = W_{ii}^{obs}$ ($i = x, y$); for example, by the use of two polarizers, the diagonal elements of cross-spectral density.

For a given incident field described by \bar{W}_{inc} , scattered intensities are obtained for different orientations of the scatterer. Therefore, an ensemble of such scattered intensities can be built and further analyzed statistically to infer the morphological information included in the polarizability α . As described in Section 2.5, one useful tool for characterizing distributions is statistical moments, in general having the form:

$$M_{i_1 i_2 \dots i_n}^{(n)} = \int_{\Omega} I_{i_1}(\Omega) I_{i_2}(\Omega) \dots I_{i_n}(\Omega) p(\Omega) d\Omega \quad (6.2)$$

where $i_1, i_2 \dots i_n = x, y$ and $p(\Omega)$ represents the probability function associated with the orientation of the diagonalized polarizability. Integration in Eq.(6.2) is performed over all orientations determined by solid angle Ω .

A plethora of applications may be described from this general concept of using moments (Eq.(6.2)) of scattered distributions to solve this inverse scattering problem described by Eq.(6.1). It will depend on the specific experimental situation and the knowledge of the physical system as to which direction to apply this concept. In general, the inverse problem may be solved for the magnitudes of the eigen values of the tensorial polarizability, its orientation, or the exciting fields' polarization with respect to some detection frame, or any combination of these unknowns.

In one simple application, where the orientation, the magnitude and the field are all delta distributed (the so called direct problem, with no stochastic element), knowing or structuring the field can be used to reveal the full tensorial polarizability [107]. Similarly, if one knows the

elements of the polarizability, the inverse scattering problem may be applied to characterize the unknown exciting field [80].

When relating SSP to the experiment, knowledge of the scattering system (distributions of excitation, orientation, magnitudes, etc.) determines the number of measurements needed and how the relationships are derived. Through out the rest of this chapter we will discuss some applications of SSP to different physical geometries and show how polarimetric moments may be related to the intrinsic material or field structure.

6.1.1. Recovering the Anisotropic Polarizability of a Scatterer

One situation of interest here is when, during the experiment, the scatterer rotates randomly in space with probability described by $p(\Omega)$. The fixed material properties defined by the unknown polarizability $\bar{\alpha}$ probed by some constant, but arbitrarily polarized incident field as depicted in Figure 6-1. In general, a fully polarized excitation field can be described in terms of three orientation angles and an ellipticity parameter; in other words, there are four independent parameters that determine the structure of the excitation field.

For a given probability function describing the orientation confinement of the polarizability ($p(\Omega)$), expressions for the scattered intensity can be derived starting from Eq. (6.1). Furthermore, the moments of the intensity distributions can be related to the material properties and the parameters of the excitation field. All in all, the scattering situation is fully described by the three elements of the diagonalized polarizability tensor $\bar{\alpha}$ in addition to the four independent incident field parameters.

In performing polarimetric intensity measurements along two orthogonal directions x and y , a situation arises when the incident field is polarized with the major axis oriented at the

bisection of the two directions of measurement. In this situation, all the moments of the two orthogonal intensity distributions are equal, and, consequently, the number of independent equations which can be used for reconstruction is reduced. Unique recovering of $\bar{\mathbf{a}}$ may still be possible by considering higher-order moments of the intensity distributions to obtain additional independent relationships. However, in this case one has to recognize that higher-order moments of the intensity distributions are more susceptible to noise [108]. Alternatively, one can choose to consider only up to the second-order moments of intensity distributions, but introduce an additional intensity measurement. For example, by performing a third measurement along the bisection of the first two orthogonal measurements, a rotation of the detection coordinate system can be applied which decreases the cross correlation of orthogonal intensity distributions. The parameters characterizing the incident field and the material properties are uncorrelated; as such, decreasing the cross-correlation of intensity ensembles allows for more independent probability distribution functions. Note that the rotation of the detection coordinate system is a linear transformation performed over all the elements of the intensity distributions, therefore, no statistical information is lost. This rotation angle θ of the coordinate system, $\tilde{\mathbf{W}}_{obs} = \bar{\mathbf{R}}(\theta) \bar{\mathbf{W}}_{obs} \bar{\mathbf{R}}(\theta)^{-1}$, can be found by minimizing the real part of the cross-correlation between the two orthogonal measurements, which is related to the intensity polarized at their bisection angle.

Let us consider the effect of the rotation

$$\bar{\mathbf{R}}(\theta) = \begin{pmatrix} \cos \theta & -\sin \theta \\ \sin \theta & \cos \theta \end{pmatrix} \quad (6.3)$$

on the first moment of cross-spectral density matrix:

$$\bar{\mathbf{M}}^{(1)} = \begin{bmatrix} \langle I_x \rangle & \langle E_x^* E_y \rangle \\ \langle E_y^* E_x \rangle & \langle I_y \rangle \end{bmatrix}. \quad (6.4)$$

Minimizing the real part of off-diagonal element the first order moment $\tilde{\mathbf{M}}^{(1)} = \bar{\mathbf{R}}(\theta)\bar{\mathbf{M}}^{(1)}\bar{\mathbf{R}}(\theta)^{-1}$ leads to the following equation (further details outlined in Appendix 0)

$$\Re\langle E_x^* E_y \rangle (\cos^2 \theta - \sin^2 \theta) + (\langle I_x \rangle - \langle I_y \rangle) \cos \theta \sin \theta = 0. \quad (6.5)$$

which can be solved to find the final expression for rotation angle θ as

$$\theta = \tan^{-1} \left(\frac{M_x^{(1)} - M_y^{(1)} \pm \sqrt{(M_x^{(1)})^2 + (M_y^{(1)})^2 - 2M_x^{(1)}M_y^{(1)} + 4\Re\langle E_x^* E_y \rangle^2}}{2\Re\langle E_x^* E_y \rangle} \right). \quad (6.6)$$

In Eq.(6.6), the sign is chosen such that in new coordinate system the condition $M_{xx}^{(1)} > M_{yy}^{(1)}$ is fulfilled. It must be clear that, in fact, θ defines the angle between the major axis of the polarization ellipse of the incident field and the x axis of the coordinate system in Figure 6-1.. The rotation we have identified eliminates the dependence on this angle and, therefore, in the new system of coordinates, the incident field is now described by only three independent parameters.

The 3rd additional measurement at 45° with respect to the first two orthogonal directions can be expressed in terms of the non-diagonal elements of the cross-correlation matrix:

$$M_{45}^{(1)} = \frac{1}{2}M_x^{(1)} + \frac{1}{2}M_y^{(1)} + \frac{1}{2}E_x^*E_y + \frac{1}{2}E_xE_y^*, \quad (6.7)$$

where $M_{45}^{(1)}$ is the first moment of the intensity distribution measured at 45° . Using Eq. (6.6), and (6.7), the angle θ is finally evaluated to be

$$\theta = \tan^{-1} \left(\frac{M_x^{(1)} - M_y^{(1)} \pm \sqrt{2(M_x^{(1)})^2 + 2(M_y^{(1)})^2 + 4M_{45}^{(1)}(M_x^{(1)} - M_y^{(1)})}}{2M_{45}^{(1)} - M_x^{(1)} - M_y^{(1)}} \right). \quad (6.8)$$

In the rotated system of coordinates, two new intensity distributions $\tilde{I}_x = \tilde{W}_{xx}^{obs}$ and $\tilde{I}_y = \tilde{W}_{yy}^{obs}$ can be defined as

$$\begin{aligned} \tilde{I}_x &= I_x \cos^2 \theta + I_y \sin^2 \theta - 2 \left(I_{45} - \frac{1}{2} I_x - \frac{1}{2} I_y \right) \cos \theta \sin \theta, \\ \tilde{I}_y &= I_x \sin^2 \theta + I_y \cos^2 \theta + 2 \left(I_{45} - \frac{1}{2} I_x - \frac{1}{2} I_y \right) \cos \theta \sin \theta. \end{aligned} \quad (6.9)$$

where I_{45} is the intensity measured along the 45° direction.

The first and second moments of distributions \tilde{W}_{xx}^{obs} and \tilde{W}_{yy}^{obs} can now be evaluated together with the corresponding cross-correlation term $M_{xy}^{(2)}$. Using Eq.(1-3) and assuming that $p(\Omega)$ corresponds to a uniform random distribution of the orientation of the diagonalized polarizability, one finds the first moments of the two rotated ensembles to be

$$\begin{aligned} M_x^{(1)} &= \frac{1}{5} ((Q_1 + 3)\varepsilon + 3 + K) \delta_1 + Q_1 \varepsilon \bar{\alpha}^2 + \bar{\alpha}^2 K, \\ M_y^{(1)} &= \frac{1}{5} ((L + 3)\varepsilon + 3) \delta_1 + \bar{\alpha}^2 \varepsilon L, \\ M_{ij}^{(2)} &= P_{ij}^{(1)}(\varepsilon) \delta_1^2 + P_{ij}^{(2)}(\varepsilon) \delta_1 \bar{\alpha}^2 + P_{ij}^{(3)}(\varepsilon) \delta_2 \bar{\alpha} + P_{ij}^{(4)}(\varepsilon) \bar{\alpha}^4. \end{aligned} \quad (6.10)$$

In the general expressions for the 2nd - order moments in Eq.(6.10), $P_{ij}^{(n)}(\varepsilon)$ are second-order polynomials with respect to the ellipticity parameter ε . The exact expressions for these polynomials are given in the Appendix 0. In addition, the following short-hand notations were used

$$\begin{aligned} \delta_1 &= (db^2 + dbdc + dc^2)/3, \quad \delta_2 = dbdc(db + dc)/2, \\ db &= \alpha_b - \bar{\alpha}, \quad dc = \alpha_c - \bar{\alpha}, \quad \bar{\alpha} = (\alpha_a + \alpha_b + \alpha_c)/3, \end{aligned} \quad (6.11)$$

$$L = \cos^2 \Phi, \quad K = \cos^2 \psi, \quad Q_1 = \sin^2 \Phi \sin^2 \psi, \quad \varepsilon = (w/\ell)^2,$$

where ℓ and w are the main axes of excitation polarization ellipse ($\ell > w$).

The expressions in Eq.(6.10) constitute the main result of SSP for a uniform distribution of polarizability orientation, as they establish the relationship between the statistical moments (up to the 2nd order) of the measured intensities and the parameters defining the anisotropic polarizability to be determined. It is worth mentioning that the α_a, α_b , and α_c values used in Eq.(6.11) refer to relative values of the polarizability tensor, rather than the actual values of the diagonalized tensor elements; a constant has been factored out and included in the propagation operator P. These relative values of the diagonal elements can be normalized with respect to the largest element (we choose α_a as a largest element of diagonalized polarizability tensor Eq.) and this allows generating a number of validity criteria for our reconstruction procedure. Using the dimensionless variables $\delta_1/\bar{\alpha}^2, \delta_2/\bar{\alpha}^3, K, L, \varepsilon$ in Eq.(6.10), one finds that they are subject to the following physical restrictions:

$$\delta_1/\bar{\alpha}^2 \in [0,1], \quad \delta_2/\bar{\alpha}^3 \in [-1,1/8], \quad \varepsilon(1-K+KL) \leq K \leq 1, \quad L \in [0,1], \quad \varepsilon \in [0,1] \quad (6.12)$$

The restrictions on K imply that the projection of the major axis of excitation polarization ellipse onto the xy plane should be greater than the projection of its minor axis. Starting from conditions expressed in Eq.(6.12) one can establish the following limiting values for the ratios between statistical moments:

$$\begin{aligned} M_y^{(1)}/M_x^{(1)} &\in [0,1], \quad M_{xx}^{(2)}/(M_x^{(1)})^2 \in [1,3.1], \\ M_{yy}^{(2)}/(M_x^{(1)})^2 &\in [0,2.1], \quad M_{xy}^{(2)}/(M_x^{(1)})^2 \in [0,1] \end{aligned} \quad (6.13)$$

These relations may be useful in practice when, in the presence of experimental errors, the measured statistical moments may shift outside the validity region.

We have now established a direct relationship between five statistical moments of the polarimetric intensity measurements ($M_x^{(1)}$, $M_y^{(1)}$, $M_{xx}^{(2)}$, $M_{yy}^{(2)}$, and $M_{xy}^{(2)}$) and the six unknown variables that determine the outcome of the random scattering process; three material parameters defining α and three parameters describing the incident field in the rotated system of coordinates. This situation represents still an underdetermined system of equations. However, any additional knowledge about the material properties or about the excitation field will allow a full description of the scattering situation, even if only the 1st and 2nd order moments are being used.

Before illustrating several examples, it is worth mentioning, that one can follow the procedure outlined above to obtain similar relations between the statistical moments of the measured intensities and material parameters for situations where the random orientation of the polarizability is described by other distribution functions. Also, the same treatment can be considered in circumstances where the experiment is performed using a polarimetric detection system based on two circular polarizations and some elliptical state measurement.

To test the theory outlined above, a series of numerical experiments were performed to model the interaction with a scatterer described by an anisotropic polarizability. The experiment was numerically simulated for random orientations of the scattering particle with respect to a fixed detection frame. For each orientation, the intensity was recorded in the three directions of polarizations as described above.

6.1.2. Far-Field Stochastic Scattering Polarimetry

One common assumption that can be made about excitation field properties is that the plane of the polarization ellipse of the excitation field is parallel to the detection plane (forward

scattering). In this case, when $\psi = 0$ and $\Phi = 0$ the expressions for the statistical moments in Eq.(6.10) becomes:

$$\begin{aligned}
M_x^{(1)} &= \frac{1}{5}(3\varepsilon + 4)\delta_1 + \bar{\alpha}^2, \\
M_y^{(1)} &= \frac{1}{5}(4\varepsilon + 3)\delta_1 + \bar{\alpha}^2\varepsilon, \\
M_{xx}^{(2)} &= \frac{3}{35}(9\varepsilon^2 + 8\varepsilon + 16)\delta_1^2 + \frac{6}{5}(4 + \varepsilon)\bar{\alpha}^2\delta_1 - \frac{8}{35}(8 + 3\varepsilon)\delta_2\bar{\alpha} + \bar{\alpha}^4, \\
M_{yy}^{(2)} &= \frac{3}{35}(16\varepsilon^2 + 8\varepsilon + 9)\delta_1^2 + \frac{6}{5}(4\varepsilon + 1)\varepsilon\bar{\alpha}^2\delta_1 - \frac{8}{35}(8\varepsilon + 3)\varepsilon\delta_2\bar{\alpha} + \varepsilon^2\bar{\alpha}^4, \\
M_{xy}^{(2)} &= \frac{3}{35}(4\varepsilon^2 + 17\varepsilon + 4)\delta_1^2 + \frac{3}{5}(\varepsilon^2 + 1)\bar{\alpha}^2\delta_1 - \frac{4}{35}(3\varepsilon^2 - 8\varepsilon + 3)\delta_2\bar{\alpha} + \varepsilon\bar{\alpha}^4.
\end{aligned} \tag{6.14}$$

In practice, in order to determine the four unknowns $\bar{\alpha}, \delta_1, \delta_2, \varepsilon$ one needs only four of the equations in Eq.(6.14). Because in an experiment the evaluation of the intensity moments is always subject to a certain procedural accuracy, we will choose a combination of the four equations that provides the minimal error in solving for the unknowns. Our estimations show that the evaluation of $M_x^{(1)}, M_y^{(1)}, M_{xx}^{(2)}$, and $M_{xy}^{(2)}$ is more stable with respect to possible experimental errors.

A series of simulations was performed for different elliptical excitation states. Table 6-1 summarizes the percent error of reconstruction for different shape parameters, different parameters of ellipticity, and different numbers of polarimetric measurements. The percent error in Table 6-1 refers to an average of the deviation in the calculation of the α_b and α_c values from the exact values of the polarizability. The polarizability of the particle is related to the shape parameters η, β , and γ through the Clausius-Mossotti expression for isotropic ellipsoids [28]:

$$\alpha_j = 4\pi\eta\beta\gamma \frac{n^2 - 1}{3 + 3L_j(n^2 - 1)} \tag{6.15}$$

where $\alpha_j = \alpha_a, \alpha_b, \alpha_c$ from Eq. , factors L_j are determined by ellipsoid shape [28], n is the refractive index of particle that was chosen to be equal 1.5 for numerical computations.

Table 6-1 Percentage error of reconstructed polarizability for different shapes of particles, different field orientations, and different number of realizations for the case of an elliptically polarized excitation field, $\psi = 0, \Phi = 0$.

		Realizations			
		η, β, γ	500	1000	2500
$\varepsilon = 0$	3,3,1	2.0	2.0	1.8	1.1
	3,2,1	1.0	0.7	0.5	0.3
	3,1,1	2.3	1.3	1.7	0.8
$\varepsilon = .15$	3,3,1	2.0	1.4	1.4	2.0
	3,2,1	1.0	0.7	0.6	0.3
	3,1,1	1.4	1.9	1.0	0.6
$\varepsilon = .3$	3,3,1	3.5	2.3	2.4	2.4
	3,2,1	2.5	1.5	1.0	1.0
	3,1,1	3.2	2.7	2.4	1.7
$\varepsilon = .65$	3,3,1	5.6	5.4	3.3	2.4
	3,2,1	4.3	3.7	2.3	1.3
	3,1,1	5.5	4.5	2.8	3.2

Obviously, the reconstruction error decreases with increasing the number of realizations of particle orientation. Also, one can notice that the error increases for larger values of ellipticity parameter ε , and this can be understood by considering the limiting case of circularly polarized excitation. In this situation, all the moments for the linear polarization measurements in the x and y directions become equal, and the system of equations becomes undetermined. In the case of circularly polarized excitation, the morphological properties of the material may be found based on circular polarization measurements, however, this situation will not be discussed here.

Another detail to which we would like to point out is that according to our numerical results the reconstruction error seems to be smaller for purely anisotropic polarizabilities when $\alpha_a \neq \alpha_b \neq \alpha_c$.

Another practical situation that is often of interest is when the incident field is in some arbitrary linear state of polarization. In this case, the general expression in Eq.(6.10) reduces to the following system of equations:

$$\begin{aligned}
M_x^{(1)} &= \bar{\alpha}^2 K + \frac{3+K}{5} \delta_1 \\
M_y^{(1)} &= \frac{3}{5} \delta_1 \\
M_{xx}^{(2)} &= \bar{\alpha}^4 K^2 + \frac{8\bar{\alpha}(K-9)K}{35} \delta_2 + \frac{42\bar{\alpha}^2 K(K+3)}{35} \delta_1 + \frac{3(3+K)^2}{35} \delta_1^2 \\
M_{xy}^{(2)} &= -\frac{12K\bar{\alpha}}{35} \delta_2 + \frac{3\bar{\alpha}^2 K}{5} \delta_1 + \frac{3(3+K)}{35} \delta_1^2
\end{aligned} \tag{6.16}$$

which may be solved for the magnitudes of the diagonal elements α_a , α_b , and α_c of the polarizability tensor from Eq.(5.12) and the polar angle ψ . In this case, the choice of the optimal four equations is unequivocal because the linearly polarized incident field moments $M_y^{(1)}$ and $M_{yy}^{(2)}$ are no longer independent: $M_{yy}^{(2)} = (15/7)(M_y^{(1)})^2$.

To test the stochastic scattering polarimetry in this situation, a series of numerical experiments were performed for various angles of the incident excitation, different anisotropies, and the different number of realizations of particle orientation. The results are displayed in Table 6-2.

Table 6-2 Percentage error of reconstructed polarizability for different shapes of particles, different field orientations, and different number of realizations for the case of a linearly polarized excitation field ($\varepsilon = 0, \Phi = 0$).

		Realizations			
		η, β, γ	500	1000	2500
$\psi = 0$	3,3,1	3.6	2.9	2.3	1.0
	3,2,1	3.1	2.0	1.7	0.8
	3,1,1	4.0	2.9	2.0	1.2
$\psi = \pi/6$	3,3,1	4.6	3.4	2.1	1.1
	3,2,1	4.2	2.4	1.5	1.1
	3,1,1	4.9	3.7	2.3	1.7
$\psi = \pi/4$	3,3,1	5.9	4.1	3.9	1.8
	3,2,1	5.6	3.8	3.0	1.4
	3,1,1	9.2	5.2	3.1	2.3
$\psi = \pi/3$	3,3,1	11.0	7.8	7.4	4.2
	3,2,1	10.3	6.5	4.3	3.4
	3,1,1	14.6	10.8	9.4	7.7

Examining the results in Table 6-2, one can easily see that there is a strong dependence of the reconstruction error on the polar angle ψ . In the case when ψ equals $\pm\pi/2$, the electric field vector is co-directed with respect to the path to observation point, and the measured intensities no longer depend on orientation of the polarizer. In this situation, the equations for the x and y -components of cross-spectral density matrix are not independent anymore. However, it is remarkable that in the case when the polar angle ψ is less than $\pi/3$, the original values of anisotropic polarizability can be recovered within about 2 percent.

In order to illustrate the accuracy of the proposed method for reconstructing unknown polarizabilities, let us consider the simple example of scattering from a GaP nano-rod (refractive index of 3.37), which is 100nm long and has an aspect ratio of 1/10. In this case, after 5000

intensity measurements for different orientations of nano-rod, we are able to retrieve the ratio of polarizability tensor components $\alpha_b / \alpha_a = 0.20 \pm 0.05$, which is in very good agreement with the exact value $\alpha_b / \alpha_a = 0.199$. The two examples discussed here exemplify experimental situations where the incident field is unknown. Of course, the general expressions in Eq.(6.10) can be simplified and may also be used in situations where the experimental geometry allows for an alignment of the incident field to some known incident polarization.

$$\begin{aligned}
 M_x^{(1)} &= \frac{4}{5} \delta_1 + \bar{\alpha}^2, \\
 M_y^{(1)} &= \frac{3}{5} \delta_1, \\
 M_{xx}^{(2)} &= \frac{6}{35} \left(8\delta_1^2 + \frac{3}{7} \bar{\alpha}^2 \delta_1 - 8\bar{\alpha} \delta_2 \right) + \bar{\alpha}^4.
 \end{aligned} \tag{6.17}$$

In this case, an ideal experimental geometry would consist of a linear excitation and a measurement performed along a co- and a crossed direction of polarization. Notably, in this particular situation, it is possible to retrieve the morphological information about the scatterer without the need for correlated intensity distributions. Practically, this means that two independent intensity distributions can be recorded at different times or locations for a randomly oriented scatterer. This approach may be of interest in situations where the scattered intensity is very small, and the requirement to measure correlated polarimetric intensity distributions can be a daunting task.

The above situation can be simplified even further when it is known a priori that the scatterer is rotationally symmetric. In this case, it is possible to obtain the shape aspect ratio by performing only a single measurement that is co-polarized to the linear excitation in a manner similar to an earlier suggestion [109]. In this situation, the first and second moments of the

detected distribution allow for such a quantification and the obtained expressions reduced from Eq.(6.10).

6.1.3. Near-Field Stochastic Scattering Polarimetry

Another application of particular interest to this dissertation is for the practice of near-field optical microscopy (NSOM). In this case, a sample is locally excited by either the field emitted through a tapered optical fiber with an aperture much smaller than the wavelength or by the field created around a sharp metallic tip placed in the close proximity the sample. The polarization state of the excitation field is usually unknown but the procedure of analyzing fluctuations of the scattered intensity can still be used even in this situation.

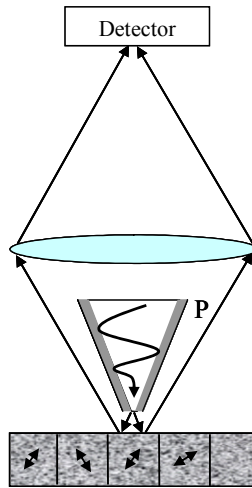


Figure 6-2 The geometry of near-field scattering polarimetry. The probe of near-field microscope P scans the heterogeneous sample having regions V_d with uniformly oriented polarizability.

When a material system is optically inhomogeneous, its properties are described by the local polarizability. For a large class of materials where the inhomogeneities are on a scale much smaller than the radiation's wavelength, one can consider that this polarizability is constant in magnitude and orientation within some volume of interaction V_d determined by the

characteristics of the near-field probe (i.e. aperture size, tip sample separation, etc). One can further assume that this effective polarizability only changes its orientation from point to point and, during a scan, all possible orientations of the effective polarizability are realized (Figure 6-2).

As opposed to the previous examples discussed, the field emerging from or surrounding the tip of a near-field microscope (NSOM) is highly non-uniform. For a transmission aperture NSOM, for instance, a common approach is to approximate this with the field produced by diffraction from a small aperture in a perfectly conducting screen [110,111]. The details of calculating the field diffracted through such an aperture are provided in Appendix 0. The interaction between this inhomogeneous electromagnetic field and a specific material system is complex and, in most cases, cannot be described analytically. The alternative is to use numerical techniques, such as the coupled dipole approximation (CDA), to calculate the scattering resulting from this interaction.

To illustrate the procedure of stochastic polarimetry outlined before, we have used CDA to simulate the near-field scanning of a material consisting of an array of tightly packed anisotropic dipoles which are locally oriented in the same direction. The far-field scattered intensities were recorded in the backward direction, as in the conventional NSOM reflection mode shown in Figure 6-3. The recorded far-field intensity ensembles were polarimetrically analyzed and the components of the polarizability tensor of the individual particles were calculated according to the method of stochastic polarimetry.

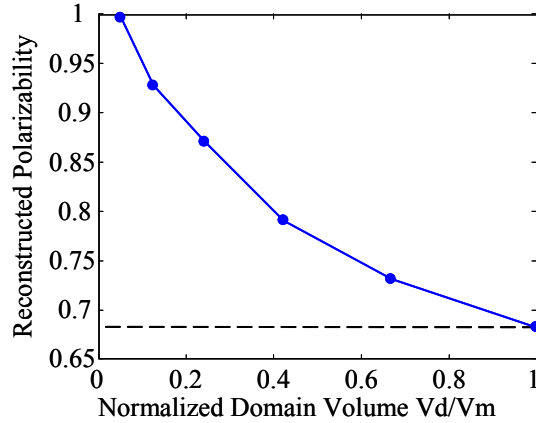


Figure 6-3 Reconstructed polarizability (the c-component of diagonalized polarizability tensor) as a function of normalized domain volume V_d/V_m where V_d is the volume of uniform orientation of anisotropic polarizability and V_m is the volume of interaction (solid line). Dashed line shows the exact value of polarizability. The parameters of CDA simulations are: tip-sample separation 10nm, modeling cube of 0.8 wavelength in size with $4 \cdot 10^3$ dipoles.

The results of anisotropic polarizability reconstruction in near-field geometry are shown in Figure 6-3. Every data point represents the result of averaging over 3000 realizations. As can be seen, the value of the calculated polarizability depends on the dimensions of the domain of uniform polarizability. Of course, the intrinsic values of the polarizability ($c/a = 0.695$) are recovered only when this domain volume is equal or larger than the volume of interaction. In practice, this volume of interaction depends on a number of factors including sample properties, tip characteristics, detection system and the average intensity of excitation [P1]. In the present simulation, the volume of interaction occupies almost the entire modeling volume of approximately $(0.8\lambda)^3$, where λ is the wavelength of incident field. Interestingly, our simulations indicate that this volume of interaction does not depend on the size of the tip's aperture. This may happen because the volume of interaction has dimensions such that the field emerging from the tip appears to originate from a point dipole. Accordingly, the size of the tip's aperture effectively influences only the amplitude of this dipole field and does not change the

overall field distribution. In the opposite situation, when there is a significant averaging over the material structure within the volume of interaction, the resulting polarizability will correspond to some effective value depending on both the intrinsic material properties and structural morphology.

As a final observation we should note that the CDA simulations show that it is possible to reconstruct the intrinsic polarizability of an anisotropic material, modeled as a collection of individual dipoles, even when accounting for the coupling between material's constituents. Moreover, a successful reconstruction can be achieved even when the excitation field is non-uniformly distributed over the region of interaction.

Before exploring further developments, one should emphasize the main characteristics of this general concept of stochastic scattering polarimetry. Essentially, we have demonstrated that the diagonal elements of the anisotropic polarizability tensor can be obtained by analyzing the statistical moments of polarimetrically measured intensity distributions. Most importantly, this information about the polarizability tensor can be recovered even in situations when the state of polarization of the incident field is unknown. In addition, the method of stochastic scattering polarimetry can be used to reconstruct the values of anisotropic polarizability both in the case of interacting nano-particles excited by uniform fields as well as in the case of non-uniform excitations that may occur, for instance, in near-field measurements.

6.2. Task Optimized Stochastic Scattering Polarimetry

In some situations, the polarizability tensor is constant, and can be directly related to the shape of a scattering particle [112,113]. However, there are circumstances when the polarizability tensor varies during the measurement; its change may be either in time, modifications of shape for instance, or from object to object when an entire ensemble is

examined. Typical examples include systems such as structurally dynamic macromolecules like DNA, nanoparticles formation in microfluidic environment [106], liquid drops containing scattering particles [100,113], or effective inhomogeneous scatterers observed in near-field microscopy [P1]. In all these cases, it is not the exact shape of one specific realization that determines the meaningful optical properties, but rather some effective polarizability that statistically represents the internal structure [P1].

As mentioned before, in general, for nonabsorbing particles, the polarizability tensor is symmetric and contains six independent components; these 6 components define the magnitude and the orientation of a scatterer. Experimentally, the 6 elements can be determined based on six independent measurements of scattered intensities, using different excitation fields. For example, as discussed in Section 5.3, a straightforward method is to use sequential excitation fields polarized along three orthogonal directions while measuring scattered intensities in two orthogonal states of polarization. Once the entire symmetric tensor is retrieved, its diagonal form and the corresponding angles of rotation can be found using the eigenvalue/eigenvector decomposition $\alpha = V \alpha_{diag} V^{-1}$ where V (the columns of eigenvectors) represents some rotation matrix operating on the diagonalized polarizability tensor (eigenvalues) Eq.(5.12)

.Usually, it is these three numbers, the eigenvalues, that one is interested in when trying to characterize a scattering object. Of course, alternative implementations can be pursued involving different geometrical orientations of sources and detectors, but all procedures will require six independent measurements to be recorded simultaneously, i.e. for the same orientation of the scattering particle. This constitutes a fully deterministic and complete approach to the polarimetric problem. In practice however, its complexity may preclude any direct application.

The expressions developed in the above Section 6.1 for SSP are specific to the situation where the anisotropic polarizability of the scattering object is fixed throughout the measurement process. Another application for this inversion procedure applied to stochastic measurements is for reconstructing a varying anisotropic polarizability. In this case, the result of a measurement will be expressed in terms of the probability distributions of the diagonal elements of the polarizability tensor.

Let us consider the situation of an optically inhomogeneous material system, where it may be considered that the dielectric properties vary randomly. From symmetry considerations, it follows directly that there is no preferential structuring of the anisotropic polarizability tensor; i.e. the main axis of the polarizability tensor is uniformly oriented in space. This implies that the three diagonal elements describing the anisotropic polarizability are random variables having the same governing probability density functions (PDF): $f_a(\alpha_a) = f_b(\alpha_b) = f_c(\alpha_c)$. In solving the stochastic problem, such symmetries can be exploited to reduce the number of necessary polarimetric measurements as we will show in the following.

Let us consider now the case of a small, optically inhomogeneous scatterer that is excited by a linearly polarized plane wave. Changes in internal structure of scatterer determine fluctuations of scattered field [114]. The magnitude of the scattered field polarized along the same direction as the incident field is

$$\begin{aligned} E_s &= v_1(\theta, \varphi, \psi)\alpha_a + v_2(\theta, \varphi, \psi)\alpha_b + v_3(\theta, \varphi, \psi)\alpha_c, \\ v_1(\theta, \varphi, \psi) + v_2(\theta, \varphi, \psi) + v_3(\theta, \varphi, \psi) &= 1, \end{aligned} \tag{6.18}$$

where $v_{1,2,3}(\theta, \varphi, \psi)$ describe the orientation of the anisotropic polarizability and are functions of the random rotations along the Euler angles θ , φ , and ψ :

$$\begin{aligned}
v_1(\theta, \varphi, \psi) &= (\cos(\psi)\cos(\theta)\cos(\varphi) - \sin(\psi)\sin(\varphi))^2, \\
v_2(\theta, \varphi, \psi) &= (\cos(\psi)\cos(\theta)\sin(\varphi) + \sin(\psi)\cos(\varphi))^2, \\
v_3(\theta, \varphi, \psi) &= \cos^2(\psi)\sin^2(\theta).
\end{aligned} \tag{6.19}$$

If we treat $v_{1,2,3}(\theta, \varphi, \psi)$ and the diagonal elements $\alpha_{a,b,c}$ of the polarizability tensor as random variables, then the stochastic equation Eq.(6.18) represents a relation between the PDF of the measured field $f_E(E_s)$ and the PDF's characterizing the random variables $\alpha_{a,b,c}$. Our problem has now been reduced to solving Eq. (6.18) for the unknown PDF's $f_a(x)$, $f_b(x)$, $f_c(x)$ using the PDF $f_E(E_s)$ of the measured co-polarized component of the scattered field.

To solve Eq.(6.18), it is necessary to know the joint probability distribution for the random variables α_a , α_b , α_c . In the simplest case, one can assume that α_a , α_b , α_c are independent and proceed as follows. First, the solution of Eq.(6.18) should be found that relates the moments of known probability functions of the random variables E_s , θ , ψ , φ to the moments of the unknown probabilities of α_a , α_b , α_c . Using Eq.(6.18) and Eq.(6.19) one can derive expressions relating the moments of the measured intensity distribution $f_E(E_s)$ to the moments of the unknown governing the polarizability distribution $f_a(x)$. The n-th order statistical moment is found from $\langle E_s^n \rangle = \int_{\Omega} (v_1\alpha_a + v_2\alpha_b + (1 - v_1 - v_2)\alpha_c)^n d\Omega$, where Ω is the solid angle. Taking into account that α_a , α_b , α_c are chosen independently from the same distribution, we finally obtain the following relationships between the moments (or equivalently, the cumulants) of the measured distribution and those of the governing distribution of the unknown probabilities

$$\langle E_s \rangle = \langle \alpha \rangle, \quad \kappa_{2E} = \frac{3}{5} \kappa_{2a} = \frac{3}{5} \sigma_a^2, \quad \kappa_{3E} = \frac{3}{7} \kappa_{3a}, \quad (6.20)$$

where $\langle \alpha \rangle = \langle \alpha_a \rangle = \langle \alpha_b \rangle = \langle \alpha_c \rangle$ is the mean, σ_a is the variance of the distribution $\{\alpha\}$, and κ_{nE} , κ_{na} are n -th order cumulants for distributions the $\{E_s\}$, and $\{\alpha\}$, respectively. Thus, we have established relationships between the moments or the cumulants of some governing distribution of polarizability elements and the moments of the measured distribution of the scattered intensity (assuming that the polarizability is real and for linear excitation, the field is the square root of the intensity).

The next step is to restore the probability distribution function $f_a(x)$ from its moments. For distribution functions that are close to Gaussian shapes, this can be done by using the so-called Edgeworth expansion [115]. Working with the cumulants expansion up to the third order, one obtains the following approximate expression for the PDF of the distribution governing the statistical properties of $f_a(\alpha)$:

$$f_a(\alpha) \approx \frac{\exp[-(\alpha - \langle \alpha \rangle)^2 / 2\sigma_a^2]}{\sqrt{2\pi}\sigma_a} \left\{ 1 + \left(\frac{(\alpha - \langle \alpha \rangle)^3}{\sigma_a^3} - \frac{3(\alpha - \langle \alpha \rangle)}{\sigma_a} \right) \frac{1}{6} \frac{\kappa_{3a}}{\sigma_a^3} \right\} \quad (6.21)$$

Note that the probability distribution in Eq. (4) contains the components of polarizability tensor mixed by angle averaging; to find the effective anisotropic properties of the inhomogeneous scatterers, the elements α_a , α_b , α_c must be ordered. Of course, during a deterministic recovery, one could easily arrange that $\alpha_a > \alpha_b > \alpha_c$ such that they have the physical meaning of ordered eigenvalues of the scattering problem. A similar ordering can also be performed in the stochastic problem by acting directly on the probability distribution given in Eq.(6.21).

Thus, in the third step of our procedure, after the governing PDF in Eq.(6.21) has been found, the probability distributions of the ordered diagonal elements can be recovered through order statistics, i.e. $\alpha_{(a)} > \alpha_{(b)} > \alpha_{(c)}$. The distributions of the ordered diagonal tensor elements $f_{x^{(k)}}(x)$ ($k=1,2,3$), can be evaluated from the original probability distribution function $f(x)$ and the cumulative distribution function $F(x)$ [116]

$$f_{x^{(k)}}(x) = \frac{3!}{(k-1)!(3-k)!} F(x)^{k-1} (1-F(x))^{3-k} f(x) \quad (6.22)$$

It is worth noting that, for a PDF $f_a(x)$ of the form in Eq.(6.21), the mean values of ordered components of the polarizability $\alpha_{(a)}$, $\alpha_{(b)}$, $\alpha_{(c)}$ can be analytically evaluated to be

$$\begin{aligned} \langle \alpha_{(a)} \rangle &= \langle \alpha \rangle + \frac{3\sigma_a}{2\sqrt{\pi}} + \frac{\kappa_{3a}}{4\sqrt{3}\pi\sigma_a^2} + \frac{\kappa_{3a}^2}{64\sqrt{\pi}\sigma_a^5} - \frac{\kappa_{3a}^3}{972\sqrt{3}\pi\sigma_a^8}, \\ \langle \alpha_{(b)} \rangle &= \langle \alpha \rangle + \frac{\sigma_a}{2\sqrt{3}\pi} \left(\frac{1}{243} \left(\frac{\kappa_{3a}}{\sigma_a^3} \right)^3 - \left(\frac{\kappa_{3a}}{\sigma_a^3} \right) \right), \\ \langle \alpha_{(c)} \rangle &= \langle \alpha \rangle - \frac{3\sigma_a}{2\sqrt{\pi}} + \frac{\kappa_{3a}}{4\sqrt{3}\pi\sigma_a^2} - \frac{\kappa_{3a}^2}{64\sqrt{\pi}\sigma_a^5} - \frac{\kappa_{3a}^3}{972\sqrt{3}\pi\sigma_a^8}. \end{aligned} \quad (6.23)$$

These expressions are useful in practice when simply the averages and not the entire distributions of the diagonal elements are required.

A numerical experiment was conducted to test the outlined procedure for reconstructing $\langle \alpha_{(a)} \rangle$, $\langle \alpha_{(b)} \rangle$, $\langle \alpha_{(c)} \rangle$. We considered the interaction volume to be an optically nonuniform sphere with a radius much smaller than wavelength. Inclusions with some specific polarizabilities were randomly placed within the volume of the host sphere. In this situation, the electromagnetic interaction is restricted to the subwavelength volume of the host sphere while the number of inclusions is kept constant from realization to realization of random packing. A

Metropolis Monte Carlo (MMC) algorithm of packing inclusions was implemented, such that a large number of realizations can be obtained efficiently. To verify the successful packing of hard spheres, the pair correlation function was calculated and compared to the analytical 3D Percus-Yevick solution [32]. For each realization of random packing, the optical response of the inhomogeneous sphere was modeled using the coupled dipole approximation (CDA) method [31].

The procedure for generating optically inhomogeneous spheres was repeated two thousand times and, for each realization, the three diagonal elements $\alpha_{a,b,c}^0$ of the polarizability tensor were calculated using the fully deterministic method based on six independent measurements as described in the introduction. The procedure of reconstructing the anisotropic polarizability was first verified through modeling a randomly oriented anisotropic object with a known degree of anisotropy. In the mean time, we have also evaluated the scattered intensity for each realization of the random packing and constructed the ensemble $\{f_E(E_s)\}$ after which the stochastic reconstruction procedure was applied to determine the averages values of the diagonal elements of the polarizability distribution. Numerical analysis shows that for moderate volume fractions of inclusions, the polarizability distributions are nearly Gaussian distributed and described well using Eq.(6.21). In Figure 6-4, we show the error $(\langle \alpha_{(a),(b),(c)} \rangle - \langle \alpha_{a,b,c}^0 \rangle) / \langle \alpha_{a,b,c}^0 \rangle$ of reconstructing the polarizability tensor components $\alpha_{a,b,c}$ using the procedure outlined before in comparison to values $\alpha_{a,b,c}^0$ obtained via the fully deterministic method. The reconstruction error is plotted as a function of volume fraction of inclusions and, as one can see, its value is quite small, well within 0.1%. The non-monotonic error for small concentrations can be

attributed to the fact that the probability distributions may no longer be described by a Gaussian distribution.

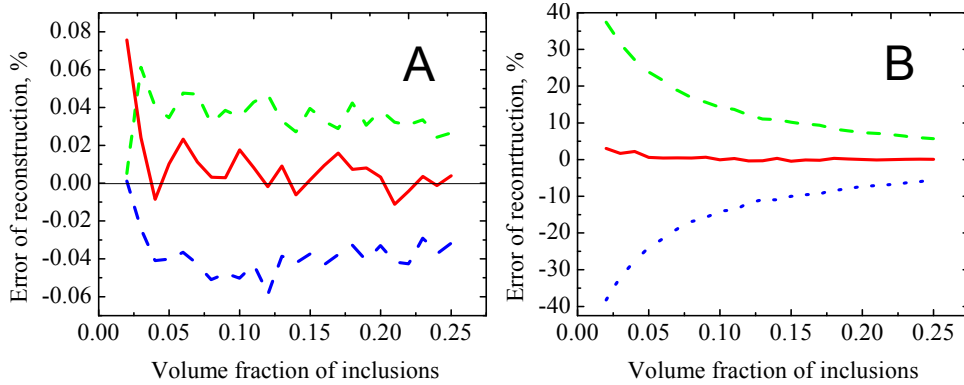


Figure 6-4 Error in reconstructing the polarizability tensor components, α_a (dashed green line), α_b (solid red line), and α_c (dotted blue line), as a function of concentration of inclusions within the sphere of interaction. The number of inclusions is constant in (A) and it varies in (B) (see text). The calculations are performed for a host sphere with radius $r_s = 0.16\lambda$ and refractive index $n_s = 1.33$ which contains inclusions of radii $r_i = 0.05\lambda$ and refractive index $n_i = 2.9$.

Figure 6-4(B) presents the results of the recovery method applied to a material system where the mechanism of confining the volume of interaction is different. In this case, the interaction is confined by a localized excitation but no restriction is placed on the number of inclusions. The volume fraction of inclusions is now evaluated over the entire ensemble of realizations of random packing. This second case corresponds, for example, to scanning of an inhomogeneous medium with the local excitation produced by a near-field optical microscope. Such a situation further complicates the scattering statistics as, in addition to structural fluctuations, further variations of the scattering intensity arise due to different numbers of inclusions for each realization of the inhomogeneous scatterer. As a result, one can see that the reconstruction error is larger in this case and can reach up to 40% at very low volume fractions. Technically, this rather large error occurs, because the fluctuation in the number of inclusions

infringes upon our assumption about the independence of polarizability tensor components. Indeed, a change in the number of inclusions in the excitation volume leads to simultaneous variations in all three components of polarizability tensor; the number fluctuations induces correlations between tensor's diagonal elements. The reconstruction procedure should now account for the fact that α_a , α_b , α_c are no longer independent, and that they are governed by some joint distribution function.

In the more general situation of both structural and number fluctuations, we can estimate bounds for the possible values of the ordered α_a , α_b , α_c [116]:

$$\langle \alpha \rangle - \sigma_a \left(\frac{3-r}{r} \right)^{1/2} \leq \langle \alpha_{(r)} \rangle \leq \langle \alpha \rangle + \sigma_a \left(\frac{r-1}{4-r} \right)^{1/2}, \quad r=1, 2, 3, \quad (6.24)$$

where $\alpha_{(1),(2),(3)} = \alpha_{(c),(b),(a)}$. According to Eq.(6.24), for an arbitrary joint PDF we have $\alpha_{(a)} - \alpha_{(c)} \leq \sigma_a \sqrt{6}$. In comparison, when using Eq.(6.23) for the case of independent α_a , α_b , α_c one obtains

$$\alpha_{(a)} - \alpha_{(c)} = \frac{3\sigma_a}{\sqrt{\pi}} - \frac{\kappa_{3a}^2}{32\sqrt{\pi}\sigma_a^5}. \quad (6.25)$$

The bounds expressed in Eq.(6.24) are valid for an arbitrary correlation between the polarizability components [116]. Thus, the values of the polarizability tensor elements that can be recovered using the fully deterministic method based on six independent measurements should lie within these bounds. Comparing Eq.(6.23) with Eq. (6.24), one can see that the maximum error of reconstruction of difference maximal and minimal values of polarizability tensor ($\alpha_{(a)} - \alpha_{(c)}$) resulting from the assumption about independence of polarizability components is about 45%. This is a rather large error, but one has to remember that its value

characterizes an inversion procedure in which an anisotropic tensor is reconstructed based on ensemble of intensities obtained only with a single polarimetric measurement.

The accuracy of reconstruction can be improved if additional measurements are available as we will show in the following. First, we note that in many cases of interest the distribution $\{\alpha\}$ resembles a Gaussian distribution. In Ref.[117], it was shown that it is possible to establish relationships between the moments of order statistics of dependent and independent variables of normal distribution. Using our definitions, these relations can be written as

$$\langle \alpha_{(a,b,c)}(\rho) \rangle = \langle \alpha \rangle + (1 - \rho)^{1/2} \left(\langle \alpha_{(a,b,c)} \rangle - \langle \alpha \rangle \right). \quad (6.26)$$

where $\rho = \left(\langle \alpha_a \alpha_b \rangle - \langle \alpha \rangle^2 \right) / \sigma_a^2$ is the covariance. To estimate the polarizability components accounting for their possible correlations, one can always make certain assumptions about the scattering object. For instance, in the case of a fluctuating number of inclusions, the covariance ρ can be estimated using the corresponding pair-distribution functions [118]. From Eq.(6.26), one can then find the real, correlated polarizability components $\langle \alpha_{(a,b,c)}(\rho) \rangle$ using the values $\langle \alpha_{(a,b,c)} \rangle$ evaluated under the assumption of their independence.

However, the possible correlations between the elements of the polarizability tensor can also be found without any a priori information entirely on the basis of polarimetric measurements. First, we note that these correlations influence directly the magnitude of the second and higher order moments:

$$\langle E_s^2 \rangle = \frac{1}{5} (3 \langle \alpha^2 \rangle + 2 \langle \alpha_a \alpha_b \rangle). \quad (6.27)$$

In order to obtain both $\langle \alpha^2 \rangle$ and $\langle \alpha_a \alpha_b \rangle$ at the same time, a second polarimetric measurement is necessary. For example, one can measure the scattered intensity through a polarizer orthogonal to the incident direction of polarization

$$\langle E_{\perp}^2 \rangle = \frac{1}{5} (\langle \alpha^2 \rangle - \langle \alpha_a \alpha_b \rangle). \quad (6.28)$$

and from the last two equations one can obtain

$$\langle \alpha_a \alpha_b \rangle = \langle E_s^2 \rangle - 3 \langle E_{\perp}^2 \rangle, \quad \langle \alpha^2 \rangle = \langle E_s^2 \rangle + 2 \langle E_{\perp}^2 \rangle. \quad (6.29)$$

Finally, using Eq.(6.29) and Eq.(6.26), the polarizability components can be found even in the case of arbitrary correlations between them. We would like to point out here that, remarkably, the two polarimetric measurements allow finding the covariance of the polarizability tensor components without knowing the nature of their correlations.

The practical reconstruction procedure can now restructures as follows. First, one must record fluctuations of scattered intensities and build corresponding ensembles for two polarization states, i.e. to perform two polarimetric measurements from which $\langle \alpha \rangle$, $\langle \alpha^2 \rangle$, $\langle \alpha_a \alpha_b \rangle$ are estimated. Second, one should reconstruct the polarizability components according to formula (6) as if they were independent. Finally, using Eq.(6.26) one can calculate the polarizability components that account for possible correlations between them.

This procedure based on two polarimetric measurements is now applied to the same scattering systems illustrated in Figure 6-4. As can be seen, there is only a small difference between the results in Figure 6-4(A) and those in Figure 6-5(A) that corresponds to the situation of independent polarizability elements.

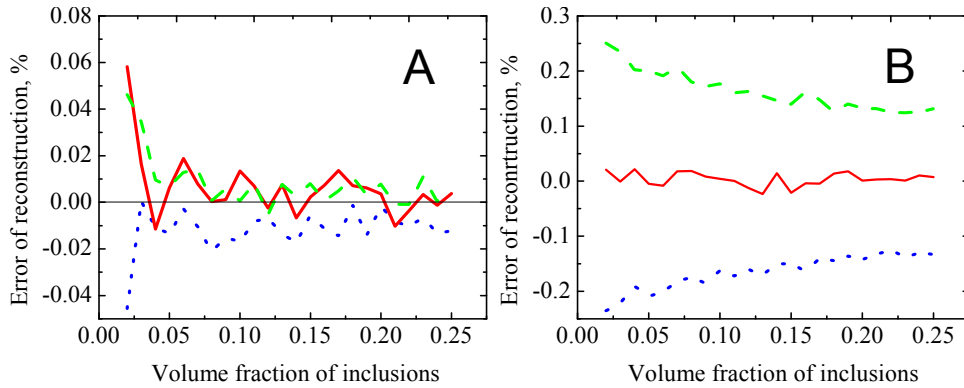


Figure 6-5 Error in reconstructing the polarizability tensor components, α_a (dashed green line), α_b (solid red line), and α_c (dotted blue line), using the two polarimetric measurements method. The number of inclusions is constant in (A) and varies in (B); the parameters for the calculations are the same as in Figure 6-4.

The small improvement by a factor of about two in the reconstruction error is due to the finite number of scatterers considered in our numerical experiment (a finite sample is in fact a type of correlation). Figure 6-5(B), on the other hand, clearly shows that in the case of number fluctuations leading to significant correlations between the polarizability elements α_a , α_b , α_c , the error of reconstruction drops by two orders of magnitude, which is a significant improvement in comparison to the case of a single polarimetric measurement. The very small error of reconstruction still visible in Figure 6-5 is attributed to the fact that real distribution of polarizability tensor components differs from Gaussian. As mentioned before, this difference is especially pronounced for small concentrations that results in relatively large error of reconstruction.

6.3. Stochastic Polarimetry Applied to Near-Field Measurements

As pointed out already in Section 5.3, the localized volume of interaction available using the tapered optical fiber of an NSOM generates a scattering response that can be described by an effective polarizability. As discussed through out this chapter, because SSP depends on relative

fluctuations of statistical ensembles, the secondary interaction may be neglected. The most powerful aspect of SSP as outlined in Section 6.1 is that it may be applied *without prior knowledge* of the exciting field, making it quite appealing to near-field microscopy where control of the exact field is difficult. This, however, requires that the polarizability be of constant throughout the measurement.

Of course, as a first step in describing the polarimetric properties of an inhomogeneous material, one could simply consider the scattering due to some effective polarizability tensor that is just randomly oriented. The degree of anisotropy that can be inferred should give some indication about the degree of depolarization that occurs in scattering from the medium when probed at this scale. In general, the excitation field emitted from the NSOM's tip is in some elliptic state and by manipulating the input state of polarization state one could perhaps optimize and minimize this ellipticity. If this is accomplished, then the task optimized treatment outlined in Section 6.2 for varying polarizability elements may describe quite accurately the physical situation and require far fewer measurements. Both of the derived relationships of Section 6.1 (for a fixed polarizability) and Section 6.2 (for a varying polarizability), yield some effective polarizability tensor that best describes the polarimetric scattering from an inhomogeneous material to an accuracy that depends on the assumptions made in the relationships derived for the moments.

To illustrate the use of SSP for describing the polarimetric response of inhomogeneous materials two materials with similar properties were chosen and experimentally probed with an NSOM. Sample A was an optical coating consisting of packed particulates of 72.5% calcium carbonate, 18.4% kaolin, and 9.1% latex. Sample B was also an optical coating with a recipe of 54.5% calcium carbonate, 36.4% kaolin, and 9.1% latex. The samples were prepared on the

same cover slip and placed close proximity such that the two samples could be measured in very similar conditions. The polarization emitted from the fiber was optimized through using an in fiber polarization scrambler while looking through a polarizer and maximizing the reflected signal when in contact. The AFM topography and the NSOM intensity are shown below in Figure 6-6.

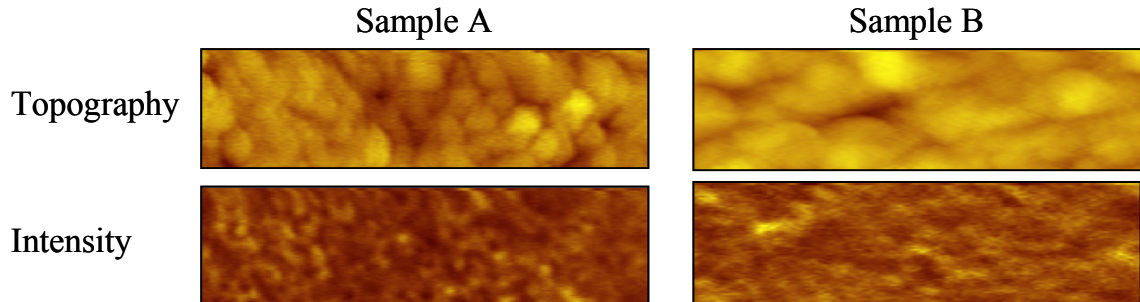


Figure 6-6 AFM measured topography (top) and NSOM measured intensity (bottom) for two optical coatings A (left) and B (right).

The RMS roughness of sample A was found to be 21.7nm whereas sample B had a roughness of 12.3nm. The roughness therefore provides a means of discriminating between the two samples; however, we still would like to see how this roughness folds into the entire scattering properties. The average intensity scattered from the two different samples was also different at 105kcps and 249 KCPS. However, when examining the normalized intensity distributions as we did in Section 5.2, we can see very similar behavior, sample A having a contrast of $C_A = 0.298$, and sample B having a contrast of $C_B = 0.295$.

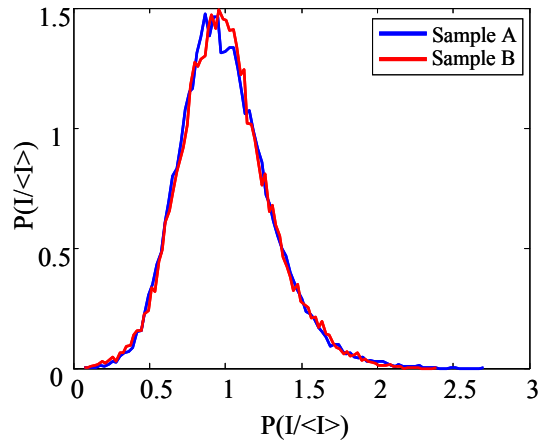


Figure 6-7 Normalized intensity distributions for samples A (blue) and B (red)

Therefore at these two different average intensities, the two different media (having also different roughness) scatter light very similarly. The larger intensity necessary to provide similar statistics for sample B can be related to its smaller RMS roughness that requires a larger interaction volume in order to have a similar level of scattering.

In order to use SSP we also performed polarimetric measurements along the optimized polarization orientation (0°), perpendicular (90°) to it, and at the bisection (45°). The distribution of the polarimetric measurements normalized by the average of the total intensity is plotted below in Figure 6-8.

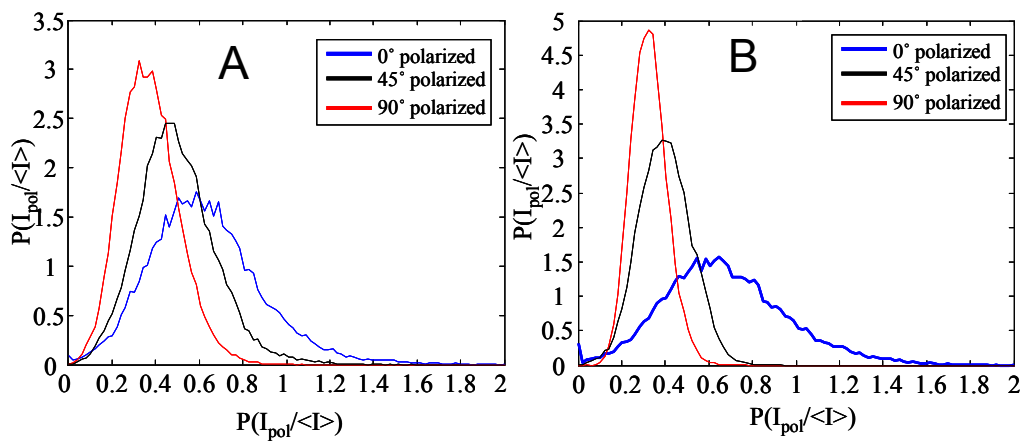


Figure 6-8 Polarimetric intensity distributions normalized by the average of the total intensity for samples A (A) and B (B).

A simple quantitative analysis of the results in Figure 6-8 clearly indicates that the polarimetric distributions are different for the two media. As expected, the largest average intensity occurs when the analysis is performed along the direction of incident polarization. Another way of presenting the polarimetric information is by plotting the measured polarization states on the Poincare sphere as shown below in Figure 6-9. As no wave plates were used in this measurement, we had to assume some handedness for the elliptical states measured.

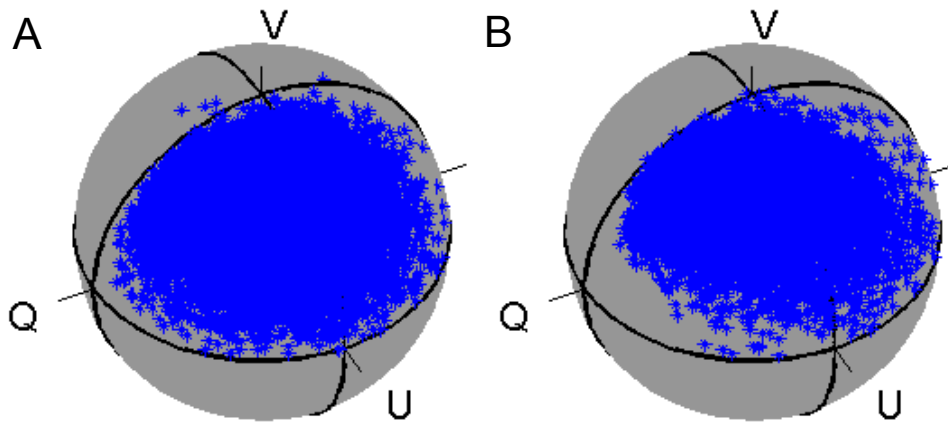


Figure 6-9 Plot of measured polarization states for samples A (A) and B (B) on the Poincare sphere

Having the distribution of Stokes vector elements, we can also calculate the overall degree of polarization or, in other words, the incoherent averaging of the Stoke vector. The degree of polarization was found to be $DOP_A = 0.948$ and $DOP_B = 0.960$, which confirms that the spread in B is more concentrated than A as can be seen in Figure 6-9.

Having access to the three distributions of polarimetric intensities, we can use the SSP procedure described in Section 6.1 and calculate the effective polarizability. Of course, this assumes that the scattered intensity distributions are the result of a single anisotropic

polarizability tensor that is uniformly oriented over the scanned area of a sample. The diagonal forms of the recovered anisotropic tensors are:

$$\alpha_{A,SSP} = \begin{bmatrix} 1 & 0 & 0 \\ 0 & 0.752 & 0 \\ 0 & 0 & 0.545 \end{bmatrix}, \text{ and } \alpha_{B,SSP} = \begin{bmatrix} 1 & 0 & 0 \\ 0 & 0.640 & 0 \\ 0 & 0 & 0.631 \end{bmatrix}. \quad (6.30)$$

As can be seen, the sample A is described by an effective polarizability that is highly anisotropic, while the polarizability corresponding to sample B resembles that of a rod shape scatterer. As a result of using inverting Eq.(6.10) in addition to the unknown polarizability tensor, we also recover information about the unknown exciting field. It was found that for these measurements:

$$\begin{aligned} \varepsilon_A &= 0.74, \Theta_A = 0.92^\circ, \Psi_A = 0.16^\circ, \Phi_A = 0^\circ \\ \varepsilon_B &= 0.68, \Theta_B = 8.53^\circ, \Psi_B = 0.28^\circ, \Phi_B = 0^\circ \end{aligned} \quad (6.31)$$

As can be seen by the reconstructed ellipticity and orientation of the ellipse, although we optimized the field to be linear exiting the probe, the reconstructed excitation field was found to be highly elliptical. This can be understood as a consequence of assuming the anisotropic polarizability to be fixed; as in addition to finding an effective anisotropic polarizability to describe the polarimetric fluctuations, this method also finds some effective field distribution.

Having reconstructed the effective unknown incident field and effective polarizability, we can recalculate the distributions performing a numerical simulation of the random orientations. In doing so, we can see how well the constant effective polarizability replicates the polarimetric scattering from the inhomogeneous material (Figure 6-10).

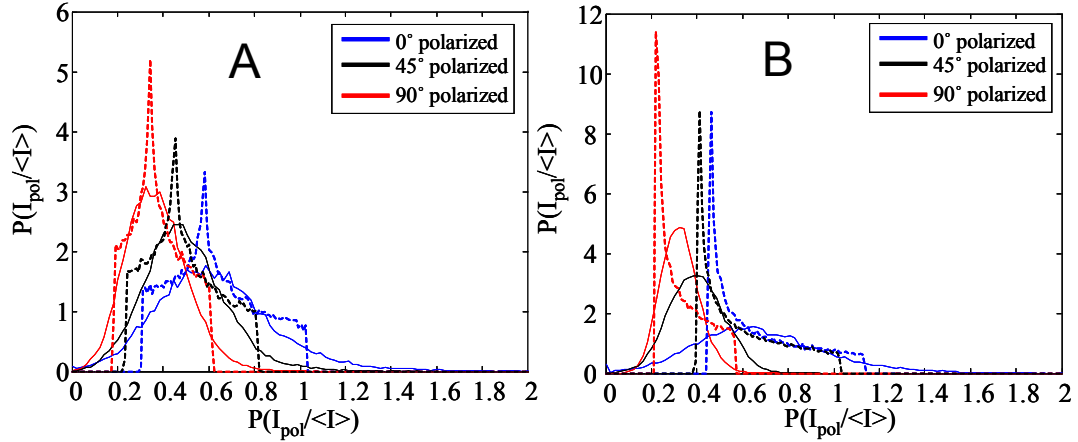


Figure 6-10 Polarimetric intensity distributions normalized by the average of the total intensity measured (solid lines) for samples A (A) and B (B) compared to the fixed anisotropic polarizability reconstructed distributions (dashed lines).

As can be seen in Figure 6-10, keeping the anisotropy fixed leads to sharp boundaries corresponding to the maximum and minimum of the polarizability tensor. The smooth edges of the measurements seen in Figure 6-8 are not replicable when both the anisotropic polarizability and exciting field are fixed. However, we can see that for Figure 6-10 (A), the dashed lines of the reconstructed polarizability provide a good estimation of the total distribution. For sample B on the other hand, we can see that the model does not accurately replicate the measurements, which could be due to the large spread of the measurement along the optimized polarization direction.

As discussed earlier, if we make certain assumptions about the incident field, for instance, it was linearly polarized as the experimental geometry was optimized for; we can apply the concept of SSP and retrieve the first moments of the varying polarizability elements as described in Section 6.2. Processing the corresponding distribution in the assumed linear polarization direction yields normalized diagonal elements of:

$$\alpha_{A,Single} = \begin{bmatrix} 1 & 0 & 0 \\ 0 & 0.814 & 0 \\ 0 & 0 & 0.618 \end{bmatrix}, \text{ and } \alpha_{B,Single} = \begin{bmatrix} 1 & 0 & 0 \\ 0 & 0.878 & 0 \\ 0 & 0 & 0.754 \end{bmatrix}. \quad (6.32)$$

As we can see, again it appears as though sample A has a higher degree of anisotropy, meaning that it redistributes the polarimetric information more than that of sample B. Having only the moments of the effective polarizability from this method we can not make a direct comparison with the reconstructed intensity distributions as done in Figure 6-10 . However, as we can see that the anisotropy must not be a constant from the disagreement shown in Figure 6-10, we can say that this method is more applicable.

To summarize all of the information in Eq.(6.30), and Eq.(6.32), we can calculate a degree of anisotropy as according to Eq.(5.13) to find that for the fixed polarizability:

$$\Delta_{A,SSP} = 0.297, \text{ and } \Delta_{B,SSP} = 0.277. \quad (6.33)$$

and when we assume a linear excitation, we find:

$$\Delta_{A,Single} = 0.236, \text{ and } \Delta_{B,Single} = 0.140. \quad (6.34)$$

As can be seen, when treated such that the polarizability elements may vary, there is a greater difference observed in the degree of anisotropy between the two samples. What's more is that that discrimination between the two samples seen in Eq.(6.34) is available from only a single polarimetric intensity distribution.

As we just observed, although having the same scalar descriptors at different interaction volumes, these two material systems show different polarimetric responses. The polarimetric scattering can be related to some anisotropy of the internal structure. To characterize the polarimetric response of these random systems, we used the method of stochastic scattering polarimetry, which makes use of relative fluctuations to statistically neglect the effects of tip-

sample interaction. Based on the available information about the measurements, and certain assumptions, SSP allows for different relationships to be derived.

In the situation where the incident field is unknown, in order to relate the measurement fluctuations back to the material system, it is required that the anisotropy be held constant throughout the measurement, fluctuations arising only from the orientation. Interpreting the scattered polarimetric distributions with such an assumption lead to a degree of anisotropy characterizing the degree of depolarization. Upon further analysis, it was observed that keeping the anisotropy fixed leads to sharp boundaries in the reconstructed polarimetric distributions which disagreed with the measurements. However, for one of the material systems, the reconstructed distribution was a good approximation of the actual measurement.

Of course, if more information about the physical system is available, more accurate relationships may be derived following the concepts of SSP. Knowing the orientation of the incident field allows one to account for a varying polarizability, removing the sharp boundaries of the polarimetric response. It was shown that under the assumption of a linear excitation, the degree of anisotropy from reconstructed from a single measurement showed a larger difference between the two material systems.

6.4. Summary

Solving the general problem of scattering from small inhomogeneous objects requires solving a linear stochastic equation relating the PDF's of measured quantities to the unknown PDF's of random variables through a set of coefficients that are themselves functions of random variables. Solutions can be found for different specific problems depending on the physical origins of the observed fluctuations. When knowing the distribution of orientations of a

scatterer, one can establish a deterministic relationship between the statistical moments of the recorded field fluctuations, the moments of the probability functions describing the orientation, and the elements of the unknown polarizability tensor describing the scatterer's shape. Finding the solution to this stochastic equation will depend on specific application constraints including prior knowledge about the tested physical system. Most importantly, because this relation is established between statistical moments of distributions, one does not need to know the exact orientation of the scatterer at any moment in time. Moreover, if the excitation field is constant during the experiment, knowledge about its state of polarization state is not required.

When information about the exciting field is available, for instance a linear excitation, the number of required measurements can be greatly reduced. We have shown that measurements of scattered intensities in one polarization state are sufficient to determine the polarizability tensor elements when considering the effective polarizability of an inhomogeneous material. Following a similar procedure, task optimized statistical methods may be designed to minimize the number of required measurements for a specific application.

Finally, we should note that employing the uniform distribution is not a conceptual limitation of this concept, as the general procedure of stochastic scattering polarimetry can also be applied to other distributions depending on the specifics of the experimental application. Also, it should be noted that when our method is applied, we obtain information not only about polarizability properties but also about properties of exciting field. As such, any known information about the material can also be used for probing the local properties of unknown electromagnetic fields [80].

CHAPTER 7: CONCLUSIONS AND SUMMARY OF ORIGINAL CONTRIBUTIONS

Light-matter interaction is complicated by the vector properties of both the electromagnetic field and the spatially varying properties of most material systems. Using electromagnetic fields as a tool to provide information about material system requires understanding how different interaction mechanisms determine variations in measurable signals. As discussed through out this dissertation, depending on the nature of the material system under scrutiny, the effects of interaction may be neglected (passive probing), exploited (active probing, or probing dynamic systems), or statistically isolated (for characterizing complex or inhomogeneous materials).

Probing passively electromagnetic fields close to the surface of a scattering object also allows identifying detailed features that depend on the polarization state of the excitation field. This information is of fundamental relevance not only for material characterization purposes but also for understanding and controlling the properties of intricate photonic structures. We have demonstrated that even in the most symmetric case of a single sphere excited by a plane wave, the light interaction with the material manifests in a complex polarization structure in the vicinity of surface. Specifically, in the scattering of light that is circularly polarized, a spiral flow of the Poynting vector emerges, as expected when considering the conservation of angular momentum. Aside from direct applications in the near-field (nano-manipulation, trapping), a complex field structure can lead to interesting effects in the far-field. A spiraling Poynting vector viewed from the far leads to a perceived shift in the location depending on the incident field's polarization.

The theoretical prediction was also confirmed in an experiment where this perceived shift was identified through a differential intensity measurement using the coupling of a single mode fiber scanned above a scattering sphere [P7]. This work demonstrates how a rather simple experimental procedure based on a passive measurement can be applied to determine the local directionality of the energy flow.

Controlling and manipulating the polarization properties of an excitation field has consequences that determine the subwavelength behavior of optical forces. As such, the results of a field-material interaction can also have useful applications in controlling dynamic systems. Unlike solids, dynamic systems are more susceptible to observable modifications of material properties in the presence of an electromagnetic field. Using an extension of CDA for multiple interacting objects, one can study their behavior in a controlled manner. We elucidated the underlying physics describing how optically interacting particles converge to stable bound locations, and how this effect depends on the incident state of polarization. Notably, we demonstrated that the near-field electromagnetic interaction can provide a new mechanism for generating optical torques [P8].

We have also provided an analysis of the conservative and non-conservative torques that arise in coupled sphere systems and how they are determined by the polarization of the exciting field. When the incident field is linearly polarized, the torques are mostly conservative and affect only the transient behaviors. For circular polarization on the other hand, the nonconservative torques are significant and lead to nontrivial phenomena. In particular, bound

P7 D. Haefner, S. Sukhov, and A. Dogariu, “Spin Hall Effect of Light in Spherical Geometry”, *Phys. Rev. Lett.* 102, 123903 (2009)

P8 D. Haefner, S. Sukhov, and A. Dogariu, “Conservative and Nonconservative Torques in Optical Binding”, *Phys. Rev. Lett.* 103, 173602 (2009)

systems not only rotate around the common center of but also around their own axes. In the intermediate case of elliptically polarized light, the conservative torque will determine a transient orbital motion, whereas the nonconservative one will lead to a continuous spin rotation. The whole system can be seen as a ‘nano-mixer’ with complex mutual rotations of constituents. The direction and speed of these rotations can be dynamically controlled through the intensity, state of polarization, and spatial profile of the incident radiation. Our estimations indicate that effects are observable under reasonable environmental conditions [P8].

The coupled dipole formalism is well suited to arbitrarily shaped objects and excitations; with the added development for modeling the near-field probe as an array of dipoles interacting with a material system, there are many avenues that one could follow. As described throughout this dissertation, CDA also permits an accurate optical force calculation, and the general model we have developed can handle multi-particle systems. In addition, although not included in this dissertation, we extended the applicability of CDA to slabs of inhomogeneous materials, through the use of 2D periodic boundary conditions [P4]. This extension currently serves as a full vectorial simulation of thin inhomogeneous films. Future applications foreseen include the modeling of optically thick slabs of material through integrating the 2D periodic boundary conditions with transfer-matrix approaches, as well as extending the available excitations to include incoherent and partially coherent fields.

P8 D. Haefner, S. Sukhov, and A. Dogariu, “Conservative and Nonconservative Torques in Optical Binding”, *Phys. Rev. Lett.* 103, 173602 (2009)

P4 S. Sukhov, D. Haefner, and A. Dogariu, “Coupled dipole method for modeling optical properties of large-scale random media”, *Phys. Rev. E* 77, 066709 (2008)

In characterizing complex or optically inhomogeneous media, one single wave-matter interaction does not yield much valuable information; rather, a statistical ensemble is required such that moments of distributions of the material properties may be discussed. For such materials, a statistical treatment of the near-field is necessary where the image parameters are interpreted as random variables. When the excitation volume is smaller than the wavelength, one must also consider scale dependent responses observed due to insufficient averaging of the microscopic material properties. That is, the observed far-field response will depend on the mesoscopic volume of interaction. A simple example of such kind of scattering systems is a medium that can be described as an array of independent scattering centers producing fields whose amplitudes and phases are random variables depending on the local topographical and dielectric properties of the material. If the structural aspects are, or can be treated as, statistically independent random variables, then their individual contributions can be separated. We have found that in this case, a simple random walk model describes well experimental observations [P1].

A complete description of the volume dependent response from inhomogeneous materials requires that the full vectorial scattering situation be addressed. The mesoscopic response from some random material may be interpreted as an array of Rayleigh scatterers with some effective polarizability describing the shape and orientation. Through numerical simulations of different random media, we found that there is a scale that corresponds to the maximum degree of anisotropy in random media, the length of which depends on the packing structure. This newly

P1 A. Apostol, D. Haefner, and A. Dogariu, "Near field characterization of effective optical interfaces" Phys. Rev. E. 74, 066603, (2006)

identified scale length corresponds to the size of an average volume where the material is most sensitive to the polarization of an applied electromagnetic field [P9].

Ideally, one would like to have some means of relating the complicated far-field observation of a scale dependence near-field interaction back to the material structure; solving an inverse problem. As with all inverse problems, the method in which the measurement is analyzed depends on the physical system, (what is known and unknown) and to the specific application at hand. To solve inverse problems in scattering from subwavelength volumes, we developed a general approach known as stochastic scattering polarimetry SSP [P2]. SSP involves using moments of measured polarimetric distributions and relating them back to the specific material or field property of interest.

We demonstrated a few possible applications of SSP, one of great interest in near-field microscopy, where when generating a highly localized excitation field typically one loses exact knowledge and control of the polarization state. Through looking at fluctuations is that the effect of a secondary interaction can typically be statistically separated. As we demonstrated [P3] when the object's anisotropy is constant through out the experiment, SSP allows for it's reconstruction without the knowledge of the incident state of polarization.

Having the anisotropy of the object remain fixed throughout the experiment is not a restriction, of SSP, and depending on what is known about the probing field, task optimized

P9 D. Haefner, S. Sukhov, and A. Dogariu, "Scale Dependent Anisotropic Polarizability in Mesoscopic Structures", *Phys. Rev. E*, 81, 016609 (2010)

P2 D. Haefner, S. Sukhov, and A. Dogariu, "Stochastic scattering polarimetry", *Phys. Rev. Lett.* 100, 043901 (2008)

P3 S. Sukhov, D. Haefner, and A. Dogariu, "Stochastic sensing of relative anisotropic polarizabilities", *Phys. Rev. A*, 77, 043820 (2008)

experimental geometries may be envisioned. We discussed one such task optimized measurement specifically to reveal the scale dependent degree of anisotropy of an inhomogeneous material. Through the use of order statistics and a known excitation, when the varying polarizability is uniformly oriented, we demonstrated that a single measurement suffices to characterize what deterministically requires 6 [P10]. Following a similar procedure, task optimized statistical methods may be derived to minimize the number of required measurements for a specific application.

There many other applications of SSP not explored in this dissertation that may be of practical interest. For instance, if the anisotropy of a small scatterer is known, then probing it with a certain field distribution and analyzing the measured fluctuations allows characterizing the orientation distribution. This concept may be used not only for fixed objects but also for dynamic systems.

P10 S. Sukhov, D. Haefner, and A. Dogariu, “Stochastic reconstruction of anisotropic polarizabilities”, *J. Opt. Soc. Am. A* 27 (4), 827 (2010)

7.1. Publications and Presentations

7.1.1. Publications in Refereed Journals

- P10 S. Sukhov, **D. Haefner**, and A. Dogariu, “Stochastic reconstruction of anisotropic polarizabilities”, *J. Opt. Soc. Am. A* **27** (4), 827 (2010)
- P9 **D. Haefner**, S. Sukhov, and A. Dogariu, “Scale Dependent Anisotropic Polarizability in Mesoscopic Structures”, *Phys. Rev. E* **81**, 016609 (2010)
- P8 **D. Haefner**, S. Sukhov, and A. Dogariu, “Conservative and Nonconservative Torques in Optical Binding”, *Phys. Rev. Lett.* **103**, 173602 (2009)
- P7 **D. Haefner**, S. Sukhov, and A. Dogariu, “Spin Hall Effect of Light in Spherical Geometry”, *Phys. Rev. Lett.* **102**, 123903 (2009)
- P6 D. Ma, **D. Haefner**, D. Bousfield, R. D. Carter, A. Dogariu, “Simultaneous Characterization of Coated Paper Topography and Optical Contrast by Near-Field Scanning Optical Microscopy (NSOM)”, *NPPRJ Vol.* **23**, Issue No. 4 (2008)
- P5 D. Ma, R. D. Carter, **D. Haefner**, and A. Dogariu, “The influence of fine kaolin and ground calcium carbonates on the efficiency and distribution of fluorescence whitening agents (FWA) in paper coating”, *NPPRJ Vol.* **23**, Issue No. 3 (2008)
- P4 S. Sukhov, **D. Haefner**, and A. Dogariu, “Coupled dipole method for modeling optical properties of large-scale random media”, *Phys. Rev. E* **77**, 066709 (2008)
- P3 S. Sukhov, **D. Haefner**, and A. Dogariu, “Stochastic sensing of relative anisotropic polarizabilities”, *Phys. Rev. A* **77**, 043820 (2008)
- P2 **D. Haefner**, S. Sukhov, and A. Dogariu, “Stochastic scattering polarimetry”, *Phys. Rev. Lett.* **100**, 043901 (2008)
- P1 A. Apostol, **D. Haefner**, and A. Dogariu, “Near field characterization of effective optical interfaces” *Phys. Rev. E* **74**, 066603, (2006)

7.1.2. Conference Presentations and Proceedings:

- C28. S. Sukhov, **D. Haefner**, and A. Dogariu, “Stochastic Scattering Approach to Determine Effective Packing Structure in Diffuse Optical Coatings”, TAPPI Advanced Coating Fundamentals Symposium, Munich, Germany, October 11-13, 2010
- C27. J. Bae, **D. Haefner**, S. Sukhov, and A. Dogariu, “Optical Properties of Diffuse Coatings under Partially Coherent Illumination”, TAPPI Advanced Coating Fundamentals Symposium, Munich, Germany, October 11-13, 2010
- C26. **D. Haefner**, S. Sukhov, and A. Dogariu, “Nonconservative Optical Torques”, CLEO/IQEC, San Jose, California, May 16 – 21, 2010
- C25. **D. Haefner**, S. Sukhov, and A. Dogariu, “Effects of Polarization in Optical Binding”, OSA Annual Meeting, San Jose, California, October 11-15, 2009
- C24. **D. Haefner**, S. Sukhov, and A. Dogariu, “Reconstructing anisotropic polarizabilities from a single polarimetric measurement”, COSI-OSA Topical Meeting, San Jose, California, October 11-15, 2009
- C23. J. Bae, **D. Haefner**, S. Sukhov, and A. Dogariu, “Full Stokes Polarimetry in the Near Field”, COSI-OSA Topical Meeting, San Jose, California, October 11-15, 2009
- C22. D Kohlgraf-Owens, **D. Haefner**, S. Sukhov, and A. Dogariu, “Sub-Surface Interferometric Near-Field Tomography”, COSI-OSA Topical Meeting, San Jose, California, October 11-15, 2009
- C21. **D. Haefner**, S. Sukhov, and A. Dogariu, “Local Anisotropic Polarizability in Mesoscopic Structures”, CLEO/IQEC, Baltimore, Maryland, May 31 – June 5, 2009
- C20. S. Sukhov, **D. Haefner**, Girish Agarwal, and A. Dogariu, “Enhanced Birefringence of Inhomogeneous Slabs”, CLEO/IQEC, Baltimore, Maryland, May 31 – June 5, 2009 (Poster)
- C19. **D. Haefner**, S. Sukhov, and A. Dogariu, “Conservation of Angular Momentum in Mie Scattering”, OSA Annual Meeting, Rochester, New York, October 19-23, 2008
- C18. **D. Haefner**, S. Sukhov, and A. Dogariu, “Near-Field Modeling of Particle-Particle Interactions”, OSA Annual Meeting, Rochester, New York, October 19-23, 2008
- C17. S. Sukhov, **D. Haefner**, and A. Dogariu, “Coupled Dipole Approximation for Modeling

- Large Scale Random Media”, OSA Annual Meeting, Rochester, New York, October 19-23, 2008
- C16. **D. Haefner**, S. Sukhov, and A. Dogariu, “Near-Field Stochastic Scattering Polarimetry”, 10th International Conference on Near-Field Optics, Buenos Aires, Argentina, September 1-5, 2008
- C15. **D. Haefner**, S. Sukhov, and A. Dogariu, “Conservation Of Angular Momentum In Mie Scattering”, 10th International Conference on Near-Field Optics, Buenos Aires, Argentina, September 1-5, 2008 (Poster)
- C14. S. Sukhov, **D. Haefner**, and A. Dogariu, “Effective Anisotropic Polarizability Of Random Media”, 10th International Conference on Near-Field Optics, Buenos Aires, Argentina, September 1-5, 2008 (Poster)
- C13. S. Sukhov, **D. Haefner**, and A. Dogariu, “Reconstructing The Local Dielectric Tensor From Near-Field Measurements”, 10th International Conference on Near-Field Optics, Buenos Aires, Argentina, September 1-5, 2008 (Poster)
- C12. S. Sukhov, **D. Haefner**, A. Dogariu, D. Ma, R. D. Carter, “Numerical Modeling of Optical Coatings Using Coupled Dipole Approximation”, TAPPI Advanced Coating Fundamentals Symposium, Montreal, QC Canada, June 11-13, 2008
- C11. **D. Haefner**, J. Ellis, S. Sukhov, and A. Dogariu, “Determining Anisotropic Polarizability of Optically Inhomogeneous Media in Near-Field Measurements” OSA Annual Meeting, San Jose, California, September 16-20, 2007
- C10. S. Sukhov, **D. Haefner**, and A. Dogariu, “Scattered Intensity Fluctuations for Characterizing Inhomogeneous Media” OSA Annual Meeting, San Jose, California, September 16-20, 2007
- C9. **D. Haefner**, J. Ellis, S. Sukhov, and A. Dogariu, “Computational Sensing of Anisotropic Polarizability in Multiply Scattering Media”, COSI-OSA Topical Meeting, Vancouver, BC, Canada, June 18-20, 2007
- C8. S. Sukhov, **D. Haefner**, and A. Dogariu, “Using Statistics of Optical Near-fields for Sensing Properties of Inhomogeneous media”, COSI-OSA Topical Meeting, Vancouver, BC, Canada, June 18-20, 2007
- C7. S. Sukhov, **D. Haefner**, A. Dogariu, “Fluctuation Polarimetry for Characterizing Optical Anisotropies”, Random Electromagnetic Fields Workshop , Orlando, Florida, May 3-4, 2007

- C6. **D. Haefner**, A. Apostol, A. Dogariu, “Coupled Dipole Description of Random Near Fields”, OSA Annual Meeting, Rochester, New York, October 8-12, 2006
- C5. A. Apostol, **D. Haefner**, A. Dogariu, “Near-Field Characterization of Effective Optical Interfaces”, OSA Annual Meeting, Rochester, New York, October 8-12, 2006
- C4. **D. Haefner**, A. Apostol, J. Ellis, A. Dogariu, “Vector Statistics of Random Near Fields Using Coupled Dipoles Approximation ”, OISE-OSA Topical Meeting, Charlotte, North Carolina, September 6-8, 2006
- C3. A. Apostol, **D. Haefner**, A. Dogariu, “NSOM Study of Optically Inhomogeneous Interfaces”, OISE-OSA Topical Meeting, Charlotte, North Carolina, September 6-8, 2006
- C2. A. Apostol, **D. Haefner**, A. Dogariu, “Spatial Correlations of Optical Fields Near Interfaces of Random Media”, OSA Annual Meeting, Tucson, Arizona, October 16-20, 2005
- C1. **D. Haefner**, A. Apostol, A. Dogariu, “Morphology dependent near-field coupling onto dielectric spheres” COSI-OSA Topical Meeting, Charlotte, North Carolina, June 6-9, 2005

APPENDIX: SUPPORTING MATERIALS

A. Derivation of Abbe-Rayleigh Resolution Limit

Here we present a simple derivation of the Abbe-Rayleigh resolution limit in terms of imaging through an optical system. In the most simple of microscopes, two lenses are used; two lenses allow for an easier method of obtaining a highly magnified image without introducing to many aberrations. A simple schematic of a two lens system is depicted below in Figure A-1.

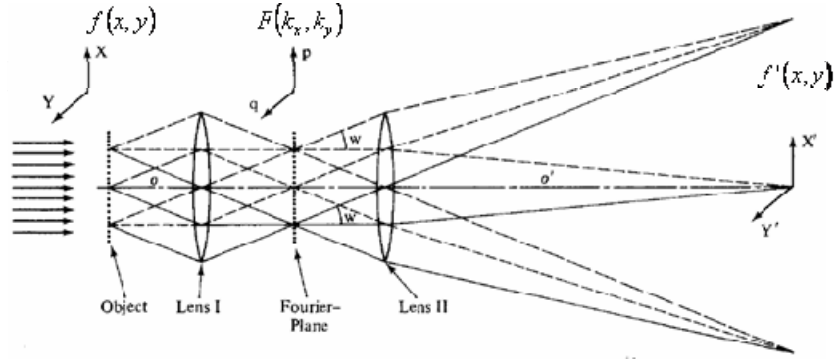


Figure A-1 Schematic of simple two lens imaging system.

To gather information about how and image is formed, we can begin with specifying an arbitrary object function to image as:

$$f(x, y). \quad (\text{A.1})$$

The relationship between the front and rear focal planes exists through a Fourier Transform. The Fourier transform of Eq.(A.1) can be expressed as.

$$F(k_x, k_y) = \mathcal{F}\{f(x, y)\} = \frac{1}{4\pi^2} \int_{-\infty}^{\infty} \int_{-\infty}^{\infty} f(x, y) \exp(i(k_x x + k_y y)) dx dy, \quad (\text{A.2})$$

where the Fourier frequencies can be defined as:

$$k_x = 2\pi R_x = \frac{-2\pi\eta}{\lambda f_1} = \frac{2\pi}{\lambda} \sin \theta_x, \text{ and } k_y = 2\pi R_y = \frac{-2\pi\xi}{\lambda f_1} = \frac{2\pi}{\lambda} \sin \theta_y. \quad (\text{A.3})$$

In Eq.(A.3), we have R_x and R_y as the spatial frequencies, and the angles θ_x and θ_y describe the limiting angles of the system in the different directions. In the imaging plane, the object is recovered through an inverse Fourier Transform.

$$f'(x', y) = \mathcal{F}^{-1} \{F(k_x, k_y)\} = \int_{-\infty}^{\infty} \int_{-\infty}^{\infty} F(k_x, k_y) \exp(-i(k_x x' + k_y y')) dk_x dk_y \quad (\text{A.4})$$

However, any real world microscope has an aperture stop creating a spatial frequency cutoff in the Fourier domain. Also there are aberrations that will also distort the image, making resolution even worse. It is the most important to understand how the microscope is changing this spectrum. If we let the modified spectrum be denoted as F' and being modified by a function dependent on the microscope, we have the following.

$$F'(k_x, k_y) = F(k_x, k_y) g(k_x, k_y) \quad (\text{A.5})$$

A1. Rectangular Aperture

In his first paper in 1873 [119], Abbe considered that the limiting function in the Fourier plane can be described in terms of a *rect* function with a width dependent on the numerical aperture of the system.

$$g(k_x, k_y) = \text{rect}\left(\frac{\eta}{2R_o}, \frac{\xi}{2R_o}\right) \quad (\text{A.6})$$

where R_o is similar to a band pass filter in the Fourier domain. R_o can be defined in terms of the spatial frequency coordinates and thus numerical aperture of the system. In terms of the:

$$R_o = \frac{\eta_o}{\lambda f_1} = \frac{-\eta_o}{\lambda f_1} = \frac{\xi_o}{\lambda f_1} = \frac{-\xi_o}{\lambda f_1} = \frac{\sin \theta_o}{\lambda} = \frac{n \sin \theta_o}{\lambda_o} \quad (\text{A.7})$$

The image formed by the microscope is then the inverse transform of F'

$$f'(x', y') = \int_{-\infty}^{\infty} \int_{-\infty}^{\infty} f(x'', y'') g(x' - x'', y' - y'') dx'' dy'' \quad (\text{A.8})$$

If the function g of the microscope is a *rect* function, then the final image will be the convolution of the object function with a sinc function, which defines the cutoff in the spatial frequency domain. To calculate the finest resolution of conventional far-field optics, as in example, we would like to image two point sources separated by a certain distance Δ . For the first situation, we will work with incoherent light, and work with the interference effects of coherent illumination later. The object function can be defined as:

$$f(x) = \delta\left(x - \frac{\Delta}{2}\right) + \delta\left(x + \frac{\Delta}{2}\right) \quad (\text{A.9})$$

Since we are dealing with incoherent light, the convolution will be with the intensity of the point image function of the microscope or:

$$g(x) = \left| \text{sinc}(2\pi R_o x) \right|^2 \quad (\text{A.10})$$

Eq.(A.8) is the image intensity, which has the analytical expression:

$$f'(x') = I(x') = \left(\text{sinc}\left(2\pi R_o \left(x' - \frac{\Delta}{2}\right)\right) \right)^2 + \left(\text{sinc}\left(2\pi R_o \left(x' + \frac{\Delta}{2}\right)\right) \right)^2. \quad (\text{A.11})$$

At this point, we must define what the criteria should be that constitutes the two objects being resolved. As with any measurement threshold, the definition is somewhat arbitrary and, in practice, depends on signal-to-noise ratio. Born and Wolf [2] consider the case of two slits to be resolved when the maximum of one is located at the first minimum of the second. Shifting both components in Eq.(A.11) by $\Delta/2$, the resolution limit for incoherent light is found to be:

$$2\pi R_o \Delta_o = \pi$$

$$\Delta_o = \frac{1}{2R_o} = \frac{\lambda}{2n \sin \theta_o} = \frac{\lambda}{2NA} \quad (\text{A.12})$$

Eq.(A.12) is the well known and common definition for the resolution limit. Having the resolution limit Δ allows us to also define a resolution limit in terms of an intensity threshold. Looking at the ratio of the intensity on axis and that of the peak, when the two objects are separated by the resolution limit shows that 2 objects can be considered resolved if the intensity ratio is smaller than 81%. This number is specific to the rectangular function used to establish the resolution limit.

Following a similar procedure, the resolution limit for coherent illumination can also be derived. However in this case the object function for will have a phase associated with it; for a plane wave at some arbitrary angle we have:

$$f(x) = \delta\left(x - \frac{\Delta}{2}\right) \exp(-ik(\Delta \sin \alpha_x)) + \delta\left(x + \frac{\Delta}{2}\right) \exp(ik(\Delta \sin \alpha_x)) \quad (\text{A.13})$$

Instead of convolving with the intensity of the point image function of the microscope, the convolution will be with the fields associated with it. Plugging in Eq.(13) into Eq.(8) results in:

$$f'(x') = \exp(-ik(\Delta \sin \alpha_x)) \times$$

$$\left(\text{sinc}\left(2\pi R_o \left(x' - \frac{\Delta}{2}\right)\right) + \text{sinc}\left(2\pi R_o \left(x' + \frac{\Delta}{2}\right)\right) \exp(2ik(\Delta \sin \alpha_x)) \right), \quad (\text{A.14})$$

where we can find the intensity to be:

$$I(x') = \left(\text{sinc} \left(2\pi R_o \left(x' - \frac{\Delta}{2} \right) \right) \right)^2 + \left(\text{sinc} \left(2\pi R_o \left(x' + \frac{\Delta}{2} \right) \right) \right)^2 + 2 \left(\text{sinc} \left(2\pi R_o \left(x' + \frac{\Delta}{2} \right) \right) \right) \left(\text{sinc} \left(2\pi R_o \left(x' - \frac{\Delta}{2} \right) \right) \right) \cos(k_o \Delta \sin \alpha) \quad (\text{A.15})$$

We can see in Eq.(A.15) that the intensity is composed of 3 parts: the two intensities of the individual point sources which is equal to the incoherent illumination and some interference term. To see the influence of all three when the two point sources are separated by the common definition for the resolution limit, we present Figure A-2. The numerical aperture was assumed to be 1 for an ideal imaging system.

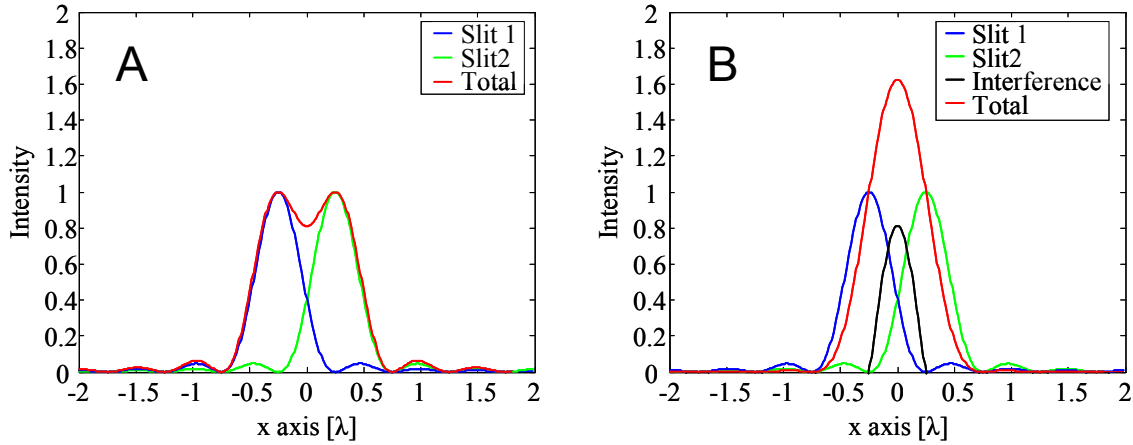


Figure A-2 Plot of incoherent illumination (A) and coherent illumination (B) of 2 point objects separated by $\lambda/2$

As we can see, Figure A-2 shows that the incoherent case does resolve the two point objects, however do to interference effects, the coherent case is not resolved. It is possible to then solve for at what distance the two objects are resolved in terms of this intensity threshold established for the incoherent case. Setting the ratio between the $x = \Delta$ and the $x = 0$ to be 0.81; solving for Δ , it is found that:

$$\Delta_o = 0.7110 \frac{\lambda}{n \sin \theta} \quad (\text{A.16})$$

Plotting the coherent case for this separation gives:

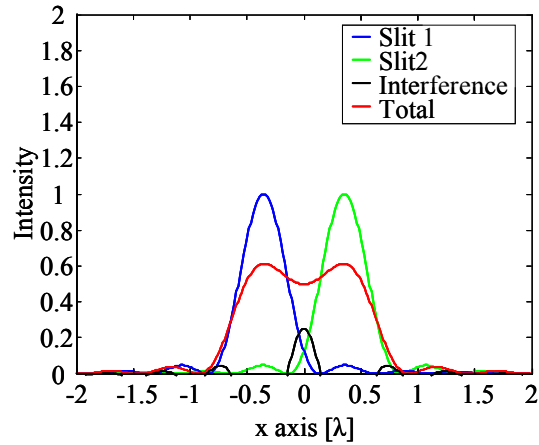


Figure A-3 Plot of coherent illumination of 2 point objects separated by 0.711λ

A2. Circular Aperture

For most optical systems, the aperture is circularly symmetric, in this case, the microscope function can be defined as:

$$G(k_x, k_y) = \text{circ}(R_o) \quad (\text{A.17})$$

Just as before, we can consider the field in the image plane to be the convolution of the object function and the Fourier Transform of the instrument function

$$G(k_x, k_y) = \text{circ}(R_o) \rightarrow g(x, y) = \frac{J_1(2\pi R_o x)}{2\pi R_o x} \frac{J_1(2\pi R_o y)}{2\pi R_o y} \quad (\text{A.18})$$

We can calculate the resolution limit in terms of two infinitesimal slits separated by some distance Δ , in the case of incoherent illumination where the object function can be written as

$$f(x) = \delta\left(x - \frac{\Delta}{2}\right) + \delta\left(x + \frac{\Delta}{2}\right). \quad (\text{A.19})$$

When dealing with an incoherent illumination we need only the intensity of the Fourier transform:

$$g(x, y) = \left| \frac{J_1(2\pi R_o x)}{2\pi R_o x} \right|^2 \quad (\text{A.20})$$

where: $R_o = n \sin \theta_o / \lambda_o$. Performing the convolution of a delta function and the incoherent point image function we find that the intensity in the image plane is:

$$f'(x') = I(x') = \left(\frac{J_1\left(2\pi R_o \left(x' - \frac{\Delta}{2}\right)\right)}{2\pi R_o \left(x' - \frac{\Delta}{2}\right)} \right)^2 + \left(\frac{J_1\left(2\pi R_o \left(x' + \frac{\Delta}{2}\right)\right)}{2\pi R_o \left(x' + \frac{\Delta}{2}\right)} \right)^2 \quad (\text{A.21})$$

With the same definition of resolution, where we would like to find the separation such that the maximum of one contribution corresponds to the minimum of the other; we can shift both, and then solve:

$$\begin{aligned} J_1(2\pi R_o \Delta_o) &= 0 \\ 2\pi R_o \Delta_o &= 3.8317 \\ \Delta_o &= \frac{0.6098}{R_o} = 0.6098 \frac{\lambda}{n \sin \theta} \end{aligned} \quad (\text{A.22})$$

Let us also look at the case of coherent slits, we can use the same definition of the object function from before.

$$f(x) = \delta\left(x - \frac{\Delta}{2}\right) \exp(-ik(\Delta \sin \alpha_x)) + \delta\left(x + \frac{\Delta}{2}\right) \exp(ik(\Delta \sin \alpha_x)) \quad (\text{A.23})$$

The microscope function again will be in terms of the fields, so we have the following:

$$g(x, y) = \frac{J_1(2\pi R_o x)}{2\pi R_o x}. \quad (\text{A.24})$$

The convolution gives the field in the image plane to be

$$f'(x') = \exp(-ik(\Delta \sin \alpha_x)) \times \left(\frac{J_1\left(2\pi R_o\left(x' - \frac{\Delta}{2}\right)\right)}{2\pi R_o\left(x' - \frac{\Delta}{2}\right)} + \frac{J_1\left(2\pi R_o\left(x' + \frac{\Delta}{2}\right)\right)}{2\pi R_o\left(x' + \frac{\Delta}{2}\right)} \exp(2ik(\Delta \sin \alpha_x)) \right), \quad (\text{A.25})$$

where the intensity can be found as

$$I(x') = \left(\frac{J_1\left(2\pi R_o\left(x' - \frac{\Delta}{2}\right)\right)}{2\pi R_o\left(x' - \frac{\Delta}{2}\right)} \right)^2 + \left(\frac{J_1\left(2\pi R_o\left(x' + \frac{\Delta}{2}\right)\right)}{2\pi R_o\left(x' + \frac{\Delta}{2}\right)} \right)^2 + 2 \left(\frac{J_1\left(2\pi R_o\left(x' + \frac{\Delta}{2}\right)\right)}{2\pi R_o\left(x' + \frac{\Delta}{2}\right)} \right) \quad (\text{A.26})$$

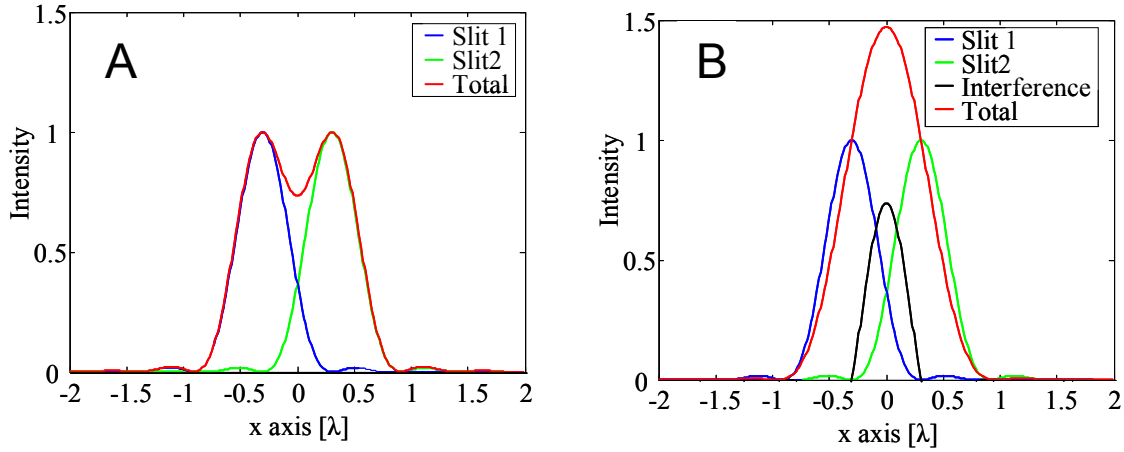


Figure A-4 Plot of incoherent illumination (A) and coherent illumination (B) of 2 point objects separated by $\lambda/2$

As we can see, due to the coherent effect of interference, at a separation of $.61\lambda$ the two slits are not resolved. So from this definition of Resolution that was established for the incoherent illumination, we can find that the 2 points can be resolved if there exist an intensity below 73.5% between them.

$$\Delta_o = \frac{0.8190}{R_o} = 0.8190 \frac{\lambda}{n \sin \theta} \quad (\text{A.27})$$

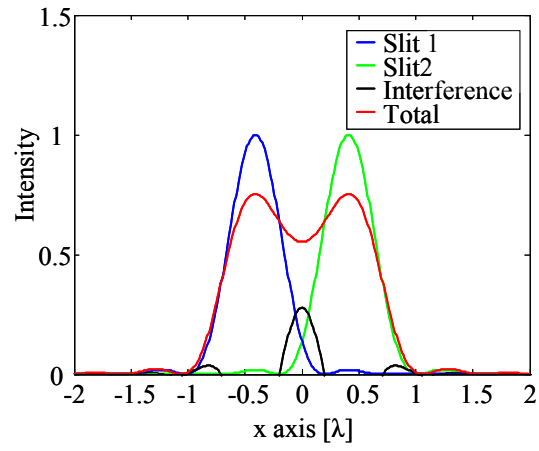


Figure A-5 Plot of coherent illumination of 2 point objects separated by 0.82λ

B. Convolution Method Details for CDA

In continuous space, the general problem is solving:

$$\int \bar{\mathbf{A}}(\mathbf{r}_1, \mathbf{r}_2) \mathbf{P}(\mathbf{r}_1) d\mathbf{r}_1 = \mathbf{E}(\mathbf{r}_2) \quad (\text{B.1})$$

for \mathbf{P} given \mathbf{E} and $\hat{A}(\vec{r}_1, \vec{r}_2)$. From the form of $\hat{A}(\vec{r}_1, \vec{r}_2) = \hat{A}(\vec{r}_1 - \vec{r}_2)$ we can write

$$\begin{aligned} \bar{\mathbf{a}}(\mathbf{r}_1) &= \bar{\mathbf{A}}(\mathbf{r}_1, \mathbf{r}_1) \\ \bar{\mathbf{A}}'(\mathbf{r}_1 - \mathbf{r}_2) &= \begin{cases} \bar{\mathbf{A}}'(0) = 0 \\ \bar{\mathbf{A}}'(\mathbf{r}_1 - \mathbf{r}_2) = \bar{\mathbf{A}}(\mathbf{r}_1, \mathbf{r}_2) \end{cases} \end{aligned} \quad (\text{B.2})$$

This equation can be reformulated, to give us:

$$\bar{\mathbf{a}}(\mathbf{r}_2) \mathbf{P}(\mathbf{r}_2) + \int \bar{\mathbf{A}}'(\mathbf{r}_1 - \mathbf{r}_2) \mathbf{P}(\mathbf{r}_1) d\mathbf{r}_1 = \mathbf{E}(\mathbf{r}_2) \quad (\text{B.3})$$

where we can now write:

$$\int \bar{\mathbf{A}}'(\mathbf{r}_1 - \mathbf{r}_2) \mathbf{P}(\mathbf{r}_1) d\mathbf{r}_1 = \bar{\mathbf{A}}'(\mathbf{r}) \otimes \mathbf{P}(\mathbf{r}). \quad (\text{B.4})$$

We would like to invert the equation for the total field:

$$\mathbf{P}(\mathbf{r}_j) \cdot [\bar{\mathbf{a}}_j]^{-1} + \sum_{k=1, k \neq j}^N [\bar{\mathbf{A}}(\mathbf{r}_j, \mathbf{r}_k)] \cdot \mathbf{P}(\mathbf{r}_k) = \mathbf{E}_{inc}(\mathbf{r}_j), \quad (\text{6.5})$$

which, may now be rewritten as:

$$\bar{\mathbf{a}}(\mathbf{r}_2) \mathbf{P}(\mathbf{r}_2) + \bar{\mathbf{A}}'(\mathbf{r}) \otimes \mathbf{P}(\mathbf{r}) = \mathbf{E}(\mathbf{r}_2), \quad (\text{B.6})$$

working in the discrete space, this means:

$$\bar{\mathbf{a}}\mathbf{P} + \bar{\mathbf{A}} \otimes \mathbf{P} = \mathbf{E} \quad (\text{B.7})$$

It is only necessary to calculate the interaction for lattice points of unique vector separations. The solution to Eq.(6.5) is much simplified when preformed in the Fourier space.

C. Derivation of Optical Forces

The Lorentz force equation gives the force acting on a point charge q in the presence of an electromagnetic field [72]:

$$\mathbf{F} = q(\mathbf{E} + \mathbf{v} \times \mathbf{B}), \quad (\text{C.1})$$

where here \mathbf{v} is the velocity, and \mathbf{E} and \mathbf{B} are the electric and magnetic fields. As most observable objects are larger than a point charge, typically one considers the change of force throughout some volume. The amount of charge in some small volume ΔV , is related to the local charge density ρ through $q = \rho\Delta V$, making the change in force over some small volume:

$$\Delta\mathbf{F} = \rho(\mathbf{E} + \mathbf{v} \times \mathbf{B})\Delta V. \quad (\text{C.2})$$

It should also be noted that a moving charge density creates a current density $\mathbf{J} = \rho\mathbf{v}$. To find the total force exerted on the object, it is necessary to integrate over the entire volume V , giving the total force:

$$\mathbf{F} = \int_V (\rho\mathbf{E} + \mathbf{J} \times \mathbf{B}) dV. \quad (\text{C.3})$$

Eq.(C.3) is general for arbitrarily sized particles. However, although equally valid, it is not always easy to understand the underlying origins of the force when it is in terms of charge and current densities. Fortunately, there are a number of coupled electromagnetic expressions that present the same quantity through different mathematical formalisms. As we will be calling on them many times through out this derivation, it is important to list the most important equations in electromagnetism, Maxwell's equations. Maxwell's equations in matter are (in SI units):

$$\begin{aligned}
\nabla \cdot \mathbf{D} &= \rho \\
\nabla \cdot \mathbf{B} &= 0 \\
\nabla \times \mathbf{E} &= -\frac{\partial \mathbf{B}}{\partial t} \\
\nabla \times \mathbf{H} &= \mathbf{J} + \frac{\partial \mathbf{D}}{\partial t}
\end{aligned} \tag{C.4}$$

where we have:

$$\begin{aligned}
\mathbf{D} &= \varepsilon_0 \mathbf{E} + \mathbf{P} \\
\mathbf{H} &= \mu_0^{-1} \mathbf{B} + \mathbf{M}
\end{aligned} \tag{C.5}$$

Substituting some of the relationships expressed in Maxwell's equations (Eq.(C.4)) into the general force equation Eq.(C.3), yields

$$\mathbf{F} = \int_V \left[\varepsilon_0 \mathbf{E} (\nabla \cdot \mathbf{E}) + \left(\frac{1}{\mu_0} \nabla \times \mathbf{B} - \varepsilon_0 \frac{\partial \mathbf{E}}{\partial t} \right) \times \mathbf{B} \right] dV. \tag{C.6}$$

The time derivative in the above expression may be simplified by expanding it as:

$$\frac{\partial \mathbf{E}}{\partial t} \times \mathbf{B} = \frac{\partial (\mathbf{E} \times \mathbf{B})}{\partial t} - \mathbf{E} \times \frac{\partial \mathbf{B}}{\partial t}, \tag{C.7}$$

and using the relationship from Maxwell's equations, $\nabla \times \mathbf{E} = -\partial \mathbf{B} / \partial t$, one can write:

$$\frac{\partial \mathbf{E}}{\partial t} \times \mathbf{B} = \frac{\partial (\mathbf{E} \times \mathbf{B})}{\partial t} + \mathbf{E} \times (\nabla \times \mathbf{E}). \tag{C.8}$$

Considering the above expression, one may readily identify the presence of the well known expression for the Poynting vector:

$$\mathbf{S} = \mu_0^{-1} \mathbf{E} \times \mathbf{B}. \tag{C.9}$$

The presence of the Poynting vector makes sense, as in discussing forces, one would expect there to be some dependence on the total energy flux of the exciting electromagnetic field.

Substituting the Poynting vector into Eq.(C.8), and Eq.(C.8) back into the expression for the Force (Eq.(C.6)) gives

$$\mathbf{F} = \int_V \left[\epsilon_0 \mathbf{E} (\nabla \cdot \mathbf{E}) + \frac{1}{\mu_0} (\nabla \times \mathbf{B}) \times \mathbf{B} + \epsilon_0 (\nabla \times \mathbf{E}) \times \mathbf{E} - \mu_0 \epsilon_0 \frac{\partial \mathbf{S}}{\partial t} \right] dV. \quad (\text{C.10})$$

To simplify this expression, one may make use of some vector identities; namely cross product of the curl of a vector may be simplified using:

$$\nabla (\mathbf{A} \cdot \mathbf{B}) = \mathbf{A} \times (\nabla \times \mathbf{B}) + \mathbf{B} \times (\nabla \times \mathbf{A}) + (\mathbf{A} \cdot \nabla) \mathbf{B} + (\mathbf{B} \cdot \nabla) \mathbf{A}; \quad (\text{C.11})$$

which when applied to the electric and magnetic fields gives

$$\begin{aligned} (\nabla \times \mathbf{E}) \times \mathbf{E} &= (\mathbf{E} \cdot \nabla) \mathbf{E} - \frac{1}{2} \nabla (\mathbf{E}^2) \\ (\nabla \times \mathbf{B}) \times \mathbf{B} &= (\mathbf{B} \cdot \nabla) \mathbf{B} - \frac{1}{2} \nabla (\mathbf{B}^2) \end{aligned} \quad (\text{C.12})$$

After some rearranging Eq. (C.10) becomes:

$$\mathbf{F} = \int_V \left[\epsilon_0 (\mathbf{E} (\mathbf{E} \cdot \nabla) + (\nabla \cdot \mathbf{E}) \mathbf{E}) + \frac{1}{\mu_0} ((\mathbf{B} \cdot \nabla) \mathbf{B}) - \frac{1}{2} \nabla \left(\epsilon_0 \mathbf{E}^2 + \frac{1}{\mu_0} \mathbf{B}^2 \right) - \mu_0 \epsilon_0 \frac{\partial \mathbf{S}}{\partial t} \right] dV \quad (\text{C.13})$$

To attempt to gain some physical insight into this other method of expressing the total force, one may observe that the second to last term of Eq. (C.13) expresses the gradient of potential energy integrated over a volume, a term common when describing forces. The last term in the expression deals with the time dependent change in momentum; and the first two terms deal with the non-gradient/non-conservative forces due to the vectoral nature of electromagnetic fields.

In terms of simplifying calculations, the expression for the force in Eq.(C.13) may be expressed in a tensorial form:

$$\nabla \cdot \bar{\bar{\mathbf{T}}} = \varepsilon_0 (\mathbf{E}(\mathbf{E} \cdot \nabla) + (\nabla \cdot \mathbf{E})\mathbf{E}) + \frac{1}{\mu_0} ((\mathbf{B} \cdot \nabla)\mathbf{B}) - \frac{1}{2} \nabla \left(\varepsilon_0 \mathbf{E}^2 + \frac{1}{\mu_0} \mathbf{B}^2 \right), \quad (\text{C.14})$$

where the elements of T can be found as:

$$T_{jk} = \varepsilon_0 \left(E_j E_k - \frac{1}{2} \delta_{jk} E^2 \right) + \frac{1}{\mu_0} \left(B_j B_k - \frac{1}{2} \delta_{jk} B^2 \right). \quad (\text{C.15})$$

This Tensor $\bar{\bar{\mathbf{T}}}$ is known as the Maxwell stress tensor. The total force may be written now in a much more compact expression:

$$\mathbf{F} = \int_V \left[\nabla \cdot \bar{\bar{\mathbf{T}}} - \mu_0 \varepsilon_0 \frac{\partial \mathbf{S}}{\partial t} \right] dV. \quad (\text{C.16})$$

Making use of the divergence theorem, one may eliminate the volume integral, and instead calculate the surface integral:

$$\mathbf{F} = \oint \bar{\bar{\mathbf{T}}} d\mathbf{a} - \mu_0 \varepsilon_0 \frac{d}{dt} \int_V \mathbf{S} dV. \quad (\text{C.17})$$

Writing the force in this form allows the individual terms to be interpreted as the first term corresponding to an integrated shear and pressure at the surface of the object, and the second relating to the integrated change in momentum throughout the volume.

C1. Electromagnetic Force on a Dipole

When the size of a scattering particle is much smaller than the wavelength of the exciting field, the scattered radiation may be treated as that of an electric dipole. As the interaction of small spheres was discussed many times throughout this dissertation, calculating the analytical expression for the total force on such an object is also of interest. The Lorentz force on an electric dipole can be most easily derived by treating the dipole as a pair of equal and opposite

charges. To characterize this charge distribution, it is useful to define the electric dipole moment, generally defined as:

$$\mathbf{p} = \int_V \rho(\mathbf{r}_0)(\mathbf{r}_0 - \mathbf{r}) d^3\mathbf{r}_0. \quad (\text{C.18})$$

For an array of point charges, the dipole moment becomes:

$$\mathbf{p}(\mathbf{r}) = \sum_j^N q_j (\mathbf{r} - \mathbf{r}_j), \quad (\text{C.19})$$

which for the two equal and opposite point charges depicted in Figure C-1, is simply

$$\mathbf{p}(\mathbf{r}) = q(\mathbf{r}_+ - \mathbf{r}_-). \quad (\text{C.20})$$

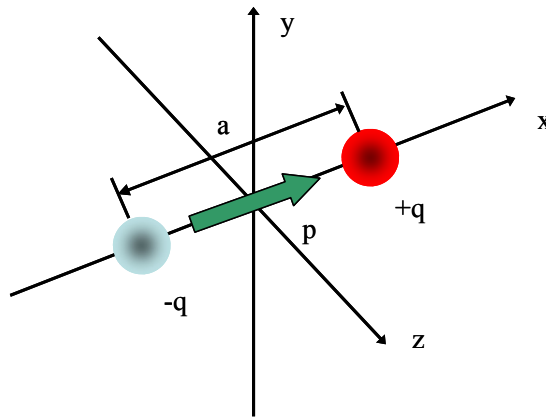


Figure C-1 Schematic of an electric dipole as two equal and opposite point charges. These two point charges, q_+ and q_- give rise to a dipole moment \mathbf{p} .

From Eq.(C.1) for the force, one can separate the contributions to the total force as that due the electric field, and that of the magnetic field. The total force due to the electric field is found as:

$$\mathbf{F}_{elec} = q(\mathbf{E}(\mathbf{r}_+) - \mathbf{E}(\mathbf{r}_-)). \quad (\text{C.21})$$

Performing a Maclaurin expansion around $\mathbf{r}=0$:

$$\begin{aligned}\mathbf{F}_{elec} &\approx q\left(\mathbf{E}(0) + (\mathbf{r}_+ \cdot \nabla)\mathbf{E}(\mathbf{r})\Big|_{\mathbf{r}=0} + O(\mathbf{r}_+^2)\right) - q\left(\mathbf{E}(0) + (\mathbf{r}_- \cdot \nabla)\mathbf{E}(\mathbf{r})\Big|_{\mathbf{r}=0} + O(\mathbf{r}_-^2)\right), \\ \mathbf{F}_{elec} &\approx q\left(\left((\mathbf{r}_+ - \mathbf{r}_-) \cdot \nabla\right)\mathbf{E}(\mathbf{r})\Big|_{\mathbf{r}=0} + O(\mathbf{r}_+^2, \mathbf{r}_-^2)\right).\end{aligned}\quad (\text{C.22})$$

We can recognize the presence of the dipole moment, allowing the total electric force to be written as:

$$\mathbf{F}_{elec} \approx (\mathbf{p} \cdot \nabla)\mathbf{E}(0). \quad (\text{C.23})$$

Now, looking to the magnetic fields contribution to the force in Eq.(C.1) for a dipole gives:

$$\mathbf{F}_{mag} = q \frac{d\mathbf{r}_+}{dt} \times \mathbf{B}(\mathbf{r}_+) - q \frac{d\mathbf{r}_-}{dt} \times \mathbf{B}(\mathbf{r}_-). \quad (\text{C.24})$$

Again performing a Maclaurin expansion around $\mathbf{r}=0$ gives:

$$\begin{aligned}\mathbf{F}_{mag} &\approx q \frac{d\mathbf{r}_+}{dt} \times (\mathbf{B}(0) + O(\mathbf{r}_+)) - q \frac{d\mathbf{r}_-}{dt} \times (\mathbf{B}(0) + O(\mathbf{r}_-)) \\ \mathbf{F}_{mag} &\approx q \left(\frac{d(\mathbf{r}_+ - \mathbf{r}_-)}{dt} \times \mathbf{B}(0) + O(\mathbf{r}_+^2, \mathbf{r}_-^2) \right).\end{aligned}\quad (\text{C.25})$$

Substituting in again the electric dipole moment and neglecting the higher order terms gives:

$$\mathbf{F}_{mag} \approx \left(\frac{d\mathbf{p}}{dt} \times \mathbf{B}(0) \right) = \frac{d}{dt}(\mathbf{p} \times \mathbf{B}(0)) - \left(\mathbf{p} \times \frac{\partial}{\partial t} \mathbf{B}(0) \right). \quad (\text{C.26})$$

Combing Eq. (C.23) and Eq.(C.26) gives the total force on a single electric dipole in terms of fields evaluate at the center:

$$\mathbf{F} = (\mathbf{p} \cdot \nabla)\mathbf{E} + \frac{d}{dt}(\mathbf{p} \times \mathbf{B}) - \left(\mathbf{p} \times \frac{\partial}{\partial t} \mathbf{B} \right). \quad (\text{C.27})$$

Using Maxwell's equations ($\partial\mathbf{B}/\partial t = -\nabla \times \mathbf{E}$), the above equation simplifies to:

$$\mathbf{F} = (\mathbf{p} \cdot \nabla)\mathbf{E} + \frac{d}{dt}(\mathbf{p} \times \mathbf{B}) + (\mathbf{p} \times (\nabla \times \mathbf{E})). \quad (\text{C.28})$$

A further simplification may be found using the identity in Eq.(C.11)

$$\mathbf{p} \times (\nabla \times \mathbf{E}) = \nabla (\mathbf{p} \cdot \mathbf{E}) - \mathbf{E} \times (\nabla \times \mathbf{p}) - (\mathbf{p} \cdot \nabla) \mathbf{E} - (\mathbf{E} \cdot \nabla) \mathbf{p}. \quad (\text{C.29})$$

If the dipole moment is fixed in space, the spatial derivatives are 0, Eq.(C.29) simplifies to:

$$\mathbf{p} \times (\nabla \times \mathbf{E}) = \nabla (\mathbf{p} \cdot \mathbf{E}) - (\mathbf{p} \cdot \nabla) \mathbf{E}. \quad (\text{C.30})$$

A fixed dipole moment also means $\nabla (\mathbf{p} \cdot \mathbf{E}) = (\mathbf{p} \cdot \nabla) \mathbf{E}$, such that the force expression is now:

$$\mathbf{F} = (\mathbf{p} \cdot \nabla) \mathbf{E} + \frac{d}{dt} (\mathbf{p} \times \mathbf{B}). \quad (\text{C.31})$$

Since for our application we are concerned with optical fields, the particle dynamics will respond to the time averaged field. For time harmonic fields, $\mathbf{p}(\mathbf{r}, t) = \Re[\mathbf{p}_0 \exp(-i\omega t)]$, $\mathbf{E}(\mathbf{r}, t) = \Re[\mathbf{E}_0 \exp(-i\omega t)]$, and $\mathbf{B}(\mathbf{r}, t) = \Re[\mathbf{B}_0 \exp(-i\omega t)]$. The time averaged force is then found from:

$$\langle \mathbf{F} \rangle = \frac{1}{2\pi} \int_0^{2\pi} \left((\mathbf{p} + \mathbf{p}^*) \cdot \nabla \right) (\mathbf{E} + \mathbf{E}^*) + \frac{d}{dt} \left((\mathbf{p} + \mathbf{p}^*) \times (\mathbf{B} + \mathbf{B}^*) \right) d(\omega t). \quad (\text{C.32})$$

After integration, the time averaged force is found to be:

$$\langle \mathbf{F} \rangle = \frac{1}{2} \Re \left[(\mathbf{p}_0 \cdot \nabla) \mathbf{E}_0^* + \frac{d}{dt} (\mathbf{p}_0 \times \mathbf{B}_0^*) \right]. \quad (\text{C.33})$$

For a time harmonic field, $d\mathbf{p}_0/dt = -i\omega\mathbf{p}_0$, such that the force is found as:

$$\langle \mathbf{F} \rangle = \frac{1}{2} \Re \left[(\mathbf{p}_0 \cdot \nabla) \mathbf{E}_0^* - i\omega (\mathbf{p}_0 \times \mathbf{B}_0^*) \right]. \quad (\text{C.34})$$

Similarly taking the time derivative of the magnetic field, and also substituting into Maxwell's equations, $\mathbf{B}_0^* = -1/i\omega \nabla \times \mathbf{E}_0^*$, allows the force from a single dipole is found in terms of the dipole moment and electric field

$$\langle \mathbf{F} \rangle = \frac{1}{2} \Re \left[(\mathbf{p}_0 \cdot \nabla) \mathbf{E}_0^* + (\mathbf{p}_0 \times (\nabla \times \mathbf{E}_0^*)) \right]. \quad (\text{C.35})$$

C2. Different, Equivalent, Expressions for the Electromagnetic Force on a Dipole

As stated earlier, due to the many coupled equations in electromagnetics, there are different, equivalent, means to express the total electromagnetic force. Depending on the situation, different methods will allow for different interpretation to the physical origin of the behavior.

For a dipole, the electric dipole moment may also be expressed as a function of both the exciting field and the intrinsic tensorial polarizability:

$$\mathbf{p}_0 = \bar{\bar{\alpha}} \mathbf{E}_0^*. \quad (\text{C.36})$$

For spherical particles, the polarizability may be treated as a scalar. Substituting a scalar polarizability describing the dipole moment into Eq.(C.35) gives:

$$\langle \mathbf{F} \rangle = \frac{1}{2} \Re \left[\alpha (\mathbf{E}_0 \cdot \nabla) \mathbf{E}_0^* + \alpha (\mathbf{E}_0 \times (\nabla \times \mathbf{E}_0^*)) \right]. \quad (\text{C.37})$$

Looking in the i th direction, the force is may be recast as:

$$\langle F_i \rangle = \frac{1}{2} \Re (\alpha \mathbf{E} \cdot \partial^i \mathbf{E}^*), \quad (\text{C.38})$$

however, this form makes physical interpretation rather difficult. Separating the force the two components of Eq. (C.37) as:

$$\begin{aligned} \langle \mathbf{F} \rangle &= \langle \mathbf{F}_1 \rangle + \langle \mathbf{F}_2 \rangle \\ \langle \mathbf{F}_1 \rangle &= \frac{1}{2} \Re [\alpha (\mathbf{E} \cdot \nabla) \mathbf{E}^*] \\ \langle \mathbf{F}_2 \rangle &= \frac{1}{2} \Re [\alpha (\mathbf{E} \times (\nabla \times \mathbf{E}^*))] \end{aligned} \quad (\text{C.39})$$

Applying some basic vector calculus identities, other forms may be found. As in general the polarizability is a complex, one physically intuitive means of expressing the force would be in terms of the real and imaginary parts of the polarizability. Working first on $\langle \mathbf{F}_1 \rangle$, separating the terms gives:

$$\frac{1}{2} \Re(\alpha (\mathbf{E} \cdot \nabla) \mathbf{E}^*) = \frac{1}{2} \Re(\alpha) \Re((\mathbf{E} \cdot \nabla) \mathbf{E}^*) - \frac{1}{2} \Im(\alpha) \Im((\mathbf{E} \cdot \nabla) \mathbf{E}^*). \quad (\text{C.40})$$

Expanding the real part of the first part gives:

$$\Re((\mathbf{E} \cdot \nabla) \mathbf{E}^*) = \frac{1}{2} ((\mathbf{E} \cdot \nabla) \mathbf{E}^* + (\mathbf{E}^* \cdot \nabla) \mathbf{E}), \quad (\text{C.41})$$

After which we may apply the vector identity of Eq.(C.11) to give the relationship:

$$(\mathbf{E} \cdot \nabla) \mathbf{E}^* = \nabla(\mathbf{E}^* \cdot \mathbf{E}) - \mathbf{E}^* \times (\nabla \times \mathbf{E}) - \mathbf{E} \times (\nabla \times \mathbf{E}^*) - (\mathbf{E}^* \cdot \nabla) \mathbf{E}, \quad (\text{C.42})$$

such that Eq.(C.41) becomes:

$$((\mathbf{E} \cdot \nabla) \mathbf{E}^*) = \frac{1}{2} (\nabla |\mathbf{E}|^2 - \mathbf{E} \times (\nabla \times \mathbf{E}^*) - \mathbf{E}^* \times (\nabla \times \mathbf{E})). \quad (\text{C.43})$$

Now, $\langle \mathbf{F}_1 \rangle$ may now be written as:

$$\langle \mathbf{F}_1 \rangle = \frac{1}{2} \Re(\alpha) (\nabla |\mathbf{E}|^2 - \mathbf{E} \times (\nabla \times \mathbf{E}^*) - \mathbf{E}^* \times (\nabla \times \mathbf{E})) - \frac{1}{2} \Im(\alpha) \Im((\mathbf{E} \cdot \nabla) \mathbf{E}^*). \quad (\text{C.44})$$

Turning out attention to $\langle \mathbf{F}_2 \rangle$, and applying a similar expansion of the real and imaginary part of the polarizability gives:

$$\begin{aligned} \langle \mathbf{F}_2 \rangle &= \frac{1}{2} \Re(\alpha (\mathbf{E} \times (\nabla \times \mathbf{E}^*))) = \frac{1}{2} \Re(\alpha) \Re(\mathbf{E} \times (\nabla \times \mathbf{E}^*)) \\ &\quad - \frac{1}{2} \Im(\alpha) \Im(\mathbf{E} \times (\nabla \times \mathbf{E}^*)) \end{aligned} \quad (\text{C.45})$$

Again expanding the first term gives:

$$\Re(\mathbf{E} \times (\nabla \times \mathbf{E}^*)) = \frac{1}{2}(\mathbf{E} \times (\nabla \times \mathbf{E}^*) + \mathbf{E}^* \times (\nabla \times \mathbf{E})), \quad (\text{C.46})$$

which upon substituting into Eq.(C.45) yields:

$$\langle \mathbf{F}_2 \rangle = \frac{1}{2} \Re(\alpha) (\mathbf{E} \times (\nabla \times \mathbf{E}^*) + \mathbf{E}^* \times (\nabla \times \mathbf{E})) - \frac{1}{2} \Im(\alpha) \Im(\mathbf{E} \times (\nabla \times \mathbf{E}^*)). \quad (\text{C.47})$$

Combining Eq.(C.44) and Eq.(C.47), the total force is found to be:

$$\langle \mathbf{F} \rangle = \frac{1}{2} \Re(\alpha) \nabla |\mathbf{E}|^2 - \frac{1}{2} \Im(\alpha) \Im(\mathbf{E} \times (\nabla \times \mathbf{E}^*)) - \frac{1}{2} \Im(\alpha) \Im((\mathbf{E} \cdot \nabla) \mathbf{E}^*). \quad (\text{C.48})$$

As a final substitution, consider again Maxwell's equations and that $\nabla \times \mathbf{E}^* = -i\omega\mu_0 \mathbf{H}^*$

$$\langle \mathbf{F} \rangle = \frac{1}{2} \Re(\alpha) \nabla |\mathbf{E}|^2 + \frac{\omega\mu_0}{2} \Im(\alpha) \Re(\mathbf{E} \times \mathbf{H}^*) - \frac{1}{2} \Im(\alpha) \Im((\mathbf{E} \cdot \nabla) \mathbf{E}^*). \quad (\text{C.49})$$

Assuming time harmonic fields, time averaging Eq.(C.9), the time averaged Poynting vector is

$$\langle \mathbf{S} \rangle = \frac{1}{2} \Re(\mathbf{E} \times \mathbf{H}^*), \quad (\text{C.50})$$

which we may readily identify in Eq.(C.49), such that we have:

$$\langle \mathbf{F} \rangle = \frac{1}{2} \Re(\alpha) \nabla |\mathbf{E}|^2 + \omega\mu_0 \Im(\alpha) \langle \mathbf{S} \rangle - \frac{1}{2} \Im(\alpha) \Im((\mathbf{E} \cdot \nabla) \mathbf{E}^*). \quad (\text{C.51})$$

This is the conventional 3 term separation of the forces due to an applied electric field onto a single dipole[73,120,121]. The first term known as the gradient force depends on the gradient of the intensity of the field; also as this term depends is the only component depending on the real part of the polarizability, the real part does not see the phase of the field. The second term is depends on the time averaged energy flux of the applied field. This term is usually referred to as the radiation pressure, and depends on the imaginary part of the polarizability; therefore, as the work accomplished by this force is considered loss, it is a nonconservative force. The third term is usually unnamed in the literature, however; recently it was shown that it

is related to the spin momentum of the applied field [74]. Let us expand the third term of the force as:

$$\frac{1}{2} \Im(\alpha) \Im((\mathbf{E} \cdot \nabla) \mathbf{E}^*) = \frac{-i}{4} \Im(\alpha) ((\mathbf{E} \cdot \nabla) \mathbf{E}^* - (\mathbf{E}^* \cdot \nabla) \mathbf{E}). \quad (\text{C.52})$$

Using the identity: $(B \cdot \nabla) A = \nabla \times A \times B - A(\nabla \cdot B) + (A \cdot \nabla) B - B(\nabla \cdot A)$, one can write:

$$(\mathbf{E}^* \cdot \nabla) \mathbf{E} = \nabla \times \mathbf{E} \times \mathbf{E}^* - \mathbf{E}(\nabla \cdot \mathbf{E}^*) + (\mathbf{E} \cdot \nabla) \mathbf{E}^* - \mathbf{E}^*(\nabla \cdot \mathbf{E})$$
 For applied fields where $\nabla \cdot \mathbf{E} = 0$,

substituting the identity into Eq.(C.52) gives:

$$\frac{1}{2} \Im(\alpha) \Im((\mathbf{E} \cdot \nabla) \mathbf{E}^*) = \frac{i}{4} \Im(\alpha) (\nabla \times \mathbf{E} \times \mathbf{E}^*). \quad (\text{C.53})$$

From which, one may recognize the time averaged spin flux density $\langle \mathbf{L}_S \rangle = \frac{\varepsilon_0}{i4\omega} (\mathbf{E} \times \mathbf{E}^*)$. Upon

substituting in the spin flux density into Eq.(C.53) gives:

$$\frac{1}{2} \Im(\alpha) \Im((\mathbf{E} \cdot \nabla) \mathbf{E}^*) = -\frac{\omega}{\varepsilon_0} \Im(\alpha) (\nabla \times \langle \mathbf{L}_S \rangle). \quad (\text{C.54})$$

Writing the total force gives:

$$\langle \mathbf{F} \rangle = \frac{1}{2} \Re(\alpha) \nabla |\mathbf{E}|^2 + \omega \mu_0 \Im(\alpha) \langle \mathbf{S} \rangle + \frac{\omega}{\varepsilon_0} \Im(\alpha) (\nabla \times \langle \mathbf{L}_S \rangle). \quad (\text{C.55})$$

The force as expressed in this way allows one to discuss the different physical origins of both the conservative and non-conservative components. The total force is now thought of as:

$$\begin{aligned} \langle \mathbf{F} \rangle &= \langle \mathbf{F}_{grad} \rangle + \langle \mathbf{F}_{press} \rangle + \langle \mathbf{F}_{spin} \rangle \\ \langle \mathbf{F}_{grad} \rangle &= \frac{1}{2} \Re(\alpha) \nabla |\mathbf{E}|^2 \\ \langle \mathbf{F}_{press} \rangle &= \omega \mu_0 \Im(\alpha) \langle \mathbf{S} \rangle \\ \langle \mathbf{F}_{spin} \rangle &= \frac{\omega}{\varepsilon_0} \Im(\alpha) (\nabla \times \langle \mathbf{L}_S \rangle) \end{aligned} \quad (\text{C.56})$$

D. Sub-sampling and Non-Gaussian Statistics

Consider some random process X composed of n independent elements. Each of the elements is a random variable picked from the same governing distribution. We would like to evaluate how the statistics (moments) of the ensemble X evolve with the number of elements making the ensemble. The random process X can be defined as:

$$X_j(n) = \{x_1, x_2, \dots, x_n\}, \quad (\text{D.1})$$

having n independent elements. The first moment of X is defined as:

$$E[x] = \mu = \int_{-\infty}^{\infty} x f_x(x) dx, \quad (\text{D.2})$$

for some probability distribution $f_x(x)$. To find how the first moment evolves with n , we can define a new random variable that acts as the first moment of the random process X

$$z_1 = \frac{1}{n} \sum_j^n x_j. \quad (\text{D.3})$$

The mean of z_1 is then found using Eq.(D.2):

$$E[z_1] = \frac{1}{n} \left(\sum_{j=1}^n \int_{-\infty}^{\infty} x_j f(x_j) dx_j \right). \quad (\text{D.4})$$

if each of the elements of the ensemble has the same distribution, then the average first moment of z_1 (X) is simply:

$$E[z_1] = \int_{-\infty}^{\infty} x f(x) dx = \mu. \quad (\text{D.5})$$

Eq.(D.5) shows that regardless of the number of elements in a subsampled distribution, and independent of the governing probability distribution, the mean is constant with sampling.

Another useful characteristic is the standard deviation, defined as the square root of the variance ($\sigma = \sqrt{\text{var}}$), where the variance is defined as:

$$\text{var} = E[(x - \mu)^2] = \int_{-\infty}^{\infty} (x - \mu)^2 f_x(x) dx = \int_{-\infty}^{\infty} x^2 f_x(x) dx - \mu^2. \quad (\text{D.6})$$

To find the variance, we can again define a random variable to represent the variance of X

$$z_2 = \frac{1}{n} \sum_{j=1}^n x_j^2 - \left(\frac{1}{n} \sum_{j=1}^n x_j \right)^2, \quad (\text{D.7})$$

however, because of the correlation between the first and second moment becomes important for a small number of elements, the calculation is not as straight forward as the mean. Another way of representing Eq.(D.7) as a summation is:

$$z_2 = g(x_1, x_2, \dots, x_n) = \frac{1}{n} \sum_{j=1}^n \left(x_j^2 \left(1 - \frac{1}{n} \right) - \sum_{k=1, k \neq j}^n \left(\frac{1}{n} (x_j x_k) \right) \right), \quad (\text{D.8})$$

where we have separated the terms dealing with x^2 and x . The end goal is to calculate the moments of z_2 . Because the elements of X are independent the integrals necessary to calculate the moments are separable; moreover, because each the elements are identically distributed, and $E[x_1 x_2] = E[x_1 x_3] = \dots = E[x_a x_b]$, we can write z_2 in terms of the correlation of some arbitrary random variable x_b of the same distribution independent of x_j , and remove the sum over k .

$$z_2' = g(x_1, x_2, \dots, x_n) = \frac{1}{n} \sum_{j=1}^n \left(x_j^2 \left(1 - \frac{1}{n} \right) - \frac{n-1}{n} x_j x_b \right), \quad (\text{D.9})$$

Now z_2' is simply a sum of independent random variables with a distribution different than that of the elements. As we saw in Eq.(D.4), for a sum of identically distributed

independent random variables, the mean is simply n times the average of one of them. Therefore can write the expectation value in terms of two arbitrary independent elements of X x_a and x_b :

$$E[z_2'] = nE\left[\frac{1}{n}\left(1 - \frac{1}{n}\right)(x_a^2 - x_a x_b)\right] = \left(1 - \frac{1}{n}\right)E[(x_a^2 - x_a x_b)], \quad (\text{D.10})$$

To calculate the expectation value of z_2 , we can use the characteristic function method [122], where the characteristic function for a function of random variables is defined in terms of joint probability distribution function.

$$\Phi_s(s, n) = \left(1 - \frac{1}{n}\right) \int_{-\infty}^{\infty} \int_{-\infty}^{\infty} \exp(is(x_a^2 - x_a x_b)) f_x(x_a, x_b) dx_a dx_b, \quad (\text{D.11})$$

As can be seen in Eq.(D.11) the characteristic function, and therefore the average variance of the ensemble X as a function of n depends on the governing probability distribution, unlike the first moment. Therefore, as a simple example, we will look at a Gaussian distributed random variable having a PDF:

$$f_x(x) = \frac{1}{\sqrt{2\pi}\sigma_0} \exp\left(\frac{-(x - \mu)^2}{2\sigma_0^2}\right), \quad (\text{D.12})$$

where here μ and σ_0 are the mean and standard deviation for an infinite number of elements. Because x_j and x_0 are independent there joint distribution is simply the multiplication of there mutual distributions. Plugging in the Gaussian distribution into Eq.(D.11) the characteristic function is found as:

$$\Phi_s(s, n) = \left(1 - \frac{1}{n}\right) \exp\left(\frac{\mu^2 \sigma_0^2 s^2}{2is\sigma_0^2 - 1 - s^2 \sigma_0^4}\right) \left(1 + \sigma_0^4 s^2 - 2is\sigma_0^2\right)^{\frac{1}{2}}, \quad (\text{D.13})$$

After finding the characteristic function, the N^{th} moment is found from [122]:

$$E[x^N] = (-i)^N \frac{\partial^N}{\partial s^N} \Phi(s) \Big|_{s=0}, \quad (\text{D.14})$$

The first moment of z^2 , the variance of X having n elements is:

$$\text{var} = \frac{n-1}{n} \sigma_0^2. \quad (\text{D.15})$$

Taking the square route, finally gives us that the standard deviation as a function of the number of elements n in the ensemble X is found as:

$$\sigma(n) = \sqrt{\frac{n-1}{n}} \sigma_0. \quad (\text{D.16})$$

We can also look at how the shape changes with n by calculating the contrast, giving us:

$$C(n) = \frac{\sqrt{\frac{n-1}{n}} \sigma_\infty}{\mu} = \sqrt{\frac{n-1}{n}} C_\infty, \quad (\text{D.17})$$

Thus, as we can see, for any subsampling of the distribution, the contrast is always smaller than the governing distribution.

E. Additional Details for SSP

E1. Polynomial Expressions for SSP

In this Appendix we present the exact form of the polynomials $P_{ij}^{(n)}(\varepsilon)$ that enter the expressions for the second order moments $M_{ij}^{(2)}$ in Eq.(8). In obtaining these results, an ensemble average was applied to the product of two intensities $I_i I_j$ and then terms containing different orders of δ_1 , and δ_2 . were collected.

$$\begin{aligned}
 P_{xx}^{(1)}(\varepsilon) &= \frac{3}{35} \left((Q_1 + 3)^2 \varepsilon^2 + 2(Q_1 K + (Q_2 + 3)) \varepsilon + (K + 3) \right), \\
 P_{xx}^{(2)}(\varepsilon) &= \frac{6}{5} \left(Q_1(Q_1 + 3) \varepsilon^2 + (2Q_1 K + Q_2) \varepsilon + K(K + 3) \right), \\
 P_{xx}^{(3)}(\varepsilon) &= \frac{8}{35} \left(Q_1(Q_1 - 9) \varepsilon^2 + (2Q_1 K - 3Q_2) \varepsilon + K(K - 9) \right), \\
 P_{xx}^{(4)} &= Q_1^2 \varepsilon^2 + 2KQ_1 \varepsilon + K^2,
 \end{aligned} \tag{E.1}$$

$$P_{yy}^{(1)}(\varepsilon) = \frac{3}{35} \left((L + 3)^2 \varepsilon^2 + 2(L + 3) \varepsilon + 9 \right), \quad P_{yy}^{(2)}(\varepsilon) = \frac{6}{5} \left(L(L + 3) \varepsilon^2 + L \varepsilon \right), \tag{E.2}$$

$$\begin{aligned}
 P_{yy}^{(3)}(\varepsilon) &= \frac{8}{35} \left(L(L - 9) \varepsilon^2 - 3L \varepsilon \right), \quad P_{yy}^{(4)}(\varepsilon) = L^2 \varepsilon^2, \\
 P_{xy}^{(1)}(\varepsilon) &= \frac{3}{35} \left((LQ_1 + Q_3 + 3) \varepsilon^2 + 2(7 + 10LK) \varepsilon + 3 + K \right), \\
 P_{xy}^{(2)}(\varepsilon) &= \frac{3}{5} \left((2LQ_1 + Q_3) \varepsilon^2 + (1 - LK) \varepsilon + K \right), \\
 P_{xy}^{(3)}(\varepsilon) &= \frac{4}{35} \left((2LQ_1 - 3Q_3) \varepsilon^2 + 2(3 + KL) \varepsilon - 3K \right), \\
 P_{xy}^{(4)}(\varepsilon) &= LQ_1 \varepsilon^2 + KL \varepsilon,
 \end{aligned} \tag{E.3}$$

where the following notations were used:

$$L = \cos^2(\Phi), \quad K = \cos^2(\psi), \quad (E.4)$$

$$Q_1 = 1 - K - L + KL, \quad Q_2 = 1 - L + KL, \quad Q_3 = 1 - K + KL.$$

The meaning of angles Φ and ψ is that depicted in Figure 6-1.

E2. Derivation of Rotation of Unknown Incident Field Angle

There are possible solutions in the case before, however, the equations are not unique when $L=K$, when we are at 45 degree incidence: If we rotate every measured M by the same angle, we would not lose any of the statistics, so in order to find a useful angle we look at the first moment and define a useful angle, also in doing this we can eliminate 1 of our 5 unknowns

$$M^1 = \begin{bmatrix} \langle E_x^* E_x \rangle & \langle E_x^* E_y \rangle \\ \langle E_y^* E_x \rangle & \langle E_y^* E_y \rangle \end{bmatrix} = \begin{bmatrix} \langle I_x \rangle & \langle E_x^* E_y \rangle \\ \langle E_y^* E_x \rangle & \langle I_y \rangle \end{bmatrix} \quad (E.5)$$

We would like a case when the cross terms are very small for the first moment. So there exist and rotation such that:

$$\tilde{M}^1 = R M^1 R^{-1} \quad (E.6)$$

where: $R = \begin{bmatrix} \cos \zeta & -\sin \zeta \\ \sin \zeta & \cos \zeta \end{bmatrix}$

$$\begin{aligned} \tilde{M}_{12}^1 &= \langle E_x^* E_y \rangle \cos^2 \zeta + (\langle I_x \rangle - \langle I_y \rangle) \cos \zeta \sin \zeta - \langle E_y^* E_x \rangle \sin^2 \zeta \\ \tilde{M}_{21}^1 &= \langle E_y^* E_x \rangle \cos^2 \zeta + (\langle I_x \rangle - \langle I_y \rangle) \cos \zeta \sin \zeta - \langle E_x^* E_y \rangle \sin^2 \zeta \end{aligned} \quad (E.7)$$

If we are willing to live with sacrificing a little statistical information that will exist in the phase, we can make the condition of the real part equal to zero so we can find this unknown angle zeta

$$\begin{aligned}
\Re(E_x^* E_y) &= \Re(E_y^* E_x) \\
\Re(E_x^* E_y) (\cos^2 \zeta - \sin^2 \zeta) + (\langle I_x \rangle - \langle I_y \rangle) \cos \zeta \sin \zeta &= 0 \\
\zeta &= \frac{\langle I_x \rangle - \langle I_y \rangle + \sqrt{\langle I_x \rangle^2 - 2\langle I_x \rangle \langle I_y \rangle + 4\Re(E_x^* E_y)^2}}{2\Re(E_x^* E_y)}, \\
\langle I_x \rangle - \langle I_y \rangle - \sqrt{\langle I_x \rangle^2 - 2\langle I_x \rangle \langle I_y \rangle + 4\Re(E_x^* E_y)^2} & \\
&\quad \quad \quad 2\Re(E_x^* E_y)
\end{aligned} \tag{E.8}$$

If we have another measurement at 45 degrees with respect to our other orthogonal measurements, we can look at this ExEy term. Also if we look at only the real part of ExEy...

$$\begin{aligned}
I_{45} &= \frac{1}{2} I_x + \frac{1}{2} I_y + \frac{1}{2} E_x^* E_y + \frac{1}{2} E_x E_y^* \\
2\Re(E_x E_y^*) &= 2\langle I_{45} \rangle - \langle I_x \rangle - \langle I_y \rangle
\end{aligned} \tag{E.9}$$

$$\begin{aligned}
\zeta &= \tan^{-1} \left(\frac{\langle I_x \rangle - \langle I_y \rangle + \sqrt{\langle I_x \rangle^2 + \langle I_y \rangle^2 - 2\langle I_x \rangle \langle I_y \rangle + 4(\langle I_{45} \rangle - .5\langle I_x \rangle - .5\langle I_y \rangle)^2}}{2(\langle I_{45} \rangle - .5\langle I_x \rangle - .5\langle I_y \rangle)} \right), \\
\zeta &= \tan^{-1} \left(\frac{\langle I_x \rangle - \langle I_y \rangle - \sqrt{\langle I_x \rangle^2 + \langle I_y \rangle^2 - 2\langle I_x \rangle \langle I_y \rangle + 4(\langle I_{45} \rangle - .5\langle I_x \rangle - .5\langle I_y \rangle)^2}}{2(\langle I_{45} \rangle - .5\langle I_x \rangle - .5\langle I_y \rangle)} \right)
\end{aligned} \tag{E.10}$$

All of the moments we are looking at deal with having distributions for 2 orthogonal directions. We can now write these distributions as a function of this new angle, and the three measurement distributions taken

$$\begin{aligned}
\tilde{I}_x &= I_x \cos^2 \zeta + I_y \sin^2 \zeta - 2E_x E_y \cos \zeta \sin \zeta \\
\therefore \tilde{I}_x &= I_x \cos^2 \zeta + I_y \sin^2 \zeta - 2(I_{45} - .5I_x - .5I_y) \cos \zeta \sin \zeta \\
\tilde{I}_y &= I_x \sin^2 \zeta + I_y \cos^2 \zeta + 2E_x E_y \cos \zeta \sin \zeta \\
\therefore \tilde{I}_y &= I_x \sin^2 \zeta + I_y \cos^2 \zeta + 2(I_{45} - .5I_x - .5I_y) \cos \zeta \sin \zeta
\end{aligned} \tag{E.11}$$

$$\eta = \frac{\sin^2 \sqrt{\nu^2 + \xi^2}}{1 + \xi^2/\nu^2}. \quad (\text{E.12})$$

E3. Numerically Modeling Near-field Excitation

There are many different approaches taken to approximate the fields generated in emission mode NSOM [123]. The simplest model consists of considering the tip to act as a electric dipole. This approximation may describe some of the characteristics of the fields far from the tip, however the influence of the tip aperture has a dramatic effect very close to the probe. However, this model can be useful in approximating the coupling between the scattered light and the probe. Another model that has been proposed makes use of the coupled dipole approximation discussed earlier [124]. In this situation, the tip is modeled by an array of dipoles with properties corresponding to the core, cladding and metallic coating. This method is a better way to model the tip, however the actual dimensions of the aperture and thickness of the coating are unique for individual tips and in the statistical situations we are concerned with, perhaps such a robust model may not be needed.

The most common method of modeling the tip is to consider the fields generated from diffraction from a small aperture in a perfectly conducting screen. This was first derived by Bethe [125], and then corrected for the near-field by Bouwkamp [110]. The Bethe-Bouwkamp solutions are both valid in their respective regions. To have such a model for our coupled dipole excitation, we require the possibility to calculate the fields at any point and have a continuous field between them. There have been a few attempts to join the fields predicted by both solutions, however the different approaches take varying amounts of time to calculate and in most cases involve numerically evaluating double integrals.

The Bouwkamp solution for the field inside the aperture is:

(E.13)

From vector diffraction theory, knowing the field in the aperture, we can find it and at arbitrary point in the half space $z > 0$ [72]

$$\vec{E}(\vec{r}') = 2\nabla \times \int_S \vec{n} \times \vec{E}^o(\vec{r}') G(r, r') ds \quad (E.14)$$

In general, the field at any location in space can be calculated by solving:

$$\begin{aligned} E_x(\vec{r}') &= \frac{1}{2\pi} \int_0^{2\pi} \int_0^a E_x^o(\vec{r}') \left(\frac{-(z-z')}{R} ik \frac{e^{ikR}}{R} \left(1 - \frac{1}{ikR} \right) \right) \rho d\rho d\phi \\ E_y(\vec{r}') &= \frac{1}{2\pi} \int_0^{2\pi} \int_0^a -E_y^o(\vec{r}') \left(\frac{(z-z')}{R} ik \frac{e^{ikR}}{R} \left(1 - \frac{1}{ikR} \right) \right) \rho d\rho d\phi \\ E_z(\vec{r}') &= \frac{1}{2\pi} \int_0^{2\pi} \int_0^a \left(E_x^o(\vec{r}') \frac{(x-x')}{R} + E_y^o(\vec{r}') \frac{(y-y')}{R} \right) \left(ik \frac{e^{ikR}}{R} \left(1 - \frac{1}{ikR} \right) \right) \rho d\rho d\phi \end{aligned} \quad (E.15)$$

Where the distance R is defined as:

$$\begin{aligned} R &= \sqrt{(x-x')^2 + (y-y')^2 + (z-z')^2} \\ R &= \sqrt{(x-\rho' \cos \phi')^2 + (y-\rho' \sin \phi')^2 + (z-\rho' \cos \phi')^2} \end{aligned} \quad (E.16)$$

As can be seen in Eq.(E.15), a singularity arises when $\rho = a$ due to the diverging fields defined at the edge of the aperture. It is possible to avoid this diverging integral by integrating by parts which gives our final expressions for the tip excitation

$$\begin{aligned} E_x(\vec{r}') &= -\frac{4za^3 ke^{ikR_o} (kR_o + i)}{3\pi R_o^3} + \\ &\frac{1}{9\pi^2 R^5} \int_0^{2\pi} \int_0^a 2ik \sqrt{a^2 - \rho'^2} (2a^2 - 2\rho'^2 + 2a^2 \cos^2 \phi + \rho'^2 \cos^2 \phi) \times \\ &\quad (x \cos \phi + y \sin \phi - \rho) ze^{ikR} (3ikR - 3 + k^2 R^2) d\rho d\phi \end{aligned} \quad (E.17)$$

$$E_y(\vec{r}') = \frac{1}{9\pi^2 R^5} \int_0^{2\pi} \int_0^a 2ik\sqrt{a^2 - \rho'^2} (2a^2 + \rho'^2) \cos\phi \sin\phi (x \cos\phi + y \sin\phi - \rho) z e^{ikR} (3ikR - 3 + k^2 R^2) d\rho d\phi \quad (\text{E.18})$$

$$E_z(\vec{r}') = \frac{-xE_x(\vec{r}')}{z} - \frac{yE_y(\vec{r}')}{z} + \int_0^{2\pi} \int_0^a \left(\frac{4ik \cos\phi \sqrt{a^2 - \rho'^2} (4a^2 - \rho'^2)}{9\pi} \right) \times \left(\frac{1}{2\pi} \left(ik \frac{e^{ikR}}{R^2} \left(1 - \frac{1}{ikR} \right) \right) + \frac{\rho (x \cos\phi + y \sin\phi - \rho) e^{ikR} (3ikR - 3 + k^2 R^2)}{2\pi R^5} \right) d\rho d\phi \quad (\text{E.19})$$

As a simple demonstration, we can examine the behavior of the above expression for both the near and far-fields seen in Figure E-1.

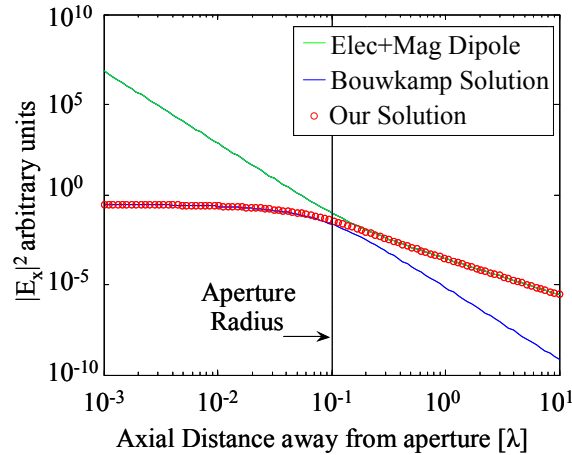


Figure E-1 Plot of magnitude of field for different models of field generated by diffraction from a small aperture. Bouwkamp, magnetic dipole, magnetic + crossed electric dipole, and the solutions found from evaluating numerically Eq.(E.17) – Eq.(E.19)

LIST OF REFERENCES

- 1 Chandra, S., Kable, E. P., Morrison, G. H., and Webb, W. W., "Calcium sequestration in the Golgi apparatus of cultured mammalian cells revealed by laser scanning confocal microscopy and ion microscopy". *J. Cell. Sci.* 100 747 (1991).
- 2 Born, M. and Wolf, E., *Principles of optics : electromagnetic theory of propagation, interference and diffraction of light*, 6th (corr.) ed. (Cambridge University Press, Cambridge, UK ; New York ;, 1997).
- 3 Hofer, W. A., Foster, A. S., and Shluger, A. L., "Theories of scanning probe microscopes at the atomic scale". *Rev. Mod. Phys.* 75 (4), 1287 (2003).
- 4 Binnig, G., Quate, C. F., and Gerber, C., "Atomic Force Microscope". *Phys. Rev. Lett.* 56 (9), 930 (1986).
- 5 Tersoff, J. and Hamann, D. R., "Theory of the scanning tunneling microscope". *Phys. Rev. B* 31 (2), 805 (1985).
- 6 Martin, Y. and Wickramasinghe, H. K., "Magnetic imaging by ``force microscopy" with 1000 [Å-ring] resolution". *Appl. Phys. Lett.* 50 (20), 1455 (1987).
- 7 Giessibl, F. J., "Advances in atomic force microscopy". *Rev. Mod. Phys.* 75 (3), 949 (2003).
- 8 Hartmann, U., "Magnetic force microscopy". *Annu. Rev. Mater. Sci.* 29, 53 (1999).
- 9 Dunn, R. C., "Near-field scanning optical microscopy". *Chem. Rev.* 99 (10), 2891 (1999).
- 10 Betzig, E. and Trautman, J. K., "Near-Field Optics: Microscopy, Spectroscopy, and Surface Modification Beyond the Diffraction Limit". *Science* 257 (5067), 189 (1992).
- 11 Balanis, C. A., *Antenna theory : analysis and design*, 2nd ed. (Wiley, New York, 1997).

-
- 12 Köhler, H., "On Abbe's Theory of Image Formation in the Microscope". *J. Mod. Optic.* 28 (12), 1691 (1981).
 - 13 Mansfield, S. M. and Kino, G. S., "Solid immersion microscope". *Appl. Phys. Lett.* 57 (24), 2615 (1990).
 - 14 Jabbour, T. G. and Kuebler, S. M., "Axial field shaping under high-numerical-aperture focusing". *Opt. Lett.* 32 (5), 527 (2007).
 - 15 Hettich, C. et al., "Nanometer Resolution and Coherent Optical Dipole Coupling of Two Individual Molecules". *Science* 298 (5592), 385 (2002).
 - 16 Synge, E. H., "A suggested method for extending the microscopic resolution into the ultramicroscopic region". *Philos Mag* 6, 356 (1928).
 - 17 Vigoureux, J. M. and Courjon, D., "Detection of nonradiative fields in light of the Heisenberg uncertainty principle and the Rayleigh criterion". *Appl. Opt.* 31 (16), 3170 (1992).
 - 18 Novotny, L. and Wolf, E., in *Progress in Optics* (Elsevier, 2007), Vol. 50, pp. 137.
 - 19 Lewis, A., Isaacson, M., Harootunian, A., and Muray, A., "Development of a 500 Å spatial resolution light microscope: I. light is efficiently transmitted through $[\lambda]/16$ diameter apertures". *Ultramicroscopy* 13 (3), 227 (1984).
 - 20 Pohl, D. W., Denk, W., and Lanz, M., "Optical stethoscopy: Image recording with resolution $\lambda/20$ ". *Appl. Phys. Lett.* 44 (7), 651 (1984).
 - 21 Yung-Hui, C. et al., "A simple chemical etching technique for reproducible fabrication of robust scanning near-field fiber probes". *Rev. Sci. Instrum.* 69 (2), 437 (1998).
 - 22 Novotny, L. and Hecht, B., *Principles of nano-optics*. (Cambridge University Press, Cambridge, 2006).
 - 23 Suh, Y. D. and Zenobi, R., "Improved Probes for Scanning Near-Field Optical Microscopy". *Adv. Mater* 12 (15), 1139 (2000).
 - 24 Yexian, Q. and Reifenberger, R., "Calibrating a tuning fork for use as a scanning probe microscope force sensor". *Rev. Sci. Instrum.* 78 (6), 063704 (2007).
 - 25 Inouye, Y. and Kawata, S., "Near-field scanning optical microscope with a metallic probe tip". *Opt. Lett.* 19 (3), 159 (1994).

-
- 26 Balistreri, M. L. M. et al., "Quantitative photon tunneling and shear-force microscopy of planar waveguide splitters and mixers". *J. Appl. Phys.* 89 (6), 3307 (2001).
- 27 Yee, K., "Numerical solution of initial boundary value problems involving maxwell's equations in isotropic media". *IEEE T. Antenn. Propag.* 14 (3), 302 (1966).
- 28 Hulst, H. C. v. d., *Light scattering by small particles*. (Dover Publications, New York, 1981).
- 29 Purcell, E. M. and Pennypacker, C. R., "Scattering and absorption of light by nonspherical dielectric grains". *Astrophys. J.* 186, 705 (1973).
- 30 DeVoe, H., "Optical Properties of Molecular Aggregates. I. Classical Model of Electronic Absorption and Refraction". *J. Chem. Phys.* 41 (2), 393 (1964).
- 31 Draine, B. T. and Flatau, P. J., "Discrete-dipole approximation for scattering calculations". *J. Opt. Soc. Am. A* 11 (4), 1491 (1994).
- 32 Tsang, L., *Scattering of electromagnetic waves. Numerical simulations*. (J. Wiley, New York, 2001).
- 33 Goodman, J. J., Draine, B. T., and Flatau, P. J., "Application of fast-Fourier-transform techniques to the discrete-dipole approximation". *Opt. Lett.* 16 (15), 1198 (1991).
- 34 Dainty, J. C., *Laser speckle and related phenomena*. (Springer-Verlag, Berlin ; New York, 1984).
- 35 Barakat, R., "Direct derivation of intensity and phase statistics of speckle produced by a weak scatterer from the random sinusoid model". *J. Opt. Soc. Am.* 71 (1), 86 (1981).
- 36 Barakat, R., "First-order Statistics of Combined Random Sinusoidal Waves with Applications to Laser Speckle Patterns". *Opt. Acta.* 21 (11), 903 (1974).
- 37 Goodman, J. W., *Statistical optics*. (Wiley, New York, 1985).
- 38 Apostol, A. and Dogariu, A., "Non-Gaussian statistics of optical near-fields". *Phys. Rev. E* 72 (2), 025602 (2005).
- 39 Courjon, D., *Near-Field Microscopy and Near-Field Optics*. (Imperial College Press, London, 2003).
- 40 Wolf, E., *Introduction to the Theory of Coherence and Polarization of Light*. (Cambridge University Press, Cambridge, England, 2007).

-
- 41 Allen, L., Barnett, S. M., and Padgett, M. J., *Optical angular momentum*. (Institute of Physics Pub., Bristol, 2003).
- 42 Li, C.-F., "Unified theory for Goos-Hänchen and Imbert-Fedorov effects". *Phys. Rev. A* 76 (1), 013811 (2007).
- 43 Bliokh, K. Y. and Bliokh, Y. P., "Conservation of Angular Momentum, Transverse Shift, and Spin Hall Effect in Reflection and Refraction of an Electromagnetic Wave Packet". *Phys. Rev. Lett.* 96 (7), 073903 (2006).
- 44 Arnoldus, H. F. and Foley, J. T., "The dipole vortex". *Opt. Comm.* 231 (1-6), 115 (2004).
- 45 Schwartz, C. and Dogariu, A., "Conservation of angular momentum of light in single scattering". *Opt. Express* 14 (18), 8425 (2006).
- 46 Arnoldus, H. F., Li, X., and Shu, J., "Subwavelength displacement of the far-field image of a radiating dipole". *Opt. Lett.* 33 (13), 1446 (2008).
- 47 Bohren, C. F. and Huffman, D. R., *Absorption and scattering of light by small particles*, Wiley Professional Paperback ed. (Wiley, New York, 1998).
- 48 Sukhov, S. V. and Krutitsky, K. V., "Discrete structure of ultrathin dielectric films and their surface optical properties". *Phys. Rev. B* 65 (11), 115407 (2002).
- 49 Shamlo, N. B., "Matlab Toolbox for High Resolution Vector Field Visualization with Application in Improving the Understanding of Crack Propagation Mechanisms", San Diego State University, 2005.
- 50 Lazzaroni, M. and Zocchi, F. E., "Optical coupling from plane wave to step-index single-mode fiber". *Opt. Comm.* 237 (1-3), 37 (2004).
- 51 Aiello, A., Lindlein, N., Marquardt, C., and Leuchs, G., "Transverse Angular Momentum and Geometric Spin Hall Effect of Light". *Phys Rev Lett* 103 (10), 100401 (2009).
- 52 Bliokh, K. Y., "Geometrodynamics of polarized light: Berry phase and spin Hall effect in a gradient-index medium". *J. Opt. A-Pure. Appl. Op.* 11 (9), 094009 (2009).
- 53 Bliokh, K. Y. and Bliokh, Y. P., "Polarization, transverse shifts, and angular momentum conservation laws in partial reflection and refraction of an electromagnetic wave packet". *Phys. Rev. E* 75 (6), 066609 (2007).
- 54 Bliokh, K. Y. and Desyatnikov, A. S., "Spin and orbital Hall effects for diffracting optical beams in gradient-index media". *Phys. Rev. A* 79 (1), 011807 (2009).

-
- 55 Bliokh, K. Y., Gorodetski, Y., Kleiner, V., and Hasman, E., "Coriolis effect in optics: unified geometric phase and spin-Hall effect". *Phys Rev Lett* 101 (3), 030404 (2008).
- 56 Bliokh, K. Y., Niv, A., Kleiner, V., and Hasman, E., "Geometrodynamics of spinning light". *Nat. Photon.* 2 (12), 748 (2008).
- 57 Gorodetski, Y., Niv, A., Kleiner, V., and Hasman, E., "Observation of the Spin-Based Plasmonic Effect in Nanoscale Structures". *Phys. Rev. Lett.* 101 (4), 043903 (2008).
- 58 Hosten, O. and Kwiat, P., "Observation of the spin hall effect of light via weak measurements". *Science* 319 (5864), 787 (2008).
- 59 Luo, H. et al., "Spin Hall effect of a light beam in left-handed materials". *Phys. Rev. A* 80 (4), 043810 (2009).
- 60 Onoda, M., Murakami, S., and Nagaosa, N., "Hall Effect of Light". *Phys. Rev. Lett.* 93 (8), 083901 (2004).
- 61 Qin, Y., Li, Y., He, H., and Gong, Q., "Measurement of spin Hall effect of reflected light". *Opt. Lett.* 34 (17), 2551 (2009).
- 62 Vuong, L. T. et al., "Electromagnetic spin-orbit interactions via scattering of subwavelength apertures". *Phys Rev Lett Accepted* (2010).
- 63 Hirsch, J. E., "Spin Hall Effect". *Phys. Rev. Lett.* 83 (9), 1834 (1999).
- 64 Liberman, V. S. and Zel'dovich, B. Y., "Spin-orbit interaction of a photon in an inhomogeneous medium". *Phys. Rev. A* 46 (8), 5199 (1992).
- 65 Dooghin, A. V., Kundikova, N. D., Liberman, V. S., and Zel'dovich, B. Y., "Optical Magnus effect". *Phys. Rev. A* 45 (11), 8204 (1992).
- 66 Corbino, O., "Azioni Elettromagnetiche Doyute Agli Ioni dei Metalli Devianti Dalla Traiettorìa Normale per Effetto di un Campo". *Il Nuovo Cimento* 1 (1), 397 (1911).
- 67 Schwartz, C. and Dogariu, A., "Backscattered polarization patterns determined by conservation of angular momentum". *J. Opt. Soc. Am. A* 25 (2), 431 (2008).
- 68 Chiou, T.-H. et al., "Circular Polarization Vision in a Stomatopod Crustacean". *Curr. Biol.* 18 (6), 429 (2008).
- 69 Depasse, F. and Vigoureux, J. M., "Optical binding force between two Rayleigh particles". *J. Phys. D Appl. Phys.* 27 (5), 914 (1994).

-
- 70 Karásek, V., Dholakia, K., and Zemánek, P., "Analysis of optical binding in one dimension". *Appl. Phys. B-Lasers O* 84 (1), 149 (2006).
- 71 Ashkin, A., "Acceleration and Trapping of Particles by Radiation Pressure". *Phys. Rev. Lett.* 24 (4), 156 (1970).
- 72 Jackson, J. D., *Classical Electrodynamics*, 3 ed. (John Wiley & Sons, Inc, New York, 1999).
- 73 Wong, V. and Ratner, M. A., "Gradient and nongradient contributions to plasmon-enhanced optical forces on silver nanoparticles". *Phys. Rev. B* 73 (7), 075416 (2006).
- 74 Albaladejo, S., Marqués, M. I., Laroche, M., and Sáenz, J. J., "Scattering Forces from the Curl of the Spin Angular Momentum of a Light Field". *Phys. Rev. Lett.* 102 (11), 113602 (2009).
- 75 Burns, M. M., Fournier, J.-M., and Golovchenko, J. A., "Optical binding". *Phys. Rev. Lett.* 63 (12), 1233 (1989).
- 76 Tatarkova, S. A., Carruthers, A. E., and Dholakia, K., "One-Dimensional Optically Bound Arrays of Microscopic Particles". *Phys. Rev. Lett.* 89 (28), 283901 (2002).
- 77 Guillon, M., Moine, O., and Stout, B., "Longitudinal Optical Binding of High Optical Contrast Microdroplets in Air". *Phys. Rev. Lett.* 96 (14), 143902 (2006).
- 78 Rodríguez, J. and Andrews, D. L., "Optical binding and the influence of beam structure". *Opt. Lett.* 33 (21), 2464 (2008).
- 79 Grzegorzczak, T. M., Kemp, B. A., and Kong, J. A., "Stable Optical Trapping Based on Optical Binding Forces". *Phys. Rev. Lett.* 96 (11), 113903 (2006).
- 80 Ellis, J. and Dogariu, A., "Optical Polarimetry of Random Fields". *Phys. Rev. Lett.* 95 (20), 203905 (2005).
- 81 Nieto-Vesperinas, M., Chaumet, P. C., and Rahmani, A., "Near-field photonic forces". *Philos Transact A Math Phys Eng Sci* 362 (1817), 719 (2004).
- 82 Mohanty, S., Andrews, J., and Gupta, P., "Optical binding between dielectric particles". *Opt. Express* 12 (12), 2746 (2004).
- 83 Barton, J. P., Alexander, D. R., and Schaub, S. A., "Theoretical determination of net radiation force and torque for a spherical particle illuminated by a focused laser beam". *J. Appl. Phys.* 66 (10), 4594 (1989).

-
- 84 Dienerowitz, M. et al., "Optical vortex trap for resonant confinement of metal nanoparticles". *Opt. Express* 16 (7), 4991 (2008).
- 85 Friese, M. E. J., Nieminen, T. A., Heckenberg, N. R., and Rubinsztein-Dunlop, H., "Optical alignment and spinning of laser-trapped microscopic particles". *Nature* 394 (6691), 348 (1998).
- 86 Miyakawa, K., Adachi, H., and Inoue, Y., "Rotation of two-dimensional arrays of microparticles trapped by circularly polarized light". *Applied Physics Letters* 84 (26), 5440 (2004).
- 87 Roichman, Y., Sun, B., Stolarski, A., and Grier, D. G., "Influence of Nonconservative Optical Forces on the Dynamics of Optically Trapped Colloidal Spheres: The Fountain of Probability". *Phys. Rev. Lett.* 101 (12), 128301 (2008).
- 88 Chaumet, P. C. and Billaudeau, C., "Coupled dipole method to compute optical torque: Application to a micropropeller". *J. Appl. Phys.* 101 (2007).
- 89 Hoekstra, A. G., Frijlink, M., Waters, L. B. F. M., and Sloot, P. M. A., "Radiation forces in the discrete-dipole approximation". *J. Opt. Soc. Am. A* 18 (8), 1944 (2001).
- 90 Keizer, J., *Statistical Thermodynamics of Nonequilibrium Processes*. (Springer, Berlin, 1987).
- 91 Chang, S. and Lee, S. S., "Optical torque exerted on a homogeneous sphere levitated in the circularly polarized fundamental-mode laser beam". *J. Opt. Soc. Am. B* 2 (11), 1853 (1985).
- 92 Reichert, M. and Stark, H., "Hydrodynamic coupling of two rotating spheres trapped in harmonic potentials". *Phys. Rev. E* 69 (3), 031407 (2004).
- 93 Sihvola, A. H. and Institution of Electrical Engineers., *Electromagnetic mixing formulas and applications*. (Institution of Electrical Engineers, London, 1999).
- 94 Schaefer, D. W. and Pusey, P. N., "Statistics of Non-Gaussian Scattered Light". *Phys. Rev. Lett.* 29 (13), 843 (1972).
- 95 Apostol, A. and Dogariu, A., "First- and second-order statistics of optical near fields". *Opt. Lett.* 29 (3), 235 (2004).
- 96 van Brakel, J., Modrý, S., and Svatá, M., "Mercury porosimetry: state of the art". *Powder Technol.* 29 (1), 1 (1981).

-
- 97 Karpov, S. V., Gerasimov, V. S., Isaev, I. L., and Markel, V. A., "Local anisotropy and giant enhancement of local electromagnetic fields in fractal aggregates of metal nanoparticles". *Phys. Rev. B* 72 (20), 205425 (2005).
- 98 Borghese, F., Denti, P., Saija, R., and Sindoni, O. I., "Optical properties of spheres containing a spherical eccentric inclusion". *J. Opt. Soc. Am. A* 9 (8), 1327 (1992).
- 99 Griaznov, V. et al., "Numerical Simulation of Light Backscattering by Spheres with Off-Center Inclusion. Application to the Lidar Case". *Appl. Opt.* 43 (29), 5512 (2004).
- 100 Videen, G. et al., "Light-scattering intensity fluctuations in microdroplets containing inclusions". *Appl. Opt.* 36 (24), 6115 (1997).
- 101 Mandel, L. and Wolf, E., *Optical coherence and quantum optics*. (Cambridge University Press, Cambridge ; New York, 1995).
- 102 Bruggeman, D. A. G., "Berechnung verschiedener physikalischer Konstanten von heterogenen Substanzen". *Ann. Phys. Leipzig* 24, 636 (1935).
- 103 Bonin, K. D. and Kresin, V. V., *Electric-dipole polarizabilities of atoms, molecules, and clusters*. (World Scientific, Singapore River Edge, NJ, 1997).
- 104 Chu, B., *Laser Light scattering: Basic Principles and Practice*, 2 ed. (Academic Press, San Diego, California, 1991).
- 105 Krichevsky, O. and Bonnet, G., "Fluorescence correlation spectroscopy: the technique and its applications". *Rep. Prog. Phys.* 65 (2), 251 (2002).
- 106 Haber, C., Ruiz, S. A., and Wirtz, D., "Shape anisotropy of a single random-walk polymer". *Proc. Natl. Acad. Sci. U S A* 97 (20), 10792 (2000).
- 107 Davis, B. J. and Carney, P. S., "Robust determination of the anisotropic polarizability of nanoparticles using coherent confocal microscopy". *J. Opt. Soc. Am. A* 25 (8), 2102 (2008).
- 108 Kendall, M. G., Stuart, A., Ord, J. K., and O'Hagan, A., *Kendall's advanced theory of statistics*, 6th ed. (Edward Arnold; Halsted Press, London, 1994).
- 109 Jakeman, E., "Polarization characteristics of non-Gaussian scattering by small particles". *Wave. Random Media* 5 (4), 427 (1995).
- 110 Bouwkamp, C. J., "Bethe's theory of diffraction by small holes". *Philips Res. Rep.* 5, 321 (1950).

-
- 111 Grober, R. D., Rutherford, T., and Harris, T. D., "Modal approximation for the electromagnetic field of a near-field optical probe". *Appl. Opt.* 35 (19), 3488 (1996).
- 112 Bates, A. P., Hopcraft, K. I., and Jakeman, E., "Particle shape determination from polarization fluctuations of scattered radiation". *J. Opt. Soc. Am. A* 14 (12), 3372 (1997).
- 113 Videen, G. et al., "Light Scattering Fluctuations of a Soft Spherical Particle Containing an Inclusion". *Appl. Opt.* 40 (24), 4054 (2001).
- 114 Merchiers, O., Saiz, J. M., González, F., and Moreno, F., "Probability density function of the intensity scattered by Rayleigh-particle aggregates. Evolution with optical properties". *J. Quant. Spectrosc. Ra.* 101 (3), 383 (2006).
- 115 Blinnikov, S. and Moessner, R., "Expansions for nearly Gaussian distributions". *Astron. Astrophys. Supplement Ser.* 130 (1), 193 (1998).
- 116 David, H. A. and Nagaraja, H. N., *Order Statistics* 3rd ed. (Wiley, New Jersey, 2003).
- 117 Owen, D. B. and Steck, G. P., "Moments of Order Statistics from the Equicorrelated Multivariate Normal Distribution". *Ann. Math. Stat.* 33 (4), 1286 (1962).
- 118 Pusey, P. N., "Number fluctuations of interacting particles". *J. Phys. A-Math. Gen.* 12 (10), 1805 (1979).
- 119 Abbe, E., "Beitrag zur Theorie des Mikroskops und der Mikroskopischen wahrnehmung". *Arch. Mikrosk. Anat. Entwicklung mech* 9, 413 (1873).
- 120 Arias-González, J. R. and Nieto-Vesperinas, M., "Optical forces on small particles: attractive and repulsive nature and plasmon-resonance conditions". *J. Opt. Soc. Am. A* 20 (7), 1201 (2003).
- 121 Wong, V. and Ratner, M. A., "Explicit computation of gradient and nongradient contributions to optical forces in the discrete-dipole approximation". *J. Opt. Soc. Am. B* 23 (9), 1801 (2006).
- 122 Andrews, L. C. and Phillips, R. L., *Mathematical Techniques for Engineers and Scientists*. (SPIE, 2003).
- 123 Courjon, D. and Bainier, C., "Near field microscopy and near field optics". *Rep. Prog. Phys.* 57 (10), 989 (1994).
- 124 Liu, A. et al., "Modeling illumination-mode near-field optical microscopy of Au nanoparticles". *J. Opt. Soc. Am. A* 18 (3), 704 (2001).

125 Bethe, H. A., "Theory of Diffraction by Small Holes". *Phys. Rev.* 66 (7-8), 163 (1944).